# INVESTIGATIONS IN NANOTECHNOLOGY: TAILORING OF MAGNETIC NANOMATERIALS FOR ELECTROMAGNETIC WAVE ABSORPTION

by

Michael John Giroux

A dissertation submitted to The Johns Hopkins University in conformity with the requirements for the degree of Doctor of Philosophy

Baltimore, Maryland

April 2019

**Abstract**

In recent years, there has been a growing interest in magnetic nanomaterials used as microwave-absorbing materials due to military and civil applications such as stealth technology and electromagnetic interference. They are used in portable electronic devices such as smart phones and mobile PCs to protect humans from exposure to electromagnetic pollution, which could increase the risk of cancer or other neural illnesses. In defense applications, the surface of ships, submarines, and aircrafts are coated with electromagnetic absorbing materials to reduce the radar cross section (RCS) and increase stealth capabilities.

Magnetic materials have long been used as radar absorbers on aircrafts, e.g., in the form of iron ball paint. The absorber is usually applied by painting the metal surface with mixtures of carbonyl iron and polymer which generates magnetic iron or ferrite particles *in situ* by decomposition and/or oxidation of iron carbonyl. While this approach has been demonstrated to be successful in reduction of the RCS, it can be expected that the poorly defined synthetic approach produces inhomogeneous layers of magnetic materials with a wide distribution of particle sizes and may also generate magnetic particles containing impurities. This lack of control over material structure makes it challenging to systematically study and improve magnetic materials for electromagnetic wave absorption.

This research explores the application of magnetic nanomaterials for electromagnetic wave absorption. We present organic solution synthesis routes towards preparation of a wide range of magnetic nanoparticles, including soft and hard magnetic materials. We have been able to manipulate the synthetic conditions to tune the particle size, shape, and composition to tailor the magnetic properties in terms of coercivity ($H_c$) and magnetization ($M_0$). We have evaluated the dependence of the permittivity (ε) and permeability (μ) of the nanoparticle assemblies on

these parameters, based on which we have further derived the correlation between the electromagnetic wave absorption characteristics and the nanoscale architectures of the materials. Our research will substantially advance the fundamental understanding of the electromagnetic wave absorption behavior of magnetic nanomaterials. The materials and technology developed in this research will also have great applications in both civilian and defense industries.

Primary Reader: Dr. Chao Wang

Secondary Readers: Dr. Michael Bevan, Dr. James Spicer

**Acknowledgements**

I would first like to thank my Ph.D. advisor, Dr. Chao Wang. It has been my great pleasure to be his student over the last five years. I appreciate all of his contributions of time, ideas, and funding to make my experiences as a doctoral student productive, stimulating, and challenging. Dr. Wang's own dedication and enthusiasm for research was both motivational and contagious. Above all, I appreciate the freedom he has granted me during the latter half of my doctoral career to explore the subject of radar absorbing magnetic nanomaterials as I saw fit, of course with his advice and guidance continuing along the way.

The other members of the Wang Lab have also contributed to my professional growth and been a source of friendship throughout my time spent at Johns Hopkins University. I would like to thank all of my undergraduate mentees for their dedication to the projects we worked on together: Cindy Jiang, Hong Joon Ahn, Alex Cocolas, and Elina Hoffmann. Their help and hard work enabled me to progress with my research projects at an increased rate and allowed for deeper exploration of the projects at hand. Additionally, I would like to give a whole-hearted thank you to the Master's students who greatly contributed to my project during the final two years of my doctoral career: Mukund Madhav Goyal and Shi Zhang. Both of their ability to quickly grasp new concepts and eagerness to perform in the lab pushed my research further and helped me to refine my leadership and project management abilities, which will serve me greatly in my future career endeavors. I would next like to thank Akshat Vij for his friendship throughout the second half of my Ph.D. Akshat and I see much of the world in a similar light, which provided for a constant source of thought provoking conversations to help pass the time as we conducted experiments and/or analyzed data in the office. I would specifically like to thank Dr. Lei Wang, postdoctoral fellow in our lab, for his friendship and mentorship throughout my time at JHU. Lei, a nanoparticle synthesis savant, was always a source of advice when I was

struggling with an experiment. In addition, Lei's friendship both inside and outside of the lab played a critical role in making my time spent at JHU enjoyable, as you can always count on him to lighten the mood and make research a little less stressful. Last, but not least, I would like to thank Dr. David Raciti for his invaluable guidance, mentorship, and friendship throughout the entirety of my doctoral studies. David was instrumental in helping me to get my feet off the ground and establish myself of a doctorate-worthy researcher. His advice concerning everything from lab procedures and research directions to student-advisor relationships was of utmost importance while navigating the pathway towards graduation, and his friendship will always be valued.

I gratefully acknowledge the funding sources that made my Ph.D. work possible. Specifically, the Air Force Office of Scientific Research (AFOSR) for providing the funding to start and establish my project during my first three years.

Lastly, I would like to thank all of my loved ones for their support and encouragement throughout my journey towards a Ph.D. My brother and sister for their support and friendship during some of the tough times, and my girlfriend, Rachel Brown, for her support at home during the times when I was ready to pull my hair out. Most importantly, words cannot express my gratitude towards my mother and father for their emotional and financial support, advice, and guidance during this journey. It would not have been possible without them.

## Table of Contents

## List of Tables

### Chapter 1. Introduction



### Chapter 2. Size-Dependent Electromagnetic Wave Absorption Properties of Iron Oxide ($Fe_3O_4$) Nanomaterials



### Chapter 3. Radar Absorbing $MFe_2O_4$ (M = Fe, Co, Cu, Mn, Mg) Nanomaterials



### Chapter 4. The Influence of Alloying on the Radar Absorption Properties of Iron, Cobalt, and Nickel Magnetic Nanomaterials

**Chapter 5. An Investigation of Radar Absorbing Wood**

## List of Figures

### Chapter 1. Introduction

**Chapter 2. Size-Dependent Electromagnetic Wave Absorption Properties of Iron Oxide ($Fe_3O_4$) Nanomaterials**

**Chapter 3. Radar Absorbing $MFe_2O_4$ (M = Fe, Co, Cu, Mn, Mg) Nanomaterials**

**Chapter 4. The Influence of Alloying on the Radar Absorption Properties of Iron, Cobalt, and Nickel Magnetic Nanomaterials**

**Chapter 5. An Investigation of Radar Absorbing Wood**

**Chapter 6. Synthesis and Biofunctionalization of Magnetic $Fe_3O_4$ Nanoparticles**

**Chapter 7. Synthesis of Magnetic and Dielectric Nanoparticle Products for Tunable Electromagnetic Wave Absorption**

# Chapter 1. Introduction

## 1.1 MOTIVATION

The purpose behind the work presented herein is to contribute to the development and understanding of how nanoscale systems can be utilized to improve various modern technologies, predominantly the stealth technology industry. The research within this dissertation thoroughly discusses the creation of tailored magnetic nanomaterials as electromagnetic wave absorbing materials in an effort to further the link between experiment and theory. This dissertation is structured as follows:

Chapter 2 explores the effect of $Fe_3O_4$ nanoparticle size on the intensity and frequency of electromagnetic wave absorption. Results show that as the particle size increases, the intensity of absorption increases while the frequency of absorption decreases. Further exploration indicates that this behavior is largely due to the increase in the imaginary portion of the complex permeability, otherwise known as the magnetic loss, of the material as the size is increased. The largest studied particle size, a micron size, is undoubtedly the most effective absorber in this study, reaching a maximum reflection loss of -19.97 dB at 6.01 GHz with a 30 vol% loading. The results are discussed both quantitatively and qualitatively, utilizing mixing rules as a method to model the system and link the magnetization ($M_s$) and coercivity ($H_c$) to the complex permeability and thus, the electromagnetic wave absorption. Previous reports have explored the size effect at a microscale level, however this study is the first report that explores the size effect on electromagnetic wave absorption at the nanoscale level.

Chapter 3 presents the effect of doping of a ferrite nanoparticle system, $\mathbf{M}Fe_2O_4$ (**M** = Fe, Co, Cu, Mn, Mg), on the intensity and frequency of electromagnetic wave absorption. Results

indicate the intensity of electromagnetic wave absorption follows the trend $CuFe_2O_4 > MgFe_2O_4 > CoFe_2O_4 \approx MnFe_2O_4 \approx Fe_3O_4$ while the frequency of absorption follows the trend $CuFe_2O_4 < CoFe_2O_4 < MnFe_2O_4 \approx MgFe_2O_4 \approx Fe_3O_4$. $CuFe_2O_4$ is by far the most effective absorber in this study, reaching a maximum reflection loss of -11.13 dB at 11.22 GHz with a 30 vol% loading. Upon further investigation it appears that the dielectric properties of these materials has much more of an influence on the electromagnetic wave absorption properties than do the magnetic properties. This study is the first report that explores the doping effect on electromagnetic wave absorption at the nanoscale level.

Chapter 4 investigates the effect of alloying on the intensity and frequency of electromagnetic wave absorption for magnetic nanoparticle systems. The system studied included the three standard magnetic elements, Fe, Co, and Ni, and their resulting bimetallic alloys, FeCo, CoNi, and $FeNi_2$. Logic would suggest that the alloyed nanoparticles would display a hybrid behavior that is a blend of the two alloyed metals, however results indicate that the alloyed nanoparticles are considerably less effective electromagnetic wave absorbers than their metallic nanoparticle counterparts. The intensity of electromagnetic wave absorption follows the trend $Fe > Co > Ni > FeNi_2 \approx CoNi \approx CoFe$ while the frequency of absorption follows the $Fe < Co < Ni < FeNi_2 \approx CoNi \approx CoFe$. Fe and Co are by far the most effective absorbers in this study, reaching a maximum reflection loss of -16.94 dB at 6.77 GHz with a 30 vol% loading and -16.38 dB at 7.95 GHz with a 40 vol% loading, respectively. This study is the first report that explores the alloying effect on electromagnetic wave absorption at the nanoscale level.

Chapter 5 explores the invention of giving an everyday material, such as wood, radar absorbing properties through the impregnation of 10 nm Fe3O4 nanoparticles into the pores of the wood. The dielectric, magnetic, and microwave absorption properties of the series of the

nanoparticle impregnated wood have been carefully investigated, and the analysis has revealed that the same principles discussed in Chapters 2-4 hold true when a radar absorbing material is embedded into a host template such as wood. In addition, we have shown that a porous material may in fact have improved electromagnetic absorption capabilities, which could lead to the development of lighter weight, more cost effective microwave absorbers for planes, submarines, or other military vessels. Not only is this the first instance of the synthesis of a radar absorbing wood, but it is one of the first studies concerning the creation of a radar absorbing material through the impregnation of magnetic nanoparticles.

Chapter 6 discusses the use of superparamagnetic iron oxide ($Fe_3O_4$) nanoparticles conjugated with targeted antibodies to develop synthesis protocols to make them viable for both public health and biomedical applications. Our efforts include the systematic investigation of appropriate particle size, phase transfer/ligand exchange techniques, and appropriate water soluble PEG ligands for adequate magnetic capture. Through antibody conjugation, these iron oxide particles have the potential to target certain cells in the body and treat specific diseases. Our protocols have been characterized by transmission electron microscopy (TEM) and dynamic light scattering (DLS), which are presented herein. These techniques are presented in an effort to increase the knowledge surrounding available biofunctionalization techniques.

Chapter 7 presents the synthesis of a variety of new promising magnetic or dielectric nanomaterials to be studied in the future for electromagnetic wave absorption. For the most part, these materials all display a shape anisotropy and can be aligned along an easy axis upon exposure to an external magnetic or electric field. Future studies should involve comparing the electromagnetic response of these materials while aligned along their easy axis and while randomly oriented in order to determine the effect of shape anisotropy on electromagnetic

properties and electromagnetic wave absorption. Also discussed is the synthesis of $Fe_{2.15}Cr_{0.85}Se_4$, a hard magnetic alloy with composition tunable coercivity and magnetization. This material has never before been explored for electromagnetic wave absorption.

The remainder of this introduction is dedicated to: (1) Discussing the theory behind nanoparticle synthesis and techniques used to select for nanoparticles of a given size, shape, and composition. (2) An overview of the history and technological development of radar absorbing materials. (3) An in depth discussion of theory design principles for electromagnetic wave absorbers. (4) An overview of the importance of vector network analyzers and how they work. (5) A discussion of superparamagnetic nanoparticles and (6) ferromagnetic nanoparticles as electromagnetic wave absorbers. (7) An overview of the broader impacts of electromagnetic wave absorbers and their relation to national defense.

## 1.2 FUNDAMENTALS OF NANOPARTICLE SYNTHESIS

Nanoparticles are of great scientific interest in modern times, serving as a bridge between bulk materials and atomic or molecular structures. Bulk materials usually have constant physical properties regardless of size, but at the nano-scale these properties often become size-dependent due to the high surface-area-to-volume ratio nanoparticles display.[1,2] Nanoparticles can be grown in a variety of shapes and sizes dependent upon the synthetic parameters, such as rods, cubes, or spheres. While the area of nanoparticle synthesis has been extensively studied dating back to Michael Faraday's gold colloids in 1856, there is still much to be investigated. A wide range of nanoparticle synthesis methods have been developed, including colloidal methods (such as organic solution synthesis), sol-gel methods, hydrothermal syntheses, and polyol methods.

Organic solution synthesis is the predominant method used for the experiments in this dissertation and will be the focus of this discussion.

Organic solution synthesis is often described as having two distinct stages: nucleation and growth. The process begins with the nucleation step, in which zero-valence metal atoms form through either the reduction of ions or the bond breaking of compounds.[3] In classical nucleation theory, this stage can be defined by the Gibb's excess free energy of the system, $\Delta G_r$.[3–6] The excess free energy contains two competing terms, the changes in the surface and bulk free energies, with their relationship described in Equations (1) and (2) below:

$$\Delta G_r = 4\pi r^2\gamma + \frac{4}{3}\pi r^3 \Delta G_V = 4\pi r^2\gamma - \frac{4}{3}\pi r^3 \times \frac{RTlnS}{V_m} \quad (1)$$

$$S = \frac{[A]_s}{[A]_{eq}} \quad (2)$$

where $r$ is the radius of the atomic clusters, $\gamma$ is the surface free energy per unit area, $R$ is the ideal gas constant, $\Delta G_v$ is the change of free energy per unit volume, $T$ is the reaction temperature, $V_m$ is the molar volume of bulk crystal, and $S$ is the ratio between solute concentrations at saturation $[A]_s$ and equilibrium $[A]_{eq}$ conditions. The relationship between $\Delta G_v$ and $S$ does not take into account the contributions from enthalpy ($\Delta G_v$) changes, a limitation of the theory.[3]

Using Equation (1) and the Boltzmann distribution, the number of clusters ($N_r$) as a function of radius can be written as:

$$N_r = N_0 \times \exp\left(-\frac{\Delta G_r}{RT}\right) = N_A[A]_{eq}S \times exp\left(-\frac{\Delta G_r}{RT}\right) \quad (3)$$

where $N_0$ is the total number of free solute atoms per unit volume in the system, and $N_A$ is Avogodro's constant.[3] From Equation (3) it can be deduced that the number of clusters exponentially decreases with the increase of the surface free energy. When the solute is undersaturated, i.e. $S \leq 1$, $\Delta G_r$ remains positive and increases with the radius of clusters, indicating that nucleation is not favorable in such systems. In fact, nucleation is only favorable when the solute is supersaturated, i.e. $S > 1$, in which case $\Delta G_r$ can decrease with an increase in cluster radius. The relationship between Equations (1) – (3) is demonstrated in Figure 1.1.

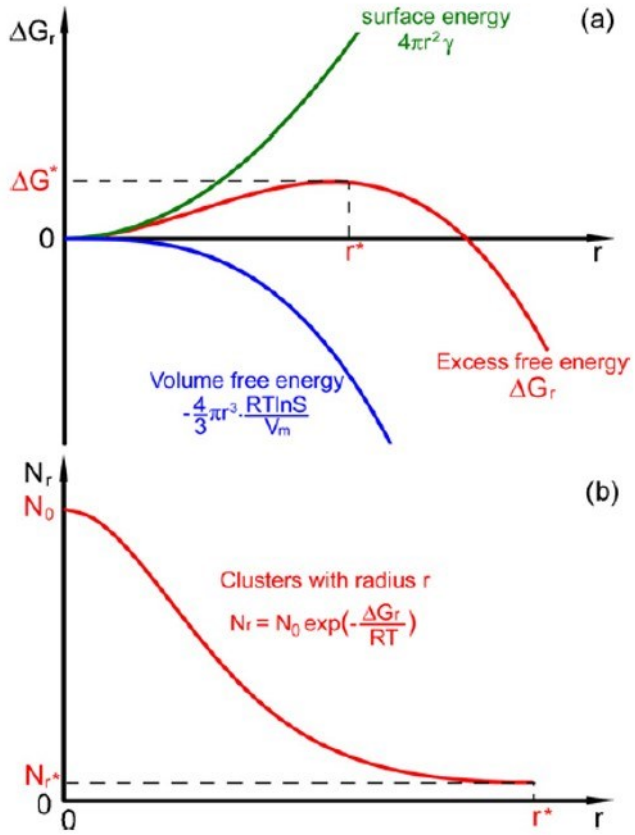


**Figure 1.1.** Illustration of (a) overall excess free energy, $\Delta G_r$, and (b) average number of clusters, $N_r$, as a function of cluster size, $r$.[3]

As illustrated in Figure 1.1(a), at the maximum of the excess free energy curve, $\Delta G_r$, there is a critical excess free energy, $\Delta G^*$, associated with the critical cluster radius, $r^*$.[7–9] At this point, the surface energy and bulk energy are equal. Prior to reaching the critical free energy, the system is in the nucleation stage in which clusters nucleate, but dissolve back into solution in order to lower the free energy of the system. However, after the clusters reach the critical radius, the system shifts to the growth stage in which the continued growth of the clusters lowers the free energy of the system.

The number of clusters achieving the critical radius, $N_r^*$, can be found by solving the equation $\frac{d\Delta G_r}{dr} = 0$:

$$r^* = -\frac{2\gamma}{\Delta G_V} = \frac{2\gamma V_m}{RT\ln S} \tag{4}$$

$$\Delta G^* = \frac{16\pi\gamma^3}{3\Delta G_V^2} = \frac{16\pi\gamma^3 V_m^2}{3(RT\ln S)^2} \tag{5}$$

$$N_r^* = N_A[A]_{eq} S \times exp\left(-\frac{\Delta G^*}{RT}\right) = N_A[A]_{eq} S \times exp\left(-\frac{16\pi\gamma^3 V_m^2}{3(RT)^3(\ln S)^2}\right) \tag{6}$$

$$\frac{dN_{r^*}}{dt} = f_0 N_A[A]_{eq} S \times exp\left(-\frac{\Delta G^*}{RT}\right) = f_0 N_A[A]_{eq} S \times exp\left(-\frac{16\pi\gamma^3 V_m^2}{3(RT)^3(\ln S)^2}\right) \tag{7}$$

where $f_0$ is the ratio of the number of clusters having the critical size over the total number of clusters.[3]

The four critical parameters ($r^*$, $\Delta G^*$, $N_{r^*}$, and $dN_{r^*}/dt$) in Equations (4) – (7) can be used to understand the nucleation process: the smaller the critical radius or maximum free excess energy is, the easier it is for nuclei to form. Based on these equations, the three most important variables controlling the nucleation process are the surface free energy, temperature of reaction, and the degree of supersaturation.[10,11] From an experimental standpoint, these are the easiest

variables to control and will allow for adjustments of the critical free energy, thus adjusting the nucleation point. If a system has high surface free energy, which leads to a large critical radius and high maximum excess free energy, it is very difficult for nucleation to occur, however, high reaction temperatures and excessive supersaturation of the reaction system can help to accelerate the nucleation rate.[10,11]

In a practical experiment, both the surface free energy and temperature of reaction are fixed, so the degree of supersaturation is the only variable available to help control nucleation and growth of the nanoparticles. In order to obtain monodisperse nanoparticles, separation of the nucleation and growth phases of the reaction is crucial. If there is not substantial separation of these two phases of the reaction, polydispersed nanoparticles will be formed as new nucleation happens simultaneously with continuous growth of existing nuclei. Typically, many syntheses will use a concept called "burst nucleation", in which forced nucleation occurs over a very short time period in order to achieve a high degree of monodispersity in the nanoparticle products.[8,12–14] The ideal case to produce monodisperse nanoparticles is depicted in the schematic in Figure 1.2(a) and LaMer's Plot in Figure 1.2(b), in which "burst nucleation" is used to create adequate separation of the nucleation and growth phases of the reaction.[12]

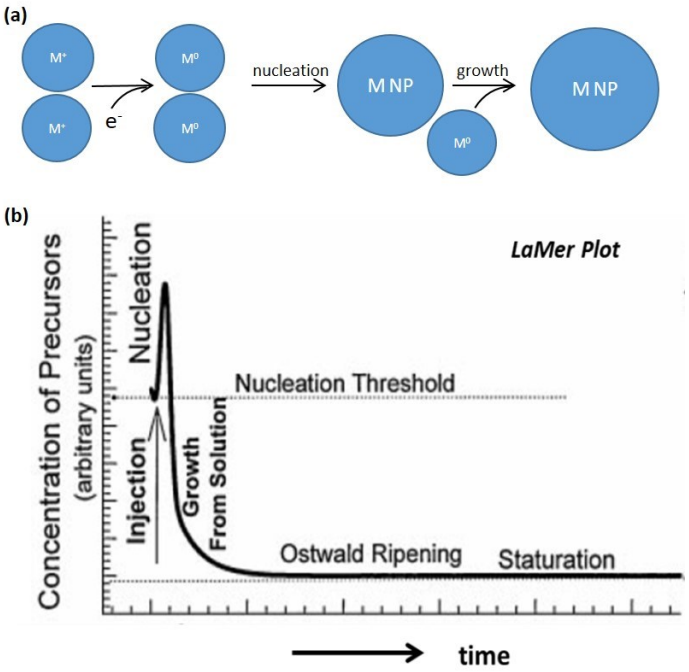


**Figure 1.2.** (a) Schematic of the nucleation and growth of metal nanoparticles. (b) LaMer's Plot depicting uniform nucleation and growth of nanoparticles via 'burst nucleation'.[15]

The shapes of metal nanoparticles can be controlled by both thermodynamic and kinetic factors, largely dictated by the parameters of the reaction system such as solvent, capping agent, and reducing agent, as the addition of the surface adsorbates helps to lower the free energy of the reaction system. When these surface adsorbates are added, it is possible for the solvent to have indirect effects by solvent-solvent interactions and can cause anisotropic growth of nanoparticles. As a result of this, a synthesis can be directed towards a desired nanoparticle shape.[16] The effect of various solvents, capping agents, and reducing agents, using platinum nanoparticles as an example, is shown in Table 1.1. It should be noted that the data presented in Table 1.1 is specific to platinum and may have different effects on other metals.

**Table 1.1.** Shape control of Pt nanoparticles in non-hydrolytic systems.[3]

| Precursor[a] | Surfactant[b] | Solvent[c] | Reductant[d] | Additive | Shape[e] | References |
|---|---|---|---|---|---|---|
| $H_2PtCl_6$ | PVP | EG | EG | $Fe^{2+}$orFe$^{3+}$ | BMP, NW, SP | [78,79] |
| | | | | $PdCl_4^{2-}$ | NW | [80] |
| | | | | $AgNO_3$ | C, CO, O | [81] |
| | | | | $NaNO_3$ | SP, O, TP, OP | [82] |
| | | | | | NW, Pl | [44,83,84] |
| $K_2PtCl_4$ | | | $K_2C_2O_4$, EG, $H_2$ | Pt seed | NW | [53] |
| $Pt(acac)_2$ | OAm | Toluene | $H_2$ | | C, TP, OP, MP | [85,86] |
| | OAc, OAm | ODE | | $Fe(CO)_5$ | C | [87–89] |
| | OAm | OAm | | | NW | [90] |
| | [BMIM][$Tf_2N$] | HDD | | | SP | [91] |
| | HDA, ACA | HDA, DPE | HDD, DDD | $AgNO_3$ | C, MP, NF, bipod, tripod, BMP. | [92–94] |
| $Pt_2(dba)_3$ | | [BMI][$BF_4$] [BMI][$PF_6$] | $H_2$ | | SP | [95] |
| | HDA | THF, toluene | CO, $H_2$ | | SP, NW | [96] |

[a] acac = acetylacetonate; dba = dibenzylidene acetone.
[b] PVP = poly(*N*-vinyl-2-pyrrolidone); OAm = oleylamine, OAc = oleic acid; HDA = hexadecylamine; and ACA = 1-adamantanecarboxylic acid.
[c] EG = ethylene glycol; ODE=1-octadecene; DPE = dipenyl ether; [BMIM][$Tf_2N$] = 1-butyl-3-methylimidazolium bis(triflylmethyl-sulfonyl) imide; [BMI][$BF_4$] = 1-*n*-butyl-3-methylimidazolium tetrafluoroborate; [BMI][$PF_6$] = 1-*n*-butyl-3-methylimidazolium hexafluorophosphate; and THF = tetrahydrofuran.
[d] HDD = 1,2-hexanedecandiol; DDD=1,2-dodecanediol.
[e] C = cube; T = tetrahedron; O = octahedron; CO=cuboctahedron; SP = spherical particle; NW = nanowire; OP = octopod; TP = Tetrapod; Pl = Plate; MP = multipod; BMP = branched multipod; NF = nanoflower.

As demonstrated in Table 1.1, the selection of the a specific nanoparticle precursor, surfactant, solvent, and reducing agent will each have an effect on the resulting shape of the nanoparticle. For clarification purposes, the shapes mentioned in Table 1.1 are shown in Figure 1.3.

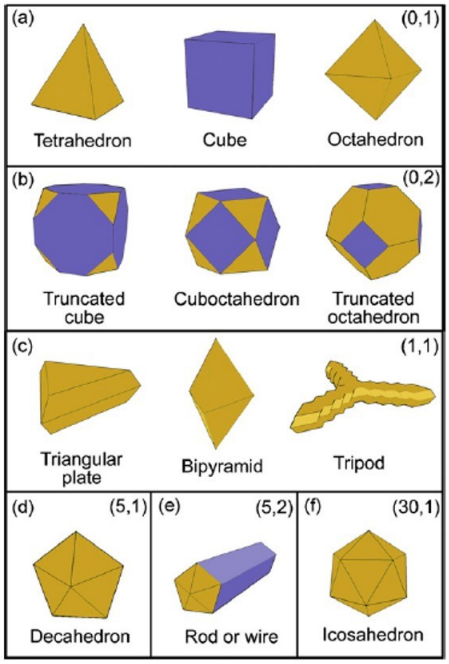


**Figure 1.3.** Selective possible shapes of nanoparticles, (a) and (b), without defects and bounded by (a) one group and (b) two groups of facets; and (c) – (f) with different numbers of defects. The notation (m, n) represents the number of defects, m and different facets, n, in crystals.[3]

As many different factors contribute to a reaction system's product, it can be quite confusing which factor is responsible for each corresponding reaction behavior. Any change in reaction parameters will produce a change in the nanoparticle product. Due to this, it remains a challenge to predict the outcome of reaction schemes without physically executing the reaction. It goes without saying that the scientific method, i.e. changing one variable at a time, is critical to uncovering the underlying mechanisms by which different parameters will affect the outcome of a synthesis reaction.

## 1.3 HISTORY AND EVOLUTION OF RADAR ABSORBING MATERIALS

The introduction of the microwave radar in World War II revolutionized the air defense situation around the world. Aircrafts could be detected at much further distances with the use of microwaves, independent of weather complications. The radar signal strength, or the signal reflected from a target, determines is detectability and is very closely related to the size and shape of the target.[17] In military terms, this reflected signal is known as the Radar Cross Section, or RCS of the material. Hence, by reducing the RCS of a target, its detectability can be decreased. For the military, the RCS reduction of aircrafts, missiles, and submarines in enemy territory is of high importance when on reconnaissance missions. At the time of the Second World War, and continuing in an ever increasingly connected society in modern times, stealth technology has taken on great importance, which is the motivation behind the research of Radar Absorbing Materials (RAMs).

Research on RAMs has been actively pursued for almost a century, with several known techniques suggested for RCS reduction:

(i) shaping,

(ii) active loading

(iii) passive loading

(iv) distributed loading.

Shaping is the process of modifying the external features of the object to reduce the reflections, usually by creating planes that are perpendicular to the incident wave and will reflect the wave in a direction that is away from the receiver.[18,19] While shaping displays many benefits as a method of RCS reduction, it has some severe limitations. These include achieving reduction in limited

regions at the expense of increasing reduction in others, a limited effective frequency range, and a constrained implementation method as the shaping must be integrated into the system design stage and not applied later on. Both active and passive loading employ the use of active (materials that reduce the RCS) and passive (materials that do not reduce the RCS) materials at selected points on the target where reflections are a maximum in order to reduce the RCS by phase cancellation. While there is some promise in these methods, they are only effective on a narrow bandwidth and are not thought of as commercially viable techniques. The distributed loading technique is by far the most useful and universal technique for the reduction of RCS and is the loading technique implemented in future chapters of this dissertation. In general, the target is covered with RAMs, usually in the form of a paint-like coating. In this case the reduction is achieved from both adsorption from the RAM and misdirection of the electromagnetic energy and is considered the most effective method to date.[20]

The earliest known research regarding RAMs was well underway by the late 1930s by Dutch scientists who developed a carbon black/titanium oxide absorber that was active in the 2 GHz region.[21] In the United States, the first absorbers, generally known as HARP (Halpern-anti-radar-paint), were developed during the mid-1940s and consisted of paints mixed with artificial dielectric materials of high permittivity or iron particles with a neoprene binder.[22] A few years later in 1952 and perhaps one of the more well-known absorbers, the Salisbury screen was developed which consisted of a resistive sheet placed at quarter wavelength from the target, spaced by a low dielectric material.[23] Due to the $\lambda/4$ spacing from the target, the Salisbury screen is able to limit the reflection of an incoming radar wave by phase cancellations between the incident and reflected wave as shown in Figure 1.4.

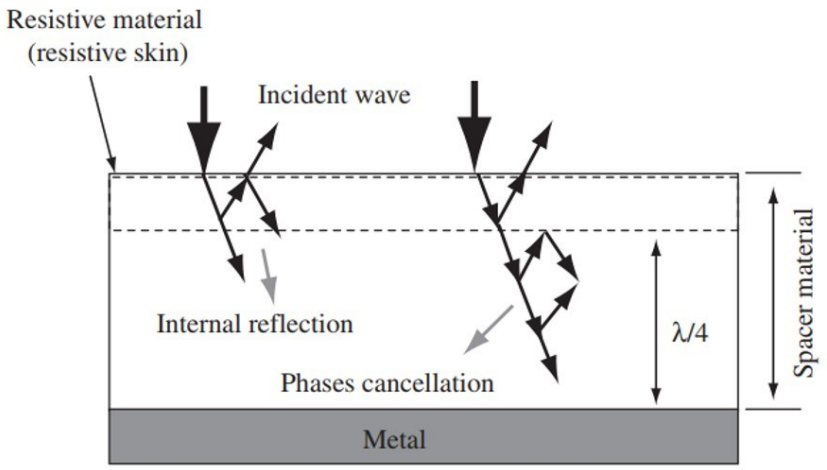


**Figure 1.4.** Layout of the Salisbury Screen, λ/4 effect, and cancellation of the electromagnetic wave phases.[24]

Magnetic materials weren't explored as RAMs until the 1960's, with the use of ferrites with low reflection coefficients which could operate a lower resonant frequencies than had been feasible with the dielectric materials previously studied. [25]

From this point, much of the research on RAMs came to a standstill until the development and popularization of the iron ball paint method as implemented on the Lockheed F-117 Nighthawk in 1983. This method was the first of its kind to synthesize an RAM *in situ.* By mixing the paint with iron pentacarbonyl, iron and/or iron oxide nanoparticles are generated upon application to the surface of the plane, thus coating the plane in a RAM. Incident radar waves induce molecular oscillations from the alternating magnetic field of the iron nanoparticles within the paint, leading to the conversion of the radar energy to thermal energy and dissipation as heat along the surface of the plane (Figure 1.5).

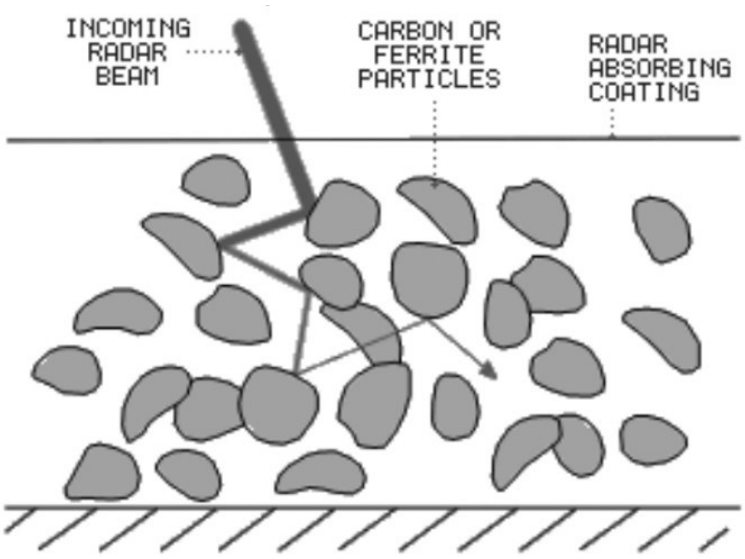


**Figure 1.5.** Depiction of the iron ball paint method for radar absorption.[26]

The advent of the iron ball paint method was the first method of its kind to employ the use nanoparticles in a RAM, and to this day is regarded as a gold standard in amongst RAMs. Unfortunately, almost all literature on RAMs is indeed classified, which makes it difficult to analyze the state-of-the-art in the field as surely the United States military has moved on from the technology used in the nearly 40 years ago in the 1980s. Reiterating this point, in the late 1980s a biotech product with ultra-wide band absorption characteristics was discovered, however the compound was immediately classified and there is little to none available information on it; it has been described as a powdery black substance with $1/10^{th}$ the weight of ferrites.[27] In more recent times, research has delved into the exploration of chiral materials as RAMs without a significant breakthrough yet apparent. While research in the area of RAMs persists nonetheless, the approach has become somewhat of a "guess and check" method in which scientists are reporting the radar absorption properties of new materials without fully understanding why the materials behave the way they do. As this type of research approach continues, it has become

increasingly necessary to reverse course and study the fundamentals of RAMs in order to gain a firm understanding of the underlying mechanisms of the science if we are to ever actually design the perfect absorber.

## 1.4 THEORY AND DESIGN PRINCIPLES FOR ELECTROMAGNETIC WAVE ABSORBERS

RAMs are characterized by their electromagnetic properties, the relative permittivity and permeability as normalized by their free space counterparts, $\varepsilon_0$ and $\mu_0$:

$$\varepsilon_r = \varepsilon/\varepsilon_0 \tag{8}$$

$$\mu_r = \mu/\mu_0 \tag{9}$$

where the relative permittivity ($\varepsilon_r$) and permeability ($\mu_r$) are generally described as complex numbers as follows:

$$\varepsilon_r = \varepsilon_r^{'} + j\varepsilon_r^{''} \tag{10}$$

$$\mu_r = \mu_r^{'} + j\mu_r^{''} \tag{11}$$

with the real component of the complex number denoted as single prime (′) and the imaginary component denoted as double prime (″). In general, the real component of the permittivity is dependent on the conductivity of the material while the imaginary component accounts for the dielectric loss in the material as an electromagnetic wave passes through. Similarly, the real component of the permeability is dependent upon the magnetization of the material while the imaginary component accounts for the magnetic loss in the material. The terms dielectric and

magnetic loss refer to the ability of a material to absorb electromagnetic energy, i.e. the higher loss a material is the better it is at absorbing electromagnetic radiation.

For conceptual convenience when classifying RAMs, Equations (10) and (11) are usually written as:

$$\varepsilon_r = \varepsilon_r^{'}(1 + j\tan\delta_e) \tag{12}$$

$$\mu_r = \mu_r^{'}(1 + j\tan\delta_m) \tag{13}$$

where:

$$\tan\delta_e = \varepsilon_r^{''}/\varepsilon_r^{'} \tag{14}$$

$$\tan\delta_m = \mu_r^{''}/\mu_r^{'} \tag{15}$$

In equations (14) and (15), $\tan\delta_e$ and $\tan\delta_m$ are known as the electric and magnetic loss tangents, respectively, and are used to determine whether to classify a materials as dielectric material or magnetic material. Logically, materials with a large dielectric loss tangent are referred to as dielectric materials while materials with a large magnetic loss tangent are referred to as magnetic materials. In both cases, the materials will absorb electromagnetic energy and convert it to heat, thus can be used to create RAMs.

When an electromagnetic wave passes through the boundary of a RAM, the refractive index, *n*, and the characteristic impedance, *Z*, of the material play a critical role in dictating the propagation of the wave through the material:

$$n = (\varepsilon_r\mu_r)^{1/2} \tag{16}$$

$$Z = [\mu/\varepsilon]^{1/2} = Z_0[\varepsilon_r/\mu_r]^{1/2} \tag{17}$$

where $Z_0$ is a constant known as the intrinsic impedance of free space and equal to 377 Ω, independent of frequency. Both *n* and *Z* are complex quantities.[17]

Most commonly, RAMs can be considered as having a flat surface and their absorption and/or reflection properties are characterized using transmission line theory, which expresses the RAM as a lossy network between free space and the scatterer and represented in terms of complex impedance. For electromagnetic waves, as with any propagating wave, reflections only occur when the wave propagates from one medium to the next. In transmission line theory, this reflection is denoted as the reflection coefficient, *r*. In the case of a wave interacting with a flat RAM and entering from free space, the reflection coefficient is defined as:

$$r = (Z_1 - Z_0)/(Z_1 + Z_0) \tag{18}$$

where $Z_1$ is the input impedance at the boundary between free space and the RAM. Thus, the condition for an RAM to have zero reflection is:

$$Z_1 = Z_0 \tag{19}$$

Equation (19) requires that the surface input impedance be independent of frequency, and real. Accounting for the complexity of practical input impedance, the input impedance for a wave entering an RAM at normal incidence at the interface with free space is given by:

$$Z_1 = Z \tanh \gamma d \tag{20}$$

where Z is the characteristic wave impedance (previously defined in Equation (17)) and *d* is the thickness of the RAM. γ is the complex propagation constant of the medium and is defined as follows:

$$\gamma = \left(j\omega\mu(\sigma + j\omega\varepsilon)\right)^{1/2} \tag{21}$$

where $\sigma$ is the electrical conductivity of the RAM and $\omega$ the angular frequency, defined as:

$$\omega = 2\pi f \tag{22}$$

In summary, the reflection coefficient of a RAM is affected by the interference of the incoming electromagnetic waves at the surface of the RAM and at the metal-RAM interface. The phase of the radiation is dependent upon $\varepsilon_r$, $\mu_r$, and the thickness of the RAM, while the amplitude of reflection depends on the loss ability in the material. For a flat RAM, as is the most common case, the reflection and absorption behavior is governed by the previously discussed transmission line theory in which a perfect absorber will attain the impedance matching condition described in Equation (20).[17]

In order to use transmission line theory to design an effective RAM it is necessary to identify suitable materials and specify their dimensions and compositions. A tradeoff exists between the size and thickness of the absorber and its efficiency of absorption. In general, the thicker a RAM is, the more effective it is as absorbing electromagnetic radiation. However, in all practical applications of RAMs, including stealth technologies and electromagnetic interference applications for modern technologies such as cell phones and laptops, an RAM must be designed as thin and light as possible. A thick coating of an RAM on a plane or submarine will lead to an increased base weight for the vessel, less ability to carry a payload, and will surely effect the aerodynamics of the system. Similarly, as portable technology trends towards smaller and smaller sizes, a RAM for inclusion in a cell phone or laptop would need to be as thin as possible so as not to increase bulkiness. The main challenge then becomes designing an absorber that is thin enough and light enough for a coating on a plane or inclusion in a cell phone without sacrificing the effectiveness of absorption.

There are two concepts used in the design of absorbers for RCS reduction: the matched characteristic impedance concept and the matched wave impedance concept.[28] The difference between the two methods stems from their nomenclature. The matched characteristic impedance concept is when the impedance of the RAM is made to be nearly equal the intrinsic impedance of free space:

$$Z = Z_0 \tag{23}$$

This condition requires that the relative permittivity and relative permeability of the absorber be equal to ensure zero reflection at the front surface of the material:

$$\varepsilon_r = \mu_r \tag{24}$$

Lastly, a matched characteristic impedance concept RAM requires that the material be thick enough so the waves are attenuated as they propagate into the material, and internal reflections from the metal backing of the absorber are attenuated on the round-trip. Typically, the matched characteristic impedance concept is used for broadband absorption methods, but it not very practically applicable due to the large thicknesses of RAMs required.[17,28]

Likewise, the matched wave impedance concept is when the wave impedance at the front surface of the absorber is made equal to the intrinsic impedance of free space. This method results in the complete absorption of the electromagnetic energy hitting the surface of the absorber. For an absorber of finite thickness backed by a conducting plate, the wave impedance is described by Equation (20). By combining Equation (19) and (20), the thickness required to create a matched wave impedance concept absorber can be determined as follows:

$$Z_0 = Z \tanh \gamma d \tag{25}$$

Typically, the matched wave impedance method is used for resonant absorption as the RAMs only absorb the electromagnetic energy at discrete frequencies dependent upon the thickness of the material. A benefit of these types of absorbers, they are usually much thinner than matched characteristic impedance concept absorbers, thus may be more applicable to modern technologies. However, since they are only effective at certain frequencies, they are actually less desirable in practical applications that are in need of broadband absorption.[17,28]

## 1.5 VECTOR NETWORK ANALYZERS AND COMPUTATION OF ELECTROMAGNETIC PARAMETERS

Radio frequency network analyzers are vital instruments for the measurement of the dielectric and magnetic properties of various materials. In general, they are used to test network component specifications and verify design simulations across various types of networks. In modern society, network analyzers are commonly used as a tool to verify performance in a Wi-Fi network, map coverage zones across a 3G or 4G cellular network, or even diagnose problem areas in a "cloud" database such as Google Drive or DropBox. In the R&D fields, engineers commonly use network analyzers at various stages of product development to characterize, test, and verify product performance. More specifically, the measurement of complex electromagnetic materials at microwave frequencies has gained an increasing importance in the research fields of materials science, microwave circuit design, RAM development, and biological research. Due to this, network analyzers have proven extremely useful tools as technology advances.

Two types of network analyzers exist: scalar network analyzers (SNA) and vector network analyzers (VNA). The SNA is the more basic of the two and is only able to measure the amplitude properties, or scalar properties, of a signal. Because of this often times SNAs are only

used to measure the characteristics of an existing signal rather than the response of a device under test. An application of SNAs is for testing amplitude responses of filters or the gain of an amplifier over a certain bandwidth. VNAs are a much more useful form of radio frequency network analyzer as they are able to measure both the amplitude and phase response of a network and can provide much more insight into the behavior of the device under test as phase is critical in elemental network analysis. Rather than simply measuring the characteristics of an existing signal like the SNA, a VNA can output a signal to a device under test and measure the response of the system. VNAs are much more accurate than SNAs and are used for many of the previously mentioned R&D applications, including the electromagnetic measurements of materials.

VNAs are designed to operate with a rather simple systematic design of their components. In general, a VNA will generate a known signal, pass the signal through a device under test, and measure the change in the signal in a set of receivers. A reflected signal is measured as it bounces off of the surface of the device under test and a transmitted signal is measured that pass through the device. (Figure 1.6).

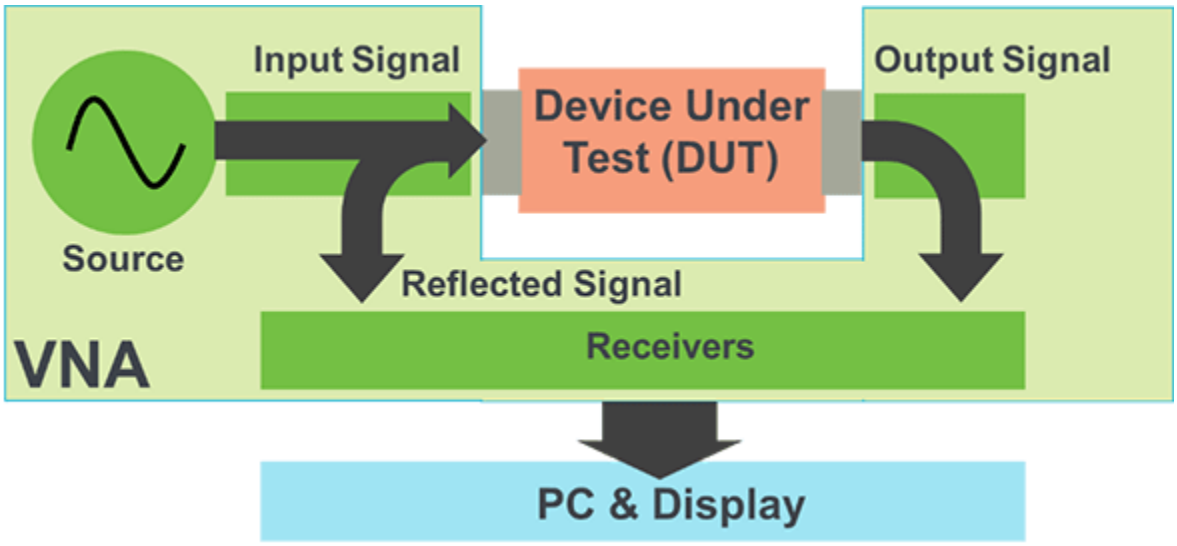


**Figure 1.6.** Basic schematic of the components of a vector network analyzer (VNA).[29]

The VNA receivers will then measure the resulting reflected and transmitted signal and compare them to the known generated signal in order to measure changes in the response. The measured results will then be processed by a computer and sent to a display for the user to interpret. In this dissertation, a Keysight FieldFox N9918A Microwave Analyzer equipped with coaxial cables and a Keysight 85051B 7 mm airline were used for measurements. The instrumental setup is detailed in Figure 1.7.

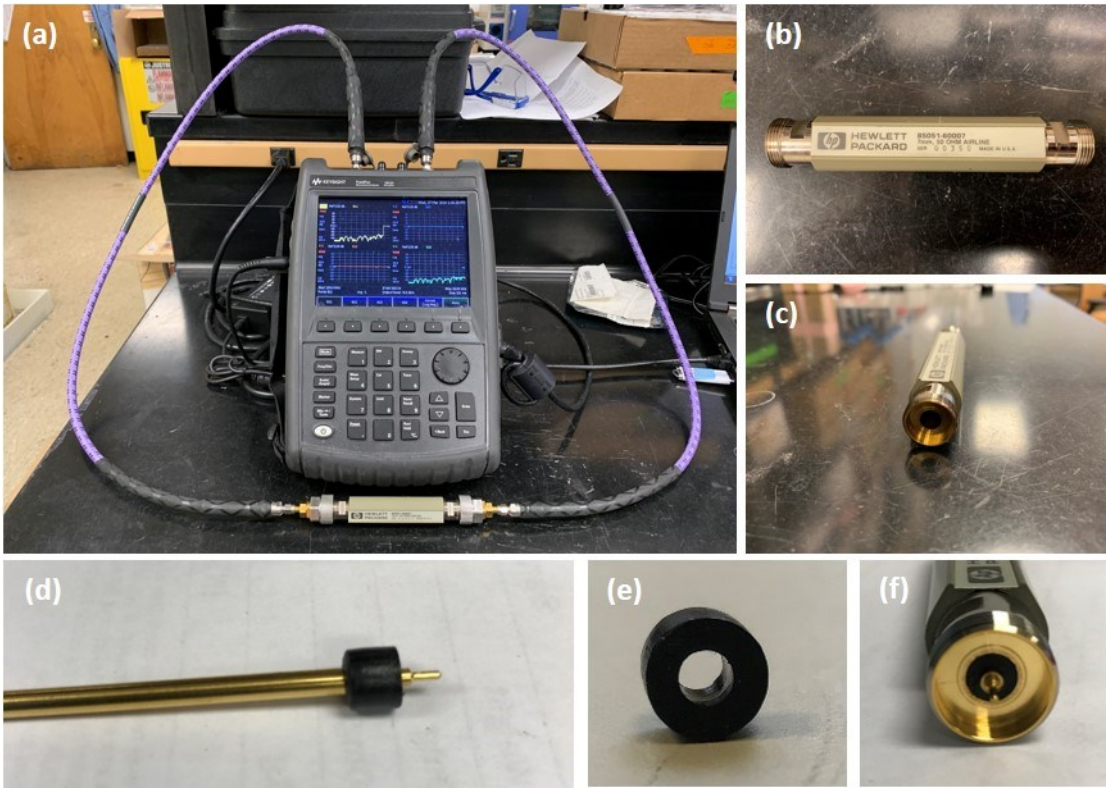


**Figure 1.7.** (a) Experimental setup of the Keysight FieldFox N9918A network analyzer equipped with a Keysight 85051B 7 mm airline. The purple cables are the coaxial cables. (b) Top view of the Keysight 85051B 7 mm airline. (c) Side view of the Keysight 85051B 7 mm airline. (d) A measurement ready nanoparticle/wax toroid fitted around the center conducting rod for the Keysight 85051B 7 mm airline. (e) A measurement ready nanoparticle/wax toroid. (f) The Keysight 85051B 7 mm airline equipped with a nanoparticle/wax toroid fitted around the center conducting rod and into the airline.

VNAs can be designed to have a varying number of ports from which signal can be generated and received. Most commonly, VNAs are designed with two ports; used in this research is a two port system. In a two port system, the VNA will measure a set of four S-parameters in order to determine the behavior of the device under test: S11, S12, S21, and S22. S11 is the response of the device under test from the signal that is generated in port 1, reflects off of the device under test, and received back in port 1. S12 is the response of the device under test from the signal that is generated in port 1, transmits through the device under test, and received in port 2. Likewise, S21 is the response of the transmission of the signal from port 2 to 1, and S22 is the reflected signal in port 2.[30]

There are four different methods that can be used for a VNA to convert S-parameters to the complex permittivity or permeability of a material:

- Nicolson-Ross-Weir method
- NIST iterative method
- New non-iterative method
- Short Circuit line method

The details of which S-parameters are required for computation and the electromagnetic properties able to be calculated from each method are given in Table 1.2 below.

**Table 1.2.** Comparison of the Conversion Methods from S-Parameters to Electromagnetic Properties[31]

| Conversion Technique | S-Parameters | Electromagnetic Properties |
|---|---|---|
| Nicolson-Ross-Weir | S11, S21, S12, S22 or S11, S21 | $\varepsilon_r$, $\mu_r$ |
| NIST iterative method | S11, S21, S12, S22 or S11, S21 | $\varepsilon_r$ |
| New non-iterative method | S11, S21, S12, S22 or S11, S21 | $\varepsilon_r$ |
| Short Circuit line method | S11 | $\varepsilon_r$ |

Each of the methods has its own advantages and limitations, however the most glaring difference between the four is in the electromagnetic properties that are able to be calculated. As shown, the Nicolson-Ross-Weir method is the only available method which can be used calculate the magnetic permeability of a device under test. As we are only interested in the effect of magnetics on the electromagnetic wave absorption of materials in this dissertation, the Nicolson-Ross-Weir method is the only method that will be discussed in depth. Table 1.3 briefly explains the differences between the four methods in more detail.

**Table 1.3.** Comparison of All Possible Measurement Techniques and Conversion Methods for the Calculation of the Complex Permittivity and Permeability from a Vector Network Analyzer[31]

| Materials/Length/Magnetics | Measurement Methods | Conversion Methods | Speed | Accuracy |
|---|---|---|---|---|
| Lossy solids/Short/Non-Magnetic | Transmission Line | Nicolson-Ross-Weir | Fast | Medium |
| Lossy solids/Short/Magnetic | Transmission Line | Nicolson-Ross-Weir | Fast | Medium |
| Lossy solids/Short/Non-Magnetic | Transmission Line | NIST iterative | Slow | Good |
| Lossy solids/Short/Non-Magnetic | Transmission Line | New non-iterative | Fast | Good |
| High Temperature Solids/Large/Non-Magnetic | Free Space | NIST iterative/New non-iterative | Slow/Fast | Good |
| High Temperature Solids/Large/Non-Magnetic | Free Space | Nicolson-Ross-Weir | Fast | Medium |

The Nicolson-Ross-Weir method for conversion of S-parameters to the electromagnetic properties of a material is quite involved and is often built into a network analysis software. This method can be applied to both the transmission line and free-space measurement, however due to the nature of the materials measured in this dissertation, only the transmission line application is discussed. Using the Nicolson-Ross-Weir method, the required S-parameters are written as:

$$S_{11} = \frac{(1-P^2)\Gamma}{1-P^2\Gamma^2} \qquad S_{21} = \frac{(1-\Gamma^2)P}{1-\Gamma^2P^2} \tag{26}$$

in which $P$ is the propagation factor given by:

$$P = e^{-jk_2d} \tag{27}$$

and where $k_2$ is the z-component of the propagation vector defined through:

$$k_2^2 = k^2 - \kappa^2 \tag{28}$$

Here $k = \omega\sqrt{\mu\varepsilon}$ is the wavenumber in the material, and $\kappa = 0$ for transmission line systems. Additionally, $\Gamma$ is the interfacial reflection coefficient given by:

$$\Gamma = \frac{Z - Z_0}{Z + Z_0} \tag{29}$$

For transmission line systems, $Z = \eta$ and $Z_0 = \eta_0$, where $\eta = \sqrt{\mu/\varepsilon}$ and $\eta_0 = \sqrt{\mu_0/\varepsilon_0}$. In order to solve the Nicolson-Ross-Weir method as originally proposed by Nicolson, Ross, and Weir, begin by defining the following intermediate quantities:

$$V_1 = S_{21} + S_{11} = \frac{P + \Gamma}{1 + \Gamma P}, \qquad V_2 = S_{21} - S_{11} = \frac{P - \Gamma}{1 - \Gamma P} \tag{30}$$

The quantities $P$ and $\Gamma$ may be determined in terms of the measured quantities of $S_{11}$ and $S_{21}$ by rearranging the expressions. First, $P$ is eliminated from the equations, resulting in a quadratic equation for $\Gamma$:

$$\Gamma^2 - 2\Gamma X + 1 = 0 \tag{31}$$

where:

$$X = \frac{1 - V_1 V_2}{V_1 - V_2} = \frac{1 - S_{21}^2 + S_{11}^2}{2S_{11}} \tag{32}$$

The solution is:

$$\Gamma = X + s_1\sqrt{X^2 - 1} \tag{33}$$

where $s_1 = \pm 1$. The sign ambiguity is usually resolved by assuming that the material is passive, since only one choice of sign satisfies the inequality $|\Gamma| \leq 1$. Once $\Gamma$ is determined, $P$ is easily found as:

$$P = \frac{V_1 - \Gamma}{1 - V_1 \Gamma} = |P| e^{j\emptyset} \tag{34}$$

where $-\pi < \emptyset \leq \pi$. Equating Equation (34) to (27) and defining the dimensionless quantity $\bar{k}_2 = k_2/k_0$, $k_2$ is found by taking the natural logarithm:

$$\bar{k}_2 = \frac{n - \frac{\emptyset}{2\pi}}{d/\lambda_0} + j\frac{\ln|P|/2\pi}{d/\lambda_0} \tag{35}$$

Here $\lambda_0 = f/c$ is the free-space wavelength. At this point, with $\bar{k}_2$ known, ε and μ are determined as follows. First define $F$:

$$F = \frac{1 - \Gamma}{1 + \Gamma} \tag{36}$$

Then, for transmission line systems:

$$\varepsilon_r = \bar{k}_2 F, \qquad \mu_r = \frac{\bar{k}_2}{F} \tag{37}$$

Finally, once the Nicolson-Ross-Weir method has been implemented to calculate the complex permittivity and complex permeability, the previously discussed transmission line theory can be utilized to calculate the absorption properties of the materials under study in terms of reflection loss using Equation (38) and (39):

$$Z_{in} = Z_0 \sqrt{\frac{\mu_r}{\varepsilon_r}} \tanh\left(j\frac{2\pi f d \sqrt{\mu_r \varepsilon_r}}{c}\right) \tag{38}$$

$$RL = 20 \log_{10} |(Z_{in} - Z_0)/(Z_{in} + Z_0)| \tag{39}$$

where $Z_0$ = 377 Ω, the impedance of free space.[32]

## 1.6 SUPERPARAMAGNETIC NANOMATERIALS AS ELECTROMAGNETIC WAVE ABSORBERS

Superparamagnetism is a form of magnetism which appears in sufficiently small ferromagnetic or ferrimagnetic nanoparticles.[33,34] By mechanism, superparamagnetism is when the size of a ferromagnetic particle is reduced to the single-domain range (~2 – 80 nm, depending on the material) and its magnetic moment can flip along its easy axis under thermal activation. The typical time between two flips is referred to as the Néel relaxation. As an artifact of this random flipping, the average magnetization appears to be zero and is referred to as the superparamagnetic state. When in the superparamagnetic state, an external magnetic field is able to magnetize the nanoparticles, similarly to a paramagnetic material, but in a more efficient pathway, giving rise to a much larger magnetic susceptibility and permeability than a paramagnetic material displays. Figure 1.8 displays the difference in magnetic hysteresis between ferromagnetism, paramagnetism, and superparamagnetism.

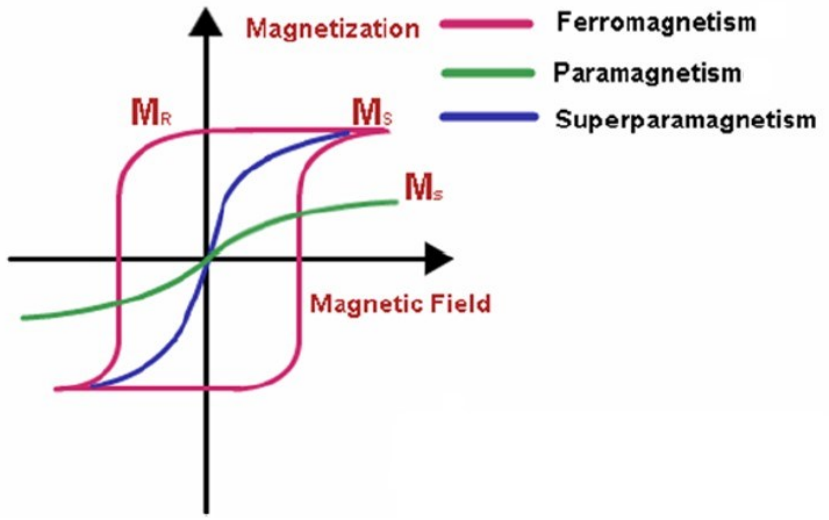


**Figure 1.8.** Comparison of the characteristic magnetic hysteresis curves of ferromagnetic, paramagnetic, and superparamagnetic materials.

Under the superparamagnetic state, the static permeability in response to a static external magnetic field, caused by the Néel relaxation, is given by:

$$\mu = \mu_0 \left(1 + \frac{V_p M_0^2}{3 k_B T}\right) \tag{40}$$

where $V_p$ is the volume of the nanoparticle, $M_0$ is the saturation magnetization, $k_B$ is the Boltzmann constant, and $T$ is the temperature.[33] It can be deduced from this relationship that the static permeability of a superparamagnetic material is thus dependent on its particle size, or volume, and its saturation magnetization ($M_0$). It is commonly accepted as reasonable to assume that $M_0$ does not vary with particle size, and the permeability of superparamagnetic nanoparticles increases with increasing size. However, in practice this assumption is invalid. $M_0$ does in fact vary with particle size, and the relationship between $M_0$, $\mu$, and particle size is somewhat unclear. For this reason, it becomes apparent the importance of utilizing organic solution synthesis to

make monodisperse nanoparticles for systematic studies of these relationships and their effect on electromagnetic wave absorption.

The dependence of the dynamic permeability, $\mu(\omega)$, is complicated by the existence of resonance absorption due to the random flipping of the magnetic moment of such small materials. The blocking frequency, $f_b$, of a superparamagnetic nanoparticle corresponds to the average rate of the random flipping over the nanoparticle's magnetic moment as a result of thermal fluctuations and is defined by:

$$f_b = f_0 exp\left(\frac{KV_p}{k_B T}\right) \tag{41}$$

where $f_0$ is a constant, $K$ is the nanoparticle's magnetic anisotropy density, and $KV_p$ is the anisotropy energy. When the frequency of the incident electromagnetic wave approaches the blocking frequency, superparamagnetic nanoparticles can exhibit resonance absorption. From Equation (41) it can be predicted that the resonance frequency of superparamagnetic nanoparticles increases exponentially with the particle size ($V_p \sim D^3$). The shift of resonance frequency will also contribute to the change of complex permeability with particle size. While the investigation of resonance absorption due to relaxation magnetization has been extensively studied (see Section 1.7), the investigation of the blocking resonance of superparamagnetic nanoparticles has seldom been reported.[35]

## 1.7 FERROMAGNETIC NANOMATERIALS AS ELECTROMAGNETIC WAVE ABSORBERS

Ferromagnetism is the basic mechanism by which materials form permanent magnets, or in other words, materials that exhibit spontaneous magnetization and retain a net magnetic moment in the absence of an external magnetic field. It is the strongest type of magnetism and is responsible for the common phenomena of magnetism in magnets encountered in everyday life. Common ferromagnetic materials include iron, cobalt, nickel, and various bimetallic or trimetallic alloys of the three.

The interaction of ferromagnetic nanomaterials and electromagnetic waves in which there is a relaxation of a magnetic moment, $\boldsymbol{M}$, with response to an external magnetic field, $\boldsymbol{H}$, are governed by the Landau-Lifshitz equation:

$$\frac{d\boldsymbol{M}}{dt} = -\boldsymbol{M} \times \left(\gamma \boldsymbol{H} - \frac{\alpha}{M_0} \cdot \frac{d\boldsymbol{M}}{dt}\right) \boldsymbol{H} \tag{42}$$

where γ is the gyromagnetic factor, α is the dimensionless Gilbert's damping parameter, and $M_0$ is the saturation magnetization of the material.[36] Considering the particular case of spherical particles assembled in random orientations, the permeability can be described as:

$$\mu(\omega) = 1 + \frac{\mu_s - 1}{1 + i\omega/\omega_\alpha - (\omega/\omega_r)^2} \tag{43}$$

with static permeability:

$$\mu_s = 1 + 4\pi M_0 / H_k \tag{44}$$

natural resonance frequency:

$$\omega_r = \gamma H_k \tag{45}$$

and relaxation frequency:

$$\omega_\alpha = \gamma H_k / \alpha \tag{46}$$

The damping parameter, α, is usually small, i.e. roughly 0.05 in Fe and Co films.[37] From Equation (43) it can be deduced that μ″ approaches a maximum when $\omega \rightarrow \omega_r$ and drops quickly when $\omega$ diverges from $\omega_r$. The appearance of strong absorption of a magnetic material at $\omega_r$ is called resonance absorption. From Equation (45) it can be deduced that the resonance frequency is dependent on the magnetocrystalline anisotropy field, $H_k$, which is defined as the field needed to saturate the magnetization. $H_k$ is usually correlated to the magnetic coercivity, $H_c$. In principle, this implies that a material with high coercivity is harder to saturate while a material with low coercivity is easier to saturate. It follows that the resonance absorption frequency of a magnetic absorber can be tuned by tailoring the coercivity of the material.

Very few reports exist in literature about tuning the relaxation magnetization resonance absorption by varying the coercivity of magnetic materials. Ohkoshi *et al.* studied gallium and aluminum substituted ε-$Fe_2O_3$ as absorbers for millimeter waves (Figure 1.9). They employed a sol-gel synthesis method followed by high-temperature calcination (1100°C – 1200°C) to synthesize the rare ε-phase iron oxide nanoparticles in a size range of 25 – 50 nm. By varying the composition of the substituted iron oxide they were able to achieve tuning in the coercivity of the material from 2.1 kOe to 15.9 kOe corresponding to resonance frequency from 35 GHz to 190 GHz. While this study is ground breaking nonetheless, it may not have any practical application as the curie temperature in the 100°C – 200°C range for ferrite-based materials is rather low and may not be compatible with high speed aviation systems which typically have high surface temperatures.[38] Thus, it is necessary to further explore the limits of ferromagnetic nanomaterials

for electromagnetic wave absorption in order to adequately develop an absorber with reasonable applicability to defense systems.

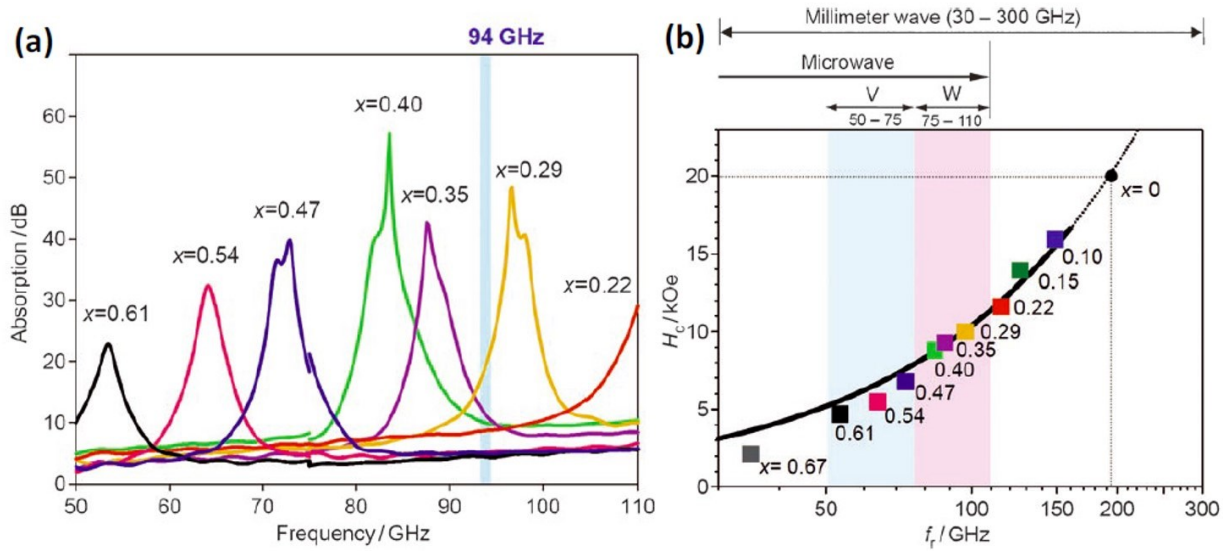


**Figure 1.9.** (a) Millimeter-wave absorption properties of $\varepsilon$-$Ga_xFe_{2-x}O_3$ with various levels of substitution; (b) Relationship between $f_r$ and $H_c$ of $\varepsilon$-$Ga_xFe_{2-x}O_3$.[39]

While Ohkoshi *et al.* have shown that it is possible to tune the resonance absorption frequency of ferromagnetic absorbers by varying the coercivity, it is quite common that ferromagnetic nanomaterials usually have low saturation magnetization ($M_0$ < 100 emu/g), which could limit the effectiveness of these materials as electromagnetic wave absorbers. From Equations (44) and (45) we can derive Snoek's law:

$$(\mu_s - 1)f = \frac{4}{3}\gamma M_0 \tag{47}$$

which indicates that the magnitude of the magnetic permeability is limited by the saturation magnetization ($M_0$), thus materials with a high $M_0$ are needed to achieve high permeability in

thin absorbers.[40] To achieve tunable resonance absorption with high permeability, it may be necessary to combine the advantages of superparamagnetic and ferromagnetic nanoparticles by exchange-coupling. Figure 1.10 demonstrates how the coupling between the soft (superparamagnetic) and hard (ferromagnetic) phases could produce magnetic materials with both high saturation magnetization and coercivity.

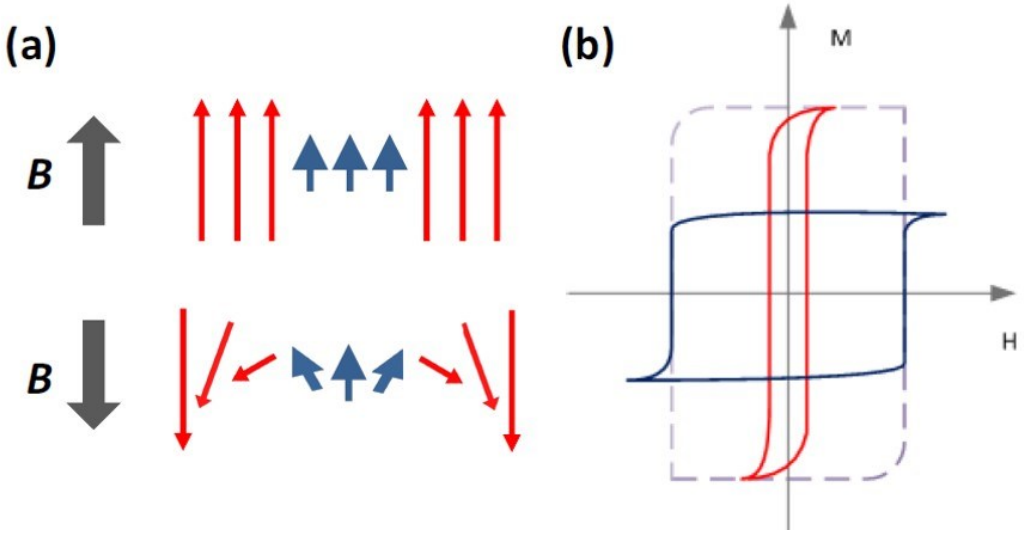


**Figure 1.10.** (a) Illustration of the moments of exchanged-coupled hard (blue) and soft (red) magnetic phases. (b) Representative hysteresis curves of soft (red), hard (blue) and exchanged spring (dashed gray) magnets. In an exchange-coupled magnetic system, the large moment of the soft phase is pinned down by the hard phase due to the interactions (exchange coupling) at the interface, and thus the composite material possesses both the high saturation magnetization of the soft phase and high coercivity of the hard phase.

## 1.8 BROADER IMPACTS AND RELEVANCE TO THE INTEREST OF NATIONAL DEFENSE

Further investigating the fundamental interactions between electromagnetic waves and magnetic nanomaterials, in particular materials with features at the sub-wavelength scale, will substantially improve the understanding of design features of the ideal electromagnetic wave absorber. Through the use of organic synthesis and the established procedures to design and control nanoscale architectures, the understanding of electromagnetic exchange-coupling and bulk/nanoscale magnetic materials will be strengthened and the developed absorbers will be applicable to a broad range of materials and technologies such as hard magnets, heterogeneous catalysts, and communication devices. Of particular interest is the application of these absorbers to reduce the electromagnetic interference of radio waves and wireless signals with the cellular and neural activities inside human bodies, or to be applied in military systems to reduce the radar cross sections of submarines, ships, and aircrafts. These technologies will be critical to national defense as technology continues to advance and new methods of protection from radar and/or electromagnetic radiation are needed.

## 1.9 REFERENCES


1. Cristina Buzea, Ivan I. Pacheco & Kevin Robbie. Nanomaterials and Nanoparticles: Sources and Toxicity. *Biointerphases* **2**, MR17–MR71 (2007).
2. Giovanni Valenti *et al.* Variable Doping Induces Mechanism Swapping in Electrogenerated Chemiluminescence of Ru(bpy)3 Core-Shell Silica Nanoparticles. *J. Am. Chem. Soc.* **138**, 15935–15942 (2016).
3. Zhenmeng Peng & Hong Yang. Designer Platinum Particles: Control of Shape, Composition in Alloy, Nanostructure and Electrocatalytic Property. *Nano Today* **4**, 143–164 (2009).
4. Von R. Becker & W. Doring. Kinetische Behandlung der Keimbildung in ubersattigten Dampfen. *Ann. Phys.* **24**, 719 (1935).
5. M. Volmer. Kinetic der Phasenbildung. *Steinfopff* **52**, 503–504 (1939).
6. M. Volmer & Z. Weber. *Z. Physik. Chem.* **119**, 227 (1926).
7. J.W. Mullin. *Crystallization*. (Oxford University Press, 1997).
8. Tadao Sugimoto, Fumiyuki Shiba, Tomohisa Sekiguchi & Hiroyuki Itoh. Spontaneous Nucleation of Monodisperse Silver Halide Particles from Homogeneous Gelatin Solution I: Silver Chloride. *Colloids and Surfaces A: Physiochem. Eng. Aspects* 183–203 (2000).
9. D.A. Porter & K.E. Easterling. *Phase Transformations in Metals and Alloys*. (Chapman & Hall, 1992).
10. Jongnam Park, Jin Joo, Soon Gu Kwon, Youngjin Jang & Taeghwan Hyeon. Synthesis of Monodisperse Spherical Nanocrystals. *Angew. Chem. Int. Ed.* **46**, 4630–4660 (2007).
11. Z.M. Peng, S.C. Yang & H. Yang. Chapter 10. in *Metallic Nanoparticles* **1**, (Wiley-VCH Verlag, 2009).

12. Victor K. LaMer & Robert H. Dinegar. Theory, Production and Mechanism of Formation of Monodispersed Hydrosols. *J. Am. Chem. Soc.* **72**, 4847–4854 (1950).
13. Howard Reiss. The Growth of Uniform Colloidal Dispersions. *J. Chem. Phys.* **19**, 482–487 (1951).
14. Xiaogang Peng, J. Wickham & A.P. Alivisatos. Kinetics of II-VI and III-V Colloidal Semiconductor Nanocrystal Growth: 'Focusing' of Size Distributions. *J. Am. Chem. Soc.* **120**, 5343–5344 (1998).
15. Natalie A. Frey, Sheng Peng, Kai Cheng & Shouheng Sun. Magnetic Nanoparticles: Synthesis, Functionalization, and Applications in Bioimiaging and Magnetic Energy Storage. *Chem. Soc. Rev.* **38**, 2532–2542 (2009).
16. Andrea R. Tao, Susan Habas & Peidong Yang. Shape Control of Colloidal Metal Nanocrystals. *Small* **4**, 310–325 (2008).
17. K. J. Vinoy & R. M. Jha. Trends in Radar Absorbing Materials. *Academy Proceedings in Engineering Sciences* **20**, 815–850 (1995).
18. E.F. Knott. *Radar Cross Section Measurements*. (SciTech Pub., 2006).
19. E. F. Knott, J. F. Shaeffer & M. T. Tuley. *Radar Cross Section*. (SciTech Pub., 2004).
20. Asoke K. Bhattacharyya & D.L. Sengupta. *Radar Cross Section Analysis and Control*. (Artech House, 1991).
21. Naamlooze Vennotschap Machinerieen.
22. C.G. Montgomery, R.H. Dicke & E. Purcell. *Principles of Microwave Circuits. Radiation Lab Series 8*. (Boston Technol., 1948).
23. W.W. Salisbury. Absorbent Body for Electromagnetic Waves. (1952).

24. Luiza de Castro Folgueras & Mirabel Cerqueira Rezende. Multilayer Radar Absorbing Material Processing by Using Polymeric Nonwoven and Conducting Polymer. *Materials Research* **11**, 245–249 (2008).
25. J.J. Bowman. *Effects of Absorbers. In Methods of Radar Cross-Section Analysis*. (Academic Press, 1968).
26. Bipin Kumar Jha & Mayur Somnath Aswale. Mechanical Aspects in Stealth Technology: Review. *IJETR* **4**, 2454–4698 (2016).
27. J.A. Adam. How to Design an 'Invisible' Aircraft. *IEEE Spectrum* **4**, 26–31 (1988).
28. H.M. Musal & H.T. Hahn. Thin Layer Electromagnetic Absorber Deisgn. *IEEE Trans. Magn.* 3851–3853 (1989).
29. What is a Vector Network Analyzer and How Does it Work? (2019).
30. Keysight FieldFox Analyzers. (2018).
31. Measurement of Dielectric Material Properties. (2019).
32. Edward J. Rothwell, Jonathan L. Frasch, Sean M. Ellison, Premjeet Chahal & Raoul O. Ouedraogo. Analysis of the Nicolson-Ross-Weir Method for Characterizing the Electromagnetic Properties of Engineered Materials. *Progress in Electromagnetics Research* **157**, 31–47 (2016).
33. J. I. Gittleman, B. Abeles & S. Bozowski. Superparamagnetism and Relaxation Effects in Granular Ni-SiO2 and Ni-Al2O3 Films. *Phys. Rev. B.* **9**, 3891–3897 (1974).
34. Unyong Jeong, Xiaowei Teng, Yong Wang, Hong Yang & Younan Xia. Superparamagnetic Colloids: Controlled Synthesis and Niche Applications. *Adv. Mater.* **19**, 33–60 (2007).

35. D. Hasegawa, H. T. Yang, T. Ogawa & M. Takahashi. Challenge of Ultra High Frequency Limit of Permeability for Magnetic Nanoparticles Assembly with Organic Polymer-Application of Superparamagnetism. *J. Magn. Magn. Mater.* **321**, 746–749 (2009).
36. Y. Liu, D. Shindo & D. J. Sellmyer. *Handbook of Advanced Magnetic Materials*. (Springer, 2006).
37. E. Van de Riet & F. Roozeboom. Ferromagnetic Resonance and Eddy Currents in High-Permeable Thin Films. *J. Appl. Phys.* **81**, 350–354 (1997).
38. R. D. Quinn & L. Gong. A Method for Calculating Transient Surface Temperatures and Surface heating Rates for High-Speed Aircraft. (2000).
39. S. I. Ohkoshi *et al.* A Millimeter-Wave Absorber Based on Gallium-Substituted Epsilon-Iron Oxide Nanomagnets. **46**, 8392–8395 (2007).
40. Dispersion and Absorption in Magnetic Ferrites at Frequencies above One Mc/S. *Physica* **14**, 207–217 (1948).

# Chapter 2. Size-Dependent Electromagnetic Absorption Properties of Iron Oxide ($Fe_3O_4$) Nanomaterials

## 2.1 INTRODUCTION

Magnetic nanomaterials have been of high interest in modern industry due to their use in an extensive array of applications such as electronics[1], optoelectronics[2], magnetic storage[3], and bio-sensing applications.[4–6] In recent years, there has been a growing interest in magnetic nanomaterials used as microwave-absorbing materials due to military and civil applications such as stealth technology and electromagnetic interference.[7] They are used in portable electronic devices such as smart phones and mobile PCs to protect humans from exposure to electromagnetic pollution, which could increase the risk of cancer or other neural illnesses.[8–10] In defense applications, the surface of ships, submarines and aircrafts are coated with electromagnetic absorbing materials to reduce the radar cross section (RCS) and increase stealth capabilities.[11–13]

Magnetic materials have long been used as radar absorbers on aircrafts, e.g., in the form of iron ball paint.[12–18] The absorber is usually applied by painting the metal surface with mixtures of carbonyl iron and polymer. This generates magnetic iron or ferrite particles *in situ* by decomposition and/or oxidation of iron carbonyl. While this approach has been demonstrated to be successful in reduction of the RCS, it can be expected that the poorly defined synthetic approach would produce inhomogeneous layers of magnetic materials with a wide distribution of particle sizes and may also generate magnetic particles containing impurities such as carbon, oxygen, and nitrogen.[19] This lack of control over material structure makes it challenging to systematically study and improve magnetic materials for electromagnetic wave absorption.

Ferrite materials have been well-explored as conventional magnetic fillers due to their high resistivity ($10^8$ – $10^{12}$ Ω cm), which makes them good candidates for the attenuation of electromagnetic waves. However, most efforts have been directed at researching the microwave absorption properties of new types of ferrites, rather than focusing on the microwave absorption properties of basic ferrite (magnetite, $Fe_3O_4$) and taking advantage of its extensive synthetic library to fine tune the particle size and morphology in order to develop a fundamental understanding of the mechanism behind the use of magnetic nanomaterials for electromagnetic wave absorption.

In Chapter 2, we report the organic solution synthesis of a series of various sized $Fe_3O_4$ nanoparticles with precise control over nanoparticle size and shape with the objective of characterizing the well-dispersed nanoparticles and make an attempt at describing the underlying physics behind the mechanism of magnetic nanomaterials for microwave absorption. A previous study has reported an inverse relationship of particle size to matching frequency in the micron range (1 – 20 μm), however, an effort is needed to determine if the established trend holds in the nanoscale range.[20] Through the use of organic solution synthesis techniques, we are able to target and obtain a specific size and morphology, which we have correlated to the magnetic loss and microwave absorption properties of our materials by measuring the complex permittivity and permeability of $Fe_3O_4$/paraffin wax composites.

## 2.2 EXPERIMENTAL METHODS

*Chemicals.* All materials (metal precursors, organic solvents, and ligands) were purchased from Sigma Aldrich. All chemicals were used as received.

*Synthesis Design.* All nanoparticles were synthesized under inert argon gas in a standard Schlenk line setup. All synthesis procedures were adapted and modified from previous reports.

### 2.2.1 Synthesis

*Synthesis of 5 nm $Fe_3O_4$ Nanoparticles.*[21] 5 nm $Fe_3O_4$ nanoparticles were synthesized by the decomposition of iron (III) acetylacetonate ($Fe(acac)_3$). In a typical synthesis, iron (III) acetylacetonate (0.706 g, 2.0 mmol) was dissolved in 20 mL diphenyl ether (DPE) containing oleic acid (1.91 mL, 6.0 mmol), oleylamine (1.97 mL, 6.0 mmol) and 1,2-hexadecanediol (2.58 g, 10.0 mmol) and refluxed for 30 min at 260°C. The precipitate was collected by centrifugation at 6000 rpm for 10 min, re-dispersed in ethanol, and centrifuged once again at 6000 rpm for 10 min. The final product was re-dispersed in hexanes and stabilized with 2-3 drops of oleylamine.

*Synthesis of 10 nm $Fe_3O_4$ Nanoparticles.*[22] 10 nm $Fe_3O_4$ nanoparticles were synthesized by the decomposition of iron (III) acetylacetonate ($Fe(acac)_3$). In a typical synthesis, iron (III) acetylacetonate (0.706 g, 2.0 mmol) was dissolved in 10 mL benzyl ether (BE) and 10 mL oleylamine, heated for 60 min at 110°C to promote decomposition of the Fe, and then refluxed for 30 min at a higher temperature (300°C). The precipitate was collected by centrifugation at 8000 rpm for 10 min, re-dispersed in ethanol, and centrifuged once again at 8000 rpm for 10 min. The final product was re-dispersed in hexanes and stabilized with 2-3 drops of oleylamine.

*Synthesis of 20 nm $Fe_3O_4$ Nanoparticles.*[21] 20 nm $Fe_3O_4$ nanoparticles were synthesized by the decomposition of iron (III) acetylacetonate ($Fe(acac)_3$) and seed-mediated growth on the previously synthesized 10 nm $Fe_3O_4$ nanoparticles. In a typical synthesis, iron (III)

acetylacetonate (0.706 g, 2.0 mmol) was dissolved in 20 mL diphenyl ether (DPE) containing oleic acid (0.64 mL, 2.0 mmol), oleylamine (0.66 mL, 2.0 mmol), 1-octadecanol (2.70 g, 10.0 mmol) and 16 mg 10 nm $Fe_3O_4$ nanoparticle seeds, heated for 60 min at 110°C to promote decomposition of the Fe, and then refluxed for 30 min at a higher temperature (300°C). The precipitate was collected by centrifugation at 6000 rpm for 10 min, re-dispersed in ethanol, and centrifuged once again at 6000 rpm for 10 min. The final product was re-dispersed in hexanes and stabilized with 2-3 drops of oleylamine.

*Synthesis of 100 nm $Fe_3O_4$ Nanoparticles.*[7] 100 nm $Fe_3O_4$ nanoparticles were synthesized by the decomposition of iron (III) acetylacetonate ($Fe(acac)_3$). In a typical synthesis, iron (III) acetylacetonate (0.353 g, 1.0 mmol) and decanoic acid (0.688 g, 4.0 mmol) were dissolved in 25 mL benzyl ether (BE), degassed for 60 min at 60°C, heated at a heating rate of 2°C /min to 200°C for 120 min to promote decomposition of the Fe, and then heated at a heating rate of 2°C /min to reflux for 60 min at a higher temperature (300°C). The precipitate was collected by centrifugation in a mixture of hexanes and toluene at 10,000 rpm for 10 min, re-dispersed in ethanol, and centrifuged in a mixture of hexanes and toluene once again at 10,000 rpm for 10 min. The final product was re-dispersed in ethanol.

*Micron $Fe_3O_4$ Nanoparticles.* Micron $Fe_3O_4$ nanoparticles (500 nm < d < 5 μm) were purchased through Sigma Aldrich.

### 2.2.2 Materials Characterization

Transmission electron microscopy (TEM) images were acquired on a 120 kV, FEI Tecnai 12 TWIN microscope. X-ray diffraction (XRD) patterns were collected on a PANalytical X'Pert[3] Powder X-Ray Diffractometer equipped with a Cu Kα radiation source (λ=0.15406). Magnetic

hysteresis loops were acquired on a MicroMag 2900 Series AGM. Small angle X-ray scattering (SAXS) data was collected by a colleague of Dr. Robert Leheny, professor from the Johns Hopkins University Physics & Astronomy Department.

### 2.2.3 Electromagnetic Absorption Studies

5, 10 and 20 nm $Fe_3O_4$ composite wax/nanoparticle samples were prepared in 20 mL scintillation vials by dispersing the appropriate amounts of paraffin wax and $Fe_3O_4$ nanoparticles in toluene to achieve nanoparticle volume fractions ranging from 15% to 40% and slowly evaporating the solvent to create a uniformly dispersed composite matrix. 100 nm and micron $Fe_3O_4$ composites were prepared in a similar fashion, but with chloroform as the solvent. The resulting composites were then molded into a toroidal shape using a Teflon mold with an outer diameter of 6.98 mm, inner diameter of 3.03 mm and thickness of 1 mm and fitted to a Keysight 85051B 7 mm airline for the microwave measurements. The complex permittivity and permeability of the composite samples were measured using a Keysight FieldFox N9918A Microwave Analyzer in the 2 – 18 GHz region and the reflection loss was calculated using the measured permittivity and permeability.

## 2.3 DISCUSSION AND RESULTS

### 2.3.1 Materials Characterization

Iron oxide nanoparticles of all sizes ranging from 5 nm to micron $Fe_3O_4$ are shown in transmission electron microscopy (TEM) images in Figure 2.1(a). Aside from the micron-sized $Fe_3O_4$ particles (purchased from Sigma-Aldrich), which show no clear morphology and a wide size distribution, all synthesized nanoparticles show a sphere-like morphology. Through size distribution analysis, mean diameters have been determined to be 5.37 nm, 9.19 nm and 18.11 nm for the 5 nm, 10 nm and 20 nm nanoparticle sizes, respectively. Size distribution profiles are shown in Figure 2.2. The mean diameter of the 100 nm nanoparticles was unable to be accurately determined from a size distribution analysis due to aggregation concerns, but was judged to be ~100 nm via TEM imaging. The micron-sized particles were purchased with a size qualification of 500 nm < d < 5 μm. Figure 2.1(b) presents the typical x-ray diffraction (XRD) pattern for the various sized $Fe_3O_4$ products. All of the peaks align with the expected pattern for a cubic magnetite structure as confirmed by their perfect agreement with JCPDS No. 00-09-0629. No other diffraction peaks besides those corresponding to $Fe_3O_4$ were observed, which indicates high purity of our as-synthesized products. Figure 2.1(c) displays the magnetic hysteresis loops of all sizes of the as-synthesized and purchased $Fe_3O_4$ nanoparticles. The saturation magnetization values ($M_s$) vary from sample to sample and were determined by assuming $M(H) = M_s + X_dH$ ($X_d$ being the high field susceptibility) at high field and extrapolating the M(H) curve to zero field (i.e. $H = 0$).[23,24] $M_s$ values were found to be 5.79, 33.57, 45.36, 41.33 and 49.50 emu $g^{-1}$, listed in order of increasing nanoparticle size (i.e. 5, 10, 20, 100 nm, and micron, respectively). All of these values are much lower than that of bulk $Fe_3O_4$ (85 – 100 emu $g^{-1}$), which is expected according to established values for saturation magnetization from a previous

size determined saturation magnetization report.[25] It is expected that there is no real trend correlating the size of the $Fe_3O_4$ nanoparticles to their saturation magnetization as this is a property dependent upon the crystallinity of the particles rather than their size.[26–28] The hysteresis curves reveal coercivities of 14.9, 5.5, 4.2, 90.7, and 120.9 Oe, once again listed in order of increasing size. It is worthy to note that the smaller size nanoparticles (5, 10 and 20 nm) exhibit coercivities that are much lower than that of bulk $Fe_3O_4$ (115 – 150 Oe). This could be due to special morphology-related shape anisotropy when considering the sub-domain size of these nanoparticles.[29] The larger sized particles (100 nm and micron sized) have coercivities comparable to that of bulk $Fe_3O_4$. Small angle X-ray scattering (SAXS) was conducted to gain a better understanding of the nanoscale features of, and to determine the degree of aggregation in the $Fe_3O_4$/wax composites used in the electromagnetic studies. Figure 2.3(a) displays the raw SAXS data of the toroidal shaped 10 nm $Fe_3O_4$/wax composites across all loadings. As evidenced by the local maximum around 0.08 $nm^{-1}$, there is a distinct size feature present across all loadings, indicating that the degree of aggregation within the wax composites is relatively similar regardless of loading. Figure 2.3(b) displays the Guinier analysis of the SAXS data. From this, the radius of gyration ($R_g$) for the set of samples measured was determined to be 211.99 ± 15.88 nm, indicating significant aggregation across all nanoparticle loadings. SAXS measurements were only conducted on the 10 nm $Fe_3O_4$/wax composites and it was assumed that the other sized $Fe_3O_4$/wax composites display similar behavior.

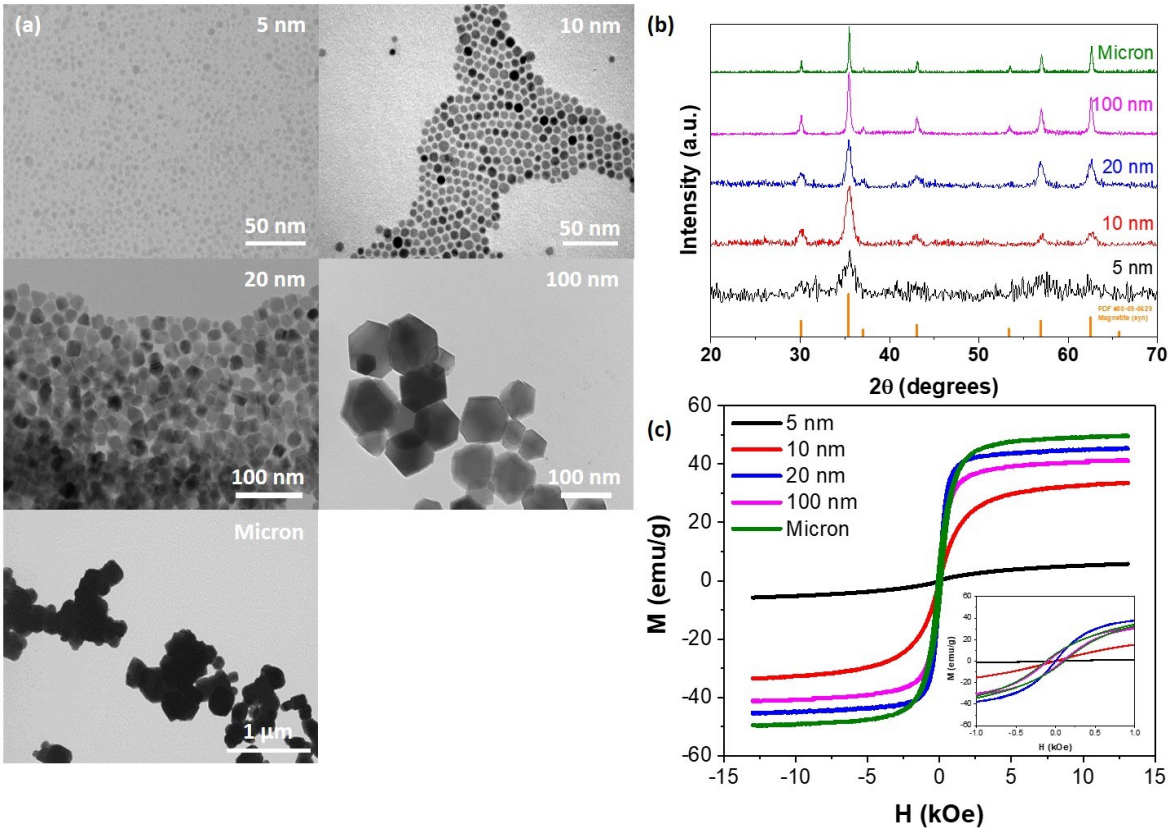


**Figure 2.1.** (a) TEM images, (b) XRD patterns and (c) hysteresis loops of 5, 10, 20, 100 nm and micron $Fe_3O_4$ nanoparticles.

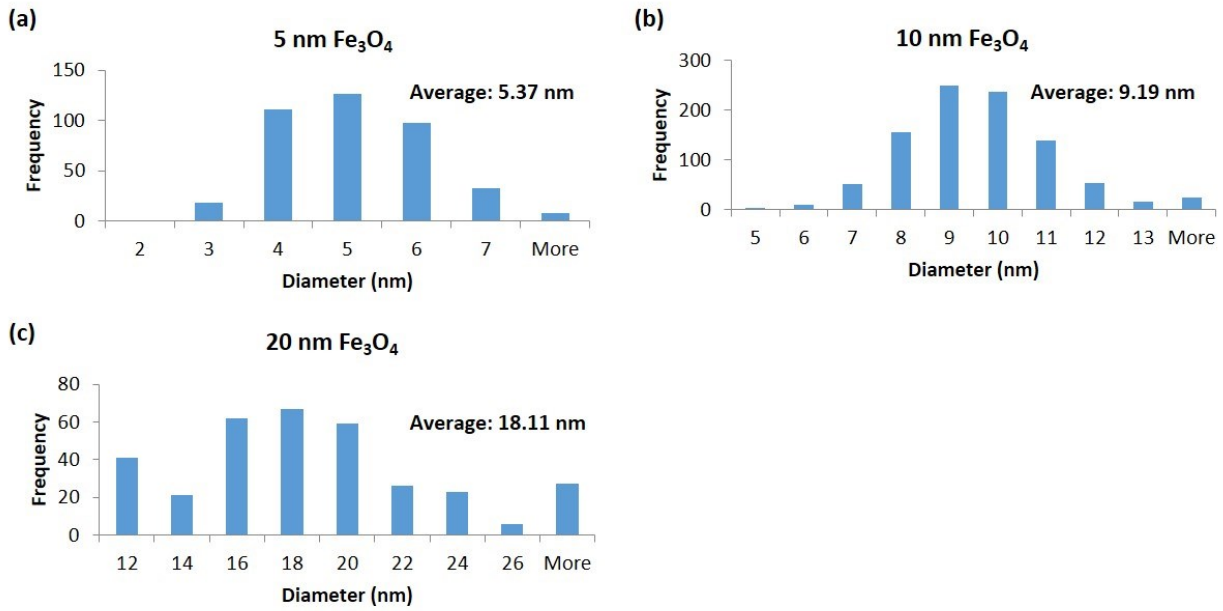


**Figure 2.2.** Size distribution profiles for (a) 5 nm $Fe_3O_4$, (b) 10 nm $Fe_3O_4$, and (c) 20 nm $Fe_3O_4$.

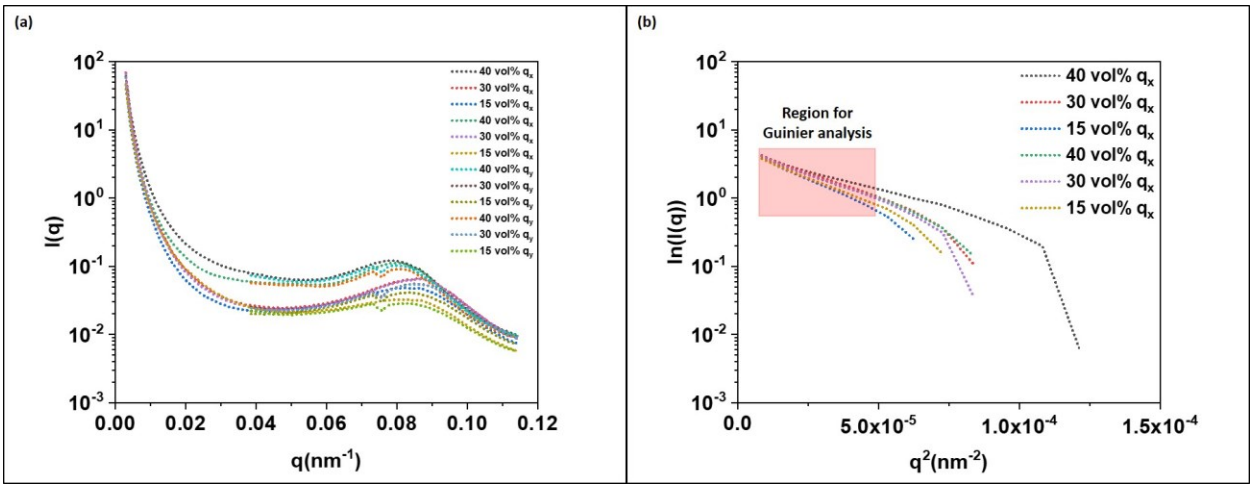


**Figure 2.3.** (a) Raw SAXS data for a 10 nm $Fe_3O_4$ nanoparticle/wax toroid at loadings of 40 vol%, 30 vol%, and 15 vol%. Two different toroids of the same composition at each loading were measured. (b) Guinier analysis of the 10 nm $Fe_3O_4$ nanoparticle/wax toroids at loadings of 40 vol%, 30 vol%, and 15 vol%. The region highlighted in red was used to determine the radius of gyration ($R_g$).

### 2.3.2 Discussion of Electromagnetic Measurements

Figure 2.4 shows the data output using 10 nm $Fe_3O_4$ nanoparticles at a 30 vol% loading as an example. Figure 2.4(a) shows the reflection loss (RL) data for varying thicknesses (1 mm – 6 mm) of 10 nm $Fe_3O_4$/paraffin wax composites at a 30 vol% nanoparticle loading. The relationship between the reflection loss of the $Fe_3O_4$/paraffin wax composite and frequency is calculated as follows:

$$Z_{in} = \sqrt{\frac{\mu_r}{\varepsilon_r}} \tanh j\left[\frac{2\pi f d \sqrt{\mu_r \varepsilon_r}}{c}\right] \quad (1)$$

$$R_L = 20log\left|\frac{Z_{in}-1}{Z_{in}+1}\right| \quad (2)$$

where $\varepsilon_r$ and $\mu_r$ are the relative complex permittivity and permeability of the wax composite, $c$ is the speed of light, $f$ is the frequency and $d$ is the thickness of the absorbing material. As shown in Figure 2.4(a), RL absorption peaks for 10 nm $Fe_3O_4$ at a 30 vol% loading across all thickness on a 0.5 mm interval from 1 mm to 6 mm can be seen with a local maximum absorption of -7.01 dB at 5.11 GHz corresponding to a 6 mm thickness. It can be seen that more intense electromagnetic wave absorption occurs at frequencies higher than our measureable range as the absorption reaches an absolute maximum of -12.25 dB at 18 GHz, once again corresponding to a 6 mm thickness. It is common for samples of increased thickness to display high intensity RL behavior at higher frequencies, however these curves are unable to be seen in the measureable frequency range of our network analyzer. Given an instrument with a more capable frequency range, these curves would be seen at frequencies of greater than 18 GHz. Figure 2.4(b) shows the real and imaginary portions of the complex permittivity and permeability across the frequency range from 2 GHz – 18 GHz for 10 nm $Fe_3O_4$ nanoparticles at a 30 vol% loading. In general, the values of both the real ($\varepsilon'$, $\mu'$) and imaginary ($\varepsilon''$, $\mu''$) portions of the complex permittivity and permeability gradually decrease with increasing frequency. For both imaginary portions, $\varepsilon''$ and $\mu''$, a much

sharper decrease can be seen early on in the frequency range, from 2 GHz < $f$ < 4 GHz. Negative values in both ε″ and μ″ may come from errors in the instrument measurement system[7].

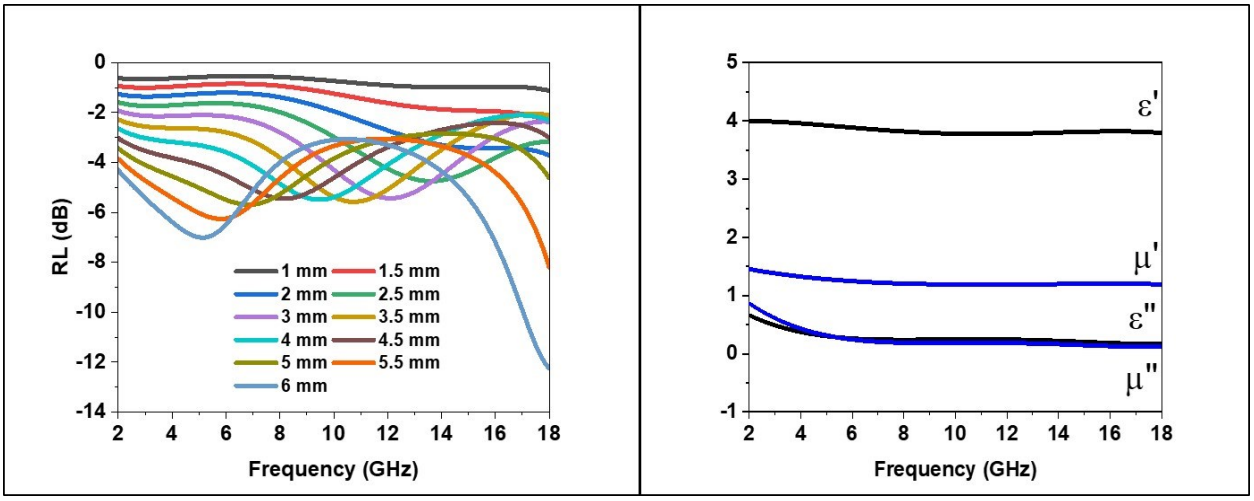


**Figure 2.4.** (a) Reflection loss for varying thicknesses (1 mm – 6 mm) of 10 nm $Fe_3O_4$/paraffin wax composites at 30 vol% nanoparticle loading. (b) Complex permittivity and permeability values for 10 nm $Fe_3O_4$/paraffin wax composites at a 1 mm thickness and 30 vol% loading.

Figures 2.5, 2.6, and 2.7 show the raw reflection loss (RL) data for all sizes of $Fe_3O_4$ (5, 10, 20, and 100 nm, and a micron size) across all nanoparticle loadings (15, 30, and 40 vol%). The previous discussion concerning Figure 2.4 can be applied to any specific size and loading in Figures 2.5, 2.6, and 2.7.

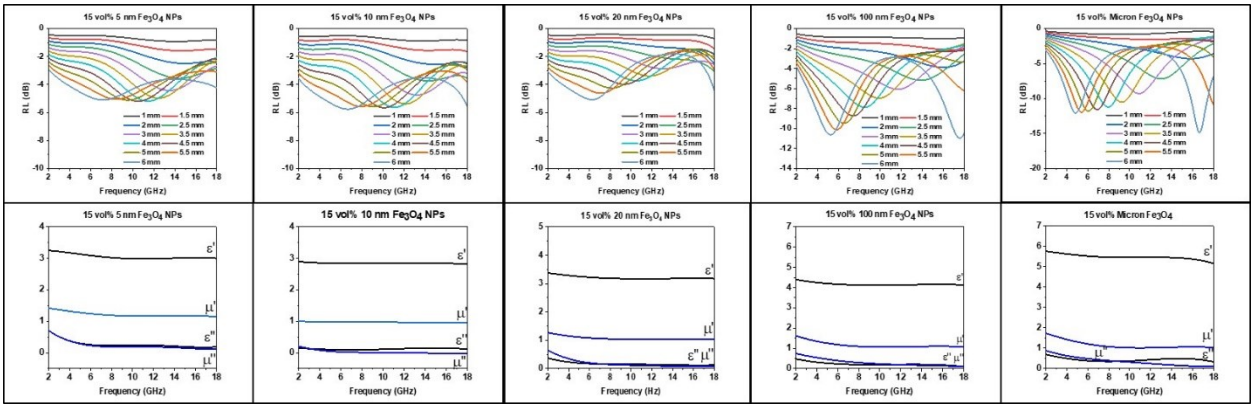


**Figure 2.5.** Raw RL Data for Varying Size $Fe_3O_4$ Nanoparticles at 15 vol% Loading

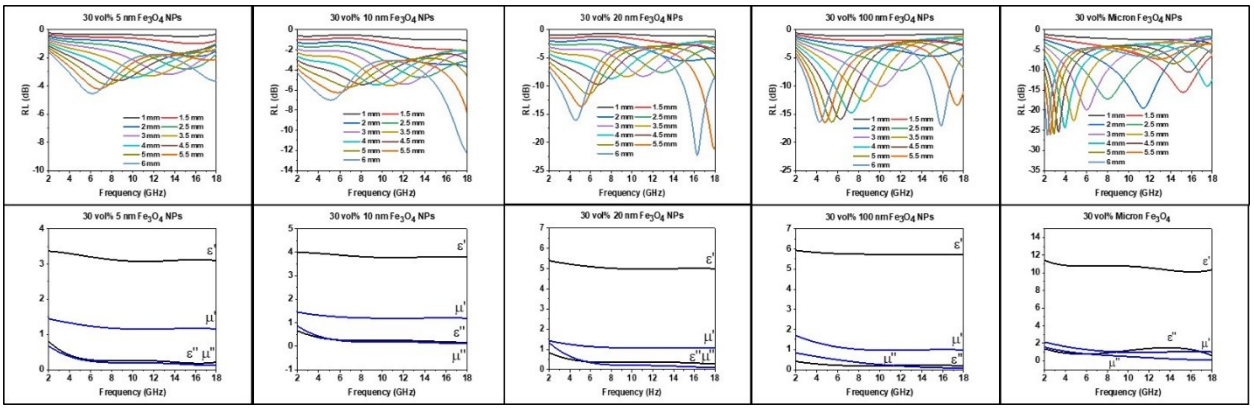


**Figure 2.6.** Raw RL Data for Varying Size $Fe_3O_4$ Nanoparticles at 30 vol% Loading

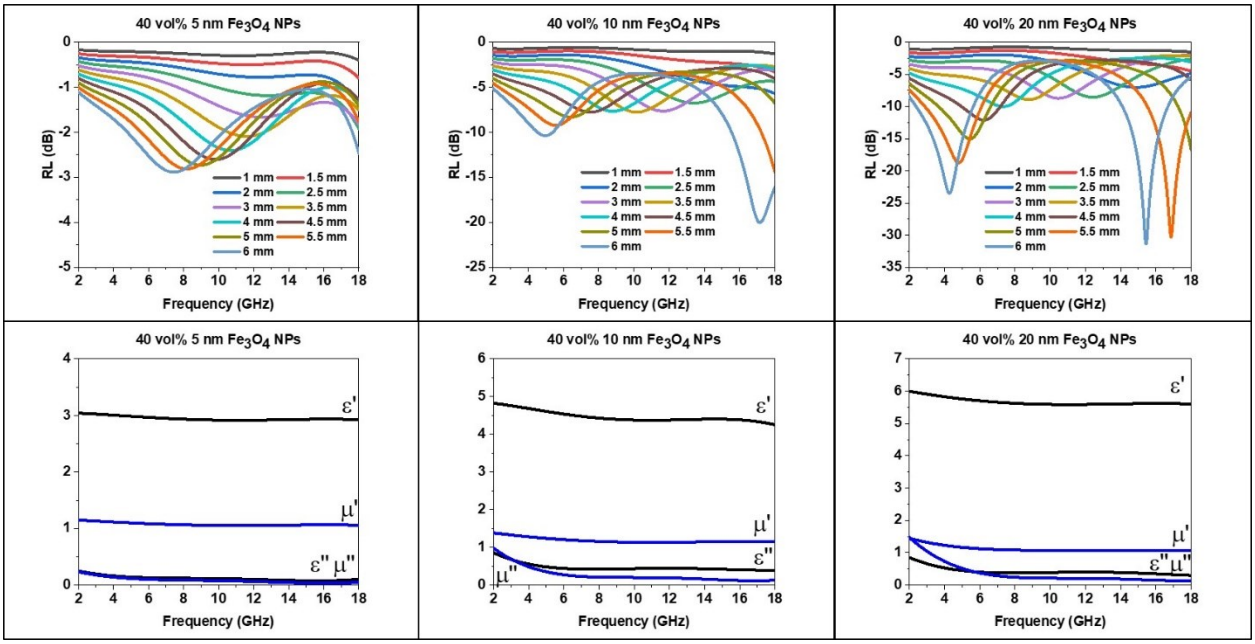


**Figure 2.7.** Raw RL Data for Varying Size $Fe_3O_4$ Nanoparticles at 40 vol% Loading

In order to discern the primary mechanism (magnetic or dielectric) for electromagnetic wave absorption displayed by the $Fe_3O_4$ nanoparticles in this study, it is necessary to look at the magnetic and dielectric loss tangents, previously discussed in Section 1.4 of the Introduction of this dissertation. Figures 2.8 and 2.9 display the magnetic and dielectric loss tangents for each size of $Fe_3O_4$ studied:

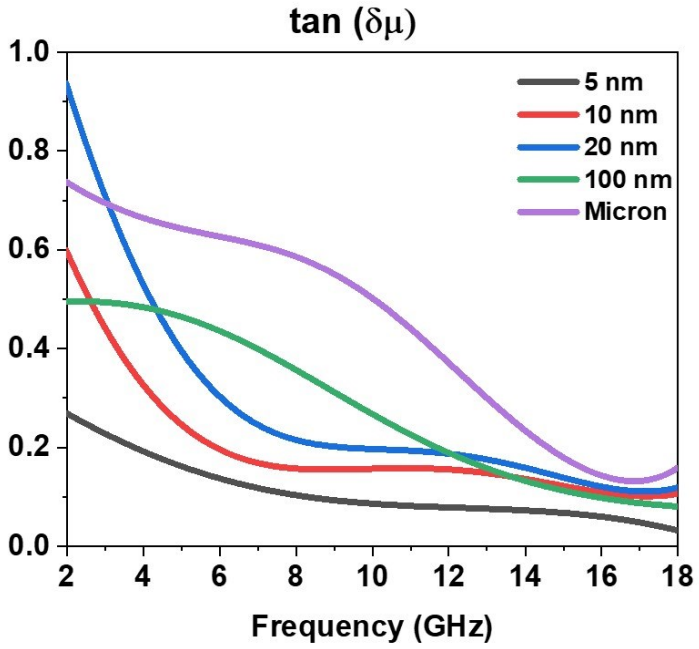


**Figure 2.8.** The magnetic loss tangent, tan(μ″/μ′), for 5, 10, 20, 100 nm and micron size $Fe_3O_4$.

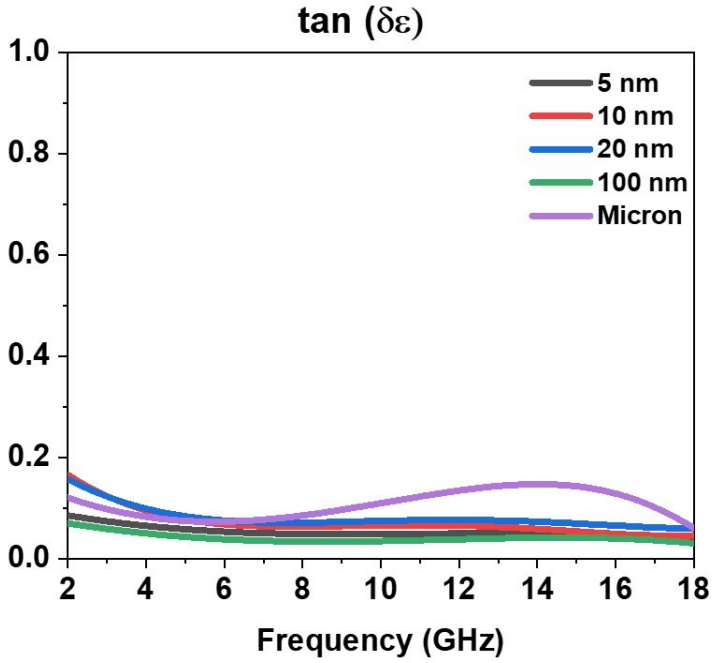


**Figure 2.9.** The dielectric loss tangent, tan(ε″/ε′), for 5, 10, 20, 100 nm and micron size $Fe_3O_4$.

As demonstrated in the Figures 2.8 and 2.9, the values of the magnetic loss tangent are much larger than the dielectric loss tangent across the entire frequency range for all sizes, indicating that the absorption mechanism is predominantly controlled by the magnetic properties of $Fe_3O_4$, rather than the dielectric properties. Thus, the magnetics will be the primary focus of the rest of this discussion.

### 2.3.3 Nanoparticle Loading Dependence Effects on Electromagnetic Wave Absorption

In order to determine the effect of nanoparticle loading on the electromagnetic absorption behavior and the materials properties (ε and μ) of our absorbers, all sizes of $Fe_3O_4$ nanoparticles were measured at varying loadings of 15, 30 and 40 vol% and the data analyzed for trends. It is worthy to note that only 5 nm, 10 nm, and 20 nm $Fe_3O_4$ nanoparticles were studied at the highest (40 vol%) loading as the inability to suspend the two larger sizes (100 nm and micron) in solution at such high loadings made it impossible to create a toroidal mold with paraffin wax. This is due to the increased rate of sedimentation for such large particle sizes. Figure 2.10(a) shows the effect of nanoparticle loading on the intensity of electromagnetic wave absorption of 10 nm $Fe_3O_4$ nanoparticles in a toroid of 3 mm thickness (the 3 mm data was chosen to use for comparison studies for ease of conceptual analysis).

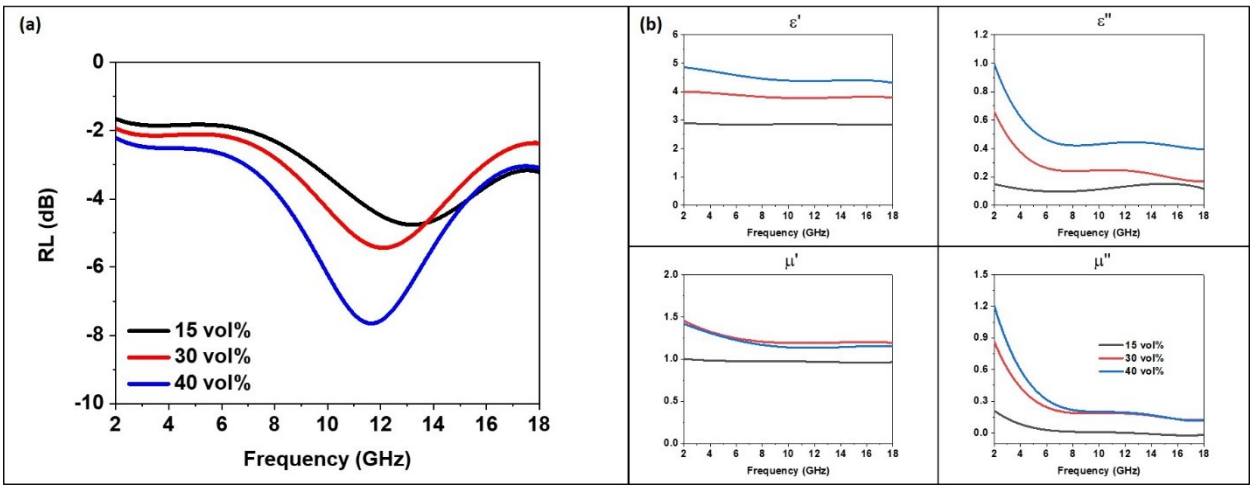


**Figure 2.10.** (a) Reflection loss for varying nanoparticle loadings (15, 30, and 40 vol%) of 10 nm $Fe_3O_4$/paraffin wax composites at a 3 mm thickness. (b) Visualization of the effect of loading on the real and imaginary portions of the permittivity and permeability of 10 nm $Fe_3O_4$ nanoparticles.

The results of the specific maximum absorption intensities for 3 mm thick wax/nanoparticle composite toroids across all loadings are summarized in Table 2.1 below:

**Table 2.1.** Nanoparticle Loading and Size Effects on Intensity of Electromagnetic Wave Absorption.

| **Loading in Wax Composite** | **5 nm $Fe_3O_4$** | **10 nm $Fe_3O_4$** | **20 nm $Fe_3O_4$** | **100 nm $Fe_3O_4$** | **Micron $Fe_3O_4$** |
|---|---|---|---|---|---|
| 15 vol% | -4.43 dB | -4.76 dB | -2.88 dB | -6.08 dB | -9.28 dB |
| 30 vol% | -3.18 dB | -5.43 dB | -8.26 dB | -10.20 dB | -19.97 dB |
| 40 vol% | -1.67 dB | -7.65 dB | -8.73 dB | X* | X* |

*X denotes samples that were unable to be measured due to dispersion problems at large sizes and high loadings.

Demonstrated in Figure 2.10(a) and summarized across all loadings in the table above, as the nanoparticle loading of the measured sample increases, the intensity of the electromagnetic wave

absorption increases as well. The reasoning behind this phenomena is relatively simple and explained by the fact that as the loading of the sample increases, the overall volume of nanoparticles increases as well, thus increasing the effective intensity of absorption. Simply put, more electromagnetic absorbing material results in greater electromagnetic absorption. It is worthy to note that the 5 nm $Fe_3O_4$ nanoparticles deviate from this trend and show a decrease in absorption intensity as the loading increases. It is thought that this is due to some interesting exchange coupling effects arising from the small size of the nanoparticles.

Figure 2.10(a) also shows the effect of nanoparticle loading on the frequency of electromagnetic wave absorption of 10 nm $Fe_3O_4$ nanoparticles in a toroid of 3 mm thickness. The results of the maximum absorption frequencies for 3 mm thick wax/nanoparticle composite toroids across all loadings are summarized in Table 2.2 below:

**Table 2.2.** Nanoparticle Loading and Size Effects on Frequency of Electromagnetic Wave Absorption.

| **Loading in Wax Composite** | **5 nm $Fe_3O_4$** | **10 nm $Fe_3O_4$** | **20 nm $Fe_3O_4$** | **100 nm $Fe_3O_4$** | **Micron $Fe_3O_4$** |
|---|---|---|---|---|---|
| 15 vol% | 13.50 GHz | 13.14 GHz | 13.03 GHz | 11.65 GHz | 10.88 GHz |
| 30 vol% | 13.41 GHz | 12.12 GHz | 11.06 GHz | 10.08 GHz | 6.01 GHz |
| 40 vol% | 12.41 GHz | 11.65 GHz | 10.46 GHz | X* | X* |

*X denotes samples that were unable to be measured due to dispersion problems at large sizes and high loadings.

Demonstrated in Figure 2.10(a) and detailed in the table above, the frequency of absorption varies inversely with the nanoparticle loading, i.e. the frequency of absorption decreases as the nanoparticle loading increases. This phenomenon can be explained using logic and the impedance matching condition for ideal electromagnetic wave absorbers:

$$\omega\mu'' d = Z_0 \quad (3)$$

As we increase the nanoparticle loading in our absorbing material, we are increasing the effective permittivity and permeability of the sample. It follows that based on the impedance matching condition, while holding thickness constant and increasing the permeability of our sample, the frequency of absorption will decrease.

Similar to the previous discussion, in order to determine the effect of nanoparticle loading and size on the materials properties (ε and μ), all sizes of $Fe_3O_4$ nanoparticles were measured at varying loadings of 15, 30 and 40 vol% and the data analyzed for trends. Figure 2.10(b) shows the effects of nanoparticle loading on the permittivity and permeability of 10 nm $Fe_3O_4$ nanoparticles in a toroid of 1 mm thickness. In agreement with previous studies, it is shown that as nanoparticle loading increases, ε′, ε″, μ′ and μ″ all increase as well[7]. The reasoning behind this phenomenon is relatively simple and once again explained by the fact that as the loading of the sample increases, the overall volume of nanoparticles increases as well, thus increasing the effective permittivity and permeability of the material. It is observed that as the nanoparticle loading is increased, both the real and imaginary portions of the permittivity and permeability increase as well.

Figures 2.11 – 2.14 show the effect of loading on the reflection loss (RL) data for 5 nm, 20 nm, 100 nm, and micron sized $Fe_3O_4$ across all nanoparticle loadings (15, 30, and 40 vol%), respectively. The previous discussion concerning the 10 nm $Fe_3O_4$ can be applied to any specific size and loading as demonstrated in Figures 2.11 – 2.14.

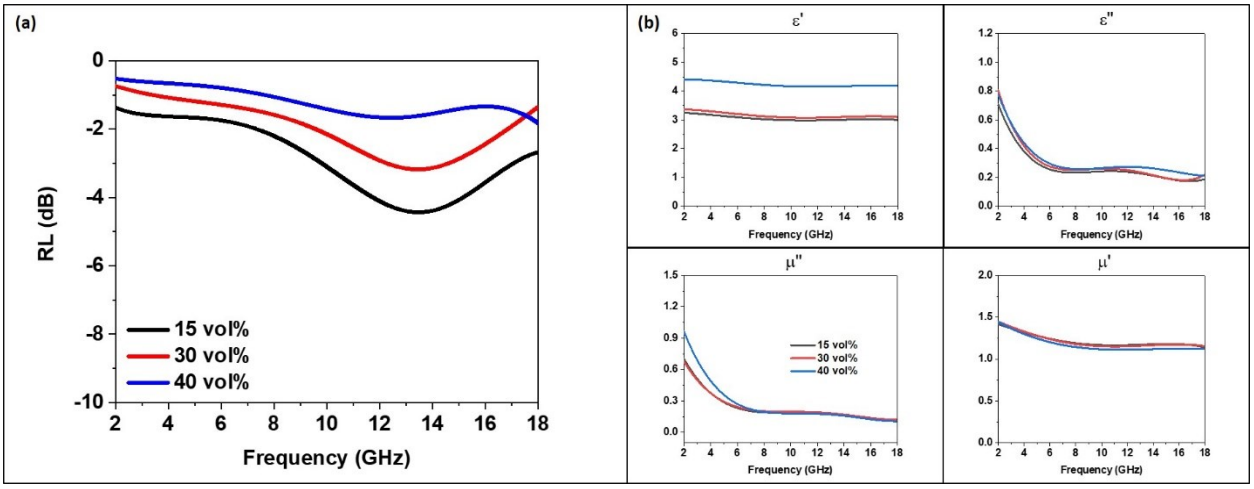


**Figure 2.11.** (a) Visualization of the effect of loading on the reflection loss resonant frequency for 5 nm $Fe_3O_4$ samples of 3 mm thickness. (b) Visualization of the effect of loading on the real and imaginary portions of the permittivity and permeability of 5 nm $Fe_3O_4$ nanoparticles.

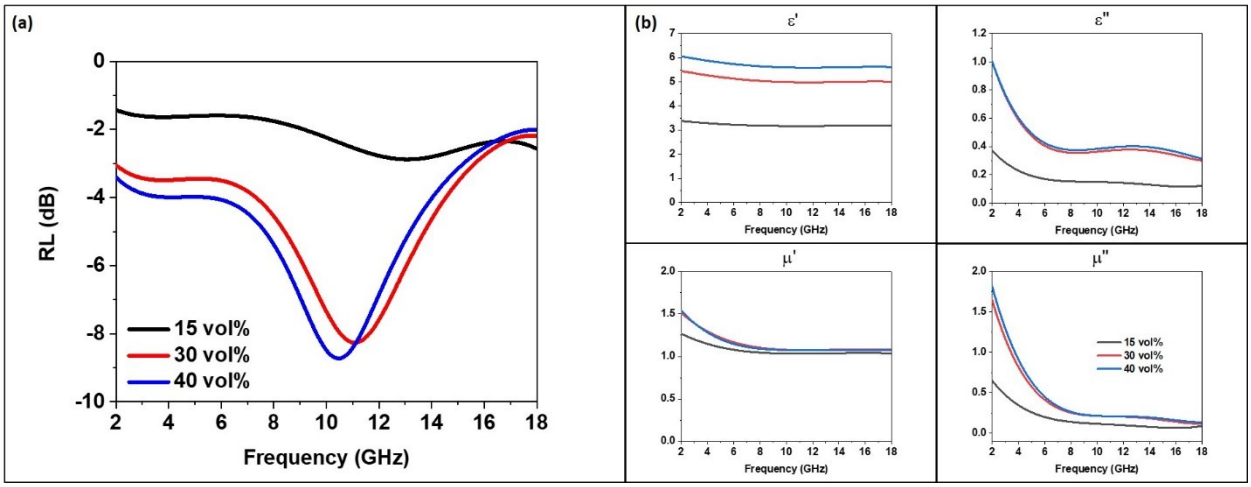


**Figure 2.12.** (a) Visualization of the effect of loading on the reflection loss resonant frequency for 20 nm $Fe_3O_4$ samples of 3 mm thickness. (b) Visualization of the effect of loading on the real and imaginary portions of the permittivity and permeability of 20 nm $Fe_3O_4$ nanoparticles.

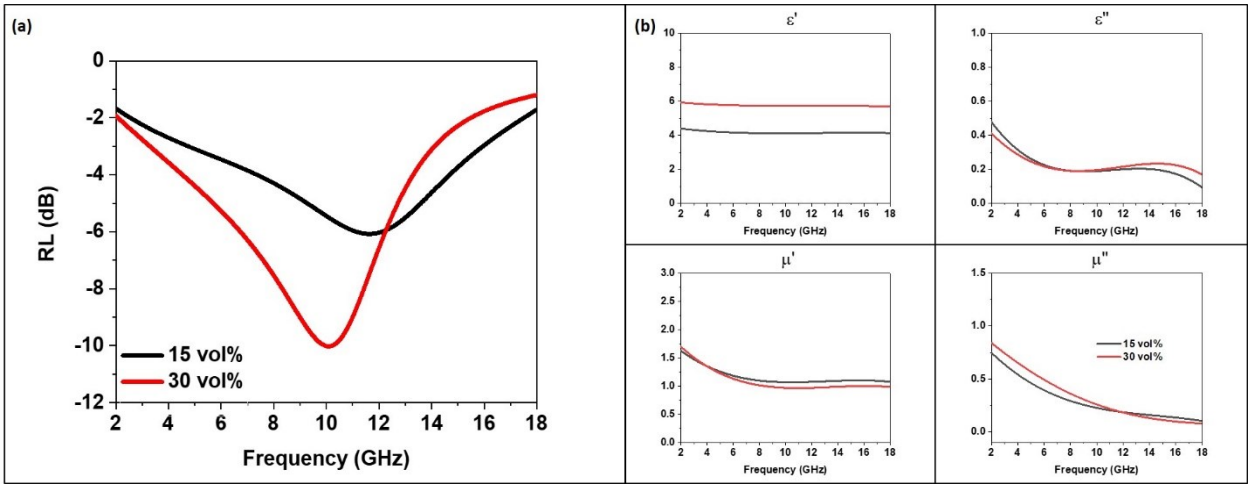


**Figure 2.13.** (a) Visualization of the effect of loading on the reflection loss resonant frequency for 100 nm $Fe_3O_4$ samples of 3 mm thickness. (b) Visualization of the effect of loading on the real and imaginary portions of the permittivity and permeability of 100 nm $Fe_3O_4$ nanoparticles.

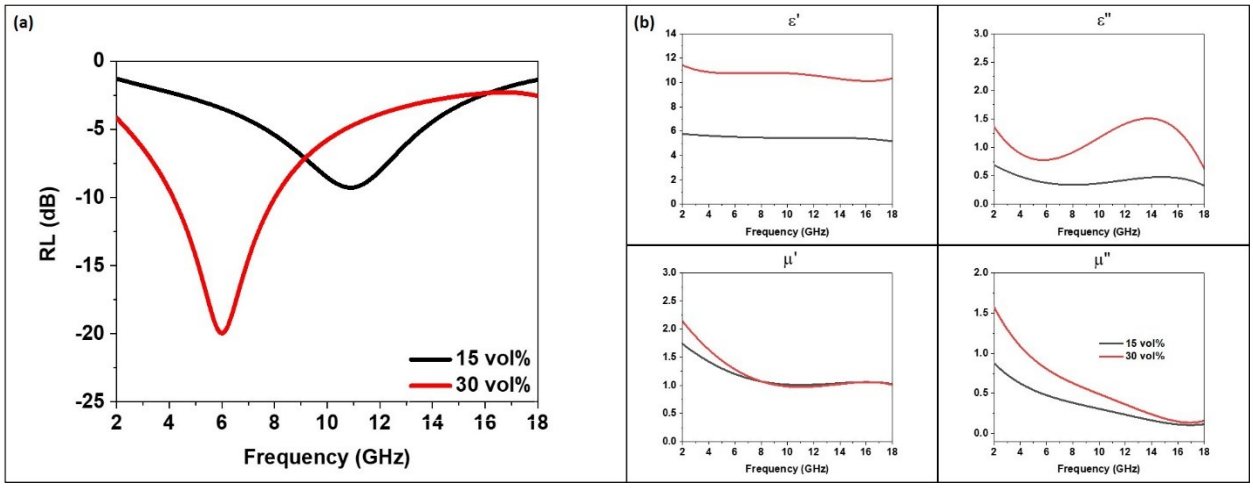


**Figure 2.14.** (a) Visualization of the effect of loading on the reflection loss resonant frequency for micron $Fe_3O_4$ samples of 3 mm thickness. (b) Visualization of the effect of loading on the real and imaginary portions of the permittivity and permeability of micron $Fe_3O_4$.

### 2.3.4 Size Dependence Effects on Electromagnetic Wave Absorption

In order to determine the effect of nanoparticle size on the materials properties of the system, all desired sizes of $Fe_3O_4$ nanoparticles were measured at varying loadings of 15, 30 and 40 vol% and the data compared, holding the loading percentage constant. As stated before, only the 5, 10 and 20 nm $Fe_3O_4$ nanoparticles were measured at the highest, 40 vol% loading due to sedimentation constraints with the larger sized particles. Figure 2.15(a) and (c) display the effect of nanoparticle size on the RL peak intensity and resonant frequency for all sizes of $Fe_3O_4$ nanoparticles at a 3 mm toroid thickness, with a 15 vol% loading and 30 vol% loading, respectively.

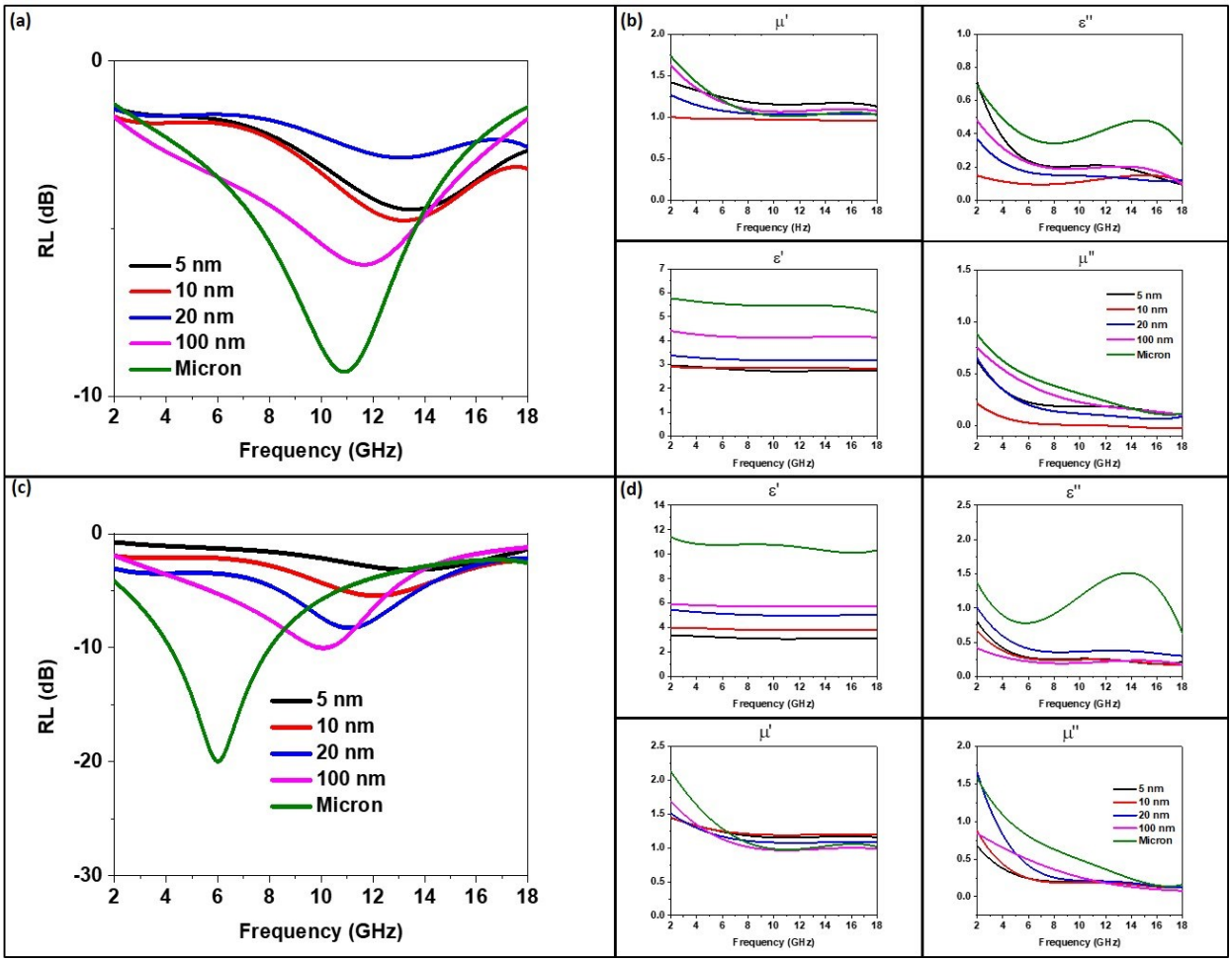


**Figure 2.15.** (a) Illustration of the effect of nanoparticle size on the reflection loss resonant frequency for $Fe_3O_4$ samples of 3 mm thickness and 15 vol% loading. (b) Illustration of the effect of nanoparticle size on the real and imaginary portions of the permittivity and permeability of $Fe_3O_4$ nanoparticles at 15 vol% loading. (c) Illustration of the effect of nanoparticle size on the reflection loss resonant frequency for $Fe_3O_4$ samples of 3 mm thickness and 30 vol% loading. (d) Illustration of the effect of nanoparticle size on the real and imaginary portions of the permittivity and permeability of $Fe_3O_4$ nanoparticles at 30 vol% loading.

As shown, the position of the RL peak shifts to lower frequencies as the size of the nanoparticle is increased. The results for the maximum absorption frequencies for 3 mm thick wax/nanoparticle composite toroids across all loadings were previously summarized in Table 2.2. As shown in the Table 2.2, we see that the mechanism of increasing the particle size

promotes a shift towards lower frequencies holds true across all sizes and loadings measured. Specifically, taking the 30 vol% loading into consideration, we see the resonance peaks at 13.41 GHz for 5 nm $Fe_3O_4$, 12.12 GHz for 10 nm $Fe_3O_4$, 11.06 GHz for 20 nm $Fe_3O_4$, 10.08 GHz for 100 nm $Fe_3O_4$ and 6.01 GHz for the micron $Fe_3O_4$. It is promising that between the 5 nm, 10 nm and 20 nm $Fe_3O_4$ nanoparticles we see the exact same shift of ~1 GHz as we double the size of the nanoparticle, giving indication that the mechanism behind nanoparticle electromagnetic wave absorption may be directly related to the size of the nanoparticle. The shift from 100 nm to the micron $Fe_3O_4$ size strays from the trend in the first three sizes, but this is obviously due to the expansive size qualification range; the micron particles are in quite a broad size range of anywhere from 500 nm to 5 μm, making it nearly impossible to draw a concrete conclusion from the corresponding data. Nevertheless, this data shows that a size increase will shift the resonance peak to a lower frequency.

When discerning the effect of nanoparticle size on the intensity of the electromagnetic wave absorption, Table 1, and Figure 2.15(a) and (c) clearly show that as the size of the nanoparticle is increased, so is the intensity of absorption. Specifically, taking the 30 vol% loading into consideration, we see the maximum absorption intensities occur at -3.18 dB for 5 nm $Fe_3O_4$, -5.43 dB for 10 nm $Fe_3O_4$, -8.26 dB for 20 nm $Fe_3O_4$, -10.20 dB for 100 nm $Fe_3O_4$ and -19.97 dB for the micron $Fe_3O_4$. The mechanism behind this process is difficult to understand and has yet to be explored in depth. Of particular interest is the extremely low intensity of the 15 vol% 20 nm $Fe_3O_4$, which deviates from the observed trend. This deviation is thought to be an anomaly due to the unique seeded-growth synthetic process by which the 20 nm $Fe_3O_4$ nanoparticles are made.

Figures 2.15(b) and (d) display the effect of nanoparticle size on the real and imaginary portions of the permittivity and permeability for all sizes of $Fe_3O_4$ nanoparticles at a 6 mm toroid thickness, with a 15 vol% loading and 30 vol% loading, respectively. The trends can be seen in each plot in Figures 2.15(b) and (d), but the generalized trends are summarized in Table 2.3 below:

**Table 2.3.** Nanoparticle Size Effects On Complex Permittivity and Permeability.

| **Material Property** | **Trend** |
|---|---|
| Real Permittivity (ε′) | Micron > 100 nm > 20 nm > 10 nm > 5 nm |
| Imaginary Permittivity (ε′′) | Micron > 20 nm > 100 nm > 10 nm > 5 nm |
| Real Permeability (μ′) | No Trend |
| Imaginary Permeability (μ′′) | Micron > 100 nm > 20 nm > 10 nm > 5 nm |
| Reflection Loss Peak (RL) | ↑ Size = Shift of RL peak to lower frequencies |

Figure 2.16(a) displays the effect of nanoparticle size on the RL peak intensity and resonant frequency and Figure 2.16(b) displays the effect of nanoparticle size on the real and imaginary portions of the permittivity and permeability for 5, 10 and 20 nm $Fe_3O_4$ nanoparticles at a 3 mm toroid thickness, with a 40 vol% loading. The previous discussion on size effects can be applied to the 5, 10, and 20 nm particles at 40 vol% loading as well.

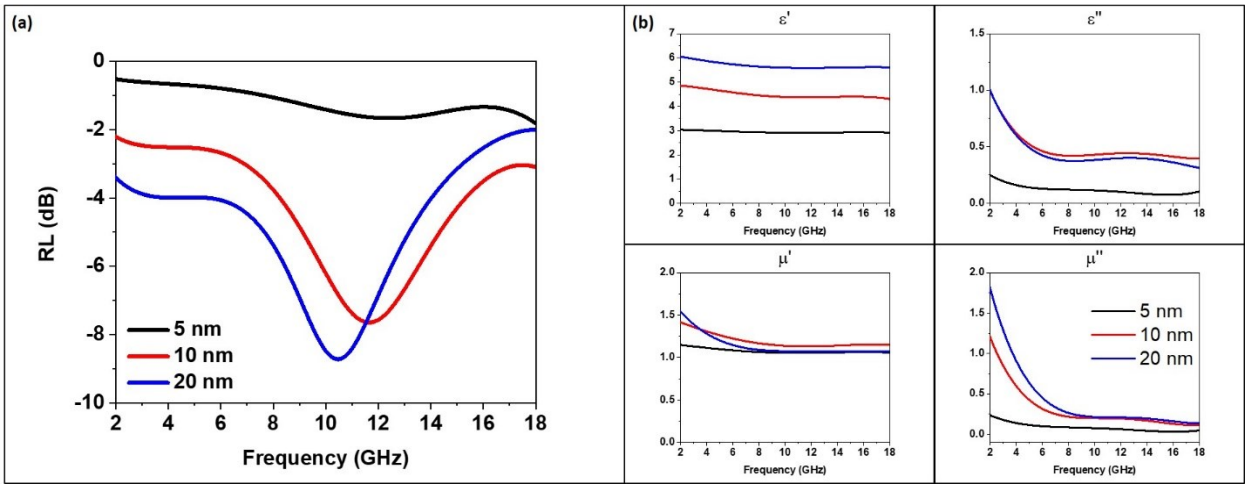


**Figure 2.16.** (a) Illustration of the effect of nanoparticle size on the reflection loss resonant frequency for $Fe_3O_4$ samples of 3 mm thickness and 40 vol% loading. (b) Illustration of the effect of nanoparticle size on the real and imaginary portions of the permittivity and permeability of $Fe_3O_4$ nanoparticles at 40 vol% loading.

As previously stated, the dielectric side (real and imaginary permittivity) of electromagnetic wave absorption has been well explored and is not the focus of our efforts. The real permittivity is thought of as the ability of a material to store electrical energy in an electric field and the imaginary permittivity is the dielectric loss dependent on conductivity.

The real permeability is thought of as the materials magnetic moment alignment to the field. The real permeability is very weakly size dependent when dealing with nanoparticles that are not perfect crystals as the alignment will be non-perfect and rather random depending on the crystallinity of each specific nanoparticle size, thus explaining a lack of an apparent trend amongst the varying sizes of the $Fe_3O_4$ nanoparticles. Mathematically, the explanation for this lack of trend can be seen by looking at the real permeability caused by the Néel relaxation of a material in the superparamagnetic state[30]:

$$\mu' = \mu_0\left(1 + \frac{V_p M_0^2}{3 k_B T}\right) \quad (4)$$

where $V_p$ is the volume of the nanoparticle, $M_0$ is the saturation magnetization, $k_B$ is the Boltzmann constant and $T$ is the temperature. Since $\frac{V_p M_0^2}{3k_B T}$ will be an extremely small number ($V_p M_0^2 << 3K_B T$ and $\frac{V_p M_0^2}{3k_B T} << 1$), any change in volume will have a negligent effect on $\mu'$.

Explaining the trends for the imaginary permeability and the RL absorption frequency are rather difficult to do. Qualitatively, the imaginary permeability is a measure of the rotation of the magnetic moment of a material around its easy axis. As the size of a material increases, rotation of the material around an axis becomes a more energy intensive process, thus explaining the increase in μ″ as the size of our $Fe_3O_4$ nanoparticles increase. This problem could be quantitatively solved by using the Landau-Lifshitz-Gilbert (LLG) equation[31,32]:

$$\frac{d\vec{M}}{dt} = \gamma(\vec{M} \; x \; \vec{H}) + \frac{\alpha}{M} \vec{M} \; x \; \frac{d\vec{M}}{dt} \tag{5}$$

which describes the change of magnetization **M** under a magnetic field **H** where $\gamma$ is the gyromagnetic ratio and $\alpha$ is the damping frequency. Using a free software such as Object Oriented Micromagnetic Framework (OOMMF) or the commercially available software, LLG Micromagnetics Simulator, an expression for the complex permeability size dependence could be derived.

The solution to the observed trend in the RL absorption peak frequencies can be solved using transmission line theory. According to transmission line theory, the reflection coefficient of an electromagnetic wave entering from free space into a material with a flat surface can be written as[33]:

$$r = \frac{Z tan\gamma d - Z_0}{Z tan\gamma d + Z_0} \tag{6}$$

Here $Z_0$ and $Z$ are the impedances of the free space and the material, and γ is the complex propagation constant. To maximize the electromagnetic wave absorption, the ideal case is to

have *r* in eq. (3) equal to zero, namely zero reflection, which requires the so-called impedance matching condition:

$$Ztanh\gamma d = Z_0 \tag{7}$$

For typical magnetic absorbers, with small conductivity, it is also accepted to assume the dielectric loss of the magnetic absorber is small ($\varepsilon'' << \varepsilon'$) and the magnetic loss is large ($\mu'' >> \mu'$), which further simplifies eq. (7):

$$\omega\mu'' d = Z_0 \tag{8}$$

In this case, the thickness, *d*, corresponds to the thickness of the wax/nanoparticle composite toroid. Based on our findings from above, holding *d* constant and varying the size of our nanoparticles, thus increasing μ″, it is clear to see that an increase in nanoparticle size (volume) will promote a downward (or leftward) shift in frequency corresponding to the RL peak.

### 2.3.5 Theoretical Model for the Calculation of the Effective Permeability

The effective permeability has been modeled following procedures established by R.F. Soohoo and described by Wu et al. in a previous report.[31,34] The steps to model the effective complex permeability are as follows:

(1) Derivation of an expression for the frequency dependent intrinsic permeability, $\mu_i$, and wave vector, **k**, from the LLG equation (eq. (5) from the previous section) substituted with the standard equations for the field and magnetization expansions and combined with Maxwell's equations:

$$\boldsymbol{H} = \boldsymbol{H_z} + \boldsymbol{h}e^{j\omega t - \varphi\hat{k}\cdot r} \tag{9}$$

$$\boldsymbol{M} = \boldsymbol{M_0} + \boldsymbol{m}e^{j\omega t - \varphi\hat{k}\cdot r} \tag{10}$$

where $\mathbf{H_z}$ is the total static magnetic anisotropy field, $\mathbf{M}_0$ is the saturation magnetization, and **m** and **h** are the small wave disturbances. The permeability tensor resulting from this derivation is shown below:

$$\mu = \frac{1}{\varepsilon}\left(\frac{\delta}{j\omega}\right)^2 \begin{bmatrix} 1-\sin^2\theta\cos^2\varphi & -\sin^2\theta\sin\varphi\cos\varphi & -\sin\theta\cos\theta\cos\varphi \\ -\sin^2\theta\sin\varphi\cos\varphi & 1-\sin^2\theta\sin^2\varphi & -\sin\theta\cos\theta\sin\varphi \\ -\sin\theta\cos\theta\cos\varphi & -\sin\theta\cos\theta\sin\varphi & 1-\cos^2\theta \end{bmatrix} \tag{11}$$

$\delta$, $\mu$, and $\kappa$, are complex numbers as follows:

$$\delta = j\omega(\mu_0\varepsilon)^{1/2}\left\{\frac{(\mu^2-\kappa-\kappa^2)\sin^2\theta+2\mu-\left[(\mu^2-\kappa-\kappa^2)^2\sin^4\theta+4\kappa^2\cos^2\theta\right]^{1/2}}{2[(\mu-1)\sin^2\theta+1]}\right\}^{1/2} \tag{12}$$

$$\mu = 1+\frac{\omega_0'\omega_m}{\omega_0'^2-\omega^2} = 1+\frac{\omega_0\omega_m[\omega_0^2-\omega^2(1-\alpha^2)]}{[\omega_0^2-\omega^2(1+\alpha^2)]^2+4\omega^2\omega_0^2\alpha^2} - j\frac{\omega_0\omega_m[\omega_0^2+\omega^2(1+\alpha^2)]}{[\omega_0^2-\omega^2(1+\alpha^2)]^2+4\omega^2\omega_0^2\alpha^2} \tag{13}$$

$$\kappa = \frac{-\omega\omega_m}{\omega_0'^2-\omega^2} = \frac{-\omega\omega_m[\omega_0^2-\omega^2(1-\alpha^2)]}{[\omega_0^2-\omega^2(1+\alpha^2)]^2+4\omega^2\omega_0^2\alpha^2} + j\frac{2\omega_m\omega^2\omega_0\alpha}{[\omega_0^2-\omega^2(1+\alpha^2)]^2+4\omega^2\omega_0^2\alpha^2} \tag{14}$$

where:

$$\omega_m = \gamma M_0 \tag{15}$$

$$\omega_0 = \gamma H_z \tag{16}$$

and:

$$\omega_0' = \omega_0 + j\omega\alpha \tag{17}$$

A in Eq. 17 is the damping coefficient. This is experimentally determined by evaluating for the best fit. The permeability tensor in Eq. 11 can be simplified in the case when **k** is along the **Z** axis. The equivalent simplified tensor is the same as the Polder tensor[35,36]:

$$\boldsymbol{\mu} = \begin{bmatrix} \mu & -j\kappa & 0 \\ j\kappa & \mu & 0 \\ 0 & 0 & 1 \end{bmatrix} \tag{18}$$

(2) Calculation of the scalar intrinsic permeability using the saturation magnetization, and the anisotropy field, $H_a$:

$$H_z = H_a = \frac{2K_1}{4\pi M_s} \tag{19}$$

where $K_1$ is the crystalline anisotropy constant, $H_a$ in units of Oe, and $M_s$ in units of G. As an example, the calculated intrinsic permeability of a single domain particle with $4\pi M_s$ of 20,000 G and $H_a$ of 600 Oe is shown in Figure 2.17 below.

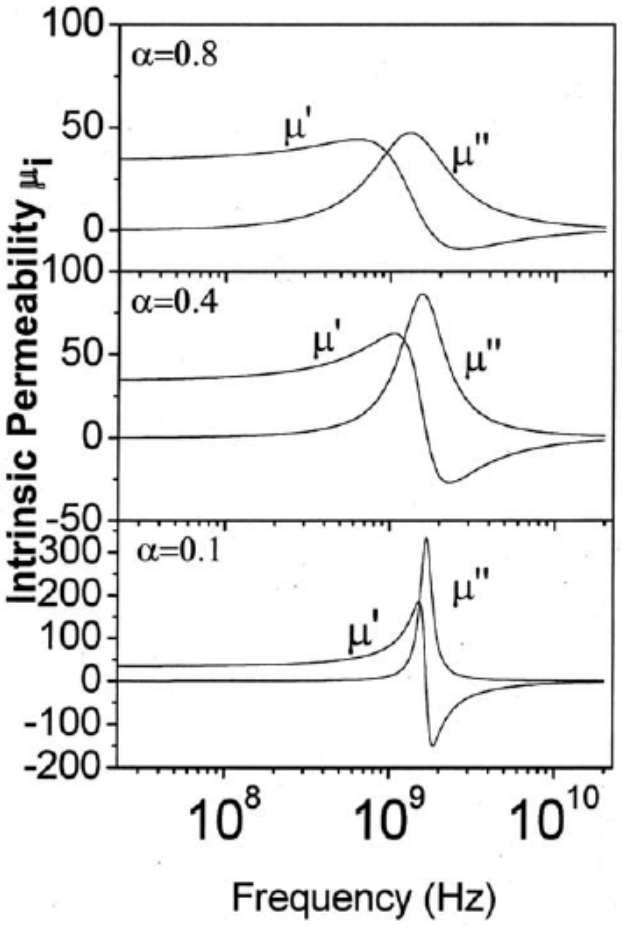


**Figure 2.17.** Calculated real part, μ′, and imaginary part, μ″, of complex intrinsic permeability for pure Fe with different damping coefficients.[34]

(3) Calculation of the effective permeability via Bruggeman's effective medium theory:

$$p\frac{\mu_i-\mu_{eff}}{\mu_i+2\mu_{eff}}+(1-p)\frac{\mu_m-\mu_{eff}}{\mu_m+2\mu_{eff}}=0 \tag{20}$$

where $p$ is the volume fraction of the magnetic particles, $\mu_i$ is the intrinsic permeability of the magnetic particles as calculated in step (2), $\mu_m$ is the permeability of the paraffin wax medium, and $\mu_{eff}$ is the effective permeability of the composite[37,38]. Steps (1), (2), and (3) were coded into MATLAB for evaluation as follows in Figure 2.18.

```
clc,clear,close all

a=0.4;
r=2.8/10^3;
Ha=600;
Ms=20000;
c=1;
p=0.3;
f=0:0.01:100;
miu_i=zeros(3,size(f,2));
miu_i_eigenvalue_real=zeros(1,size(f,2));
miu_i_eigenvalue_imag=zeros(1,size(f,2));
for w=f
   wm=r*Ms;
   w0=r*Ha;
   w1=w0+1i*w*a;
   u=1+((w1*wm)/((w1)^2-w^2));
   k=(-1)*w*wm/((w1)^2-w^2);
   miu_tensor=[u, -1i*k, 0;
      1i*k, u, 0;
      0, 0, 1;];
   miu_i(:,c)=eig(miu_tensor);%Finding eigenvalues
   c=c+1;
end
%%
miu_i_real=real(miu_i);
miu_i_eigenvalue_real(1:147)=max(miu_i_real(1:2,1:147));
miu_i_eigenvalue_real(148:end)=min(miu_i_real(1:2,148:end));
miu_i_imag=-1*imag(miu_i);
miu_i_eigenvalue_imag(1:end)=max(miu_i_imag(1:2,1:end));
miu_i_eigenvalue=miu_i_eigenvalue_real+1i*miu_i_eigenvalue_imag;
miu_eff=((3*p*miu_i_eigenvalue)/4 - miu_i_eigenvalue/4 + (3*p)/4 +(9*p^2*miu_i_eigenvalue.^2 - 18*p^2*miu_i_eigenvalue + 9*p^2 -
6*p*miu_i_eigenvalue.^2 + 18*p*miu_i_eigenvalue - 12*p + miu_i_eigenvalue.^2 + 4*miu_i_eigenvalue + 4).^(1/2)/4 + 1/2);
%Bruggeman theory
miu_eff_real=real(miu_eff);
miu_eff_imag=imag(miu_eff);
miu_i_eigenvalue_realmax=max(miu_i_real(1:2,1:end));
miu_i_eigenvalue_realmin=min(miu_i_real(1:2,1:end));


%%  plot the intrinsic permeability
figure,
semilogx(f, miu_i_eigenvalue_real,'k');
hold on
semilogx(f, miu_i_eigenvalue_imag,'r');
hold off

%%  plot the effective permeability
figure,
semilogx(f, miu_eff_real,'k');
hold on
semilogx(f, miu_eff_imag,'r');
hold off
legend('\mu eff'' ', '\mu eff''','Location','NorthEast')
%% plot the max and min curves of real part eigenvalues
figure,
semilogx(f, miu_i_eigenvalue_realmax,'k');
hold on
semilogx(f, miu_i_eigenvalue_realmin,'r');
hold off
legend('Real max eigenvalue', ' Real min eigenvalue','Location','NorthEast')
```

**Figure 2.18.** MATLAB Code for the Theoretical Model of the Single-Domain Effective Permeability

The resulting calculated $\mu_{eff}$ from this procedure is valid for single domain particles. The critical size for $Fe_3O_4$ has been reported to be 76 nm, indicating that all particles in this study besides the micron-sized particles can be modeled using this approach.[39] For the micron-sized particles, an extra multi-domain step is required and the skin effect needs to be considered, as detailed in previous reports.[34] The intrinsic permeability of a multi-domain nanoparticle can be calculated as a simple average of the intrinsic permeability of each individual domain within the particle as follows:

$$\langle \mu_i \rangle = \frac{\sum_1^N \mu_i(\theta,\Phi)}{N} \tag{21}$$

Once the intrinsic permeability of the multi-domain particle has been calculated, the effective permeability is calculated using a modified, extended Bruggeman's effective medium theory which accounts for the skin effect:

$$p\frac{A\mu_i-\mu_{eff}}{A\mu_i+2\mu_{eff}} + (1-p)\frac{\mu_m-\mu_{eff}}{\mu_m+2\mu_{eff}} = 0 \tag{22}$$

The parameter $A$ is given by:

$$A(d,p,\mu,f) = \frac{2(kd\cos kd-\sin kd)}{\sin kd-kd\cos kd-k^2d^2\sin kd} \tag{23}$$

with the wave number:

$$k = (1+i)\left(\frac{\pi f\mu_i}{\rho\varepsilon_0 c^2}\right) \tag{24}$$

where $d$ is the particle diameter, ρ is the electric resistivity, and $f$ is the microwave frequency.[40] The steps to calculate the effective permeability of a multi-domain particle were coded into MATLAB for evaluation as follows in Figures 2.19 and 2.20.

```
clc; clear all; close all;

%Define constants:
alpha=0.8;
%b=0*pi/180; %angle of domain wrt to z axis
r=2.8/10^3;
Ha=584;
Ms=21500;

%%
num_domains = 10000;
for d = 1:num_domains
   %generate random angle between 0 and pi/2
   b = rand()*pi/2;
   %Iterate through the range of frequencies and obtain mu's
   c=1;
   for f=logspace(-1, 2, 2000)
      w=f;
      wm=r*Ms;
      w0=r*Ha;
      x=1+(w0*wm*(w0^2-w^2*(1-alpha^2)))/((w0^2-w^2*(1+alpha^2))^2+4*w^2*w0^2*alpha^2)-1i*((w*alpha*wm*(w0^2+w^2*(1+alpha^2)))/((w0^2-
w^2*(1+alpha^2))^2+4*w^2*w0^2*alpha^2));
      k=-1*w*wm*(w0^2-w^2*(1+alpha^2))/((w0^2-w^2*(1+alpha^2))^2+4*w^2*w0^2*alpha^2)+1i*2*wm*w^2*w0*alpha/((w0^2-
w^2*(1+alpha^2))^2+4*w^2*w0^2*alpha^2);
      u_left=((x^2-x-k^2)*(sin(b)).^2+2*x+sqrt((x^2-x-k^2)^2*(sin(b)).^4+4*k^2*(cos(b)).^2))/(2*((x-1)*(sin(b)).^2+1));
      u_right=((x^2-x-k^2)*(sin(b)).^2+2*x-sqrt((x^2-x-k^2)^2*(sin(b)).^4+4*k^2*(cos(b)).^2))/(2*((x-1)*(sin(b)).^2+1));

      real_left = real(u_left);
      real_right = real(u_right);
      imag_left = imag(u_left);
      imag_right = imag(u_right);

      D=[f; real_left; real_right; imag_left; imag_right];
      U_data(:,c)=D;
      u_data=U_data';
      c=c+1;
   end
   data_raw = U_data';% columns: freq, real left, real right, imag left, imag right
   frequencies = data_raw(:,1);
   real_left = data_raw(:, 2); real_right = data_raw(:, 3);
   imag_left = -data_raw(:, 4); imag_right = -data_raw(:, 5);

   if d == 1
     u_real = ones(length(imag_right), num_domains);
     u_imag = ones(length(imag_right), num_domains);
   end
   %Combine left and right side of the plot (separated at max of real part)
   max_index = find(imag_left == max(imag_left));
   u_real(:,d) = real_left;
   u_imag(:,d) = imag_left;
   for i = (max_index+1):length(real_left)
      u_real(i,d) = real_right(i);
      u_imag(i,d) = imag_right(i);
   end
end

%average over the domains
u_real = mean(u_real, 2);
u_imag = mean(u_imag, 2);

%%
figure,
semilogx(frequencies, u_real); hold on;
semilogx(frequencies, u_imag)
grid on;
title('Intrinsic Permeability vs. Frequency of bcc Fe');
xlabel('Frequency (GHz)'); ylabel('Permeability');
legend('\mu" (Real Part)', '\mu"" (Imaginary Part)','Location','NorthEast')
save data.mat u_real u_imag frequencies
```

**Figure 2.19.** MATLAB Code for the Theoretical Model of the Multi-Domain Intrinsic Permeability

```
clc,clear,close all
load data.mat
f=frequencies;
d=1*10^-6;
v=0.15;
c=3*10^8;
ui=u_real+1i*u_imag;
k=(1+1i)*sqrt((pi*f.*ui*10^9)/(10^(-7)*c^2));
A=2*(k.*d.*(cos(k*d))-(sin(k*d)))./((sin(k.*d))-k.*d.*(cos(k.*d))-k.^2.*d.^2.*(sin(k.*d)));
ui_eff=((9*(A.*ui*v).^2) - 6*(A.*ui).^2*v + (A.*ui).^2 - 18*A.*ui*v^2 + 18*A.*ui*v+4*A.*ui + 9*v.^2 - 12*v+4).^(1/2)/4 - (A.*ui)/4 - (3*v)/4
+ (3*A.*ui*v)/4 + 1/2;
ui_eff_real=real(ui_eff);
ui_eff_imag=imag(ui_eff);
figure,
semilogx(frequencies, ui_eff_real,'r'); hold on;
semilogx(frequencies, ui_eff_imag,'k'); hold off;
grid on;
title('Effective Permeability with skin effect vs. Frequency ');
xlabel('Frequency (GHz)'); ylabel('Permeability');
legend('\mu'' (Real Part)', '\mu'''' (Imaginary Part)','Location','NorthEast')
```

**Figure 2.20.** MATLAB Code for the Theoretical Model of the Multi-Domain Effective Permeability Accounting for Skin Effect

Figure 2.21 shows the agreement between the measured and simulated effective complex permeability for 10 nm $Fe_3O_4$ nanoparticles at a (a) 15 vol%, (b) 30 vol%, and (c) 40 vol% loading. The agreement between the experimental and simulated values is acceptable, indicating that the magnetic nanoparticle/wax composites behave according to standard mixing theories. The experimental and simulated curves have roughly the same curve shape, however are slightly off in magnitude. This could be due to experimental conditions that were unaccounted for in the simulations.[34]

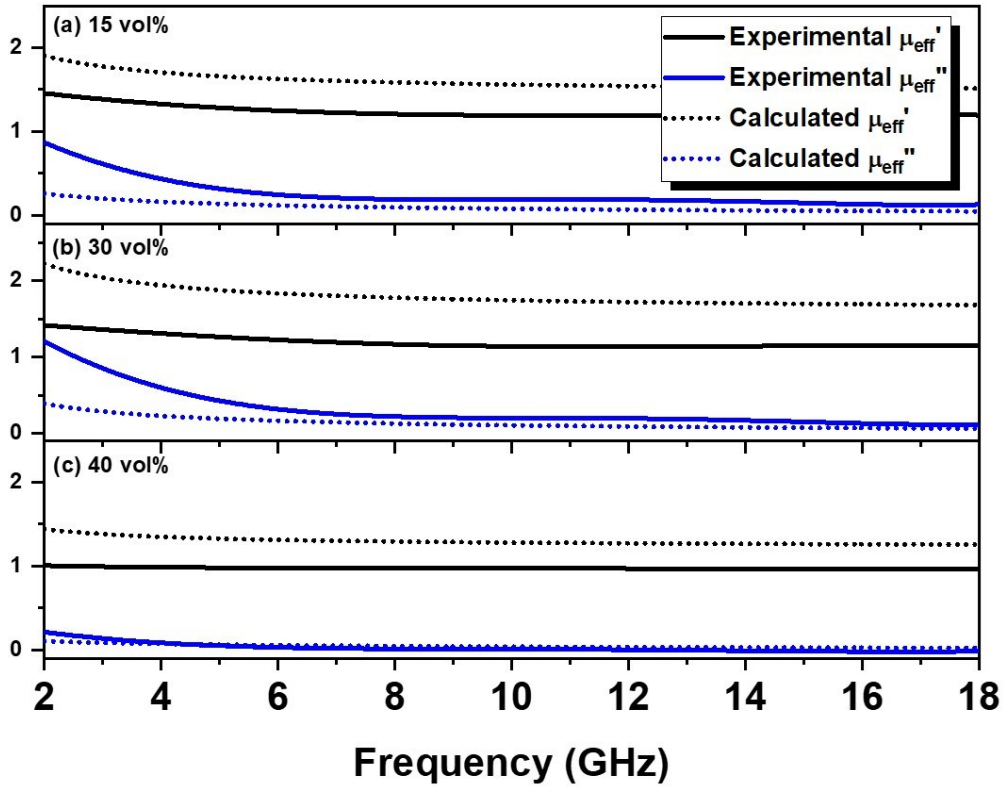


**Figure 2.21.** Calculated real part, μ′, and imaginary part, μ″, of the complex effective permeability for 10 nm $Fe_3O_4$ nanoparticles at volume fractions of (a) 15 vol%, (b) 30 vol%, and (c) 40 vol%.

Simulation results for all other sizes and loadings of $Fe_3O_4$ nanoparticles are shown in Figures 2.22 – 2.25.

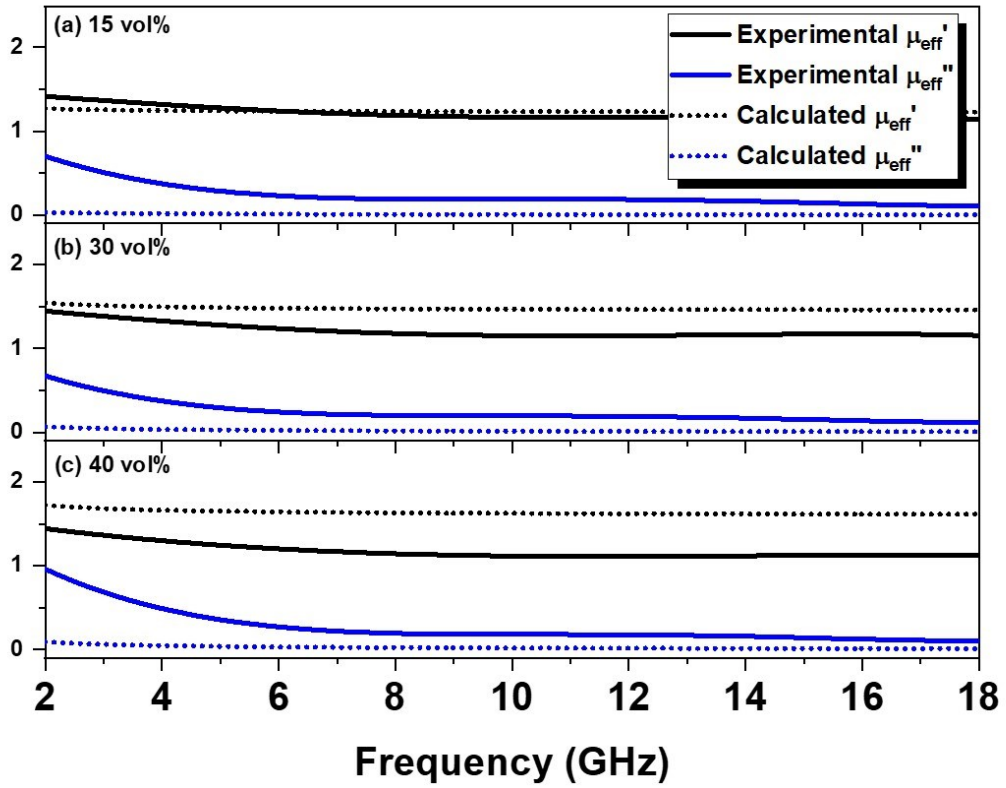


**Figure 2.22.** Calculated real part, μ′, and imaginary part, μ″, of the complex effective permeability for 5 nm $Fe_3O_4$ nanoparticles at volume fractions of (a) 15 vol%, (b) 30 vol%, and (c) 40 vol%.

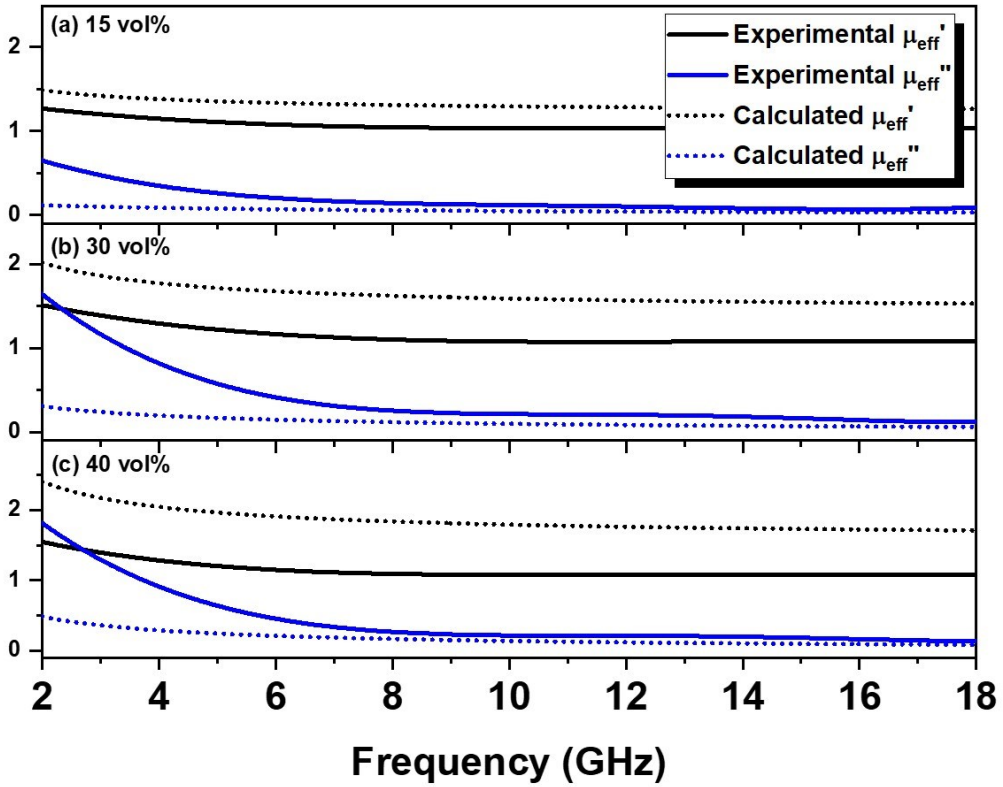


**Figure 2.23.** Calculated real part, μ′, and imaginary part, μ″, of the complex effective permeability for 20 nm $Fe_3O_4$ nanoparticles at volume fractions of (a) 15 vol%, (b) 30 vol%, and (c) 40 vol%.

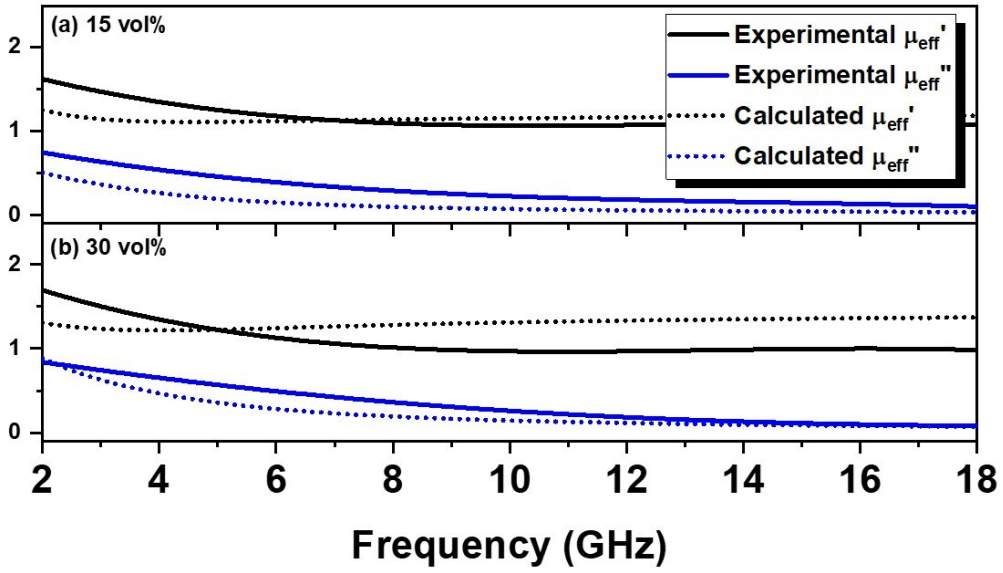


**Figure 2.24.** Calculated real part, μ′, and imaginary part, μ″, of the complex effective permeability for 100 nm $Fe_3O_4$ nanoparticles at volume fractions of (a) 15 vol% and (b) 30 vol%.

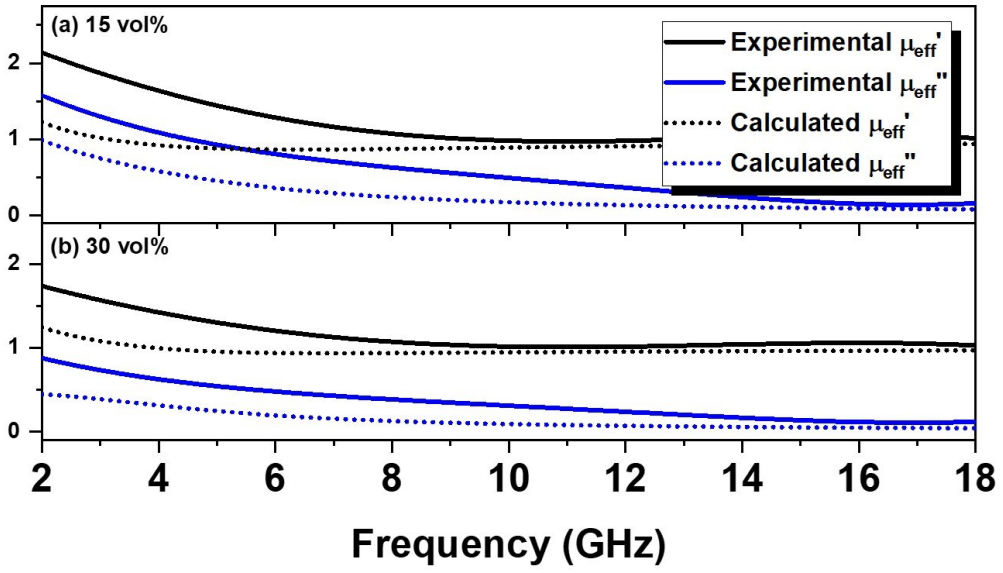


**Figure 2.25.** Calculated real part, μ′, and imaginary part, μ″, of the complex effective permeability for micron-sized $Fe_3O_4$ at volume fractions of (a) 15 vol% and (b) 30 vol%.

### 2.3.6 Effect of $M_s$ and $H_a$ on the Effective Permeability

From Eq. 13, 15, and 16 it can be determined the effect of $M_s$ and $H_a$ on the complex permeability of a particle. Values for $M_s$ and $H_a$ are discussed in section 2.3.1. For the real portion of the permeability, there is no real influence of $M_s$ or $H_a$ to be observed, as the "1 +" term in the real portion of Eq. 13 will dominate the result. For the imaginary portion of the permeability, as the $M_s$ and/or $H_a$ of a particle increase, so too should the imaginary portion of the permeability, with $M_s$ will having a more dominant effect than $H_a$ due to the underlying mathematics behind this phenomenon. To illustrate this effect, a simulation has been conducted holding one of $M_s$ or $H_a$ constant and varying the other to determine the effects. A 15 vol% volume fraction was assumed. These results are shown in Figures 2.26 and 2.27.

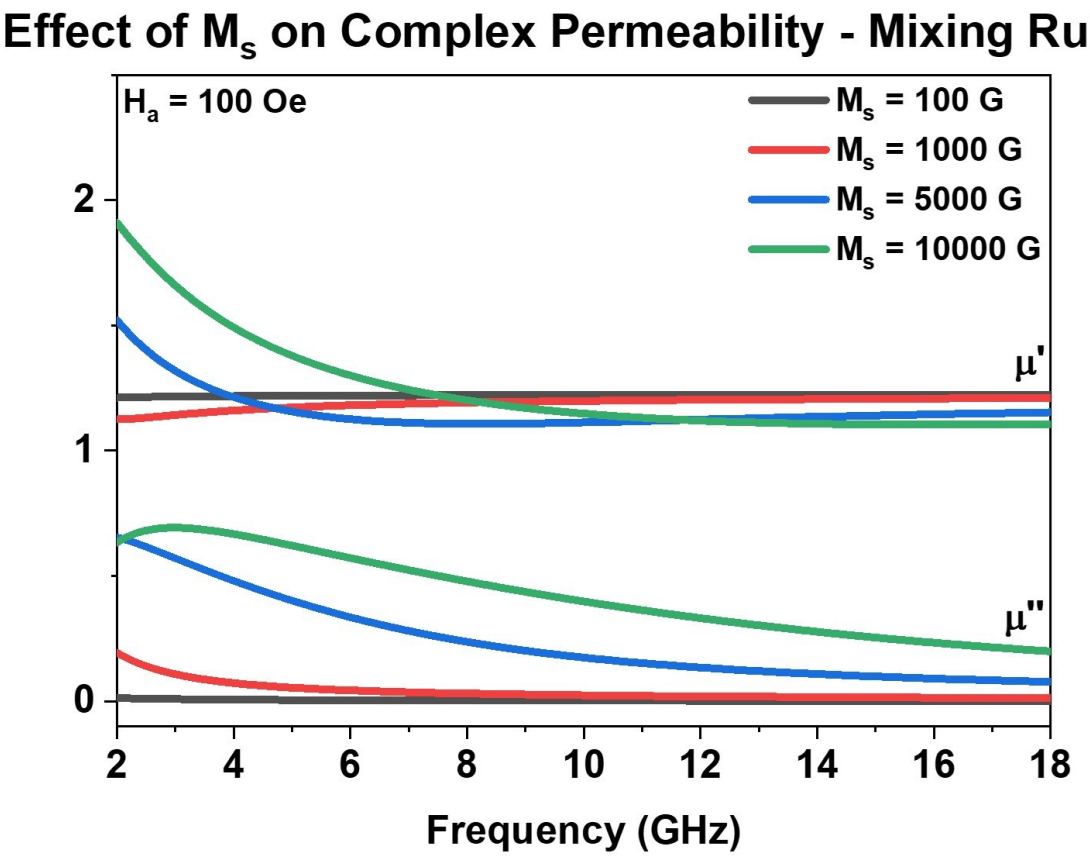


**Figure 2.26.** The effect of $M_s$ on the effective complex permeability, assuming a volume fraction of 15 vol%.

As shown in Figure 2.26, $M_s$ has a unique effect on both the real and imaginary portion of the complex permeability. For the real portion, increasing the $M_s$ will result in an increased amplitude for the curve shape of the real permeability, however no real trend can be determined over the 2 – 18 GHz frequency range. For the imaginary permeability, it is straight forward. As $M_s$ is increased, so too is the imaginary permeability.

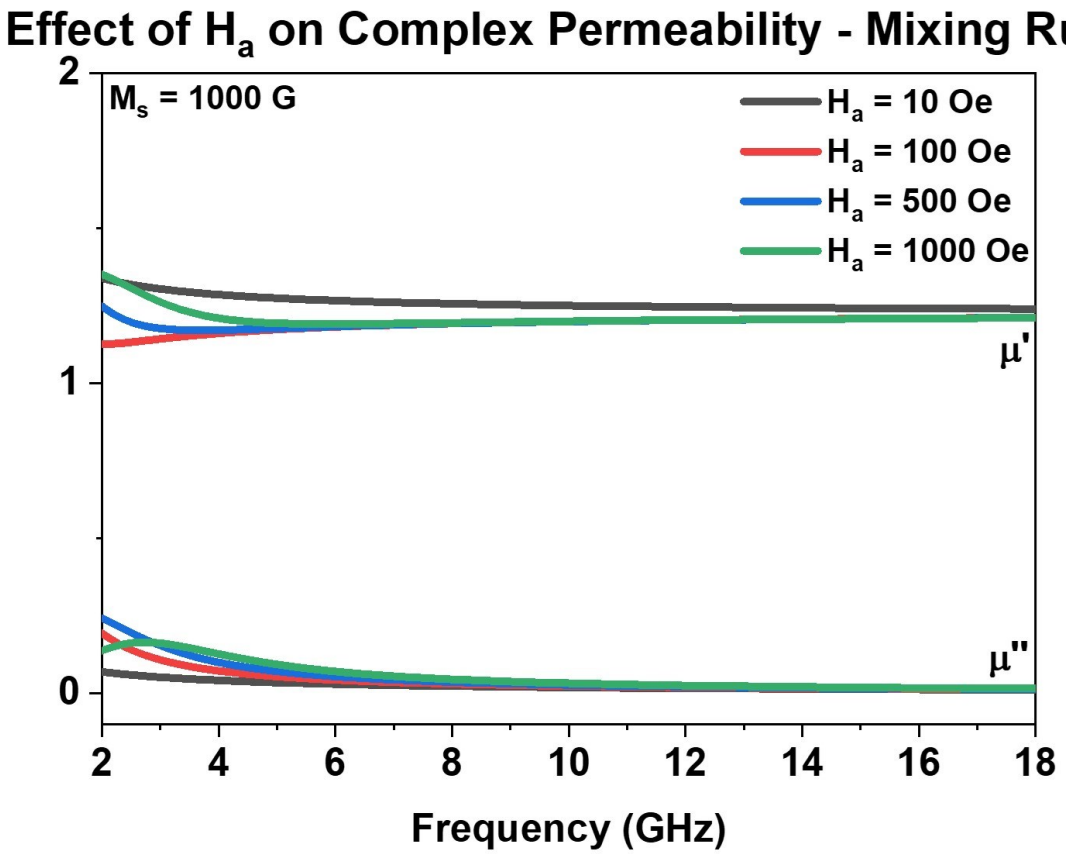


**Figure 2.27.** The effect of $H_a$ on the effective complex permeability, assuming a volume fraction of 15 vol%.

As shown in Figure 2.27, the same observations for the effect of $M_s$ hold for the effect of $H_a$, i.e. increasing the $H_a$ will result in an increased amplitude for the curve shape of the real permeability and an increased imaginary permeability. It is easily noticeable that the effect of $H_a$ is weaker than the effect of $M_s$, as the magnitude of increase in the imaginary permeability and amplitude increase in the real permeability is much smaller.

These simulated results are reflected in the experimental data shown in previous figures 2.15 and 2.16. The observed trends for complex permeability as well as $M_s$ and $H_a$ are summarized in Table 2.4 below:

**Table 2.4** $M_s$ and $H_a$ Effects On Complex Permeability.

| Material Property | Trend |
|---|---|
| Real Permeability (μ′) | No Trend |
| Imaginary Permeability (μ″) | Micron > 100 nm > 20 nm > 10 nm > 5 nm |
| $M_s$ | Micron > 20 nm > 100 nm > 10 nm > 5 nm |
| $H_a$ | Micron > 100 nm > 5 nm > 10 nm > 20 nm |

As demonstrated in the observed trends, our experimental data agrees with the mathematical and simulated trends previously discussed, i.e. there is no observed influence of $M_s$ or $H_a$ on the real portion of the permeability, while there is a direct relationship between the $M_s$ and $H_a$ and the imaginary portion of the permeability, with the $M_s$ having a more dominant effect.

When comparing the imaginary permeability with the $M_s$ data, the only size of particle that deviates from the observed trend in $M_s$ is the 20 nm $Fe_3O_4$ nanoparticles, which actually have a larger $M_s$ than the 100 nm $Fe_3O_4$ nanoparticles. Based on this observation and the mathematics alone, it would be expected that the 20 nm $Fe_3O_4$ nanoparticles would have a larger imaginary permeability than the 100 nm $Fe_3O_4$ nanoparticles, however, this is not the case. This discrepancy is resolved when taking into account the lesser effect of the $H_a$ on the imaginary permeability of the nanoparticles. The 20 nm $Fe_3O_4$ nanoparticles actually have the lowest $H_a$ of all of the particles under study, which will slightly counteract the effect of $M_s$ on the imaginary permeability, thus providing reason for the lower observed imaginary permeability.

### 2.3.7 Effect of the Complex Permeability on the Electromagnetic Wave Absorption Behavior

Extending the conversation in Section 2.3.6 regarding the effect of $M_s$ and $H_c$ on the complex permeability, it can also be simulated the effect of the complex permeability of the electromagnetic wave absorption behavior of a material. Equations (1) and (2) govern the mathematics behind this process. However, due to the complex nature of the permeability, it can be difficult to mathematically determine the effect of its individual components, μ′ and μ″. To graphically visualize this effect, a simulation has been conducted first by manipulating the value of μ′ while holding μ″, ε′, and ε″ constant, and second by manipulating the value of μ″ while holding μ′, ε′, and ε″ constant and plotting the resulting reflection loss behavior. The experimentally measured data for the 15 vol% 10 nm $Fe_3O_4$ wax toroid was used as a basis for these simulations. The results are shown in Figures 2.28 and 2.29.

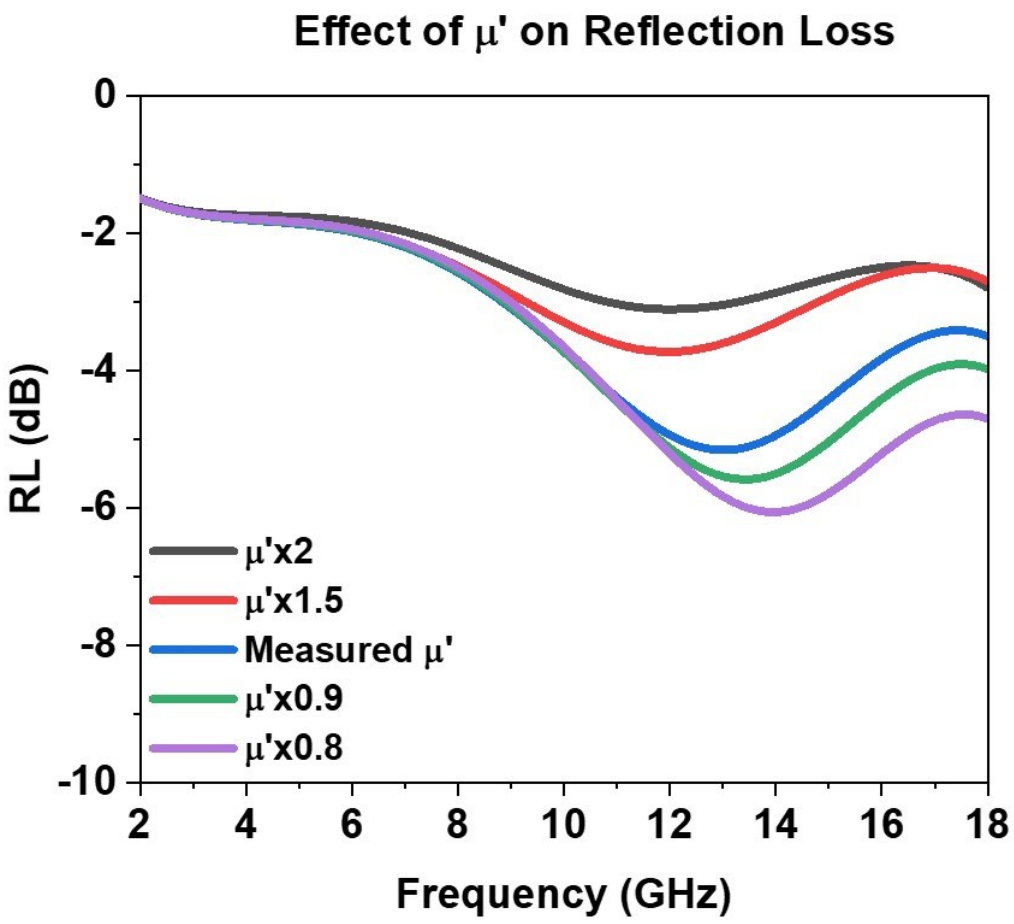


**Figure 2.28.** The effect of μ′ on the reflection loss, plotted by manipulating the experimentally measured data for 10 nm $Fe_3O_4$ at a loading of 15 vol%. μ″, ε′, and ε″ were held constant during these simulations.

As shown in Figure 2.28, μ′ has an inverse effect on the electromagnetic wave absorption behavior, i.e. as the real portion of the permeability is increased, the intensity of electromagnetic wave absorption is decreased.

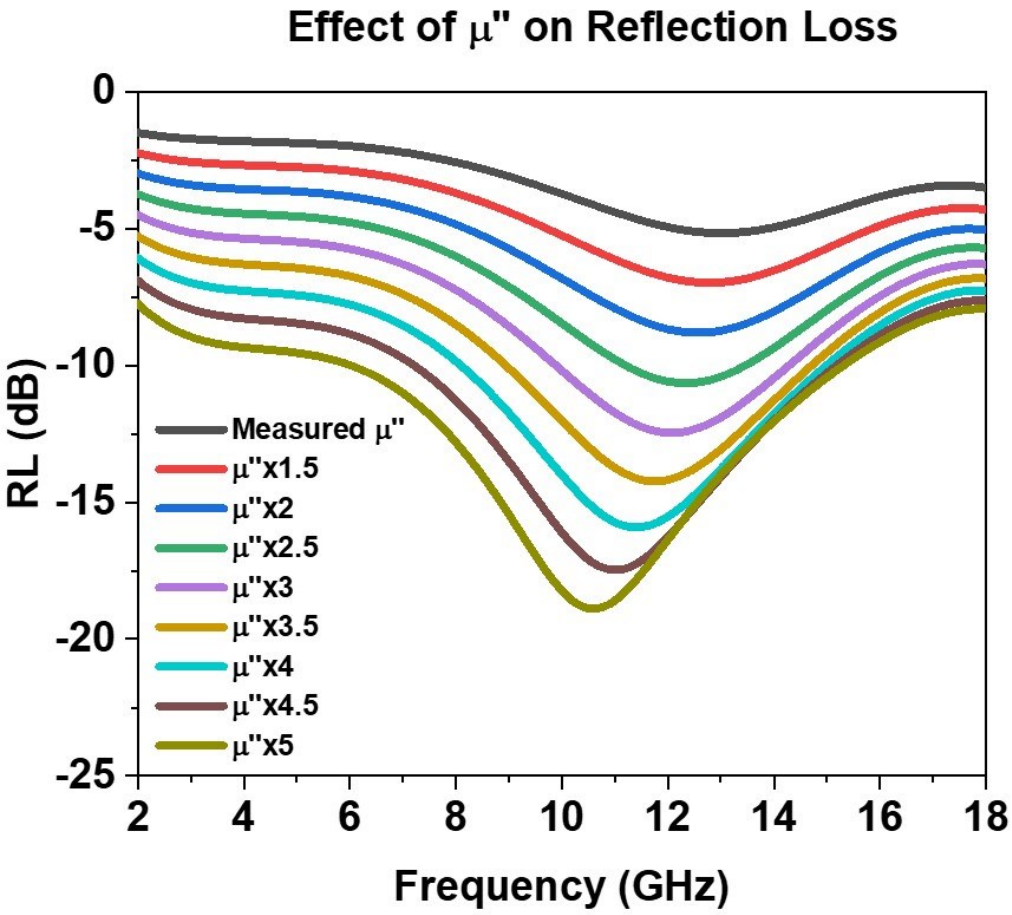


**Figure 2.29.** The effect of μ″ on the reflection loss, plotted by manipulating the experimentally measured data for 10 nm $Fe_3O_4$ at a loading of 15 vol%. μ′, ε′, and ε″ were held constant during these simulations.

As shown in Figure 2.29, μ″ has a direct effect on the electromagnetic wave absorption behavior, i.e. as the imaginary portion of the permeability is increased, the intensity of electromagnetic wave absorption is increased as well.

These simulated results may seem straight forward at first, however the real mechanism is a bit more complex. The electromagnetic wave absorption behavior is not simply governed by the real or imaginary portion of the permeability independently and in fact depends on the magnetic loss tangent of the material as discussed in Section 1.4 of the Introduction of this

dissertation. As a reminder, materials with a large dielectric loss tangent are referred to as dielectric materials while materials with a large magnetic loss tangent are referred to as magnetic materials. The higher the magnetic or dielectric loss of a material, the more effective that material is at absorbing electromagnetic waves and converting electromagnetic energy into thermal energy. In the simulations in this section, we are simply adjusting the ratio of the imaginary portion of the permeability to the real portion, thus affecting the magnetic loss tangent and the electromagnetic wave absorption properties; as we increase the magnetic loss tangent, the more effective at absorbing electromagnetic energy the material becomes.

### 2.3.8 Mixing Rules for Electromagnetic Wave Absorption

The last phenomenon we have analyzed is the mixing of two sizes of $Fe_3O_4$ nanoparticles and the effect it has on the intensity and position of the reflection loss peaks. In order to create these mixed composites we have combined two different nanoparticle sizes at concentrations of 7.5 vol%, maintaining a total nanoparticle concentration of 15 vol%, and measured their resulting electromagnetic properties. In an effort to be able to establish a trend, we mixed sizes of 5 nm and 20 nm $Fe_3O_4$, 5 nm and 100 nm $Fe_3O_4$, and 5 nm and micron $Fe_3O_4$ and plotted their corresponding reflection loss data. Using the 5 nm/micron $Fe_3O_4$ mixture as an example, shown in Figure 2.30, we are able to see that the resultant mixed nanoparticle reflection loss peaks mirror the position of the larger size and the intensity of the smaller size, i.e. the 15 vol% 5 nm/micron $Fe_3O_4$ mixed data mirrors the position of the 15 vol% micron $Fe_3O_4$ composite, yet displays a decreased intensity due to the influence of the 5 nm $Fe_3O_4$ contributions.

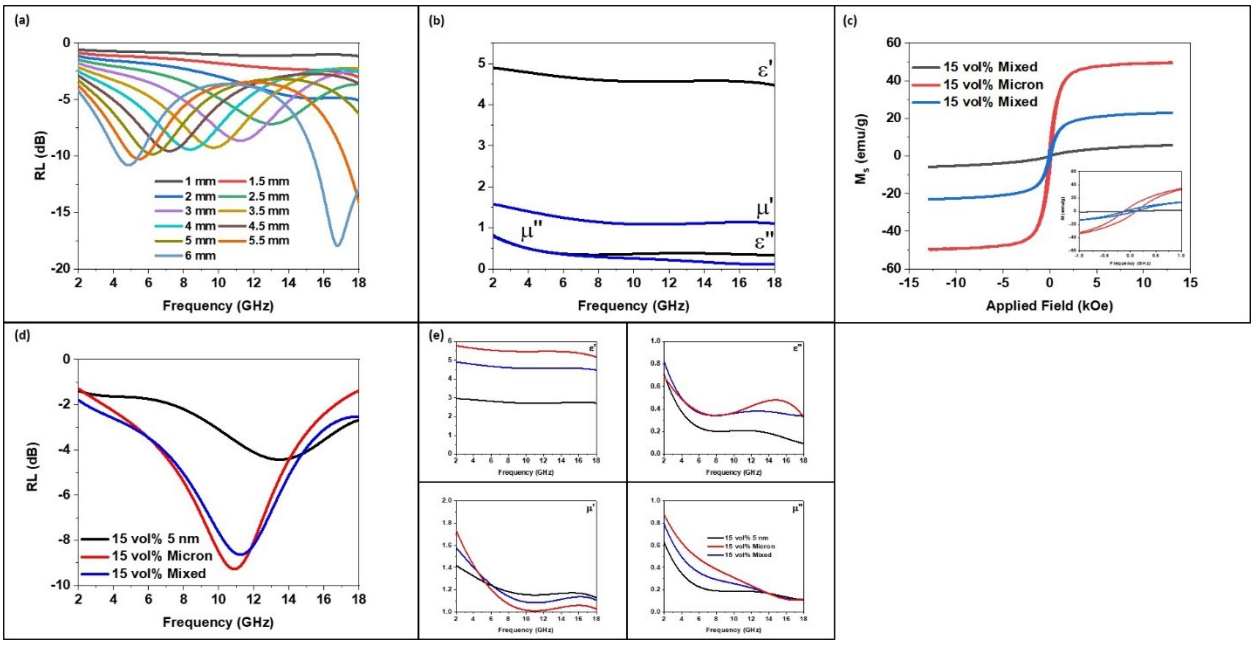


**Figure 2.30.** (a) Reflection loss data for a 15 vol% loading 5 nm (7.5 vol%)/micron(7.5 vol%) $Fe_3O_4$ composite of thicknesses 1 to 6 mm. (b) Complex permittivity and permeability values for a 15 vol% loading 5 nm (7.5 vol%)/micron(7.5 vol%) $Fe_3O_4$ composite of thicknesses at a 1 mm thickness. (c) Hysteresis loops of 5 nm and micron $Fe_3O_4$ nanoparticles and their mixed 15 vol% composite. (d) Overlay of the reflection loss data for a 3 mm thick 15 vol% 5 nm/micron $Fe_3O_4$ composite with the corresponding 6 mm thick 15 vol% 5 nm $Fe_3O_4$ composite and 15 vol% micron $Fe_3O_4$ composite. (e) Overlay of the real and imaginary permittivity and permeability data for a 1 mm thick 15 vol% 5 nm/micron $Fe_3O_4$ composite with the corresponding 1 mm thick 15 vol% 5 nm $Fe_3O_4$ composite and 15 vol% micron $Fe_3O_4$ composite.

This observation can easily be explained when thinking of the mechanisms by which the two magnetic nanoparticles of different sizes interact. Logically, the absorption frequency for mixed size particles mirrors that of the larger sized particle as the average size of the mixed particles is governed by the larger particles. On the other hand, the intensity of the absorption peak is increased due to magnetic exchange coupling effects between the particles, leading to a better dipole alignment with the magnetic field of the incoming electromagnetic wave and thus influencing the intensity of absorption. This discussion can be applied to the 5 nm/20 nm and 5 nm/100 nm mixed data as well as demonstrated by Figures 2.31 and 2.32, respectively.

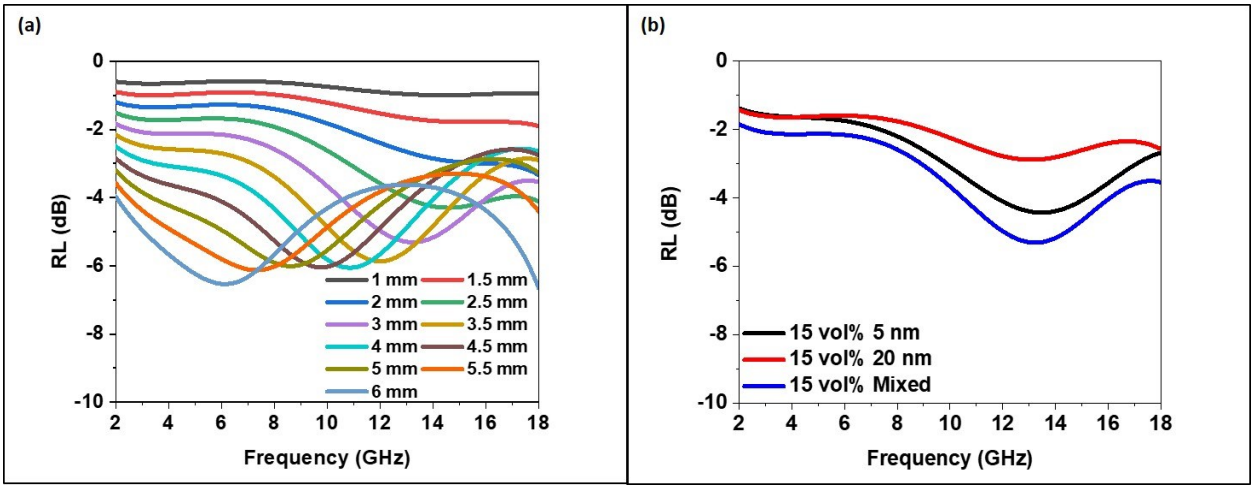


**Figure 2.31.** (a) Reflection loss data for a 15 vol% loading 5 nm (7.5 vol%)/20 nm(7.5 vol%) $Fe_3O_4$ nanoparticle composite of thicknesses 1 to 6 mm. (b) Overlay of the reflection loss data for a 3 mm thick 15 vol% 5 nm/20 nm $Fe_3O_4$ nanoparticle composite with the corresponding 3 mm thick 15 vol% 5 nm $Fe_3O_4$ composite and 15 vol% 20 nm $Fe_3O_4$ composite.

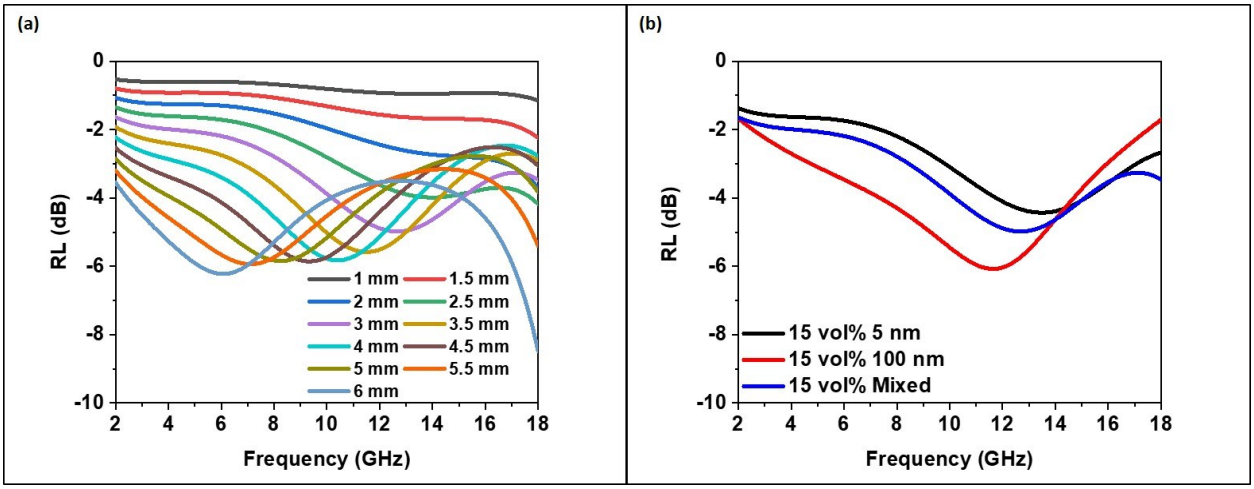


**Figure 2.32.** (a) Reflection loss data for a 15 vol% loading 5 nm (7.5 vol%)/100 nm (7.5 vol%) $Fe_3O_4$ composite of thicknesses 1 to 6 mm. (b) Overlay of the reflection loss data for a 3 mm thick 15 vol% 5 nm/100 nm $Fe_3O_4$ composite with the corresponding 3 mm thick 15 vol% 5 nm $Fe_3O_4$ composite and 15 vol% 100nm $Fe_3O_4$ composite.

## 2.4 CONCLUSIONS

Our work has made great strides in developing a fundamental understanding of the mechanisms of magnetic nanoparticle electromagnetic wave absorption. This chapter presented one of the first known systematic studies to approach magnetic electromagnetic wave absorbing materials by design. We have proven the ability to fine tune the resonant frequency of a material through the use of nanoparticle organic solution synthesis and strict control over the size of our particles. We have also shed light on a mechanism by which the exchange coupling of two different sized particles may work, controlling the intensity of the resonant absorption peak through the addition of smaller sized nanoparticles and the position by larger particles. This data shows much promise in developing the understanding of the mechanism of nanoparticle electromagnetic absorption and should be used as a basis for which to build off of. In the future, this knowledge may be able to be used to develop more complex systems to tune the specific location and intensity of relevant absorption peaks for a desired effect.

## 2.5 REFERENCES


1. R. Gensler, P. Groppel, V. Muhrer & N. Müller. *J. Part. Syst. Charact.* **19**, 293–299 (2002).
2. M. Salerno *et al.* Fluorescence imaging of surface plasmon fields. *Appl. Phys. Lett.* **10**, 404–406 (2002).
3. M. Todorovic, S. Schultz, J. Wong & A Scherer. Writing and reading of single magnetic domain per bit perpendicular patterned media. *Appl. Phys. Lett.* **74**, 2516–2518 (1999).
4. M. Rutnakornpituk *et al.* Formation of cobalt nanoparticle dispersions in the presence of polysiloxane block copolymers. *Polymer* **43**, 2337–2348 (2002).
5. R. S. Molday & D. Mackenzie. Immunospecific ferromagnetic iron-dextran reagents for the labeling and magnetic separation of cells. *J Immunol Methods* **52**, 353–367 (1982).
6. A. Jordan *et al. J. Magn. Magn. Mater.* **194**, 185 (1999).
7. S. Ni *et al.* Hydrothermal synthesis and microwave absorption properties of Fe3O4 nanocrystals. *J. Phys. D: Appl. Phys.* **42**, (2009).
8. National Research Council (U.S.). Committee on Identification of Research Needs Relating to Potential Biological or Adverse Health Effects of Wireless Communications Devices. *Identification of Research Needs Relating to Potential Biological or Adverse Health Effects of Wireless Communication Devices*. (National Academic Press, 2008).
9. E. Seidenberg & H. Schimpf. Aspects of automatic target recognition with a two-frequency millimeter wave SAR. *P. Soc. Photo-Opt. Ins.* **4033**, 167–177 (2000).
10. A. Ahlbom *et al.* Possible effects of electromagnetic fields (EMF) on human health--opinion of the scientific committee on emerging and newly identified health risks (SCENIHR. *Toxicology* **246**, 248–250 (2008).
11. E. F. Knott, J. F. Shaeffer & M. T. Tuley. *Radar Cross Section*. (SciTech Pub., 2004).

12. K. J. Vinoy & R. M. Jha. *Radar Absorbing Materials: From Theory to Design and Characterization*. (Kluwer Academic Publishers, 1996).
13. K. J. Vinoy & R. M. Jha. Trends in Radar Absorbing Materials. *Academy Proceedings in Engineering Sciences* **20**, 815–850 (1995).
14. M. J. Park, J. H. Choi & S. S. Kim. Microwave Absorption Properties of FSS-impacted Composites as a Broadband Microwave Absorber. *IEEE Trans. Magn.* **36**, 3272–3274 (2000).
15. Y. Wang & M. N. Afsar. Measurement of Complex Permittivity and Permeability of Carbonyl Iron Powders at Microwave Frequencies. *Microwave and Optical Technology Letters* **42**, (2004).
16. K. A. Korolev, S. Chen, Z. J. Li & M. N. Afsar. Millimeter-Wave Transmittance and Reflectance Measurement on Pure and Diluted Carbonyl Iron. *IEEE Transactions on Instrumentation and Measurement* **59**, (2010).
17. Y.B. Feng, T. Qiu, C. Y. Shen & X. Y. Li. Electromagnetic and absorption properties of carbonyl iron/rubber radar absorbing materials. *IEEE Transactions on Magnetics* **42**, 363–368 (2006).
18. S. Kimura, T. Kato, T. Hyodo, Y. Shimizu & M. Egashira. Electromagnetic wave absorption properties of carbonyl iron-ferrite/PMMA composites fabricated by hybridization method. *J. Magn. Magn. Mater.* **312**, 181–186 (2007).
19. A. E. Robinson. The preparation of magnesium-manganese ferrite for microwave applications. *Proceedings of the IEE - Part B: Radio and Electronic Engineering* **104**, 159–164 (1957).

20. Jae-Man Song *et al.* Dependence of Electromagnetic Wave Absorption on Ferrite Particle Size in Sheet-Type Absorbers. *Journal of the Korean Physical Society* **42**, 671–675 (2003).
21. Shouheng Sun *et al.* Monodisperse MFe2O4 (M = Fe, Co Mn) Nanoparticles. *J. Am. Chem. Soc.* 273–279 (2004).
22. Jin Xie, Chenjie Xu, Nathan Kohler, Yanglong Hou & Shouheng Sun. Controlled PEGylation of Monodisperse Fe3O4 Nanoparticles for Reduced Non-Specific Uptake by Macrophage Cells. *Adv. Mater.* **19**, 3163–3166 (2007).
23. R. Grössinger. A critical examination of the law of approach to saturation. *Phys. Status. Solidi. A* **66**, 665–674 (1981).
24. X. Batlle *et al.* Magnetic study of M-type doped barium ferrite nanocrystalline powders. *J. Appl. Phys.* **74**, 3333 (1993).
25. G. F. Goya, T. S. Berquó, F.C. Fonseca & M. P. Morales. Static and dynamic magnetic properties of spherical magnetite nanoparticles. *J. Appl. Phys.* **94**, 3520 (2003).
26. P. Guardia, J. Peréz-Juste, A. Labarta, X. Batlle & L. M. Liz-Marzán. Heating rate influence on the synthesis of iron oxide nanoparticles: The case of decanoic acid. *Chem Commun.* **36**, 6108–6110 (2010).
27. Yuko Ichiyanagi & Saori Yamada. The size-dependent magnetic properties of Co3O4 nanoparticles. *Polyhedron* **24**, 2813–2816 (2005).
28. Shouhu Xuan, Yi-Xiang J. Wang, Jimmy C. Yu & Ken Cham-Fai Leung. Tuning the Grain Size and Particle Size of Superparamagnetic Fe3O4 Microparticles. *Chem. Mater.* **21**, 5079–5087 (2009).
29. M. H. Cao *et al.* Single-Crystal Dendritic Micro-Pines of Magnetic α-Fe2O3 : Large-Scale Synthesis, Formation Mechanism, and Properties. *Angew. Chem.* **44**, 4197 (2005).

30. J. I. Gittleman, B. Abeles & S. Bozowski. Superparamagnetism and Relaxation Effects in Granular Ni-SiO2 and Ni-Al2O3 Films. *Phys. Rev. B.* **9**, 3891–3897 (1974).
31. R. F. Soohoo. *Microwave Magnetics*. (Harper and Row Publishers, 1985).
32. L. Z. Wu, J. Ding, H. B. Jiang, L. F. Chen & C. K. Ong. Particle size influence to the microwave properties of iron based magnetic particulate composites. *JMMM* **285**, 233–239 (2005).
33. Wolfgang J. R. Hoefer. The Transmission-Line Matrix Method - Theory and Applications. *IEEE Transactions on Microwave Theory and Techniques* **33**, 882–893 (1985).
34. L.Z. Wu *et al.* High Frequency Complex Permeability of Iron Particles in a Nonmagnetic Matrix. *J. Appl. Phys.* **99**, (2006).
35. D. Polder. On the Phenomenology of Ferromagnetic Resonance. *Phys. Rev. B.* **73**, 1120 (1948).
36. G. T. Rado. Theory of the Microwave Permeability Tensor and Faraday Effect in Nonsaturated Ferromagnetic Materials. *Phys. Rev.* **89**, 529 (1953).
37. Ari Sihvola. *Electromagnetic Mixing Formulas and Applications*. (Institute of Electrical Engineers, 1999).
38. L. Olmedo, G. Chateau, C. Deleuze & J. L. Forveille. Microwave Characterization and Modelization of Magnetic Granular Materials. *J. Appl. Phys.* **10**, 6992–6994 (1993).
39. Qing Li *et al.* Correlation Between Particle Size/Domain Structure and Magnetic Properties of Highly Crystalline Fe3O4 Nanoparticles. *Sci. Rep.* **7**, (2017).
40. A. Berthault, D. Rousselle & G. Zerah. Magnetic Properties of Permalloy Microparticles. *J. Magn. Magn. Mater.* 477–480 (1992).

# Chapter 3. Radar Absorbing $MFe_2O_4$ (M = Fe, Co, Cu, Mn, Mg) Nanomaterials

## 3.1 INTRODUCTION

Ferrite nanoparticles of the formula **M**$Fe_2O_4$ (**M** = Fe, Co, Cu, Mn, Mg, etc.) are of particular technological interest in modern society because their electrical and magnetic properties can be tailored for various applications by varying the chemical identity of the $M^{2+}$ ion.[1] Relevant applications include, but are not limited to, electronic devices,[2] high density magnetic recording devices,[3] contrast agents in medical resonance imaging (MRI),[4,5] gas sensors,[6] magnetically guided vehicles for drug delivery,[7] and electromagnetic wave absorbers. For example, cobalt ferrites ($CoFe_2O_4$) are reported to possess high magnetic anisotropy,[1,8,9] making them good candidates for hard magnets used in high frequency applications such as telecommunications or radar systems,[10] while manganese ferrites ($MnFe_2O_4$) are reported to possess low blocking temperatures and a high saturation magnetization,[11] arising from the ability of the $Mn^{2+}$ ion to substitute into the tetrahedral holes of the spinel unit cell due to its five unpaired electrons.[12] This immense tunability in chemical composition and bonding makes spinel ferrites ideal candidates for understanding and controlling the magnetic properties of nanoparticles through the variation of chemistry at the atomic level.[13] Depending on the chemical identity of the $M^{2+}$ ion, spinel ferrites can be designed to have application-specific, desirable properties such as high magnetic permeability, electrical resistivity, coercivity, or saturation magnetization and are interesting candidates for future high performance electromagnetic devices.[14–16] However, interestingly enough, spinel ferrites have yet to be systematically explored as prospects for electromagnetic wave absorption.

Electromagnetic wave absorbing materials play an important role in modern industry. They are used for many technological applications, with perhaps their single most prominent use as electromagnetic wave absorbers in portable electronic devices such as smart phones and mobile PCs to protect humans from exposure to electromagnetic pollution, which has been linked to an increased risk of developing cardiac/vascular diseases, cancer, or neural illnesses.[17–19] In the defense sector, a large area of research which has been gaining increasing attention in recent years, electromagnetic absorbing materials are painted onto the surface of aircrafts and ships to reduce the radar cross section (RCS) of a desired vessel, usually a plane, ship, or submarine.[20–22] The process by which electromagnetic absorbing materials work is through converting electromagnetic energy to thermal energy and dissipating the heat across the surface of the structure they are coating. When exposed to an external magnetic field (i.e. radar), the magnetic dipoles present in the paint mixture orient to the magnetic field. When the external field changes directions fast, the dipoles lag the impressed field variations and torque is exerted which consumes the electromagnetic energy and dissipates it as heat along the surface of the vessel. As this process is repeated, the incoming electromagnetic energy is absorbed and dissipated rather than being reflected back towards the receiver, thus decreasing the RCS of the vessel.[23]

As stated in our previous work, magnetic materials have long been used as radar absorbers on aircrafts, usually in the form of iron ball paint.[14,21,22,24–27] The absorber is usually applied by painting the metal surfaces with mixtures of carbonyl iron and polymer, with magnetic iron or ferrite particles generated *in situ* by the decomposition or oxidation of iron carbonyl. However, while this approach has been demonstrated to be successful in the reduction of the radar cross section (RCS), it is expected that the poorly defined synthetic approach

produces inhomogeneous layers of magnetic materials with a wide distribution of particles sizes. Impurities such as carbon, oxygen, and nitrogen may also be produced which can inhibit the effectiveness of the electromagnetic wave absorber.[28] It follows that due to the lack of control over material structures by conventional electromagnetic absorber synthesis methods, it makes it challenging to systematically study and improve existing magnetic materials for electromagnetic wave absorption.

In Chapter 3, we propose a systematic investigation of various spinel ferrite (**M**$Fe_2O_4$, **M** = Fe, Co, Cu, Mn, Mg) magnetic nanomaterials for electromagnetic wave absorption as a means of improving the existing library of materials for electromagnetic wave absorbing materials and to potentially give insight into the mechanisms by which ferrite nanomaterials behave when exposed to electromagnetic radiation. As previously stated, the tunability of spinel ferrites makes them an excellent candidate for discerning the mechanisms by which their magnetic properties work at the atomic level. Considering this fact, we have developed directed syntheses of uniform size and shape for each of the ferrites listed above through the use of organic solution synthesis techniques. We have then correlated the dielectric and magnetic properties of our materials to the electromagnetic absorption properties by measuring the complex permittivity and permeability of the ferrites through use of a vector network analyzer (VNA). From this data, we have drawn trends and conclusions concerning the electromagnetic wave absorption properties of ferrites to help further the understanding of EM wave absorption and expand the knowledge in the field.

## 3.2 EXPERIMENTAL METHODS

*Chemicals.* All materials (metal precursors, organic solvents, and ligands) were purchased from Sigma Aldrich. All chemicals were used as received.

*Synthesis Design.* All nanoparticles were synthesized under inert argon gas in a standard Schlenk line setup. All synthesis procedures were adapted and modified from a previous report.[8]

### 3.2.1 Synthesis

*Synthesis of 5 nm $Fe_3O_4$ Nanoparticles.* 5 nm $Fe_3O_4$ nanoparticles were synthesized by the decomposition of iron (III) acetylacetonate ($Fe(acac)_3$). In a typical synthesis, iron (III) acetylacetonate (0.706 g, 2.0 mmol) was dissolved in 20 mL diphenyl ether (DPE) containing oleic acid (1.91 mL, 6.0 mmol), oleylamine (1.97 mL, 6.0 mmol) and 1,2-hexadecanediol (2.58 g, 10.0 mmol) and refluxed for 30 min at 260°C. The precipitate was collected via centrifugation at 6000 rpm for 10 min, re-dispersed in ethanol, and centrifuged once again at 6000 rpm for 10 min. The final product was re-dispersed in hexanes and stabilized with 2-3 drops of oleylamine.

*Synthesis of 5 nm $CoFe_2O_4$ Nanoparticles.* 5 nm $CoFe_2O_4$ nanoparticles were synthesized by the decomposition of iron (III) acetylacetonate ($Fe(acac)_3$) and cobalt (II) acetylacetonate ($Co(acac)_2$). In a typical synthesis, iron (III) acetylacetonate (0.353 g, 1.0 mmol) and cobalt (II) acetylacetonate (0.129 g, 0.50 mmol) were dissolved in 25 mL benzyl ether (BE) containing oleic acid (0.92 mL, 2.9 mmol), oleylamine (5 mL, 15.2 mmol) and 1,2-tetradecanediol (1.15 g, 5.0 mmol). The reaction mixture was then heated for 60 min at 110°C as a water removal step, heated for 120 min at 210°C to promote the decomposition of Fe and Co, and then refluxed for 30 min at a higher temperature (300°C). The precipitate was collected via centrifugation at 8000 rpm for 10 min, re-dispersed in ethanol, and centrifuged once again at 8000 rpm for 10 min. The final product was re-dispersed in hexanes and stabilized with 2-3 drops of oleylamine.

*Synthesis of 5 nm $CuFe_2O_4$ Nanoparticles.* 5 nm $CuFe_2O_4$ nanoparticles were synthesized by the decomposition of iron (III) acetylacetonate ($Fe(acac)_3$) and copper (II) acetylacetonate ($Cu(acac)_2$). In a typical synthesis, iron (III) acetylacetonate (0.353 g, 1.0 mmol) and copper (II) acetylacetonate (0.183 g, 0.70 mmol) were dissolved in 25 mL benzyl ether (BE) containing oleic acid (0.92 mL, 2.9 mmol), oleylamine (10 mL, 30.4 mmol) and 1,2-hexadecanediol (1.29 g, 5.0 mmol). The reaction mixture was then heated for 60 min at 110°C as a water removal step, heated for 120 min at 210°C to promote the decomposition of Fe and Cu, and then refluxed for 30 min at a higher temperature (300°C). The precipitate was collected via centrifugation at 8000 rpm for 10 min, re-dispersed in ethanol, and centrifuged once again at 8000 rpm for 10 min. The final product was re-dispersed in hexanes and stabilized with 2-3 drops of oleylamine.

*Synthesis of 5 nm $MnFe_2O_4$ Nanoparticles.* 5 nm $MnFe_2O_4$ nanoparticles were synthesized by the decomposition of iron (III) acetylacetonate ($Fe(acac)_3$) and manganese (II) acetylacetonate ($Mn(acac)_2$). In a typical synthesis, iron (III) acetylacetonate (0.353 g, 1.0 mmol) and manganese (II) acetylacetonate (0.190 g, 0.75 mmol) were dissolved in 25 mL benzyl ether (BE) containing oleic acid (0.92 mL, 2.9 mmol), oleylamine (1 mL, 3.04 mmol) and 1,2-tetradecanediol (1.15 g, 5.0 mmol). The reaction mixture was then heated for 60 min at 110°C as a water removal step, heated for 120 min at 210°C to promote the decomposition of Fe and Mn, and then refluxed for 30 min at a higher temperature (300°C). The precipitate was collected via centrifugation at 8000 rpm for 10 min, re-dispersed in ethanol, and centrifuged once again at 8000 rpm for 10 min. The final product was re-dispersed in hexanes and stabilized with 2-3 drops of oleylamine.

*Synthesis of 5 nm $MgFe_2O_4$ Nanoparticles.* 5 nm $MgFe_2O_4$ nanoparticles were synthesized by the decomposition of iron (III) acetylacetonate ($Fe(acac)_3$) and magnesium (II)

acetylacetonate ($Mg(acac)_2$). In a typical synthesis, iron (III) acetylacetonate (0.706 g, 2.0 mmol) and magnesium (II) acetylacetonate (0.219 g, 0.85 mmol) were dissolved in 25 mL benzyl ether (BE) containing oleic acid (1.91 mL, 6.0 mmol), oleylamine (7.89 mL, 24.0 mmol) and 1,2-hexadecanediol (2.58 g, 10.0 mmol). The reaction mixture was then heated for 60 min at 110°C as a water removal step, heated for 120 min at 210°C to promote the decomposition of Fe and Mg, and then refluxed for 30 min at a higher temperature (300°C). The precipitate was collected via centrifugation at 8000 rpm for 10 min, re-dispersed in ethanol, and centrifuged once again at 8000 rpm for 10 min. The final product was re-dispersed in hexanes and stabilized with 2-3 drops of oleylamine.

### 3.2.2 Materials Characterization

Transmission electron microscopy (TEM) images were acquired on a 120 kV, FEI Tecnai 12 TWIN microscope. X-ray diffraction (XRD) patterns were collected on a PANalytical X'Pert$^3$ Powder X-Ray Diffractometer equipped with a Cu Kα radiation source (λ=0.15406). ). Energy dispersive x-ray spectroscopy (EDX) data were collected on a JEOL 6700F Scanning Electron Microscope (SEM) equipped with energy dispersive spectroscopy capabilities. Magnetic hysteresis loops were acquired on a MicroMag 2900 Series AGM.

### 3.2.3 Electromagnetic Absorption Studies

All **M**$Fe_2O_4$ (**M** = Fe, Co, Cu, Mn, Mg) composite wax/nanoparticle samples were prepared in 20 mL scintillation vials by dispersing the appropriate amounts of paraffin wax and $Fe_3O_4$ nanoparticles in toluene to achieve nanoparticle volume fractions ranging from 15% to 40% and slowly evaporating the solvent to create a uniformly dispersed composite matrix. The resulting composites were then molded into a toroidal shape using a Teflon mold with an outer diameter of 6.98 mm, inner diameter of 3.03 mm and thickness of 1 mm and fitted to a Keysight 85051B 7 mm airline for the microwave measurements. The complex permittivity and

permeability of the composite samples were measured using a Keysight FieldFox N9918A Microwave Analyzer in the 2 – 18 GHz region and the reflection loss was calculated used the measured permittivity and permeability.

## 3.3 DISCUSSION AND RESULTS

### 3.3.1 Materials Characterization

Metal ferrite (**M**$Fe_2O_4$, **M** = Fe, Co, Cu, Mn, Mg) nanoparticles of size ~5 nm are shown in transmission electron microscopy (TEM) images in Figure 3.1(a). All synthesized nanoparticles show a sphere-like morphology. Through size distribution analysis, mean diameters have been determined to be 5.37 nm ($Fe_3O_4$), 5.77 ($CoFe_2O_4$), 6.26 nm ($CuFe_2O_4$), 5.92 nm ($MnFe_2O_4$), and 5.05 nm ($MgFe_2O_4$). Size distribution profiles are shown in Figure 3.2. All nanoparticles (besides $Fe_3O_4$) were synthesized in a 1:2 **M**:Fe metal ratio, as determined by energy dispersive x-ray spectroscopy (EDX). The EDX results are summarized in Table 3.1 below:

**Table 3.1.** EDX data for all **M**$Fe_2O_4$ (**M** = Mn, Co, Mg, Cu) nanoparticles.

| Material | Weight % M | Weight % Fe | Atomic % M | Atomic % Fe | Ratio Fe:M |
|---|---|---|---|---|---|
| $Fe_3O_4$ | - | - | 0 | 100 | - |
| **Mn**$Fe_2O_4$ | 33.42 | 66.58 | 33.78 | 66.22 | 1.96:1 |
| **Co**$Fe_2O_4$ | 34.19 | 65.81 | 32.99 | 67.01 | 2.03:1 |
| **Mg**$Fe_2O_4$ | 17.81 | 82.19 | 33.23 | 66.77 | 2.01:1 |
| **Cu**$Fe_2O_4$ | 39.49 | 60.51 | 36.46 | 63.54 | 1.75:1 |

Figure 3.1(b) presents the typical x-ray diffraction (XRD) pattern for the various sized **M**$Fe_2O_4$ products. All of the peaks align with the expected patterns as confirmed by their agreement with JCPDS No. 00-019-0629 ($Fe_3O_4$), No. 01-079-1744 ($CoFe_2O_4$), No. 00-025-0283 ($CuFe_2O_4$), No. 00-010-0319 ($MnFe_2O_4$), and No. 00-036-0398 ($MgFe_2O_4$). No other diffraction peaks besides those corresponding to the appropriate metal ferrite were observed, which indicates high purity of our as-synthesized products. Figure 3.1(c) displays the magnetic hysteresis loops of all the as-synthesized metal ferrite nanoparticles. The saturation magnetization values ($M_s$) vary

from sample to sample and were determined by assuming $M(H) = M_s + X_dH$ ($X_d$ being the high field susceptibility) at high field and extrapolating the M(H) curve to zero field (i.e. $H = 0$).[29,30] $M_s$ values were found to be 5.791 ($Fe_3O_4$), 10.049 ($CoFe_2O_4$), 18.096 ($CuFe_2O_4$), 16.806 ($MnFe_2O_4$), and 9.573 ($MgFe_2O_4$) emu $g^{-1}$. All of these values are much lower than that of the corresponding bulk ferrites (85 – 100 emu $g^{-1}$), which is expected due to the nanoscale size of the materials as established in previous literature.[31] The saturation magnetization behavior of all samples is also as expected, resulting in the following trend: $CuFe_2O_4$ > $MnFe_2O_4$ > $CoFe_2O_4$ > $MgFe_2O_4$ > $Fe_3O_4$. $Fe_3O_4$, $CoFe_2O_4$, $MnFe_2O_4$, and $MgFe_2O_4$ display superparamagnetic behavior while $CuFe_2O_4$ displays soft ferromagnetic behavior. $Fe_3O_4$, $CoFe_2O_4$, and $MgFe_2O_4$ display similar $M_s$ values due to a similar cation distribution within the inverse spinel structure with the $Fe^{3+}$ ions occupying the tetrahedral sites and the $\mathbf{M}^{2+}$ (**M** = Fe, Co, Mg) ions occupying the octahedral sites. $MnFe_2O_4$ displays a slightly higher saturation magnetization; since both $Mn^{2+}$ and $Fe^{3+}$ have five unpaired electrons, both ions will occupy the tetrahedral sites and a the $Mn^{2+}$ ions will have a greater influence on the total magnetization than it's octahedral counterparts ($Fe_3O_4$, $CoFe_2O_4$, and $MgFe_2O_4$).[12] $CuFe_2O_4$ displays the highest saturation magnetization due to its ferromagnetic nature.[32] The hysteresis curves reveal coercivities of 30.23 ($Fe_3O_4$), 29.64 ($CoFe_2O_4$), 132.78 ($CuFe_2O_4$), 12.37 ($MnFe_2O_4$), and 6.52 ($MgFe_2O_4$) Oe. It is worthy to note that the smaller size nanoparticles in this study exhibit coercivities that are much lower than that of bulk materials, again due to the nanoscale size of the materials. This could be due to special morphology-related shape anisotropy when considering the sub-domain size of these nanoparticles.[33] As expected, the $Fe_3O_4$, $CoFe_2O_4$, $MnFe_2O_4$, and $MgFe_2O_4$ display superparamagnetic coercivities, while the $CuFe_2O_4$ displays a soft ferromagnetic coercivity.

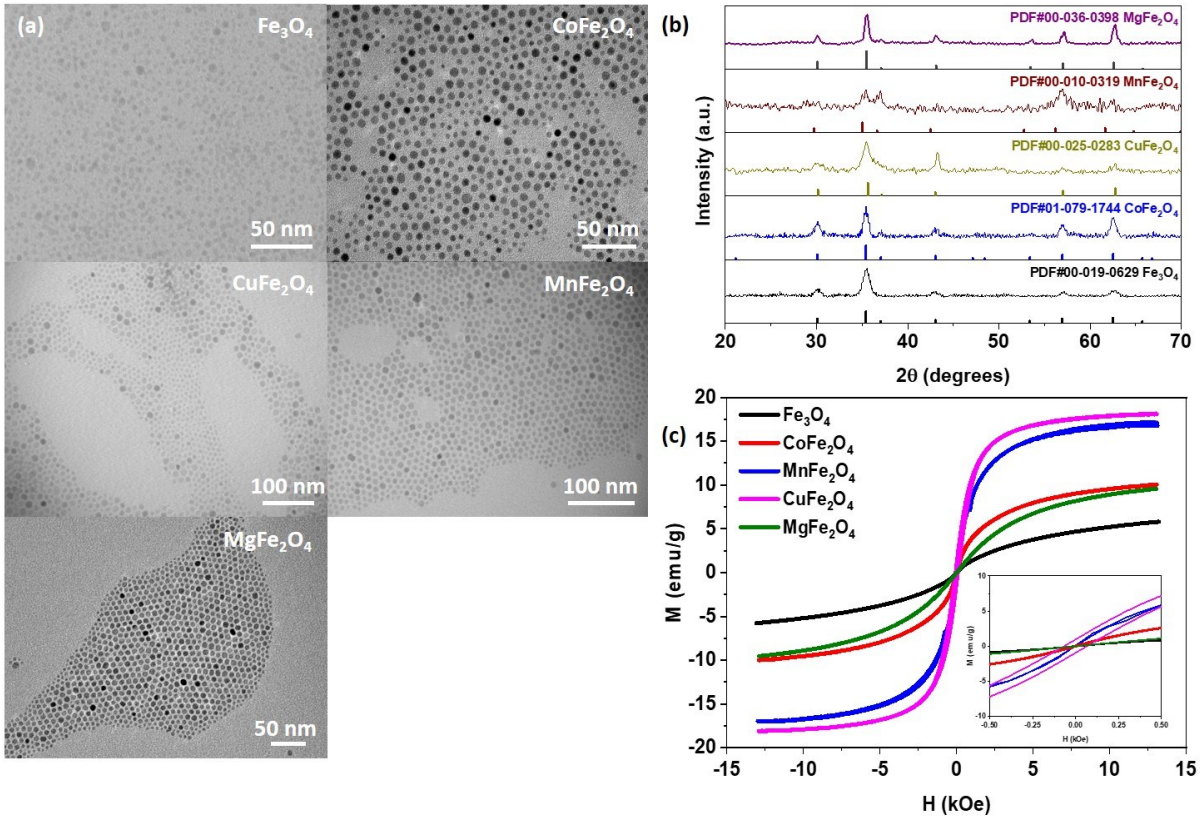


**Figure 3.1.** (a) TEM images, (b) XRD patterns and (c) hysteresis loops of 5 nm **M**$Fe_2O_4$ (**M** = Fe, Co, Cu, Mn, Mg) nanoparticles.

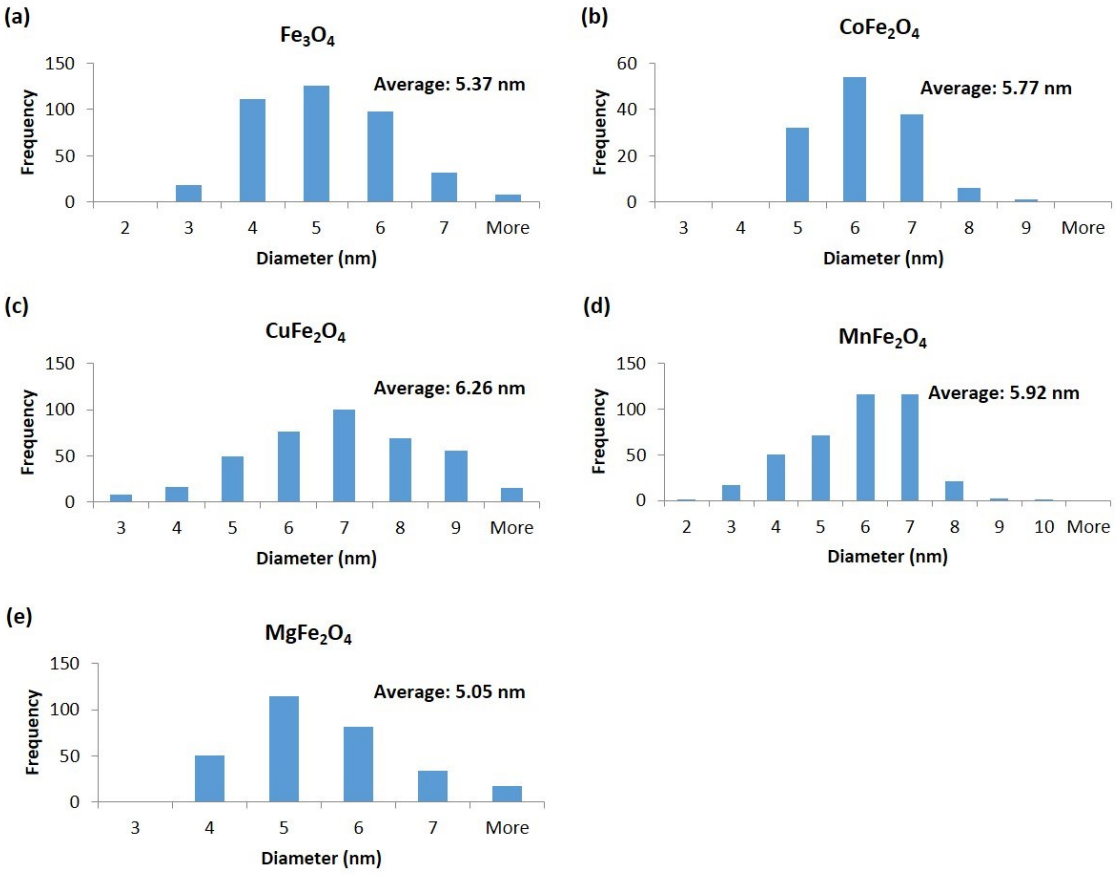


**Figure 3.2.** Size distribution profiles for 5 nm (a) $Fe_3O_4$, (b) $CoFe_2O_4$, (c) $CuFe_2O_4$, (d), $MnFe_2O_4$, and (e) $MgFe_2O_4$ nanoparticles.

### 3.3.2 Discussion of Electromagnetic Measurements

Figure 3.3 shows a typical data output using 5 nm $Fe_3O_4$ nanoparticles at a 30 vol% loading. Figure 3.3(a) shows the reflection loss (RL) data for varying thicknesses (1 mm – 6 mm) of 5 nm $Fe_3O_4$/paraffin wax composites at a 30 vol% nanoparticle loading. The relationship between the reflection loss of the $Fe_3O_4$/paraffin wax composite and frequency is calculated as follows:

$$Z_{in} = \sqrt{\frac{\mu_r}{\varepsilon_r}} \tanh j\left[\frac{2\pi f d\sqrt{\mu_r \varepsilon_r}}{c}\right] \quad (1)$$

$$R_L = 20log\left|\frac{Z_{in}-1}{Z_{in}+1}\right| \quad (2)$$

where $\varepsilon_r$ and $\mu_r$ are the relative complex permittivity and permeability of the wax composite, $c$ is the speed of light, $f$ is the frequency and $d$ is the thickness of the absorbing material. As shown in Figure 3.3(a), RL absorption peaks for 5 nm $Fe_3O_4$ at a 30 vol% loading across all thickness on a 0.5 mm interval from 1 mm to 6 mm can be seen with a local maximum absorption of -4.54 dB at 6.16 GHz corresponding to a 6 mm thickness. Figure 3.3(b) shows the real and imaginary portions of the complex permittivity and permeability across the frequency range from 2 GHz – 18 GHz for 5 nm $Fe_3O_4$ nanoparticles at a 30 vol% loading. In general, the values of both the real ($\varepsilon'$, $\mu'$) and imaginary ($\varepsilon''$, $\mu''$) portions of the complex permittivity and permeability gradually decrease with increasing frequency. For both imaginary portions, $\varepsilon''$ and $\mu''$, a much sharper decrease can be seen early on in the frequency range, from 2 GHz < $f$ < 4 GHz. Negative values in both $\varepsilon''$ and $\mu''$ may come from errors in the instrument measurement system.[34]

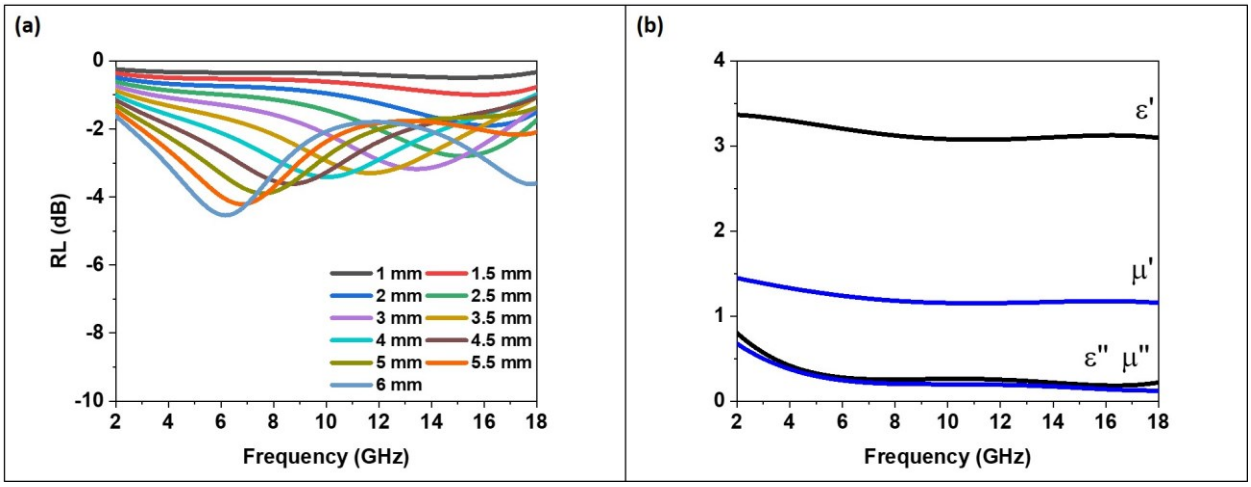


**Figure 3.3** (a) Reflection loss for varying thicknesses (1 mm – 6 mm) of 5 nm $Fe_3O_4$/paraffin wax composites at 30 vol% nanoparticle loading. (b) Complex permittivity and permeability values for 30 vol% 5 nm $Fe_3O_4$/paraffin wax composites at a 1 mm thickness.

Figures 3.4, 3.5, and 3.6 show the raw reflection loss (RL) data for all loadings of $MFe_2O_4$ (M = Fe, Co, Cu, Mn, Mg) across all nanoparticle loadings (15, 30, and 40 vol%). The previous discussion concerning Figure 3.3 can be applied to any specific size and loading in Figures 3.4, 3.5, and 3.6.

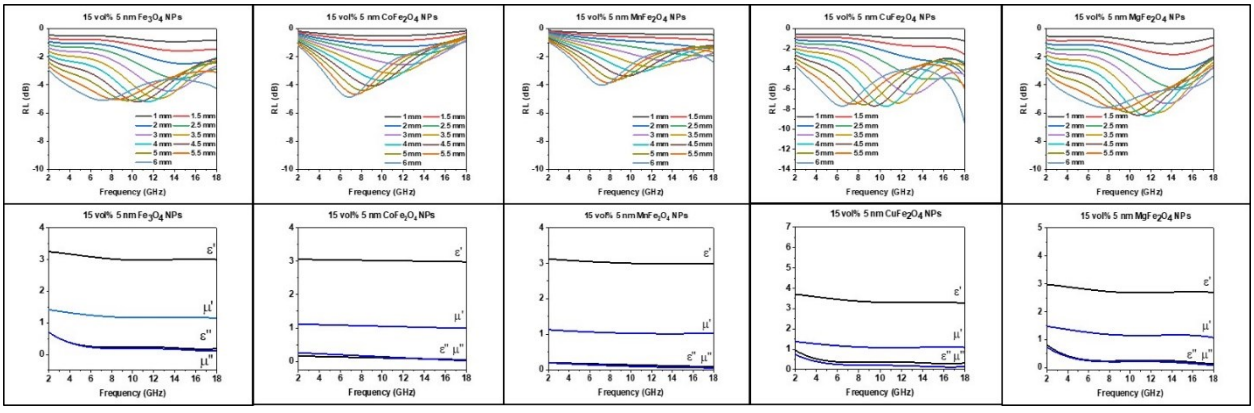

**Figure 3.4.** Raw RL Data for **M**$Fe_2O_4$ (**M** = Fe, Co, Cu, Mn, Mg) Nanoparticles at 15 vol% Loading.

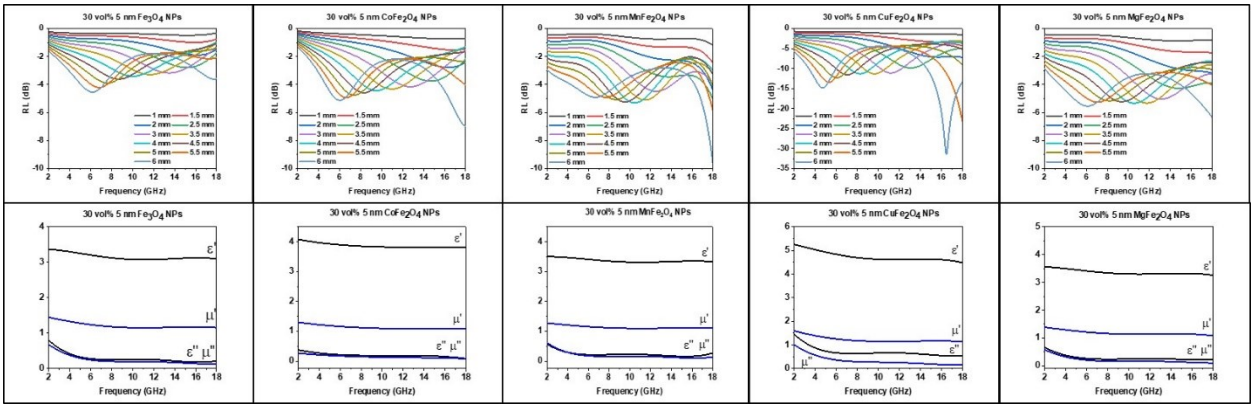


**Figure 3.5.** Raw RL Data for **M**$Fe_2O_4$ (**M** = Fe, Co, Cu, Mn, Mg) Nanoparticles at 30 vol% Loading.

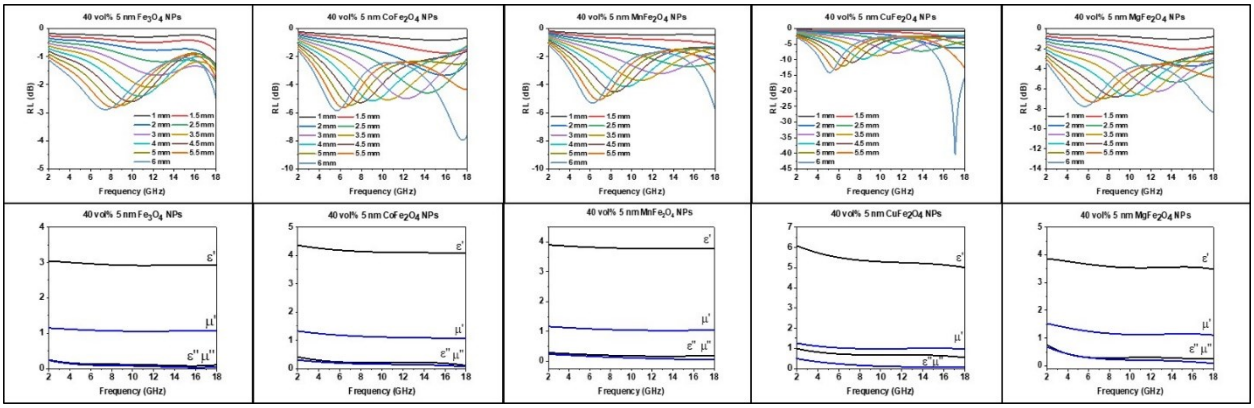


**Figure 3.6.** Raw RL Data for **M**$Fe_2O_4$ (**M** = Fe, Co, Cu, Mn, Mg) Nanoparticles at 40 vol% Loading.

Similarly to Section 2.3.2, it is once again necessary to discern the primary mechanism (magnetic or dielectric) for electromagnetic wave absorption displayed by the ferrite nanoparticles in this study. Figures 3.7 and 3.8 display the magnetic and dielectric loss tangents for the ferrites studied:

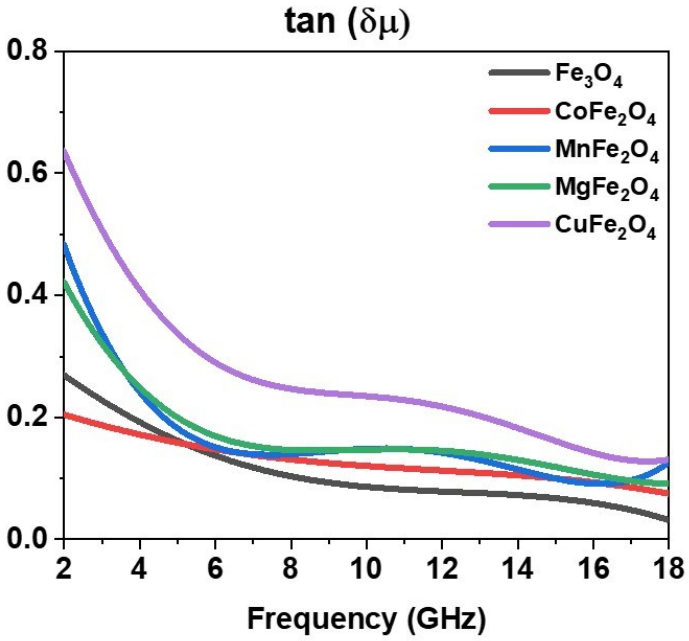


**Figure 3.7.** The magnetic loss tangent, tan(μ″/μ′), for 5 nm $Fe_3O_4$, $CoFe_2O_4$, $MnFe_2O_4$, $MgFe_2O_4$, and $CuFe_2O_4$.

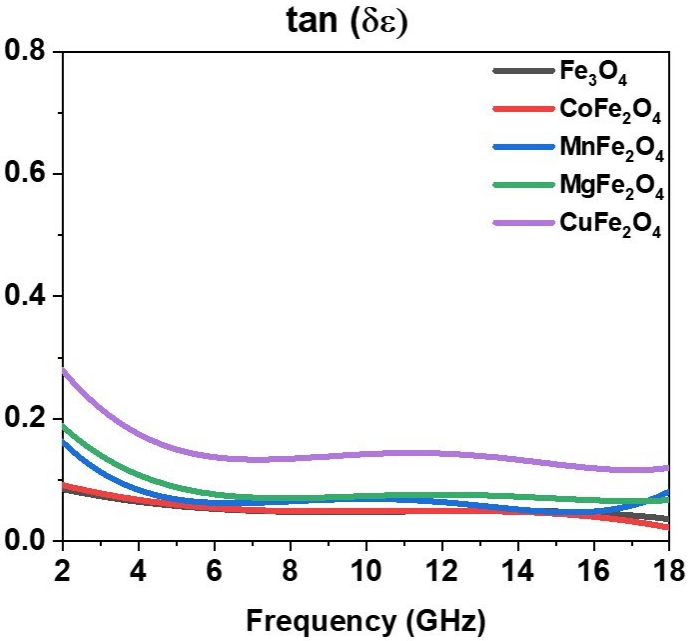


**Figure 3.8.** The dielectric loss tangent, tan(ε″/ ε ′), for 5 nm $Fe_3O_4$, $CoFe_2O_4$, $MnFe_2O_4$, $MgFe_2O_4$, and $CuFe_2O_4$.

As demonstrated in the Figures 3.7 and 3.8, the values of the magnetic loss tangents are much larger than the dielectric loss tangents across the entire frequency range for all sizes, indicating that the absorption mechanism is predominantly controlled by the magnetic properties of the ferrites, rather than the dielectric properties. However, while still lower, the values of the dielectric loss tangents are much more comparable to the magnetic loss tangents, suggesting that the dielectrics have more influence on the electromagnetic properties displayed by the ferrite system in question. This is discussed more in depth in future sections.

### 3.3.3 Nanoparticle Loading Dependence Effects on Electromagnetic Wave Absorption

The effects of loading dependence on the materials properties and reflection loss data of the system were measured at varying loadings of 15, 30 and 40 vol% for all $\mathbf{M}Fe_2O_4$ (**M** = Fe, Co, Cu, Mn, Mg) nanoparticle samples and the data analyzed for trends. Figure 3.9 shows the effect of nanoparticle loading on the intensity of electromagnetic wave absorption (Figure 3.9(a)), the complex permittivity, and the complex permeability (Figure 3.9(b)) of 5 nm $CoFe_2O_4$ nanoparticles in a toroid of 3 mm thickness. In agreement with previous studies and the data presented in Chapter 2 of this dissertation, it is shown that as nanoparticle loading increases, $\varepsilon'$, $\varepsilon''$, $\mu'$ and $\mu''$ all increase as well.[34,35] The reasoning behind this phenomena is explained by the fact that as the loading of the sample increases, the overall volume of nanoparticles increases as well, thus increasing the effective permittivity and permeability of the material. Holding true to this, it is observed that as the nanoparticle loading is increased, the complex permittivity and permeability increase as well, thus increasing the intensity of electromagnetic wave absorption and decreasing the maximum absorption frequency.

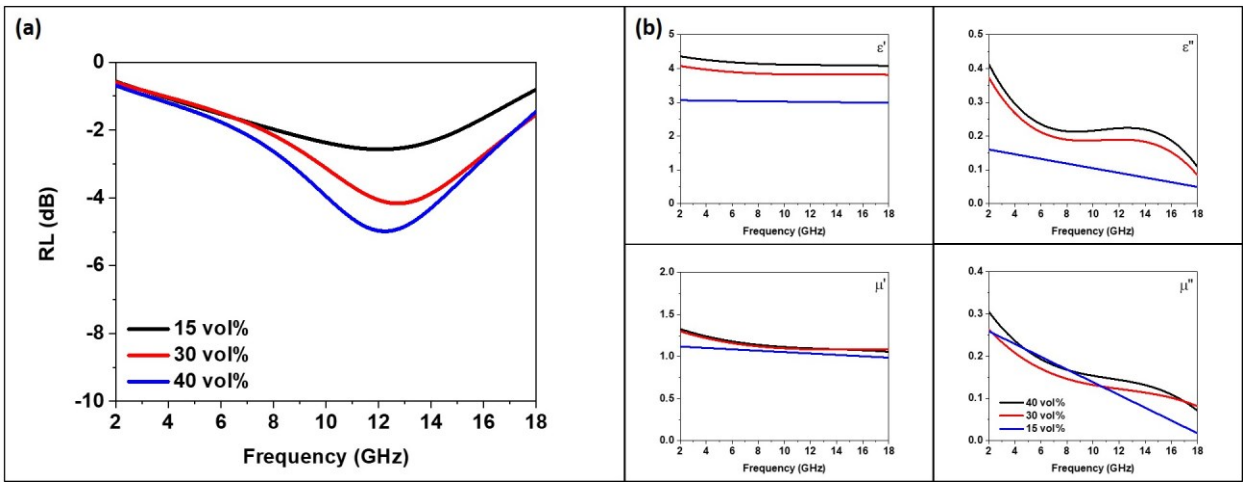


**Figure 3.9.** (a) Reflection loss for varying nanoparticle loadings (15, 30, and 40 vol%) of 5 nm $CoFe_2O_4$/paraffin wax composites at a 6 mm thickness. (b) Visualization of the effect of loading on the real and imaginary portions of the permittivity and permeability of 5 nm $CoFe_2O_4$ nanoparticles.

Figures 3.10 – 3.13 show the effect of loading on the reflection loss (RL) data for 5 nm $Fe_3O_4$, $MnFe_2O_4$, $CuFe_2O_4$, $MgFe_2O_4$ across all nanoparticle loadings (15, 30, and 40 vol%), respectively. The previous discussion concerning the 5 nm $CoFe_2O_4$ can be applied to any specific size and loading as demonstrated in Figures 3.10 – 3.13.

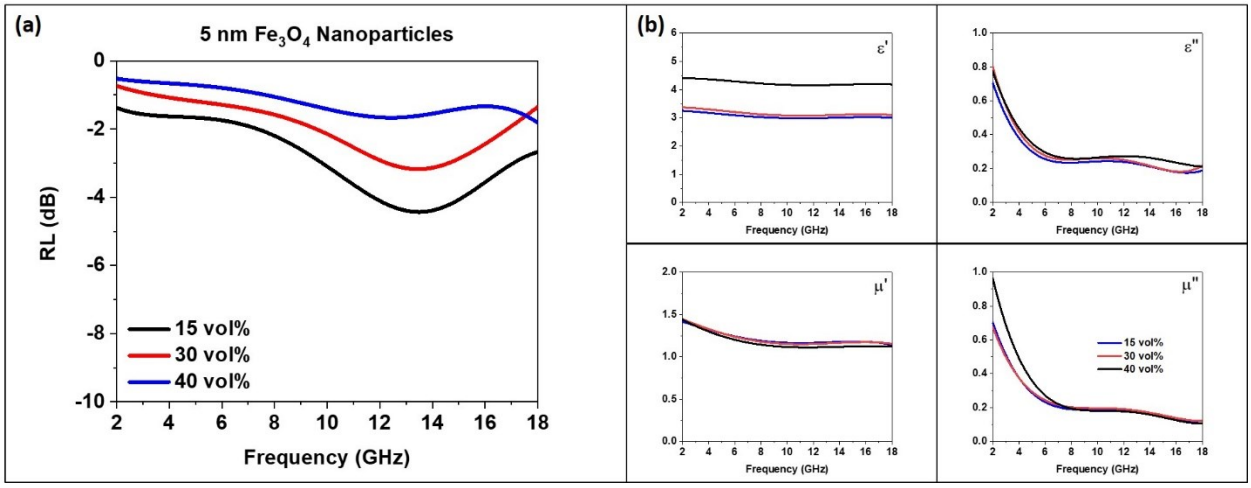


**Figure 3.10.** (a) Reflection loss for varying nanoparticle loadings (15, 30, and 40 vol%) of 5 nm $Fe_3O_4$/paraffin wax composites at a 3 mm thickness. (b) Visualization of the effect of loading on the real and imaginary portions of the permittivity and permeability of 5 nm $Fe_3O_4$ nanoparticles.

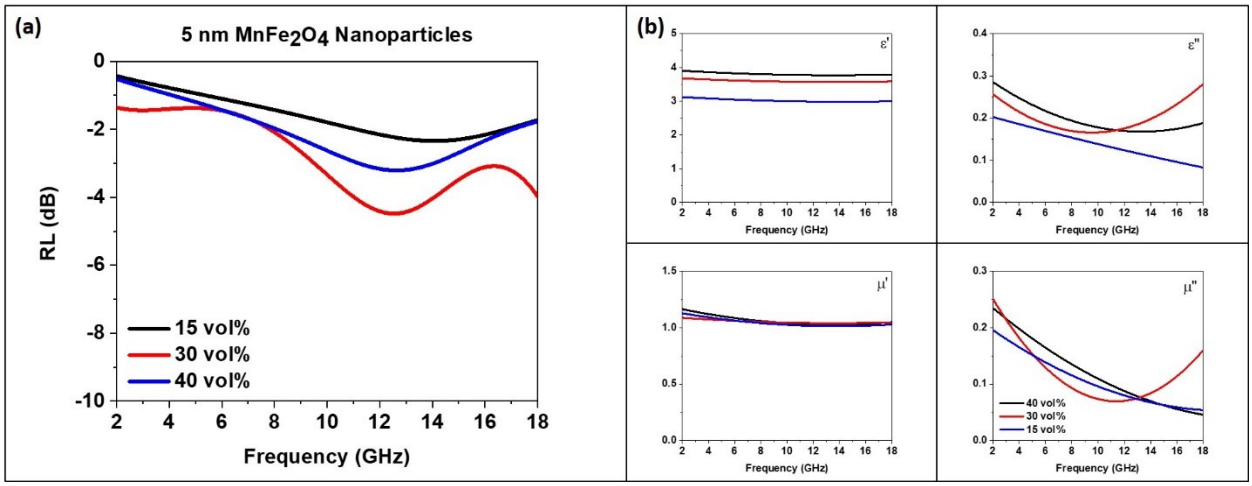


**Figure 3.11.** (a) Reflection loss for varying nanoparticle loadings (15, 30, and 40 vol%) of 5 nm $MnFe_2O_4$/paraffin wax composites at a 3 mm thickness. (b) Visualization of the effect of loading on the real and imaginary portions of the permittivity and permeability of 5 nm $MnFe_2O_4$ nanoparticles.

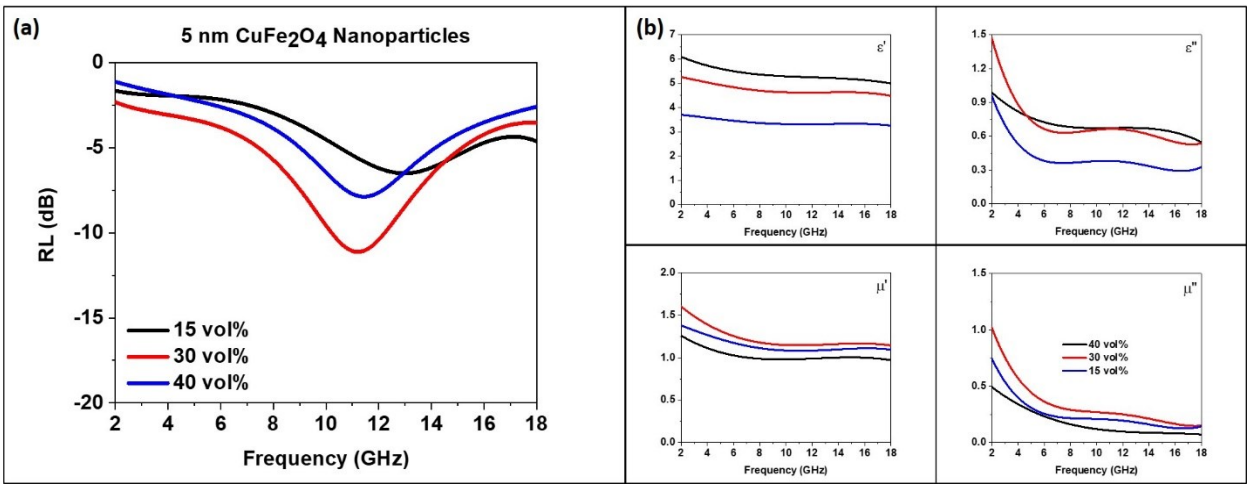


**Figure 3.12.** (a) Reflection loss for varying nanoparticle loadings (15, 30, and 40 vol%) of 5 nm $CuFe_2O_4$/paraffin wax composites at a 3 mm thickness. (b) Visualization of the effect of loading on the real and imaginary portions of the permittivity and permeability of 5 nm $CuFe_2O_4$ nanoparticles.

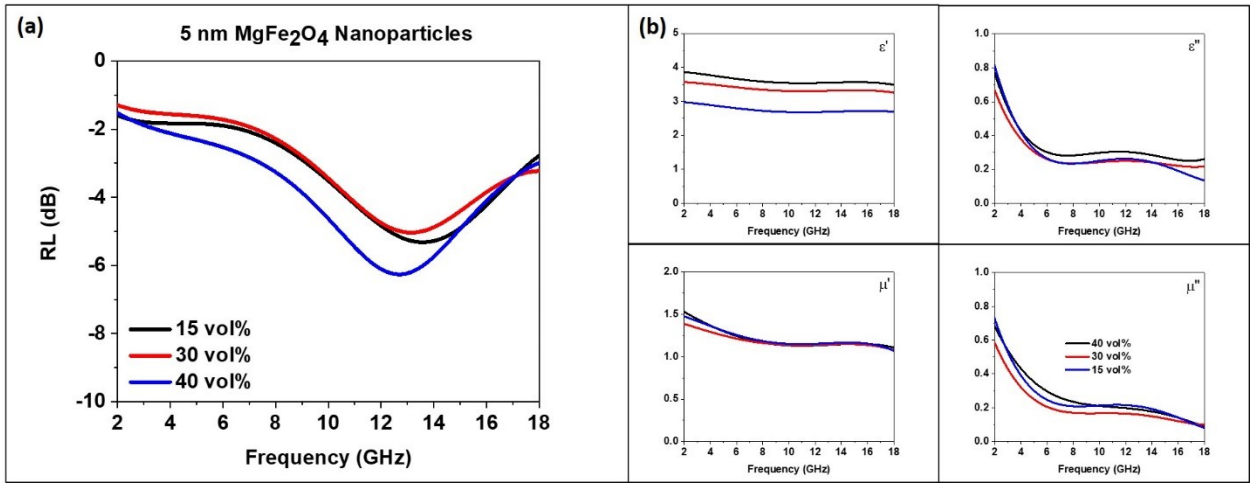


**Figure 3.13.** (a) Reflection loss for varying nanoparticle loadings (15, 30, and 40 vol%) of 5 nm $MgFe_2O_4$/paraffin wax composites at a 3 mm thickness. (b) Visualization of the effect of loading on the real and imaginary portions of the permittivity and permeability of 5 nm $MgFe_2O_4$ nanoparticles.

### 3.3.4 Doping Dependence Effects on Electromagnetic Wave Absorption

To determine the effect of doping (i.e. changing the $M^{2+}$ ion) on the maximum absorption frequencies of the ferrite systems, all **M**$Fe_2O_4$ (**M** = Fe, Co, Cu, Mn, Mg) nanoparticles were measured at varying loadings of 15, 30 and 40 vol% and the data compared, holding the loading percentage constant. Figure 3.14 (a) and (c) display the effect of $M^{2+}$ ion doping on the RL peak resonant frequency for all studied ferrites in the **M**$Fe_2O_4$ nanoparticle series at a 3 mm toroid thickness, with a 30 vol% loading and 40 vol% loading, respectively.

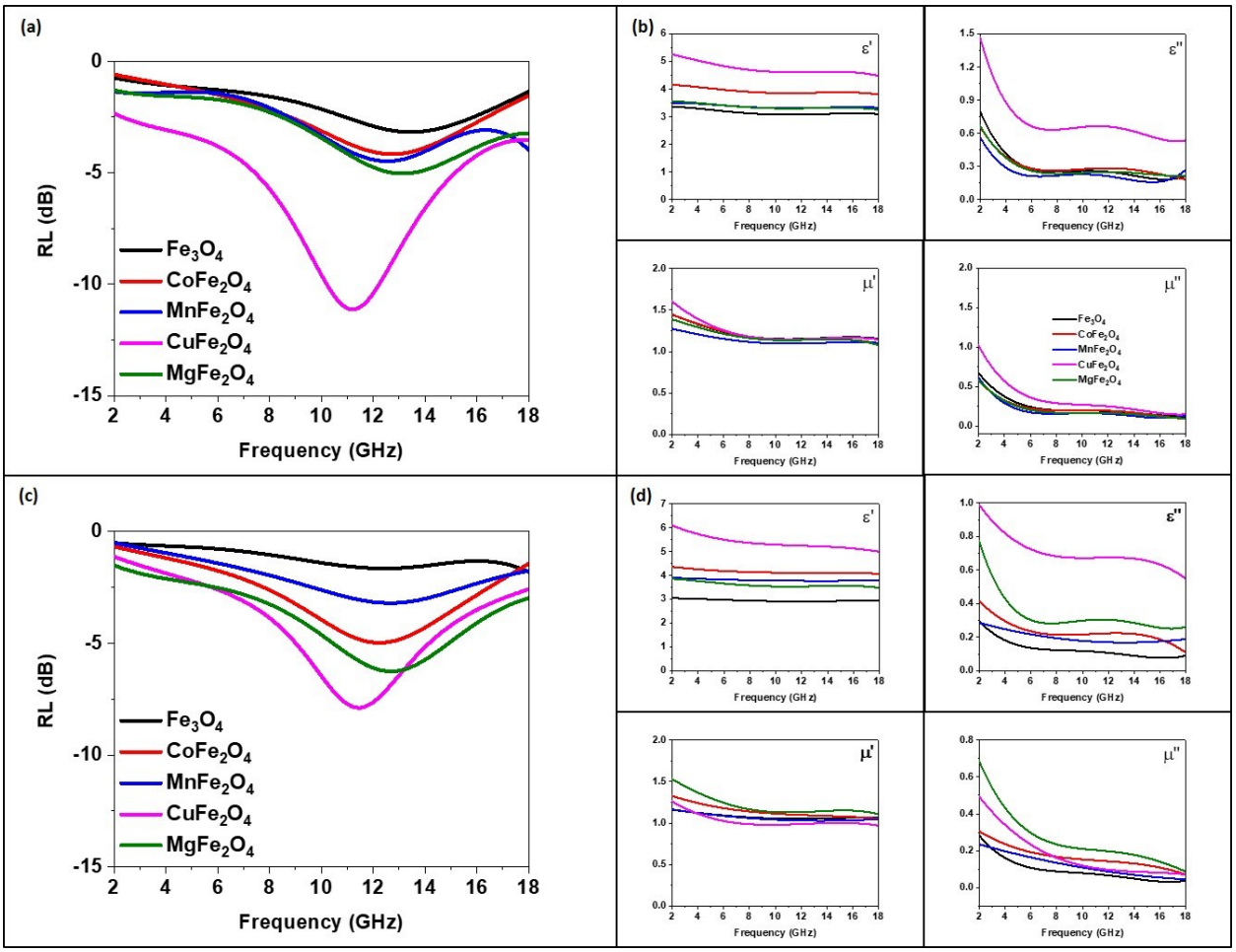


**Figure 3.14.** (a) Illustration of the effect of ferrite type on the reflection loss resonant frequency for **M**$Fe_2O_4$ (**M** = Fe, Co, Cu, Mn, Mg) samples of 6 mm thickness and 30 vol% loading. (b) Illustration of the effect of ferrite type on the real and imaginary portions of the permittivity and permeability of **M**$Fe_2O_4$ nanoparticles at 30 vol% loading. (c) Illustration of the effect of ferrite type on the reflection loss resonant frequency for **M**$Fe_2O_4$ samples of 6 mm thickness and 40 vol% loading. (d) Illustration of the effect of ferrite type on the real and imaginary portions of the permittivity and permeability of **M**$Fe_2O_4$ nanoparticles at 40 vol% loading.

As shown in Figure 3.14 (a) and (c), the trend for RL resonant electromagnetic wave absorption frequency, listed in order of increasing resonant frequency, is as follows: $CuFe_2O_4$ < $CoFe_2O_4$ < $MnFe_2O_4$ ≈ $MgFe_2O_4$ ≈ $Fe_3O_4$. The results of the specific peak positions for 3 mm thick wax/nanoparticle composite toroids across all loadings are summarized in Table 3.2 below:

**Table 3.2.** Ferrite-Based Nanoparticle Doping Effects on Resonant Frequency of Electromagnetic Wave Absorption.

| Loading in Wax Composite | $CuFe_2O_4$ | $CoFe_2O_4$ | $MnFe_2O_4$ | $MgFe_2O_4$ | $Fe_3O_4$ |
|---|---|---|---|---|---|
| 15 vol% | 12.97 GHz | 12.07 GHz | 14.08 GHz | 13.59 GHz | 13.50 GHz |
| 30 vol% | 11.22 GHz | 12.81 GHz | 12.59 GHz | 13.08 GHz | 13.41 GHz |
| 40 vol% | 11.44 GHz | 12.27 GHz | 12.67 GHz | 12.67 GHz | 12.41 GHz |

Specifically, taking the 40 vol% loading data into consideration, we see the resonance peaks at 11.44 GHz for $CuFe_2O_4$, 12.17 GHz for $CoFe_2O_4$, 12.67 GHz for $MnFe_2O_4$, 12.67 GHz for $MgFe_2O_4$, and 12.41 GHz for $Fe_3O_4$. $MnFe_2O_4$, $MgFe_2O_4$, and $Fe_3O_4$ have been described as roughly equal to each other as the maximum absorption frequencies for these materials fall within ~0.5 GHz of one another across all loadings, and the ordering of the positioning of the maximum absorption frequencies varies slightly. It is rather interesting that these three ferrites behave relatively similarly. It may be worth an extensive effort to uncover the exact mechanism by which the ferrite particles absorb electromagnetic radiation in order to further understand and potentially predict where absorption peaks may lie.

The previously described trend, again listed in order of increasing resonant frequency, $CuFe_2O_4 < CoFe_2O_4 < MnFe_2O_4 \approx MgFe_2O_4 \approx Fe_3O_4$, holds true for all loading percentages, aside from two slight deviations. First, while the 15 vol% and 40 vol% data show that $CoFe_2O_4$ should have a lower maximum absorption frequency than $MnFe_2O_4$, the 30 vol% data shows the ordering for the maximum absorption frequency for these two ferrites is reversed. In fact, $MnFe_2O_4$ displays a lower maximum absorption frequency than $CoFe_2O_4$, with values of 12.59 GHz and 12.81 GHz, respectively. This deviation from the trend is difficult to explain, but is suspected to be due to a unique contribution to the magnetization of $MnFe_2O_4$ from the $Mn^{2+}$

cations as previously discussed. The second deviation from the trend is concerning the positioning of the $CoFe_2O_4$ maximum absorption frequency at 15 vol% as the lowest absorption frequency among the measured ferrites, at 12.07 GHz. This deviation is thought to be explained by some excess aggregation of particles during the sample preparation stage, resulting in a larger effective size of the particles and thus, a lower maximum absorption frequency. It is tough to gauge the degree of aggregation in the paraffin wax composites as most x-ray or electron beam imaging techniques will melt the wax, causing damage to instruments. An appropriate imaging technique for this purpose has not yet been thought of. The relationship between the size of a particle and absorption frequency has been discussed in Chapter 2, as well as a prior publication.[35]

Similarly, to determine the effect of doping (i.e. changing the $M^{2+}$ ion) on intensity of electromagnetic absorption for the ferrite systems, all $\mathbf{M}Fe_2O_4$ (**M** = Fe, Co, Cu, Mn, Mg) nanoparticles were measured at varying loadings of 15, 30 and 40 vol% and the data compared, holding the loading percentage constant. Figure 3.14 (a) and (c) display the effect of $M^{2+}$ ion doping on the intensity of electromagnetic absorption for all studied ferrites in the $\mathbf{M}Fe_2O_4$ nanoparticle series at a 3 mm toroid thickness, with a 30 vol% loading and 40 vol% loading, respectively. As shown in Figure 3.14 (a) and (c), the trend for RL resonant electromagnetic wave absorption frequency, listed in order of increasing intensity of electromagnetic wave absorption, is as follows: $CoFe_2O_4 \approx MnFe_2O_4 \approx Fe_3O_4 < MgFe_2O_4 < CuFe_2O_4$. The results of the specific peak positions for 3 mm thick wax/nanoparticle composite toroids across all loadings are summarized in Table 3.3 below:

**Table 3.3.** Ferrite-Based Nanoparticle Doping Effects on Intensity of Electromagnetic Wave Absorption.

| Loading in Wax Composite | $CuFe_2O_4$ | $CoFe_2O_4$ | $MnFe_2O_4$ | $MgFe_2O_4$ | $Fe_3O_4$ |
|---|---|---|---|---|---|
| 15 vol% | -6.51 dB | -2.57 dB | -2.34 dB | -5.32 dB | -4.43 dB |
| 30 vol% | -11.13 dB | -4.16 dB | -4.48 dB | -5.03 dB | -3.18 dB |
| 40 vol% | -7.88 dB | -4.99 dB | -3.21 dB | -6.26 dB | -1.67 dB |

Taking the 30 vol% loading data into consideration, we see maximum electromagnetic absorption intensities of -11.13 dB for $CuFe_2O_4$, -5.03 dB for $MgFe_2O_4$, -4.48 dB for $MnFe_2O_4$, -4.16 dB for $CoFe_2O_4$, and -3.18 dB for $Fe_3O_4$. Across all measured loadings, the $CuFe_2O_4$ nanoparticles are the most effective electromagnetic absorber, followed by $MgFe_2O_4$. There are no apparent trends amongst $MnFe_2O_4$, $CoFe_2O_4$, and $Fe_3O_4$, aside from all three displaying less effective absorption properties than $MgFe_2O_4$ and $CuFe_2O_4$ regardless of loading. In fact, the highest absorption intensity amongst the three, -4.99 dB at a 40 vol% loading of $CoFe_2O_4$, is still less effective than the lowest observed absorption intensity for $MgFe_2O_4$, -5.03 dB at a 30 vol% loading, and $CuFe_2O_4$ is most effective across all loadings. This behavior is largely due to the soft ferromagnetic nature of $CuFe_2O_4$ and the superparamagnetic nature of $MnFe_2O_4$, $CoFe_2O_4$, $MgFe_2O_4$, and $Fe_3O_4$ as previously discussed.

Figures 3.14 (b) and (d) display the effect of doping on the real and imaginary portions of the permittivity and permeability for all measured ferrite nanoparticles at a 1 mm toroid thickness, with a 30 vol% loading and 40 vol% loading, respectively. The trends can be seen in each plot in Figures 3.14 (b) and (d), but the generalized trends are summarized in Table 3.4 below:

**Table 3.4.** Ferrite-Based Nanoparticle Trends in Complex Permittivity and Permeability.

| Material Property | Trend |
|---|---|
| Real Permittivity (ε′) | $CuFe_2O_4 > CoFe_2O_4 > MnFe_2O_4 > MgFe_2O_4 > Fe_3O_4$ |
| Imaginary Permittivity (ε′′) | $CuFe_2O_4 > MgFe_2O_4 > CoFe_2O_4 > MnFe_2O_4 > Fe_3O_4$ |
| Real Permeability (μ′) | $MgFe_2O_4 > CoFe_2O_4 > Fe_3O_4 > MnFe_2O_4 > CuFe_2O_4$ |
| Imaginary Permeability (μ′′) | $MgFe_2O_4 > CoFe_2O_4 > CuFe_2O_4 > MnFe_2O_4 > Fe_3O_4$ |
| Frequency of Reflection Loss Peak (RL) | $Fe_3O_4 > MgFe_2O_4 > MnFe_2O_4 > CoFe_2O_4 > CuFe_2O_4$ |

Figure 3.15 (a) displays the effect of doping on the RL peak intensity and resonant frequency and Figure 3.15 (b) displays the effect of doping on the real and imaginary portions of the permittivity and permeability for 5 nm **M**$Fe_2O_4$ (**M** = Fe, Co, Cu, Mn, Mg) nanoparticles at a 3 mm toroid thickness, with a 15 vol% loading. The previous discussion on doping effects can be applied to the 5 nm **M**$Fe_2O_4$ (**M** = Fe, Co, Cu, Mn, Mg) nanoparticles at 15 vol% loading as well.

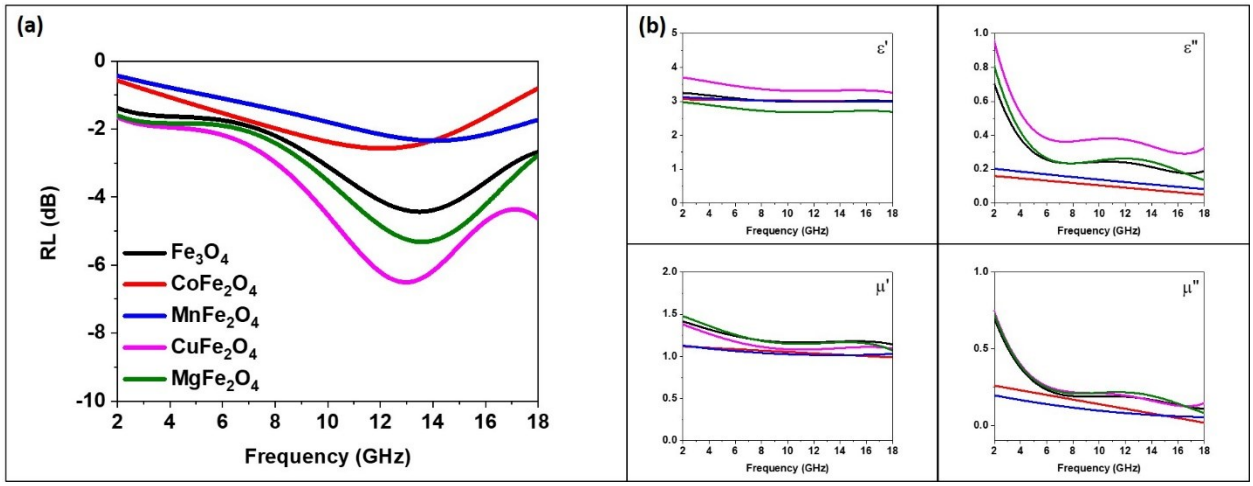


**Figure 3.15.** (a) Illustration of the effect of ferrite type on the reflection loss resonant frequency for $MFe_2O_4$ (M = Fe, Co, Cu, Mn, Mg) samples of 3 mm thickness and 15 vol% loading. (b) Illustration of the effect of ferrite type on the real and imaginary portions of the permittivity and permeability of $MFe_2O_4$ nanoparticles at 15 vol% loading.

Explaining the apparent trends (or lack thereof) in the real and imaginary permittivity and permeability of nanoscale ferrites is rather tough to do and has yet to be explored in depth in the literature. In conceptual terms, the real permittivity is thought of as the ability of a material to store electrical energy in an electrical field and the imaginary permittivity is the dielectric loss of the material, dependent on conductivity. The real permeability is typically defined as the ability of a material to align its magnetic moment to an external magnetic field and the imaginary permeability is the measure of the rotation of a material around its easy axis. As we can see from the trends described in the above table, the only material property that aligns with the observed trend in reflection loss peak position is the real permittivity, as the absorption frequency decreases with increasing real permittivity. This result strongly indicates that the dielectric properties of ferrites have more influence of their electromagnetic absorption behavior than the magnetic properties do. This conclusion is further supported when looking at the trend in the imaginary permittivity and realizing that aside from $MgFe_2O_4$, the trend here also follows the same ordering as the trends for the real permittivity and absorption frequency. In fact, this phenomenon has been previously reported by other studies indicating that the imaginary permittivity, $\varepsilon''$, increases with a decrease in absorption frequency.[36] The unique result from $MgFe_2O_4$, seemingly out of place, is thought to be due to contributing effects from the spinel structure and the smaller electron cloud of the $Mg^{2+}$ ions in comparison with the other d-block ions in this study ($Fe^{2+}$, $Co^{2+}$, $Cu^{2+}$, and $Mn^{2+}$).

When looking at the influence of the magnetic properties on the electromagnetic absorption behavior of the ferrites under study, it is relatively easy to understand why there are no logical trends that can be discerned from the data. According to our previous study concerning the effect of nanoparticle size on electromagnetic absorption behavior, we have

determined that as the size of a nanoparticle increases, the imaginary permeability increases, and thus the frequency of absorption is shifted to lower values. This trend is explained through the Landau-Lifshitz-Gilbert equation (LLG) as discussed in our previous work.[35] In the current study, all of the nanoparticles have a very similar size in between around 5 nm. With no definitive changes in the size of the particles under study, it makes sense that we may not see a large variation in the value of the imaginary permeability, and in turn, a weak influence on the electromagnetic absorption behavior. This phenomenon can be seen visually from Figure 3.14 (b) and (d) when taking into account that the magnitude of the difference from the highest to lowest imaginary permeability (~0.2) is much less than that of the real or imaginary permittivity (~5.0 and ~0.9, respectively). Since there is not a large variation in the imaginary permeability of the ferrites under study, it follows that we would not see a large influence from the magnetic properties on the absorption frequencies, while the dielectrics dominate this behavior due to the large variation among samples.

As previously stated and discussed in a Chapter 2, the real permeability is dependent upon the crystallinity of each sample rather than the magnetization or size of the material.[35] Again, as all of the samples under study are of the same size, and all of the spinel or inverse spinel structure, it follows that their crystal sizes are very similar as well. This explains the lack of an apparent trend amongst the varying ferrites in this study. Mathematically, the explanation for this lack of trend can be seen by looking at the real permeability caused by the Néel relaxation of a material in the superparamagnetic state[37]:

$$\mu' = \mu_0 \left(1 + \frac{V_p M_0^2}{3 k_B T}\right) \tag{3}$$

where $V_p$ is the volume of the nanoparticle, $M_0$ is the saturation magnetization, $k_B$ is the Boltzmann constant and $T$ is the temperature. Since $\frac{V_p M_0^2}{3k_B T}$ will be an extremely small number ($V_p M_0^2 << 3K_B T$ and $\frac{V_p M_0^2}{3k_B T} << 1$), any change in volume will have a negligent effect on μ′.

### 3.3.5 Theoretical Model for the Calculation of the Effective Permeability for Ferrites

The effective permeability has been modeled following procedures established by R.F. Soohoo and described by Wu et al. in a previous report.[38,39] This was discussed in detail in Chapter 2. As previously stated, the resulting calculated $\mu_{eff}$ from this procedure is valid for single domain particles. The critical size for ferrites has been reported to be around 80 nm, indicating that all particles in this study can be modeled using this approach.[40]

Figure 3.16 shows the agreement between the measured and simulated effective complex permeability for 5 nm $Fe_3O_4$ nanoparticles at a (a) 15 vol%, (b) 30 vol%, and (c) 40 vol% loading. The agreement between the experimental and simulated values is acceptable, indicating that the magnetic nanoparticle/wax composites behave according to standard mixing theories. The experimental and simulated curves have roughly the same curve shape, however are slightly off in magnitude. This could be due to experimental conditions that were unaccounted for in the simulations.[39]

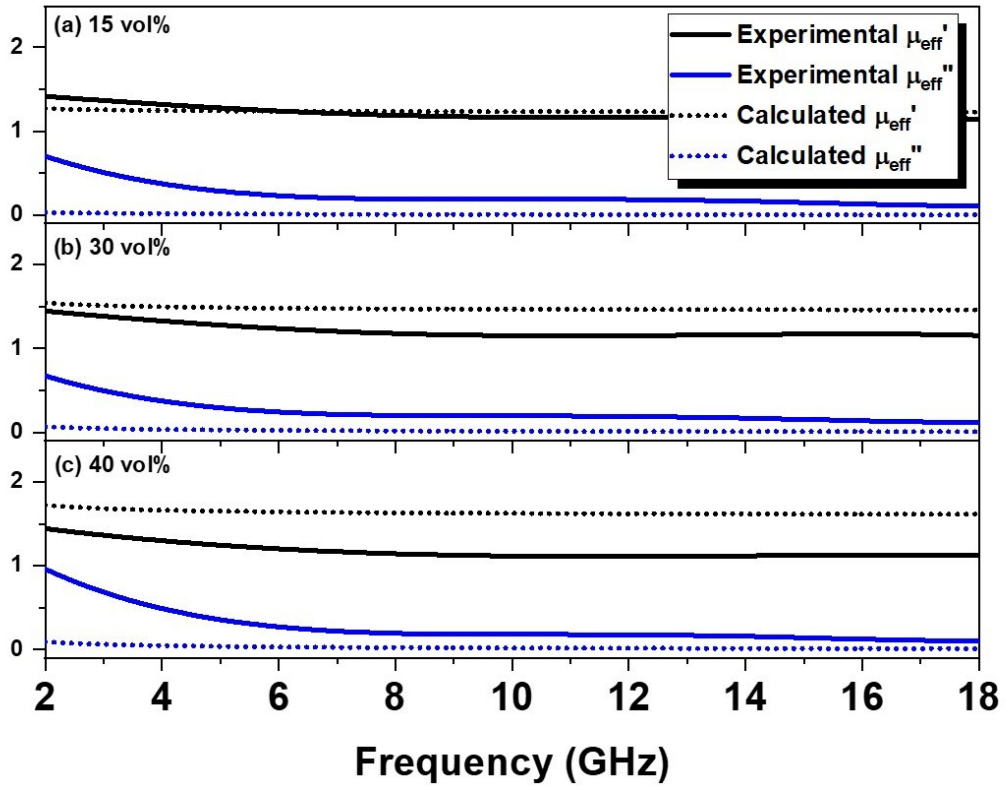


**Figure 3.16.** Calculated real part, μ′, and imaginary part, μ″, of the complex effective permeability for 5 nm $Fe_3O_4$ nanoparticles at volume fractions of (a) 15 vol%, (b) 30 vol%, and (c) 40 vol%.

Simulation results for all other sizes and loadings of $Fe_3O_4$ nanoparticles are shown in Figures 3.17 – 3.20.

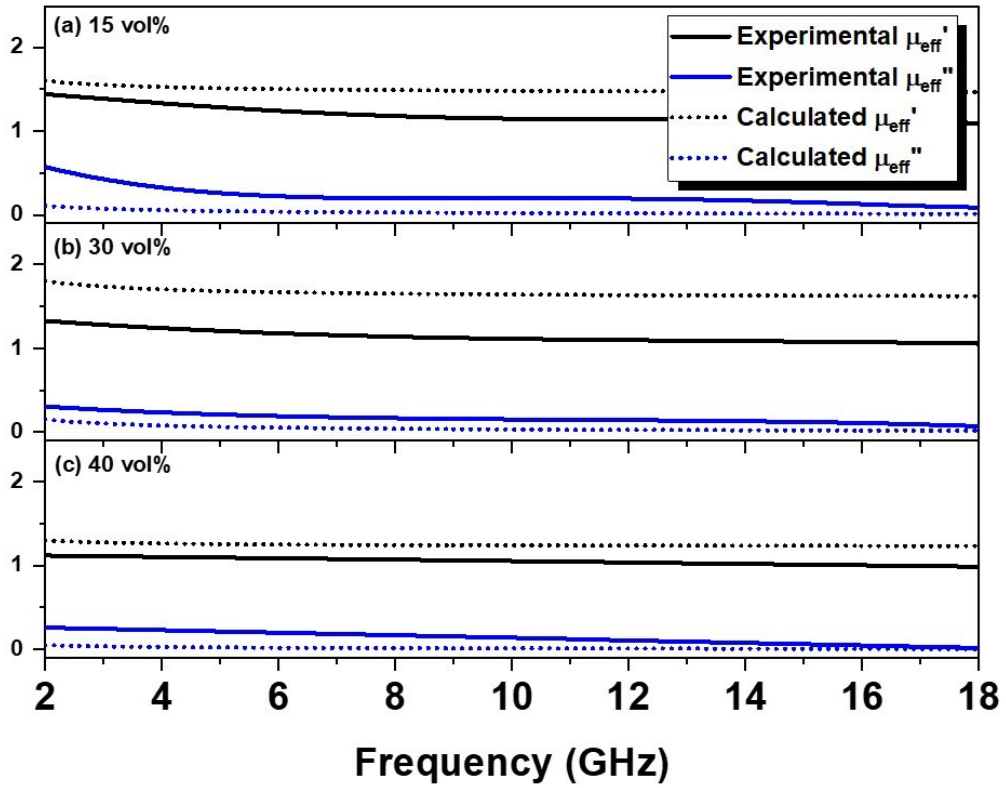


**Figure 3.17.** Calculated real part, μ′, and imaginary part, μ″, of the complex effective permeability for 5 nm $CoFe_2O_4$ nanoparticles at volume fractions of (a) 15 vol%, (b) 30 vol%, and (c) 40 vol%.

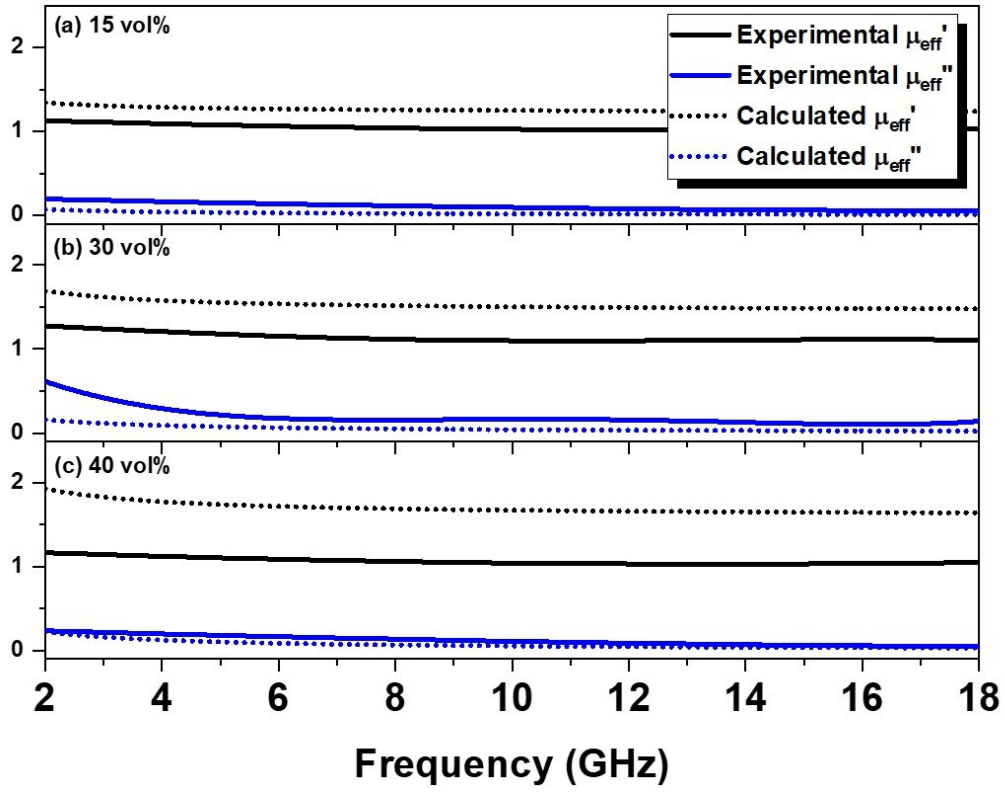


**Figure 3.18.** Calculated real part, μ′, and imaginary part, μ″, of the complex effective permeability for 5 nm $MnFe_2O_4$ nanoparticles at volume fractions of (a) 15 vol%, (b) 30 vol%, and (c) 40 vol%.

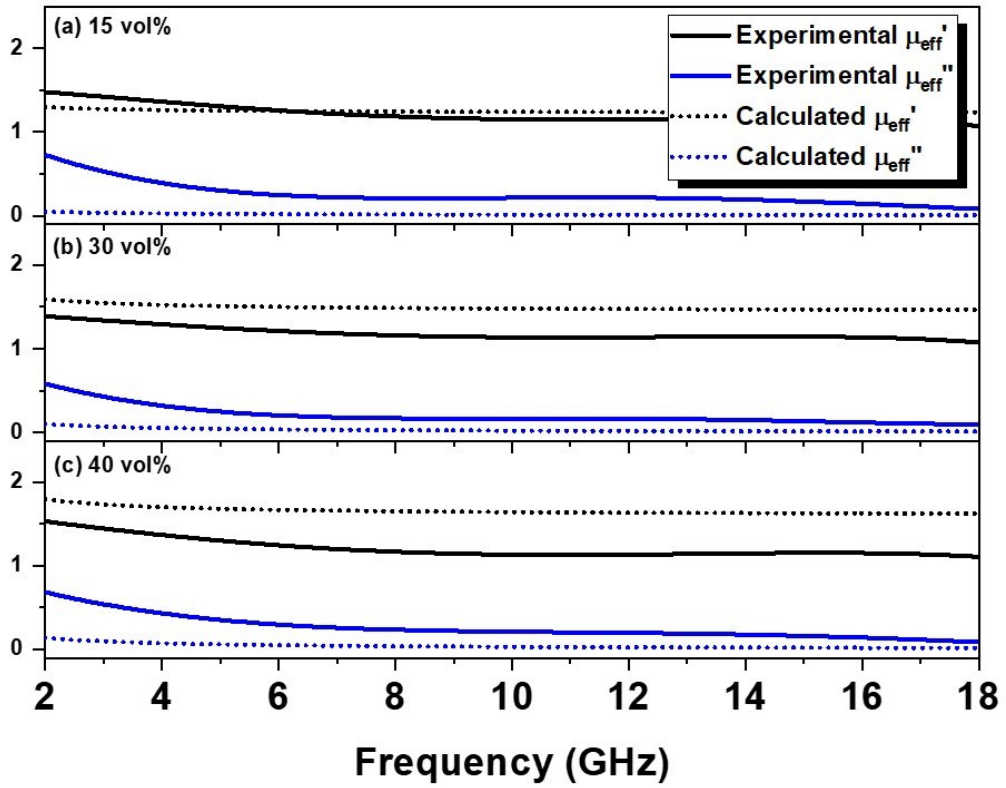


**Figure 3.19.** Calculated real part, μ′, and imaginary part, μ″, of the complex effective permeability for 5 nm $MgFe_2O_4$ nanoparticles at volume fractions of (a) 15 vol%, (b) 30 vol%, and (c) 40 vol%.

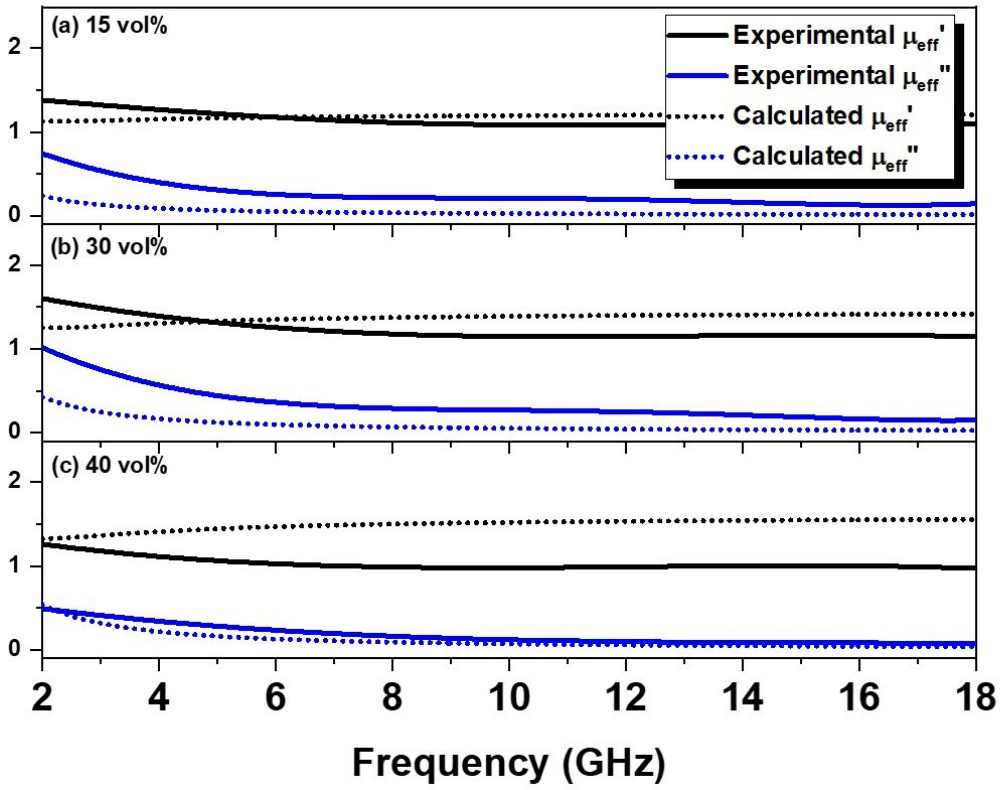


**Figure 3.20.** Calculated real part, μ′, and imaginary part, μ″, of the complex effective permeability for 5 nm $CuFe_2O_4$ nanoparticles at volume fractions of (a) 15 vol%, (b) 30 vol%, and (c) 40 vol%.

## 3.4 CONCLUSIONS

In conclusion, modifications of existing methods for the synthesis of **M**$Fe_2O_4$ (**M** = Fe, Co, Cu, Mg, Mn) nanoparticles via organic solution synthesis and thermal decomposition of the corresponding metal acetylacetonates have been implemented to produce nanoparticles of size 5 nm and **M**:Fe composition of 1:2. The dielectric, magnetic and microwave absorption properties of the series of ferrites have been carefully investigated. Our analysis has revealed that ferrites of such small sizes are weak microwave absorbers in the frequency range from 10 – 18 GHz. We have shed light on some thought provoking trends including that the frequency of absorption follows the following: $CuFe_2O_4 < CoFe_2O_4 < MnFe_2O_4 \approx MgFe_2O_4 \approx Fe_3O_4$. In addition, the data gives reason to believe that the microwave absorption properties of ferrites are largely governed by the dielectric behavior of the material rather than the magnetic behavior. This study discussed in Chapter 3 should be used as building block towards developing a library of the microwave absorption behavior of common magnetic nanomaterials with the aim of increasing fundamental knowledge of microwave absorbing materials. In the future, this study could help in the development of electromagnetic wave absorbers by design.

## 3.5 REFERENCES


1. K. O. Abdulwahab *et al.* A One-Pot Synthesis of Monodispersed Iron Cobalt Oxide and Iron Manganese Oxide Nanoparticles from Bimetallic Pivalate Clusters. *Chem. Mater.* **26**, 999–1013 (2014).
2. M. Sugimoto. The Past, Preset, and Future of Ferrites. *J. Am. Ceram. Soc.* **82**, 269–279 (1999).
3. S. P. Gubin, Y. I. Spichkin, G. Y. Yurkov & A. M. Tishin. Nanomaterial for High-Density Magnetic Data Storage. *Russ. J. Inorg. Chem.* **47**, 32–67 (2002).
4. C. W. Jung & P. Jacobs. Physical and chemical properties of superparamagnetic iron oxide MR contrast agents: ferumoxides, ferumoxtran, ferumoxsil. *Magn. Reson. Imaging* **13**, 661–674 (1995).
5. P. Majewski & B. Thierry. Functionalized Magnetite Nanoparticles - Synthesis, Properties, and Bio-Applications. *Crit. Rev. Solid State Mater. Sci.* **32**, 203–215 (2007).
6. C. V. G. Reddy, S. V. Manorama & V. J. Rao. Preparation and characterization of ferrites as gas sensor materials. *J. Mater. Sci. Lett.* **19**, 775–778 (2000).
7. U. Hafeli, W. Schutt, J. Teller & J. Zborowski. *Scientific and Clinical Applications of Magnetic Carriers*. (Plenum Press, 1997).
8. S. Sun *et al.* Monodisperse MFe2O4 (M = Fe, Co, Mn) Nanoparticles. *J. Am. Chem. Soc.* **126**, 273–279 (2004).
9. A. J. Rondinone, A. C. S. Samia & Z. J. Zhang. Characterizing the magnetic anisotropy constant of spinel cobalt ferrite nanoparticles. *J. Appl. Phys. Lett.* **76**, 3624–3626 (2000).
10. D. S. Mathew & R. Juang. An overview of the structure and magnetism of spinel ferrite nanoparticles and their synthesis in microemulsions. *Chem. Eng. J.* **129**, 51–65 (2007).

11. A. J. Rondinone, C. Liu & Z. J. Zhang. Determination of Magnetic Anisotropy Distribution and Anisotropy Constant of Manganese Spinel Ferrite Nanoparticles. *J. Phys. Chem. B* **105**, 7967–7971 (2001).
12. H. Zhu, Y. Huang, S. Zheng, L. Wu & S. Sun. Monodisperse MxFe3-xO4 (M = Fe, Cu, Co, Mn) Nanoparticles and Their Electrocatalysis for Oxygen Reduction Reaction. *Nano Lett.* **13**, 2947–2951 (2013).
13. C. Liu, B. Zuo, A. J. Rondinone & Z. J. Zhang. Reverse Micelle Synthesis and Characterization of Superparamagnetic MnFe2O4 Spinel Ferrite Nanocrystallites. *J. Phys. Chem. B.* **104**, 1141–1145 (2000).
14. P.C. Fannin, S. W. Charles, D. Vincent & A. T. Giannitsis. Measurement of high-frequency complex permittivity and conductivity of magnetic fluids. *J. Magn. Magn. Mater.* **252**, 80–82 (2002).
15. N. Matsushita, T. Nakamura & M. Abe. Ni-Zn-Co ferrite films prepared at 90/spl deg/C having /spl mu/"=30 at 3 GHz. *IEEE Trans. Magn.* **38**, 3111–3113 (2002).
16. N. Matsushita, C. P. Chong, T. Mizutani & M. Abe. Ni-Zn films with high permeability at 1 GHz prepared at 90C. *J. Appl. Phys.* **91**, 7376–7378 (2002).
17. National Research Council (U.S.). Committee on Identification of Research Needs Relating to Potential Biological or Adverse Health Effects of Wireless Communications Devices. *Identification of Research Needs Relating to Potential Biological or Adverse Health Effects of Wireless Communication Devices*. (National Academic Press, 2008).
18. E. Seidenberg & H. Schimpf. Aspects of automatic target recognition with a two-frequency millimeter wave SAR. *P. Soc. Photo-Opt. Ins.* **4033**, 167–177 (2000).

19. A. Ahlbom *et al.* Possible effects of electromagnetic fields (EMF) on human health--opinion of the scientific committee on emerging and newly identified health risks (SCENIHR. *Toxicology* **246**, 248–250 (2008).
20. E. F. Knott, J. F. Shaeffer & M. T. Tuley. *Radar Cross Section*. (SciTech Pub., 2004).
21. K. J. Vinoy & R. M. Jha. Trends in Radar Absorbing Materials. *Academy Proceedings in Engineering Sciences* **20**, 815–850 (1995).
22. K. J. Vinoy & R. M. Jha. *Radar Absorbing Materials: From Theory to Design and Characterization*. (Kluwer Academic Publishers, 1996).
23. A. P. Mouritz. *Introduction to Aerospace Materials*. (Woodhead Publishing, 2012).
24. M. J. Park, J. H. Choi & S. S. Kim. Microwave Absorption Properties of FSS-impacted Composites as a Broadband Microwave Absorber. *IEEE Trans. Magn.* **36**, 3272–3274 (2000).
25. K. A. Korolev, S. Chen, Z. J. Li & M. N. Afsar. Millimeter-Wave Ttransmittance and Reflectance Measurement on Pure and Diluted Carbonyl Iron. *IEEE Transactions on Instrumentation and Measurement* **59**, (2010).
26. Y.B. Feng, T. Qiu, C. Y. Shen & X. Y. Li. Electromagnetic and absorption properties of carbonyl iron/rubber radar absorbing materials. *IEEE Transactions on Magnetics* **42**, 363–368 (2006).
27. S. Kimura, T. Kato, T. Hyodo, Y. Shimizu & M. Egashira. Electromagnetic wave absorption properties of carbonyl iron-ferrite/PMMA composites fabricated by hybridization method. *J. Magn. Magn. Mater.* **312**, 181–186 (2007).

28. A. E. Robinson. The preparation of magnesium-manganese ferrite for microwave applications. *Proceedings of the IEE - Part B: Radio and Electronic Engineering* **104**, 159–164 (1957).
29. R. Grössinger. A critical examination of the law of approach to saturation. *Phys. Status. Solidi. A* **66**, 665–674 (1981).
30. X. Batlle *et al.* Magnetic study of M-type doped barium ferrite nanocrystalline powders. *J. Appl. Phys.* **74**, 3333 (1993).
31. G. F. Goya, T. S. Berquó, F.C. Fonseca & M. P. Morales. Static and dynamic magnetic properties of spherical magnetite nanoparticles. *J. Appl. Phys.* **94**, 3520 (2003).
32. D. Wagner. *Introduction to the Theory of Magnetism*. **48**, (Elsevier Ltd., 1972).
33. M. H. Cao *et al.* Single-Crystal Dendritic Micro-Pines of Magnetic α-Fe2O3 : Large-Scale Synthesis, Formation Mechanism, and Properties. *Angew. Chem.* **44**, 4197 (2005).
34. S. Ni *et al.* Hydrothermal synthesis and microwave absorption properties of Fe3O4 nanocrystals. *J. Phys. D: Appl. Phys.* **42**, (2009).
35. Michael Giroux *et al.* Size-Dependent Electromagnetic Absorption Properties of Iron Oxide (Fe3O4) Nanomaterials. *In Preparation.*
36. A. A. Khurram, S. A. Rakha, P. Zhou, M. Shafi & A. Munir. Correlation of electrical conductivity, dielectric properties, microwave absorption, and matrix properties of composites filled with graphene nanoplatelets and carbon nanotubes. *J. Appl. Phys.* **118**, 044105 (2015).
37. J. I. Gittleman, B. Abeles & S. Bozowski. Superparamagnetism and Relaxation Effects in Granular Ni-SiO2 and Ni-Al2O3 Films. *Phys. Rev. B.* **9**, 3891–3897 (1974).
38. R. F. Soohoo. *Microwave Magnetics*. (Harper and Row Publishers, 1985).

39. L.Z. Wu *et al.* High Frequency Complex Permeability of Iron Particles in a Nonmagnetic Matrix. *J. Appl. Phys.* **99**, (2006).
40. Qing Li *et al.* Correlation Between Particle Size/Domain Structure and Magnetic Properties of Highly Crystalline Fe3O4 Nanoparticles. *Sci. Rep.* **7**, (2017).

# Chapter 4. The Influence of Alloying on the Radar Absorption Properties of Iron, Cobalt, and Nickel Magnetic Nanomaterials

## 4.1 INTRODUCTION

Alloys have long been critical to the development of civilization, dating back over five millennia.[1] From the accidental discovery of arsenical bronze giving birth to the Bronze Age in 2500 BC, to the discovery of steel (iron and carbon) in 300 BC, and to the industrial revolution, alloying has been critical to the advancement of society and has had the potential to change technology entirely.[1–4] Since the industrial revolution, applications of alloys have shifted away from use as tools and/or building materials to more modern alloys which are engineered to achieve desired chemical or physical properties, eventually leading to the development of high entropy alloys (HEAs), which include five or more principal elements to the alloy.[1,5] Such modern alloys may exhibit desirable properties including, high hardness, excellent ductility, improved electrical or thermal properties, high corrosion resistance, and electromagnetic interference (EMI) properties.[6–12]

In recent times much attention has been given to the use of HEAs as EMI as it is well known that they can effectively absorb electromagnetic waves by either mitigating the electromagnetic loss or converting the electromagnetic energy into thermal energy (heat).[6,13–21] A wide range of HEAs have been studied for this purpose, the most predominant of which are a derivative of the FeCoNiCrAl parent alloy.[6,7,11,22,23] For instance, Yang reported the electromagnetic wave absorption properties of the $FeCoNiCrAl_{0.8}$ HEA with a superb reflection loss (-41.8 dB), while Zhang reported excellent shielding effectiveness of a high energy ball milled AlCoCrFeNi alloy.[6,22] Of great importance for electromagnetic wave absorption with this

new class of HEAs is outstanding magnetic properties, leading to the ability to balance both the complex permittivity and complex permeability and combine both dielectric and magnetic losses, resulting in an improved absorption capability.[6,24–28] Worthy of note in recent literature, Chen investigated the magnetic properties of Fe0.6CoNiCrAl, reporting a saturation magnetization ($M_s$) of 50.70 emu/g and coercivity ($H_c$) of 31.3 Oe, while Lu further improved upon this, reporting an $M_s$ of 59 emu/g and $H_c$ of 36.6 Oe.[29,30]

The outstanding magnetic properties that HEAs exhibit make them promising candidates as electromagnetic wave absorbing materials. Obviously, the magnetic properties of the HEAs previously discussed arise from the contributions of the magnetic metal components, Fe, Ni, and Co, however, there has yet to be a systematic study about the behavior of each of these components individually and how their properties change when alloyed. In Chapter 4, we propose a systematic investigation of the three most common magnetic elements (Fe, Co, and Ni) and their binary alloys (FeNi, CoNi, and CoFe) as materials for electromagnetic wave absorption. Similarly to our previous work, this study should be used as a method of improving the existing library of materials for electromagnetic wave absorbing materials and to potentially give insight into the mechanisms by which alloying magnetic nanomaterials influences electromagnetic radiation. As previously stated, HEAs are an excellent candidate for electromagnetic wave absorption, yet an effort is needed to discern the mechanisms by which their properties behave on a much simpler scale. Considering this fact, we have developed directed syntheses of uniform size and shape for each of the magnetic metals and magnetic metal alloys listed above through the use of organic solution synthesis techniques. We have then correlated the dielectric and magnetic properties of our materials to the electromagnetic absorption properties by measuring the complex permittivity and permeability of the metals

through use of a vector network analyzer (VNA). From this data, we have attempted to draw trends and conclusions concerning the electromagnetic wave absorption properties of magnetic metal and magnetic metal alloys to help further the understanding of EM wave absorption and expand the knowledge in the field.

## 4.2 EXPERIMENTAL METHODS

*Chemicals.* All materials (metal precursors, organic solvents, and ligands) were purchased from Sigma Aldrich. All chemicals were used as received.

*Synthesis Design.* All nanoparticles were synthesized under inert argon gas in a standard Schlenk line setup. Synthesis procedures were either our own methods or adapted and modified from previous reports.

### 4.2.1 Synthesis

*Synthesis of 10 nm Co Nanoparticles.*[31] 10 nm Co nanoparticles were synthesized by the decomposition of dicobalt octacarbonyl ($Co_2(CO)_8$). In a typical synthesis, a 10 mL solution of dichlorobenzene (DCB) containing oleic acid (0.2 mL, 0.6 mmol) and dioctylamine (0.34 mL, 2.1 mmol) was heated for 60 min at 120°C as a water removal step. The solution was then heated to reflux at 180°C and a second solution of dicobalt octacarbonyl (0.54 g, 1.6 mmol) dissolved in 3 mL of DCB was injected. The resulting solution was refluxed for 20 min at this temperature (180°C) after which the heat source was removed and the reaction cooled to room temperature. The precipitate was collected via centrifugation in ethanol at 8000 rpm for 10 min, re-dispersed in a hexanes/ethanol mixture, and centrifuged once again at 8000 rpm for 10 min. The final product was dispersed in hexanes.

*Synthesis of 10 nm Fe Nanoparticles.*[32] 10 nm Fe nanoparticles were synthesized by the decomposition of iron pentacarbonyl ($Fe(CO)_5$). In a typical synthesis, a 20 mL solution of 1-octadecene (1-ODE) containing oleylamine (0.3 mL, 0.9 mmol) was heated for 30 min at 120°C as a water removal step. The solution was then heated to 240°C and a second solution containing iron pentacarbonyl (0.7 mL, 5.2 mmol) in 2 mL of 1-ODE was injected. The resulting solution was maintained at this temperature (240°C) for 5 min after which the heat source was removed

and the reaction cooled to room temperature. The precipitate was collected via centrifugation in isopropanol at 8000 rpm for 10 min, re-dispersed in a hexanes/isopropanol mixture, and centrifuged once again at 8000 rpm for 10 min. The final product was dispersed in hexanes.

*Synthesis of 10 nm Ni Nanoparticles.*[33] 10 nm Ni nanoparticles were synthesized by the decomposition of nickel (II) acetylacetonate ($Ni(acac)_2$). In a typical synthesis, nickel (II) acetylacetonate (0.513 g, 2.0 mmol) was dissolved in 10 mL of oleylamine and the reaction mixture was then heated to 130°C for 60 min as a water removal step. The solution was then heated to 220°C at which point trioctylphosphine (TOP) (1.4 mL, 3.1 mmol) and borane tert-butylamine complex (BTB) (0.017 g, 0.2 mmol) dissolved in 1 mL of oleylamine were simultaneously injected. The resulting reaction mixture was maintained at this temperature (220°C) for 30 min after which the heat source was removed and the reaction cooled to room temperature. The precipitate was collected via centrifugation in ethanol at 8000 rpm for 10 min, re-dispersed in a hexanes/ethanol mixture, and centrifuged once again at 8000 rpm for 10 min. The final product was dispersed in hexanes.

*Synthesis of 10 nm CoFe Alloy Nanoparticles.* 10 nm CoFe alloy nanoparticles were synthesized by the decomposition of iron (III) acetylacetonate ($Fe(acac)_3$) and cobalt (II) acetylacetonate ($Co(acac)_2$). In a typical synthesis, iron (III) acetylacetonate (0.141 g, 0.4 mmol) and cobalt (II) acetylacetonate (0.103 g, 0.4 mmol) were dissolved in 20 mL 1-octadecene (1-ODE) containing trioctylphosphine (TOP) (0.27 mL, 0.6 mmol). The reaction mixture was then heated for 30 min at 110°C as a water removal step, and heated to 150°C for the injection of borane tert-butylamine complex (BTB) (0.216 g, 2.5 mmol) dissolved in oleylamine (2 mL, 6.0 mmol). After the injection, the reaction was heated to 180°C, maintained at this temperature for 120 min, and cooled to room temperature. The precipitate was collected via centrifugation in a small amount

of ethanol and isopropanol at 8000 rpm for 10 min, re-dispersed in a hexanes/ethanol/isopropanol mixture, and centrifuged once again at 8000 rpm for 10 min. The final product was dispersed in hexanes.

*Synthesis of 10 nm CoNi Alloy Nanoparticles.* 10 nm CoNi alloy nanoparticles were synthesized by the decomposition of cobalt (II) acetylacetonate ($Co(acac)_2$) and nickel (II) acetylacetonate ($Ni(acac)_2$). In a typical synthesis, cobalt (II) acetylacetonate (0.230 g, 0.9 mmol) and nickel (II) acetylacetonate (0.205 g, 0.8 mmol) were dissolved in 20 mL 1-octadecene (1-ODE). The reaction mixture was then heated for 30 min at 110°C as a water removal step, then heated to 150°C at which point trioctylphosphine (TOP) (0.54 mL, 1.2 mmol) and borane tert-butylamine complex (BTB) (0.043 g, 0.5 mmol) dissolved in oleylamine (2 mL, 6.0 mmol) were simultaneously injected. After the injection, the reaction was heated to 180°C, maintained at this temperature for 60 min, and cooled to room temperature. The precipitate was collected via centrifugation in a small amount of ethanol and isopropanol at 8000 rpm for 10 min, re-dispersed in a hexanes/ethanol/isopropanol mixture, and centrifuged once again at 8000 rpm for 10 min. The final product was dispersed in hexanes.

*Synthesis of 10 nm $FeNi_2$ Alloy Nanoparticles.*[34] 10 nm $FeNi_2$ nanoparticles were synthesized by the decomposition of iron (III) acetylacetonate ($Fe(acac)_3$) in the presence of 10 nm Ni seeds synthesized according the previously discussed method (insert citation). In a typical synthesis, iron (III) acetylacetonate (0.132 g, 0.375 mmol) and 50 mg of 10 nm Ni seeds were dissolved in oleylamine (17.5 mL, 53.2 mmol). The reaction mixture was then heated for 60 min at 130°C as a water removal step and then refluxed for 30 min at a higher temperature (300°C). The precipitate was collected via centrifugation in a hexanes/acetone mixture at 8000 rpm for 10 min,

re-dispersed in hexanes/acetone, and centrifuged once again at 8000 rpm for 10 min. The final product was dispersed in hexanes.

### 4.2.2 Materials Characterization

Transmission electron microscopy (TEM) images were acquired on a 120 kV, FEI Tecnai 12 TWIN microscope. X-ray diffraction (XRD) patterns were collected on a PANalytical X'Pert$^3$ Powder X-Ray Diffractometer equipped with a Cu Kα radiation source (λ=0.15406). Energy dispersive x-ray spectroscopy (EDX) data were collected on a JEOL 6700F Scanning Electron Microscope (SEM) equipped with energy dispersive spectroscopy capabilities. Magnetic hysteresis loops were acquired on a MicroMag 2900 Series AGM.

### 4.2.3 Electromagnetic Absorption Studies

All composite wax/nanoparticle samples were prepared in 20 mL scintillation vials by dispersing the appropriate amounts of paraffin wax and nanoparticles in toluene to achieve nanoparticle volume fractions ranging from 15% to 40% and slowly evaporating the solvent to create a uniformly dispersed composite matrix. The resulting composites were then molded into a toroidal shape using a Teflon mold with an outer diameter of 6.98 mm, inner diameter of 3.03 mm and thickness of 1 mm and fitted to a Keysight 85051B 7 mm airline for the microwave measurements. The complex permittivity and permeability of the composite samples were measured using a Keysight FieldFox N9918A Microwave Analyzer in the 2 – 18 GHz region and the reflection loss was calculated used the measured permittivity and permeability.

## 4.3 DISCUSSION AND RESULTS

### 4.3.1 Materials Characterization

Magnetic nanoparticles (Co, Fe, Ni, CoFe, CoNi, $FeNi_2$) of size ~10 nm are shown in transmission electron microscopy (TEM) images in Figure 4.1(a). All synthesized nanoparticles show a sphere-like morphology. Through size distribution analysis, mean diameters have been determined to be 11.44 nm (Co), 11.76 nm (Fe), 10.54 nm (Ni), 11.71 nm (FeCo), 10.31 nm (CoNi), and 11.52 nm ($FeNi_2$). Size distribution profiles are shown in Figure 4.2. The FeCo and CoNi nanoparticles were synthesized in a 1:1 ratio and the $FeNi_2$ nanoparticles in a 1:2 ratio, as determined by energy dispersive x-ray spectroscopy (EDX). The $FeNi_2$ nanoparticles were synthesized in a 1:2 ratio rather than a 1:1 ratio due to instability of the Fe-Ni binary system as the atomic percent of Fe increases above 35%.[34] The EDX results are summarized in Table 4.1 below:

**Table 4.1.** EDX data for alloyed nanoparticles.

| Material | Mass % $M_1$ | Mass % $M_2$ | Atomic % $M_1$ | Atomic % $M_2$ | Ratio $M_1$:$M_2$ |
|---|---|---|---|---|---|
| **Co** | 100 | - | 100 | - | - |
| **Fe** | 100 | - | 100 | - | - |
| **Ni** | 100 | - | 100 | - | - |
| **CoFe** | 50.35 | 49.65 | 49 | 51 | 1:1 |
| **CoNi** | 46 | 54 | 47 | 53 | 1:1 |
| **FeNi** | 34.60 | 65.40 | 35.74 | 64.26 | 1:2 |

Figure 4.1(b) presents the typical x-ray diffraction (XRD) pattern for the metal and metal alloy products. The measured patterns for Co, Fe, CoFe, and CoNi display no defined peaks, indicating a small layer of amorphous oxide on the surface of the nanoparticles. This is expected as the nanoparticles will quickly oxidize upon exposure to air during the collection process after synthesis. For Ni and FeNi, all of the peaks align with the expected patterns as confirmed by

their agreement with JCPDS No. 00-004-0850 (Ni) and No. 00-038-0419 ($FeNi_2$). The pattern for Ni displays no other peaks, indicating high purity of the Ni nanoparticle product. The pattern for $FeNi_2$ displays extremely small peaks at 35.6°, 57.7°, and 63.2° which could indicate the presence of a minute amount of impurities such as iron oxide or nickel oxide. Figure 4.1(c) displays the magnetic hysteresis loops of all the as-synthesized metal ferrite nanoparticles. The saturation magnetization values ($M_s$) vary from sample to sample and were determined by assuming $M(H) = M_s + X_dH$ ($X_d$ being the high field susceptibility) at high field and extrapolating the M(H) curve to zero field (i.e. $H = 0$).[35,36] $M_s$ values were found to be 1.76 (Fe), 18.004 (Co), 14.259 (Ni), 0.440 (CoFe), 4.149 (CoNi), and 9.270 ($FeNi_2$) emu $g^{-1}$. All of these values are much lower than that of the corresponding bulk metals and metal alloys, which is expected due to the nanoscale size of the materials as established in previous literature.[37] It is peculiar that the Co and CoFe nanoparticles display a paramagnetic nature with such low values for $M_s$ since it was expected that these particles would display a superparamagnetic nature. The paramagnetic nature that is observed could be reconciled by assuming that the particles may have completely oxidized into an amorphous phase during the shipment process, as the particles had to be shipped to a collaborator for the magnetic hysteresis to be recorded. To be safe, the saturation magnetization of these particles should be double checked in a manner that ensures there is no oxidation. The other four samples (Co, Ni, CoNi, and $FeNi_2$) display a superparamagnetic nature as expected. The hysteresis curves reveal coercivities of 41.15 (Fe), 16.07 (Co), 0.39 (Ni), 41.70 (CoFe), 1.39 (CoNi), and 474.24 ($FeNi_2$) Oe. It is worthy to note that the smaller size nanoparticles in this study exhibit coercivities that are much lower than that of bulk materials, again due to the nanoscale size of the materials. This could be due to special morphology-related shape anisotropy when considering the sub-domain size of these nanoparticles.[38] All measured

particles besides $FeNi_2$ display superparamagnetic coercivity values as expected. The $FeNi_2$ nanoparticles display a slightly ferromagnetic coercivity, which is expected from established reports.

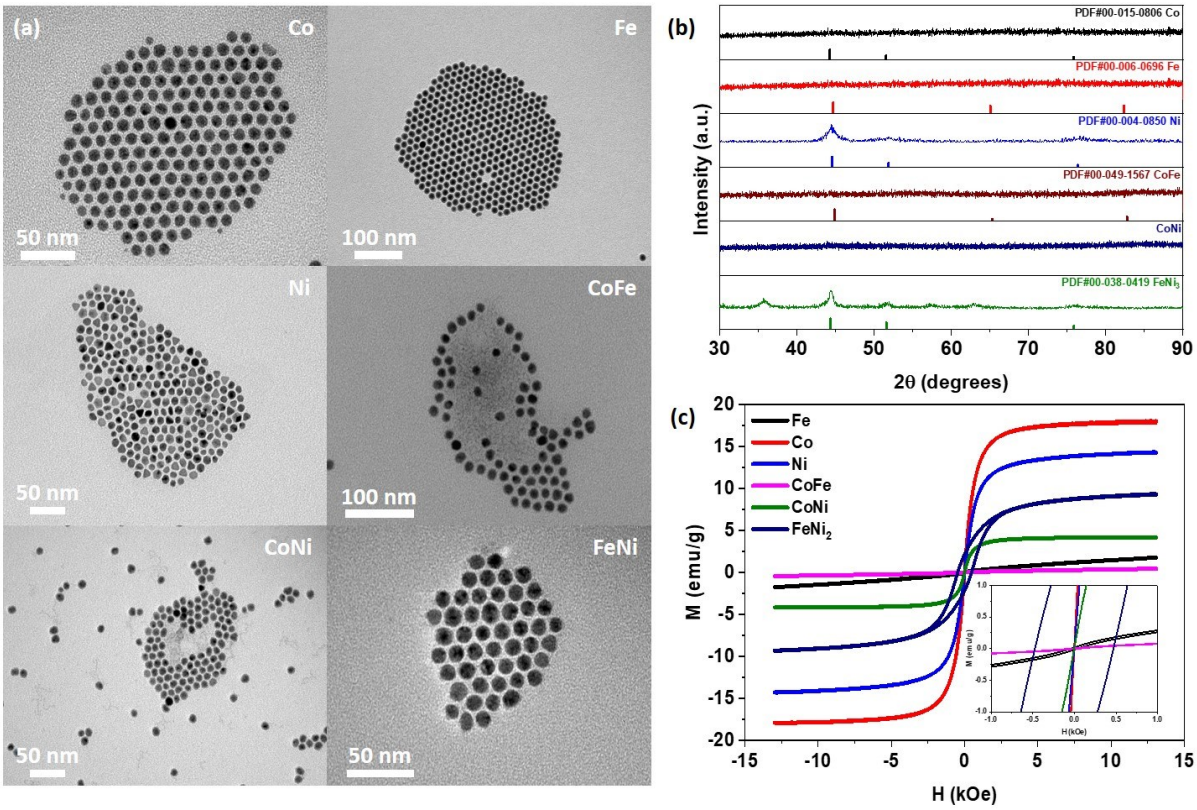


**Figure 4.1.** (a) TEM images, (b) XRD patterns and (c) hysteresis loops of ~10 nm alloyed nanoparticles.

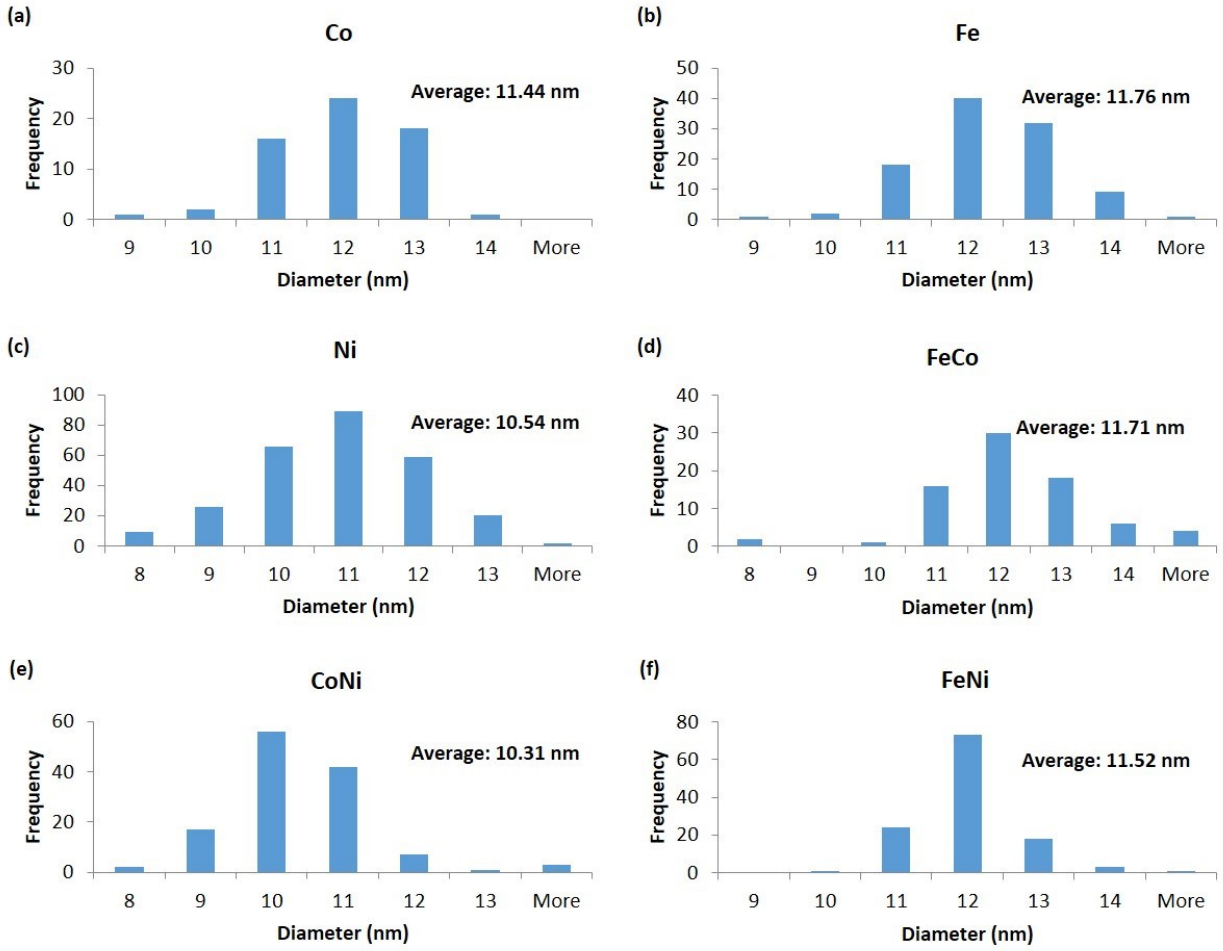


**Figure 4.2.** Size distribution profiles for 10-12 nm (a) Co, (b) Fe, (c) Ni, (d) FeCo, (e) CoNi, and (f) $FeNi_2$ nanoparticles.

### 4.3.2 Discussion of Electromagnetic Measurements

Figure 4.3 shows a typical data output using 10 nm Fe nanoparticles at a 40 vol% loading. Figure 4.3(a) shows the reflection loss (RL) data for varying thicknesses (1 mm – 6 mm) of 10 nm Fe/paraffin wax composites at a 40 vol% nanoparticle loading. The relationship between the reflection loss of the Fe/paraffin wax composite and frequency is calculated as follows:

$$Z_{in} = \sqrt{\frac{\mu_r}{\varepsilon_r}} \tanh j\left[\frac{2\pi f d\sqrt{\mu_r \varepsilon_r}}{c}\right] \quad (1)$$

$$R_L = 20log\left|\frac{Z_{in}-1}{Z_{in}+1}\right| \quad (2)$$

where $\varepsilon_r$ and $\mu_r$ are the relative complex permittivity and permeability of the wax composite, $c$ is the speed of light, $f$ is the frequency and $d$ is the thickness of the absorbing material. As shown in Figure 4.3(a), RL absorption peaks for 10 nm Fe at a 40 vol% loading across all thickness on a 0.5 mm interval from 1 mm to 6 mm can be seen with a local maximum absorption of -28.89 dB at 4.33 GHz corresponding to a 6 mm thickness. Figure 4.3(b) shows the real and imaginary portions of the complex permittivity and permeability across the frequency range from 2 GHz – 18 GHz for 10 nm Fe nanoparticles at a 40 vol% loading. In general, the values of both the real ($\varepsilon'$, $\mu'$) and imaginary ($\varepsilon''$, $\mu''$) portions of the complex permittivity and permeability gradually decrease with increasing frequency. For both imaginary portions, $\varepsilon''$ and $\mu''$, a much sharper decrease can be seen early on in the frequency range, from 2 GHz < $f$ < 4 GHz. Negative values in both $\varepsilon''$ and $\mu''$ may come from errors in the instrument measurement system.[39]

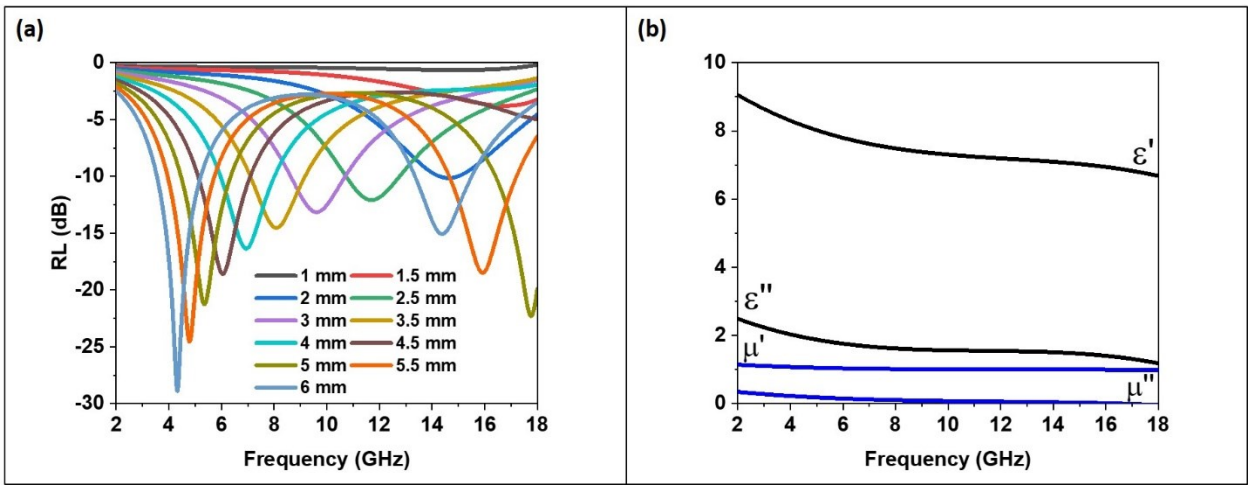


**Figure 4.3** (a) Reflection loss for varying thicknesses (1 mm – 6 mm) of 10 nm Fe/paraffin wax composites at 40 vol% nanoparticle loading. (b) Complex permittivity and permeability values for 40 vol% 10 nm $Fe_3O_4$/paraffin wax composites at a 1 mm thickness.

Figures 4.4, 4.5, and 4.6 show the raw reflection loss (RL) data for all loadings of magnetic metal and metal alloys across all nanoparticle loadings (15, 30, and 40 vol%). The previous discussion concerning Figure 4.3 can be applied to any specific size and loading in Figures 4.4, 4.5, and 4.6.

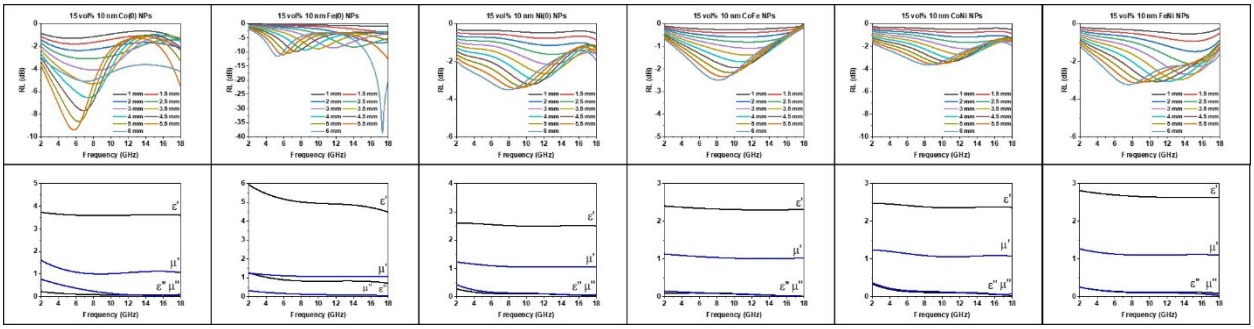

**Figure 4.4.** Raw RL Data for Alloyed Nanoparticles at 15 vol% Loading.

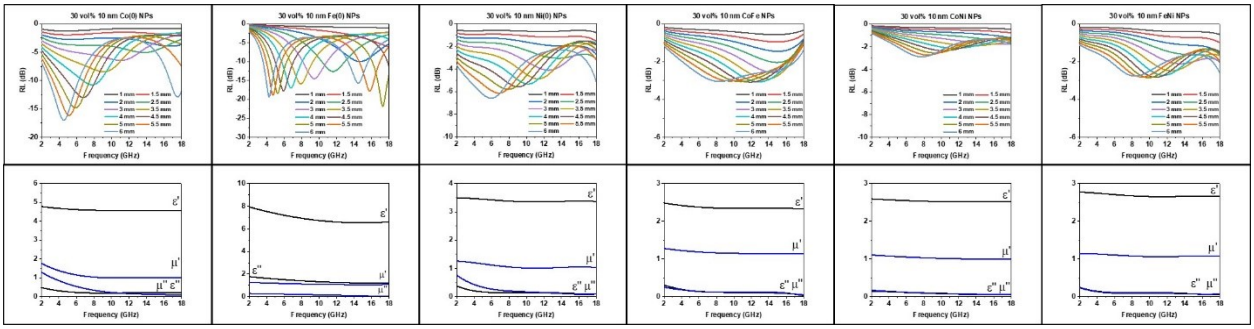


**Figure 4.5.** Raw RL Data for Alloyed Nanoparticles at 30 vol% Loading.

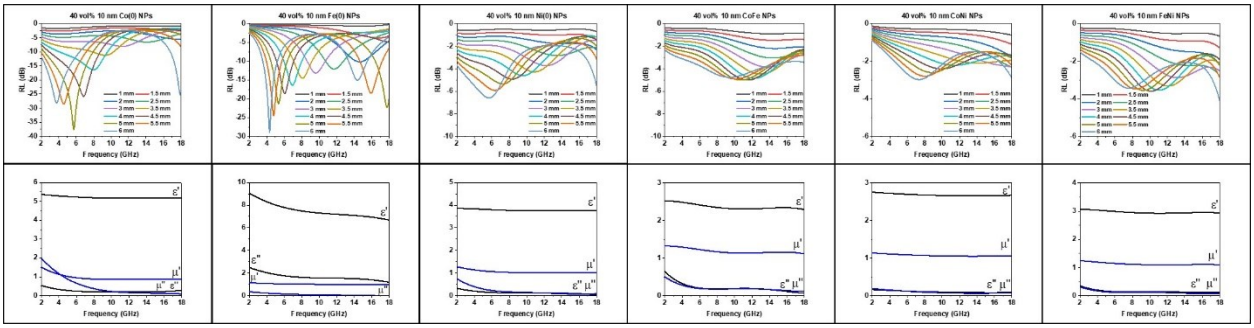


**Figure 4.6.** Raw RL Data for Alloyed Nanoparticles at 40 vol% Loading.

Once again, it is necessary to discern the primary mechanism (magnetic or dielectric) for electromagnetic wave absorption displayed by the alloyed nanoparticles in this study. Figures 4.7 and 4.8 display the magnetic and dielectric loss tangents for the nanoparticles studied:

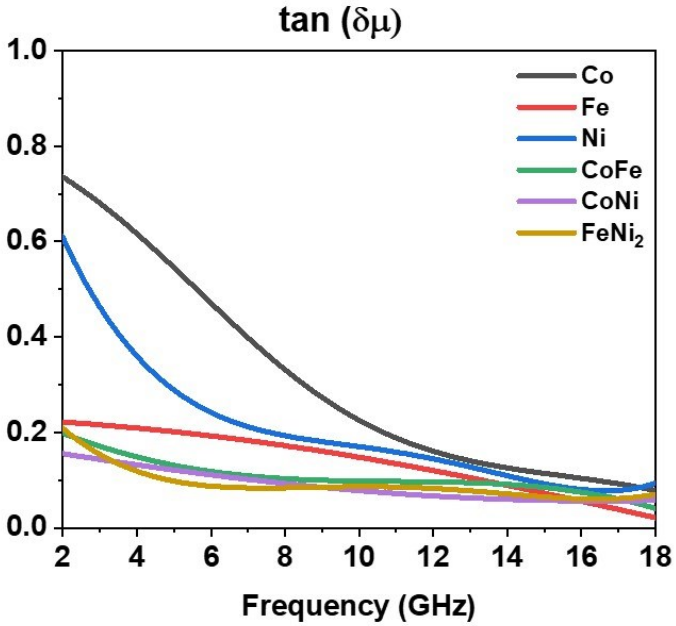


**Figure 4.7.** The magnetic loss tangent, tan(μ″/μ′), for 10 nm Co, Fe, Ni, CoFe, CoNi, and $FeNi_2$ nanoparticles.

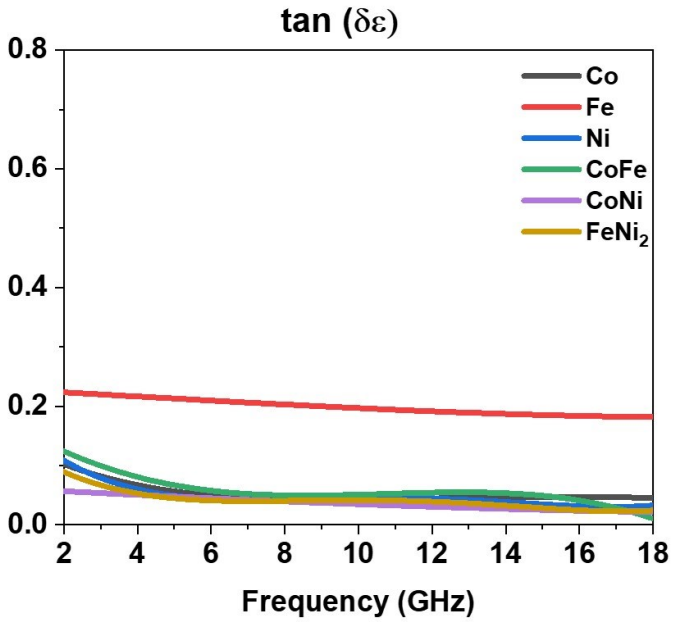


**Figure 4.8.** The dielectric loss tangent, tan(ε″/ε′), for 10 nm Co, Fe, Ni, CoFe, CoNi, and $FeNi_2$ nanoparticles.

As demonstrated in the Figures 4.7 and 4.8, the values of the magnetic loss tangents are much larger than the dielectric loss tangents across the entire frequency range for all nanoparticles studied, indicating that the absorption mechanism is predominantly controlled by the magnetic properties, rather than the dielectric properties.

### 4.3.3 Nanoparticle Loading Dependence Effects on Electromagnetic Wave Absorption

The effects of loading dependence on the materials properties and reflection loss data of the system were measured at varying loadings of 15, 30 and 40 vol% for all metal (Co, Fe, Ni) and metal alloy (CoFe, CoNi, FeNi) nanoparticle samples and the data analyzed for trends. Figure 4.9 shows the effect of nanoparticle loading on the intensity of electromagnetic wave absorption (Figure 4.9(a)), the complex permittivity, and the complex permeability (Figure 4.9(b)) of 10 nm Co nanoparticles in a toroid of 4 mm thickness. In agreement with previous studies and the data presented in Chapters 2 and 3 of this dissertation, it is shown that as nanoparticle loading increases, $\varepsilon'$, $\varepsilon''$, $\mu'$ and $\mu''$ all increase as well.[39,40] The reasoning behind this phenomena is explained by the fact that as the loading of the sample increases, the overall volume of nanoparticles increases as well, thus increasing the effective permittivity and permeability of the material. Holding true to this, it is observed that as the nanoparticle loading is increased, the complex permittivity and permeability increase as well, thus increasing the intensity of electromagnetic wave absorption and decreasing the maximum absorption frequency.

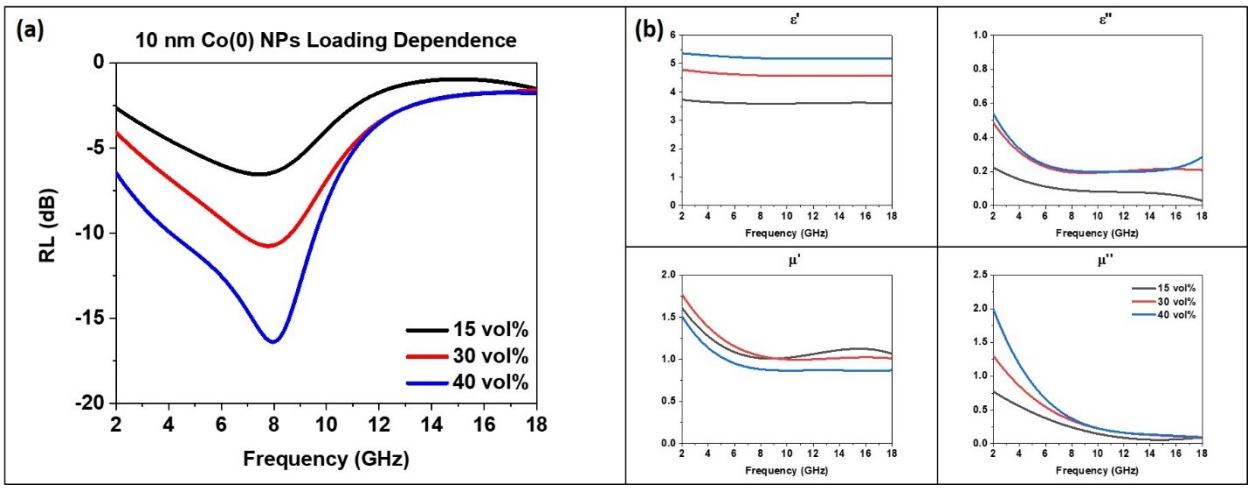


**Figure 4.9.** (a) Reflection loss for varying nanoparticle loadings (15, 30, and 40 vol%) of 10 nm Co/paraffin wax composites at a 4 mm thickness. (b) Visualization of the effect of loading on the real and imaginary portions of the permittivity and permeability of 10 nm Co nanoparticles.

Figures 4.10 – 4.14 show the effect of loading on the reflection loss (RL) data for 10 nm Fe, Ni, CoFe, CoNi, and $FeNi_2$ across all nanoparticle loadings (15, 30, and 40 vol%), respectively. The previous discussion concerning the 10 nm Co can be applied to any specific size and loading as demonstrated in Figures 4.10 – 4.14.

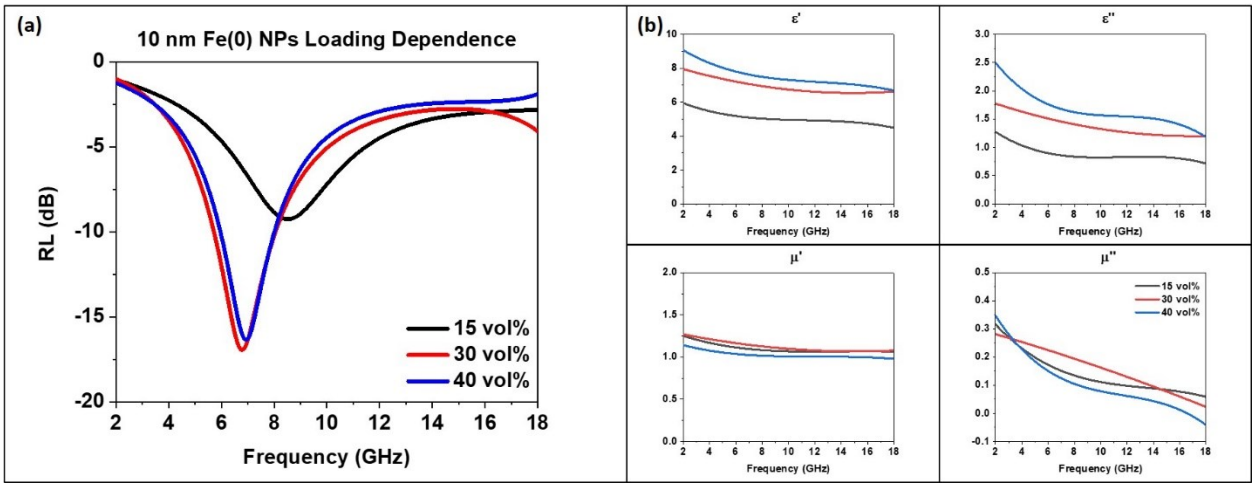


**Figure 4.10.** (a) Reflection loss for varying nanoparticle loadings (15, 30, and 40 vol%) of 10 nm Fe/paraffin wax composites at a 4 mm thickness. (b) Visualization of the effect of loading on the real and imaginary portions of the permittivity and permeability of 10 nm Fe nanoparticles.

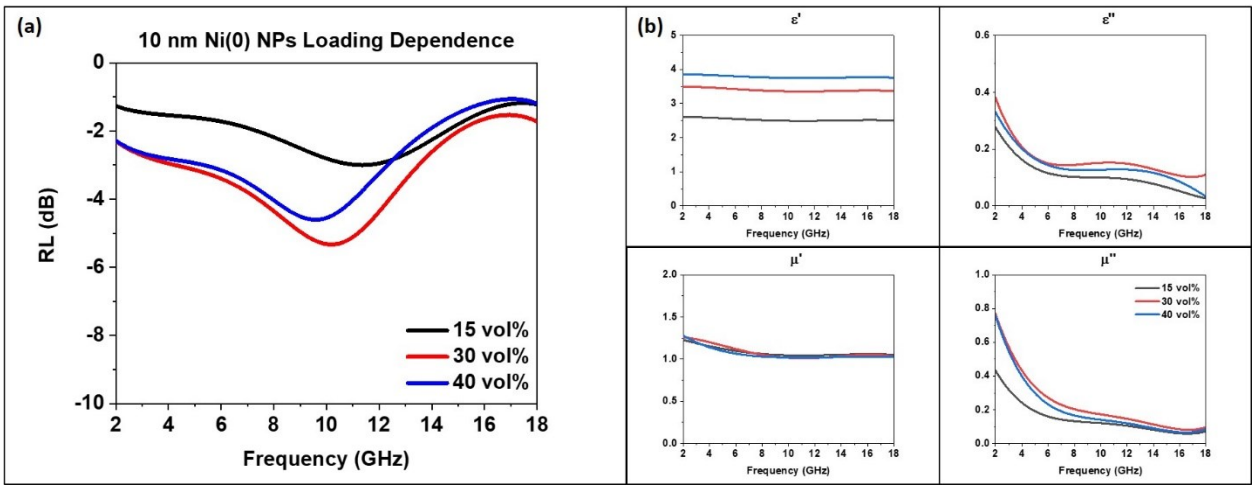


**Figure 4.11.** (a) Reflection loss for varying nanoparticle loadings (15, 30, and 40 vol%) of 10 nm Ni/paraffin wax composites at a 4 mm thickness. (b) Visualization of the effect of loading on the real and imaginary portions of the permittivity and permeability of 10 nm Ni nanoparticles.

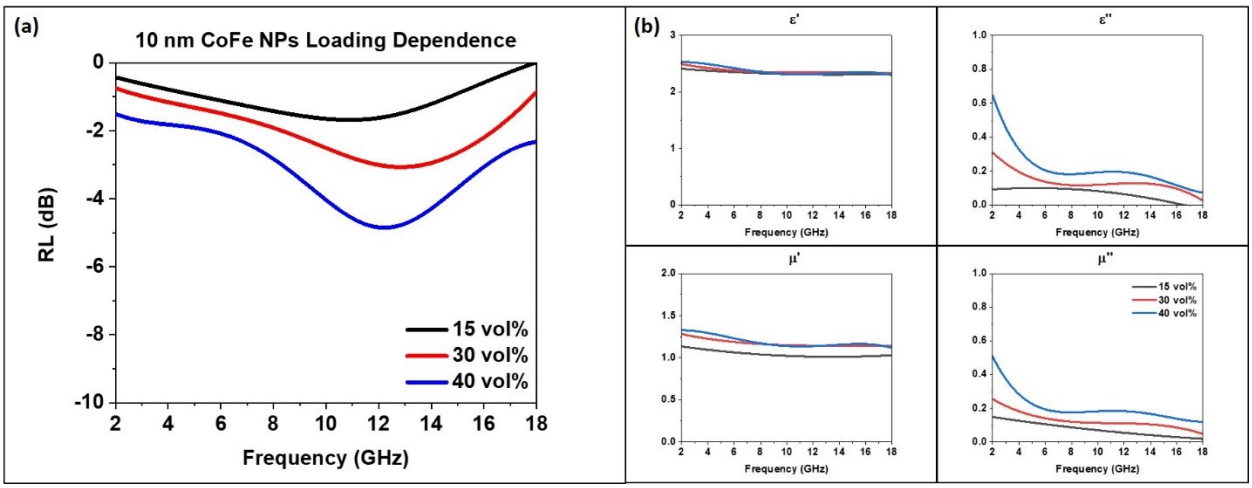


**Figure 4.12.** (a) Reflection loss for varying nanoparticle loadings (15, 30, and 40 vol%) of 10 nm CoFe/paraffin wax composites at a 4 mm thickness. (b) Visualization of the effect of loading on the real and imaginary portions of the permittivity and permeability of 10 nm CoFe nanoparticles.

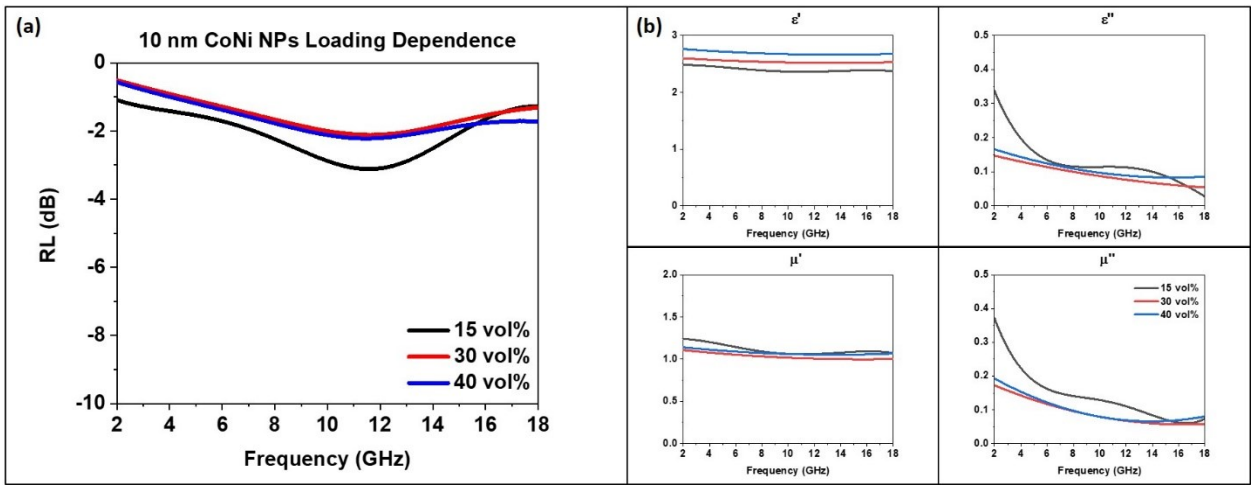


**Figure 4.13.** (a) Reflection loss for varying nanoparticle loadings (15, 30, and 40 vol%) of 10 nm CoNi/paraffin wax composites at a 4 mm thickness. (b) Visualization of the effect of loading on the real and imaginary portions of the permittivity and permeability of 10 nm CoNi nanoparticles.

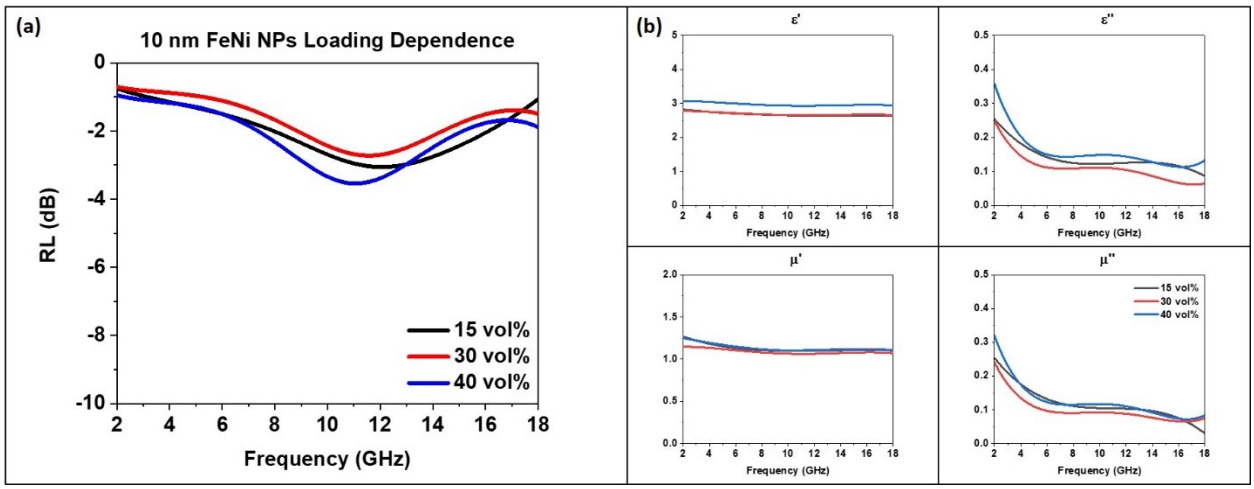


**Figure 4.14.** (a) Reflection loss for varying nanoparticle loadings (15, 30, and 40 vol%) of 10 nm FeNi/paraffin wax composites at a 4 mm thickness. (b) Visualization of the effect of loading on the real and imaginary portions of the permittivity and permeability of 10 nm FeNi nanoparticles.

### 4.3.4 Alloying Dependence Effects on Electromagnetic Wave Absorption

To determine the effect of alloying on the maximum absorption frequencies of the metal/metal alloy systems, all metal and metal alloy nanoparticles were measured at varying loadings of 15, 30 and 40 vol% and the data compared, holding the loading percentage constant. Figure 4.15 (a) and (c) display the effect of alloying on the RL peak resonant frequency for all studied metal and metal alloy nanoparticle series at a 4 mm toroid thickness, with a 30 vol% loading and 40 vol% loading, respectively.

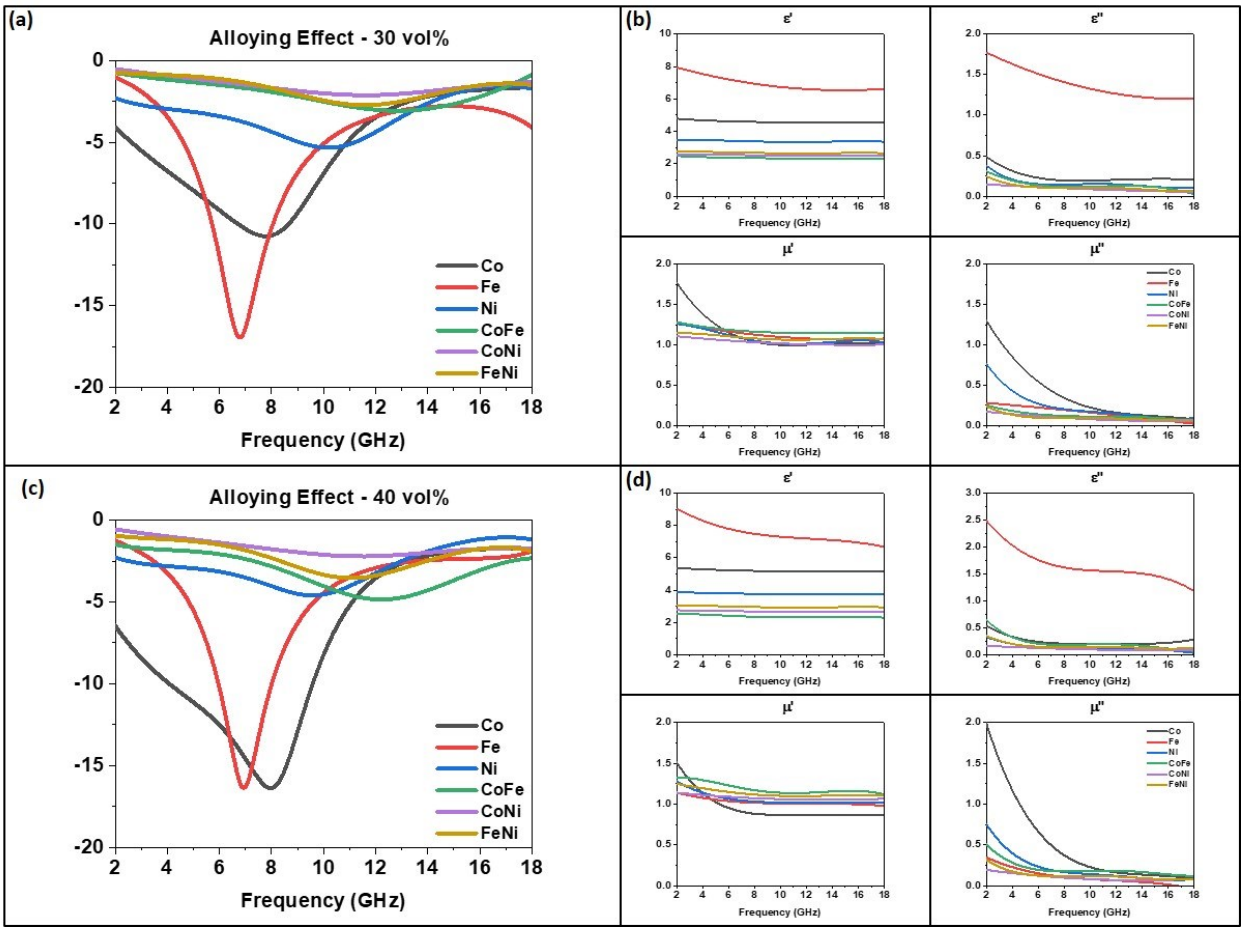


**Figure 4.15.** (a) Illustration of the effect of alloying on the reflection loss resonant frequency for samples of 4 mm thickness and 30 vol% loading. (b) Illustration of the effect of ferrite type on the real and imaginary portions of the permittivity and permeability of alloyed nanoparticles at 30 vol% loading. (c) Illustration of the effect of alloying on the reflection loss resonant frequency for samples of 4 mm thickness and 40 vol% loading. (d) Illustration of the effect of alloying on the real and imaginary portions of the permittivity and permeability of alloyed nanoparticles at 40 vol% loading.

As shown in Figure 4.15 (a) and (c), the trend for RL resonant electromagnetic wave absorption frequency, listed in order of increasing resonant frequency, is as follows: Fe < Co < Ni < $FeNi_2$ ≈ CoNi < CoFe. The results of the specific peak positions for 4 mm thick wax/nanoparticle composite toroids across all loadings are summarized in Table 4.2 below:

**Table 4.2.** Alloying Effects on Resonant Frequency of Electromagnetic Wave Absorption.

| Loading in Wax Composite | Fe | Co | Ni | CoFe | CoNi | $FeNi_2$ |
|---|---|---|---|---|---|---|
| 15 vol% | 8.51 GHz | 7.44 GHz | 11.33 GHz | 10.91 GHz | 11.60 GHz | 12.05 GHz |
| 30 vol% | 6.77 GHz | 7.80 GHz | 10.21 GHz | 12.79 GHz | 11.53 GHz | 11.60 GHz |
| 40 vol% | 6.92 GHz | 7.95 GHz | 9.54 GHz | 12.18 GHz | 11.53 GHz | 11.02 GHz |

Specifically, taking the 40 vol% loading data into consideration, we see the resonance peaks at 6.92 GHz for Fe, 7.95 GHz for Co, 9.54 GHz for Ni, 11.02 GHz for $FeNi_2$, 11.53 GHz for CoNi, and 12.18 GHz for CoFe. CoNi and $FeNi_2$ have been described as roughly equal to each other as the maximum absorption frequencies for these materials fall within ~0.5 GHz of one another across all loadings, and the ordering of the positioning of the maximum absorption frequencies varies slightly.

The previously described trend, again listed in order of increasing resonant frequency, : Fe < Co < Ni < $FeNi_2$ ≈ CoNi < CoFe, holds true for all loading percentages aside from two slight deviations in the 15 vol% dataset, where the Co and CoFe nanoparticles are out of position. In fact, Co displays lowest maximum absorption frequency in the 15 vol% dataset (second lowest in the 30 vol% and 40 vol% datasets) while CoFe displays the third lowest maximum absorption frequency (highest in the 30 vol% and 40 vol% datasets) with values of 7.44 GHz and 10.91 GHz, respectively. These deviations from the trend are difficult to explain, but could be due to varying degrees of aggregation of particles during the sample preparation stage, resulting in an altered effective size and thus, a different maximum absorption frequency. It is tough to gauge the degree of aggregation in the paraffin wax composites as most x-ray or electron beam imaging techniques will melt the wax, causing damage to instruments. An appropriate imaging technique for this purpose has not yet been thought of. The relationship

between the size of a particle and absorption frequency has been discussed in Chapters 2 and 3, as well as a prior publication.[40]

Similarly, to determine the effect of alloying on the intensity of electromagnetic absorption for the metal/metal alloy systems, all metal and metal alloy nanoparticles were measured at varying loadings of 15, 30 and 40 vol% and the data compared, holding the loading percentage constant. Figure 4.15 (a) and 4 (c) display the effect of alloying on the intensity of electromagnetic absorption for all studied metal and metal alloy nanoparticle series at a 4 mm toroid thickness, with a 30 vol% loading and 40 vol% loading, respectively. As shown in Figure 4.15 (a) and (c), the trend for RL resonant electromagnetic wave absorption intensity, listed in order of increasing intensity of electromagnetic wave absorption, is as follows: CoNi ≈ CoFe ≈ $FeNi_2$ ≈ Ni < Co < Fe. The results of the specific peak intensities for 4 mm thick wax/nanoparticle composite toroids across all loadings are summarized in Table 4.3 below:

**Table 4.3.** Alloying Effects on Intensity of Electromagnetic Wave Absorption.

| **Loading in Wax Composite** | **Fe** | **Co** | **Ni** | **CoFe** | **CoNi** | **$FeNi_2$** |
|---|---|---|---|---|---|---|
| 15 vol% | -9.26 dB | -6.54 dB | -3.00 dB | -1.68 dB | -3.12 dB | -3.06 dB |
| 30 vol% | -16.94 dB | -10.74 dB | -5.33 dB | -3.07 dB | -2.12 dB | -2.72 dB |
| 40 vol% | -16.35 dB | -16.38 dB | -4.61 dB | -4.85 dB | -2.22 dB | 3.54 dB |

Taking the 30 vol% loading data into consideration, we see maximum electromagnetic absorption intensities of -16.94 dB for Fe, -10.74 dB for Co, -5.33 dB for Ni, -3.07 dB for CoFe, -2.72 dB for $FeNi_2$, and -2.12 dB for CoNi. Across all measured loadings, the Co and Fe nanoparticles are by far the most effective electromagnetic absorbers. There are no apparent trends amongst Ni, CoFe, CoNi, and $FeNi_2$, aside from all four displaying ineffective absorption intensities of below -6 dB across all loadings. In fact, the highest absorption intensity amongst

the four, -5.44 dB at a 30 vol% loading of Ni, is still less effective than the lowest observed absorption intensity for either Co or Fe: -6.54 dB at a 15 vol% loading of Co nanoparticles.

Figures 4.15 (b) and 4 (d) display the effect of alloying on the real and imaginary portions of the permittivity and permeability for all measured ferrite nanoparticles at a 1 mm toroid thickness, with a 30 vol% loading and 40 vol% loading, respectively. The trends can be seen in each plot in Figures 4.15 (b) and (d), but the generalized trends are summarized in Table 4.4 below:

**Table 4.4.** Ferrite-Based Nanoparticle Trends in Complex Permittivity and Permeability.

| **Material Property** | **Trend** |
|---|---|
| Real Permittivity ($\varepsilon'$) | Fe > Co> Ni > $FeNi_2$ ≈ CoNi ≈ CoFe |
| Imaginary Permittivity ($\varepsilon''$) | Fe > Co> Ni > $FeNi_2$ ≈ CoNi ≈ CoFe |
| Real Permeability ($\mu'$) | No trend |
| Imaginary Permeability ($\mu''$) | Co > Ni > Fe ≈ CoFe ≈ CoNi ≈ $FeNi_2$ |
| Frequency of Reflection Loss Peak (RL) | Fe > Co > Ni > $FeNi_2$ ≈ CoNi ≈ CoFe |

Figure 4.16 (a) displays the effect of doping on the RL peak intensity and resonant frequency and Figure 4.16 (b) displays the effect of alloying on the real and imaginary portions of the permittivity and permeability for 10 nm magnetic metal and metal alloy nanoparticles at a 4 mm toroid thickness, with a 15 vol% loading. The previous discussion on alloying effects can be applied to the alloy nanoparticles at 15 vol% loading as well.

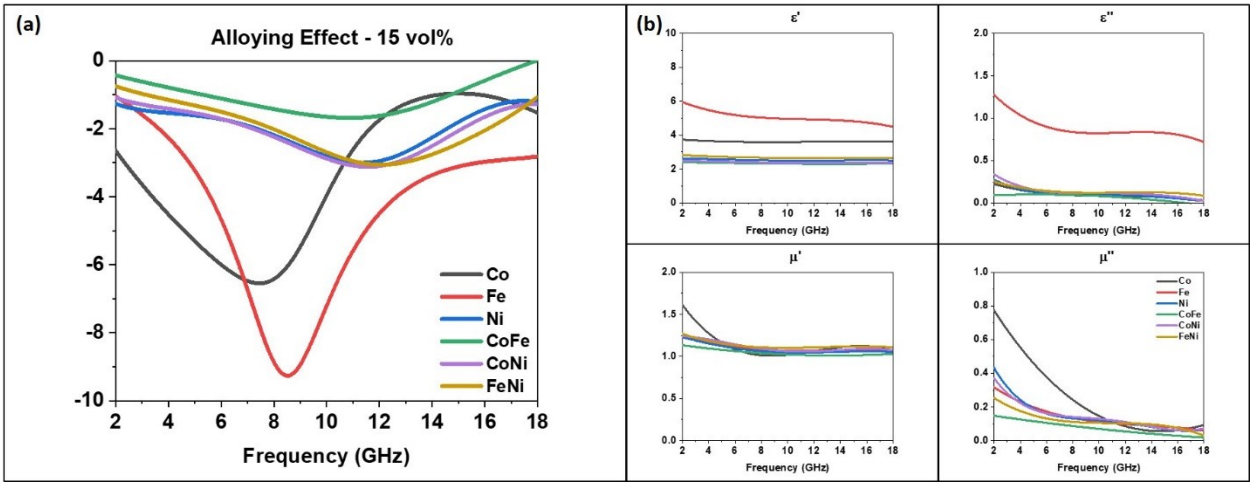


**Figure 4.16.** (a) Illustration of the effect of alloying on the reflection loss resonant frequency for samples of 4 mm thickness and 15 vol% loading. (b) Illustration of the effect of ferrite type on the real and imaginary portions of the permittivity and permeability of alloyed nanoparticles at 15 vol% loading.

Explaining the apparent trends (or lack thereof) in the real and imaginary permittivity and permeability of nanoscale metals and metal alloys is a topic that has received little attention. In previous reports and in Chapters 2 and 3, we have detailed the conceptual understanding of the complex permittivity and permeability.[40,41] Briefly, the real permittivity is thought of as the ability of a material to store electrical energy in an electrical field and the imaginary permittivity is the dielectric loss of the material, dependent on conductivity. The real permeability is defined as the ability of a material to align its magnetic moment to an external magnetic field and the imaginary permeability is the measure of the rotation of a material around its easy axis. Our data shows the following trend for the complex permittivity and the reflection loss frequency: Fe > Co > Ni > $FeNi_2$ ≈ CoNi ≈ CoFe. Similar to our previous study regarding the radar absorption properties of a series of ferrites, we can see from the trends described above that this result strongly indicates that the dielectric properties of metals and metal alloys have more influence of

their electromagnetic absorption behavior than the magnetic properties do.[41] This conclusion is further supported in literature as it has been previously reported that an increase in imaginary permittivity, ε″, causes a decrease in absorption frequency.[42]

The same discussion from our previous studies in Chapters 2 and 3 apply when looking at the influence of the magnetic properties on the electromagnetic absorption behavior of the metals and metal alloys under study. According to our previous study concerning the effect of nanoparticle size on electromagnetic absorption behavior, we have determined that as the size of a nanoparticle increases, the imaginary permeability increases, and thus the frequency of absorption is shifted to lower values. This trend is explained through the Landau-Lifshitz-Gilbert equation (LLG) as discussed in our previous work.[40] In the current study, all of the nanoparticles have a very similar size of ~ 10 nm. With no definitive changes in the size of the particles under study, it makes sense that we may not see a large variation in the value of the imaginary permeability, and in turn, a weak influence on the electromagnetic absorption behavior. This phenomenon can be seen visually from Figure 4.15(b) and 4.15(d) when taking into account that the magnitude of the difference from the highest to lowest imaginary permeability (~0.5) is much less than that of the real or imaginary permittivity (~6.0 and ~1.5, respectively). Since there is not a large variation in the imaginary permeability of the nanomaterials under study, it follows that we would not see a large influence from the magnetic properties on the absorption frequencies, while the dielectrics dominate this behavior due to the large variation among samples.

As previously stated and discussed in Chapters 2 and 3, the real permeability is dependent upon the crystallinity of each sample rather than the magnetization or size of the material.[40] Again, as all of the samples under study are of the same size it follows that their

crystal sizes are very similar as well. This explains the lack of an apparent trend amongst the varying ferrites in this study. Mathematically, the explanation for this lack of trend can be seen by looking at the real permeability caused by the Néel relaxation of a material in the superparamagnetic state[43]:

$$\mu' = \mu_0 \left(1 + \frac{V_p M_0^2}{3 k_B T}\right) \quad (3)$$

where $V_p$ is the volume of the nanoparticle, $M_0$ is the saturation magnetization, $k_B$ is the Boltzmann constant and $T$ is the temperature. Since $\frac{V_p M_0^2}{3 k_B T}$ will be an extremely small number ($V_p M_0^2 << 3K_B T$ and $\frac{V_p M_0^2}{3 k_B T} << 1$), any change in volume will have a negligent effect on μ′.

### 4.3.5 Theoretical Model for the Calculation of the Effective Permeability

The effective permeability has been modeled following procedures established by R.F. Soohoo and described by Wu et al. in a previous report.[21,44] This was discussed in detail in Chapter 2. As previously stated, the resulting calculated $\mu_{eff}$ from this procedure is valid for single domain particles. The critical size for common materials has been reported to be well over the studied particle size of 10 nm, indicating that all particles in this study can be modeled using this approach.[45]

Figure 4.17 shows the agreement between the measured and simulated effective complex permeability for 10 nm Fe nanoparticles at a (a) 15 vol%, (b) 30 vol%, and (c) 40 vol% loading. The agreement between the experimental and simulated values is acceptable, indicating that the magnetic nanoparticle/wax composites behave according to standard mixing theories. The experimental and simulated curves have roughly the same curve shape, however are slightly off

in magnitude. This could be due to experimental conditions that were unaccounted for in the simulations.[44]

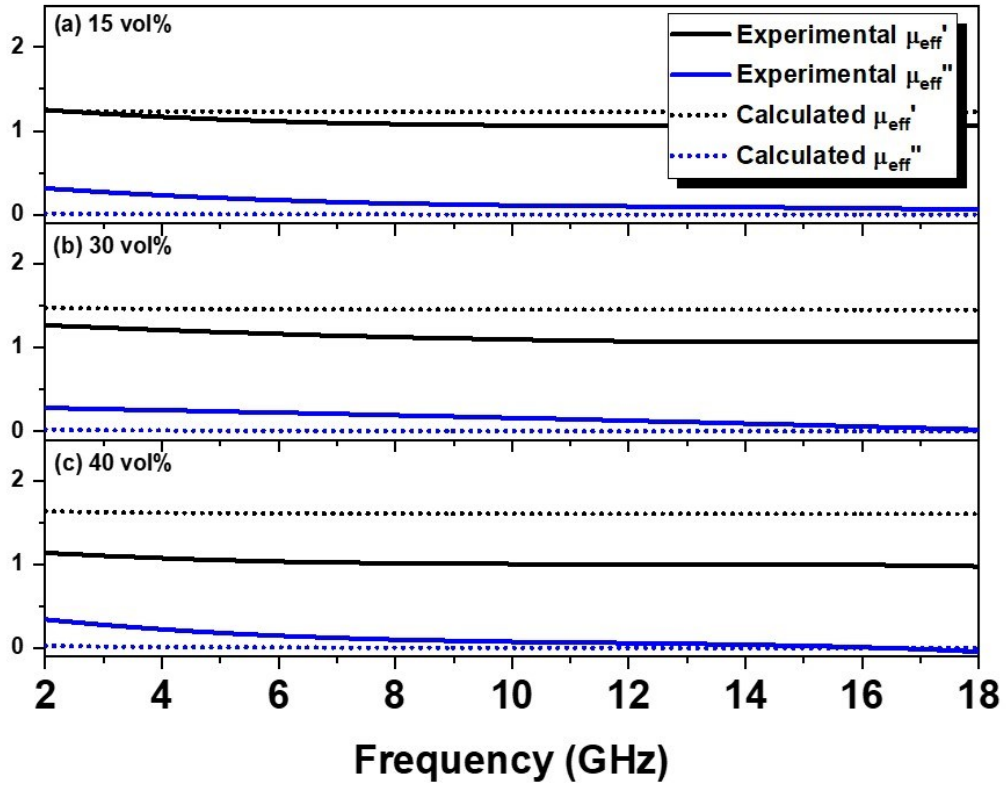


**Figure 4.17.** Calculated real part, μ′, and imaginary part, μ″, of the complex effective permeability for 10 nm Fe nanoparticles at volume fractions of (a) 15 vol%, (b) 30 vol%, and (c) 40 vol%.

Simulation results for all other sizes and loadings of alloyed nanoparticles are shown in Figures 4.18 – 4.22.

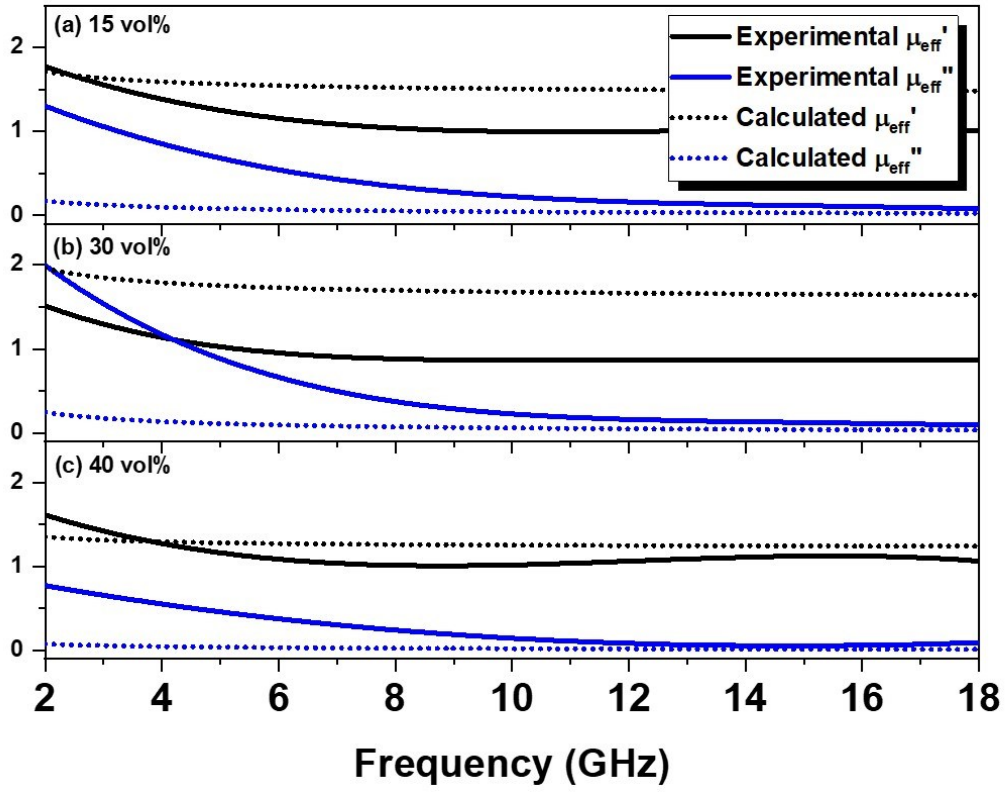


**Figure 4.18.** Calculated real part, μ′, and imaginary part, μ″, of the complex effective permeability for 10 nm Co nanoparticles at volume fractions of (a) 15 vol%, (b) 30 vol%, and (c) 40 vol%.

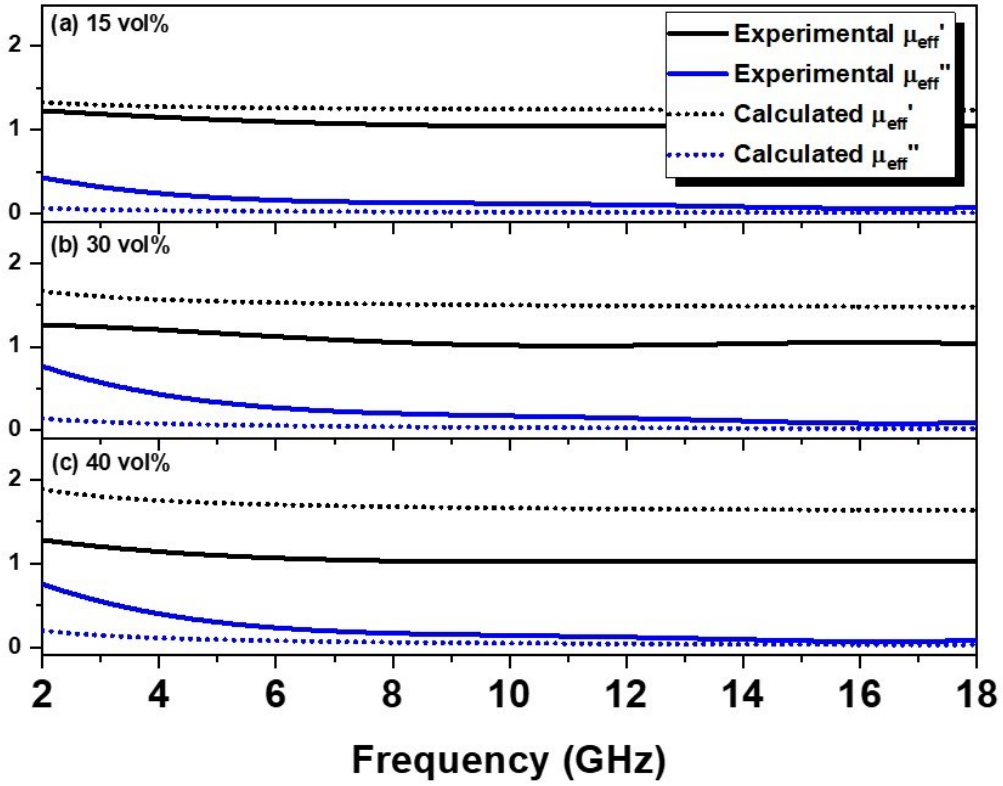


**Figure 4.19.** Calculated real part, μ′, and imaginary part, μ″, of the complex effective permeability for 10 nm Ni nanoparticles at volume fractions of (a) 15 vol%, (b) 30 vol%, and (c) 40 vol%.

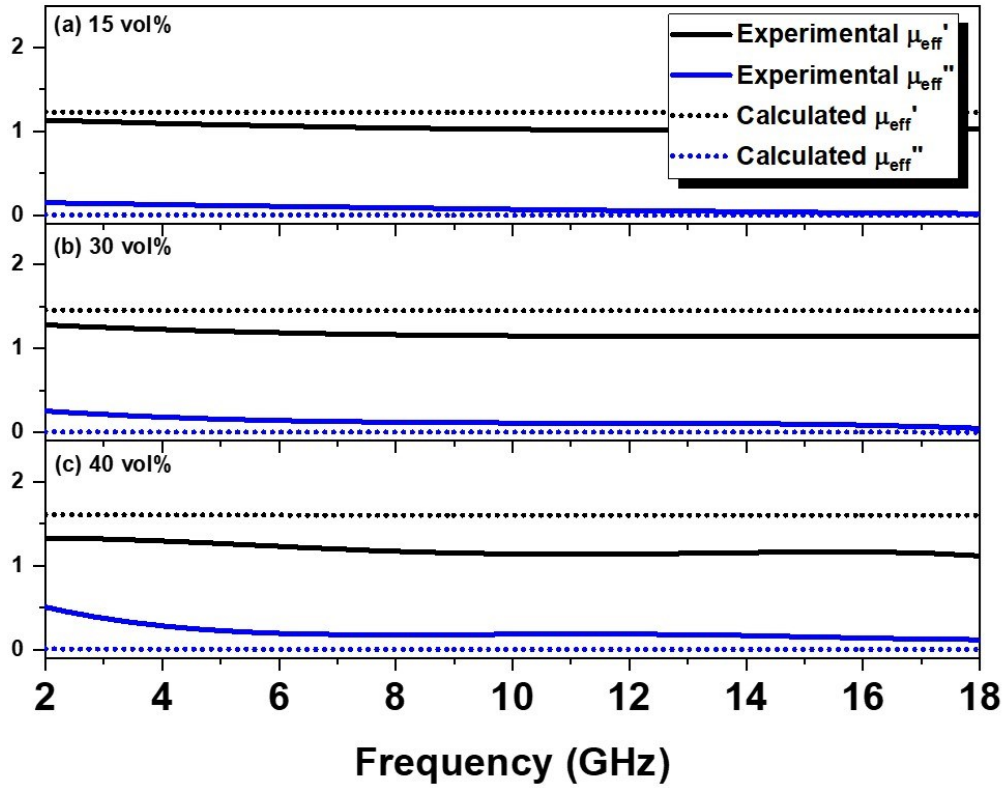


**Figure 4.20.** Calculated real part, μ′, and imaginary part, μ″, of the complex effective permeability for 10 nm CoFe nanoparticles at volume fractions of (a) 15 vol%, (b) 30 vol%, and (c) 40 vol%.

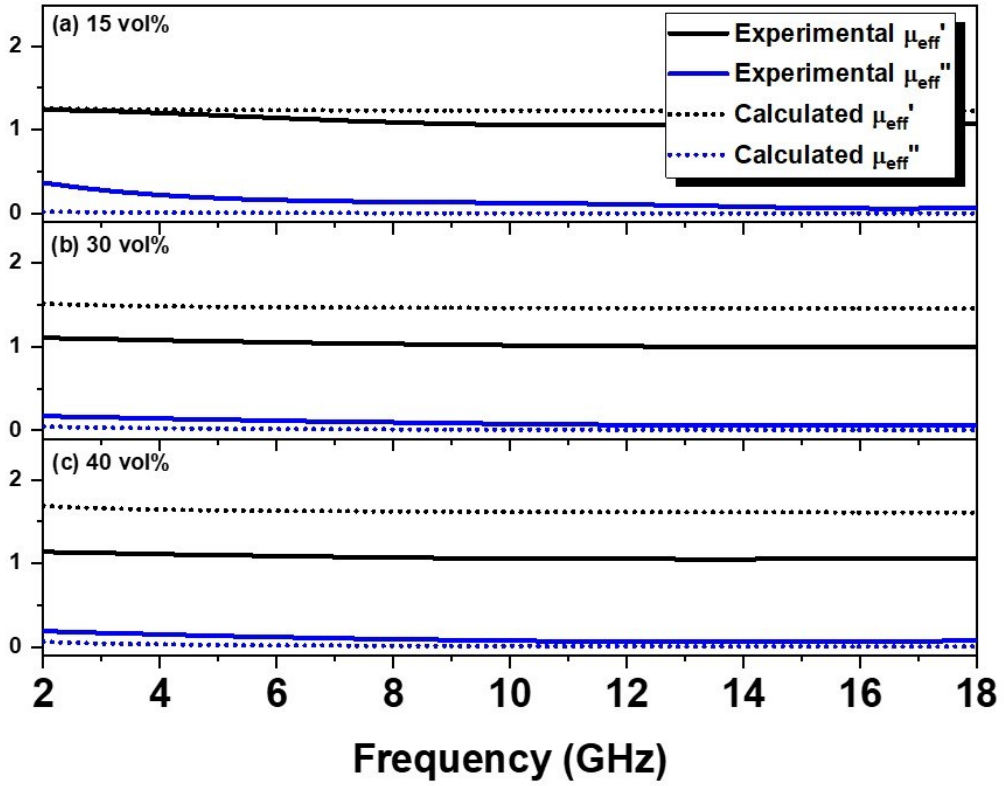


**Figure 4.21.** Calculated real part, μ′, and imaginary part, μ″, of the complex effective permeability for 10 nm CoNi nanoparticles at volume fractions of (a) 15 vol%, (b) 30 vol%, and (c) 40 vol%.

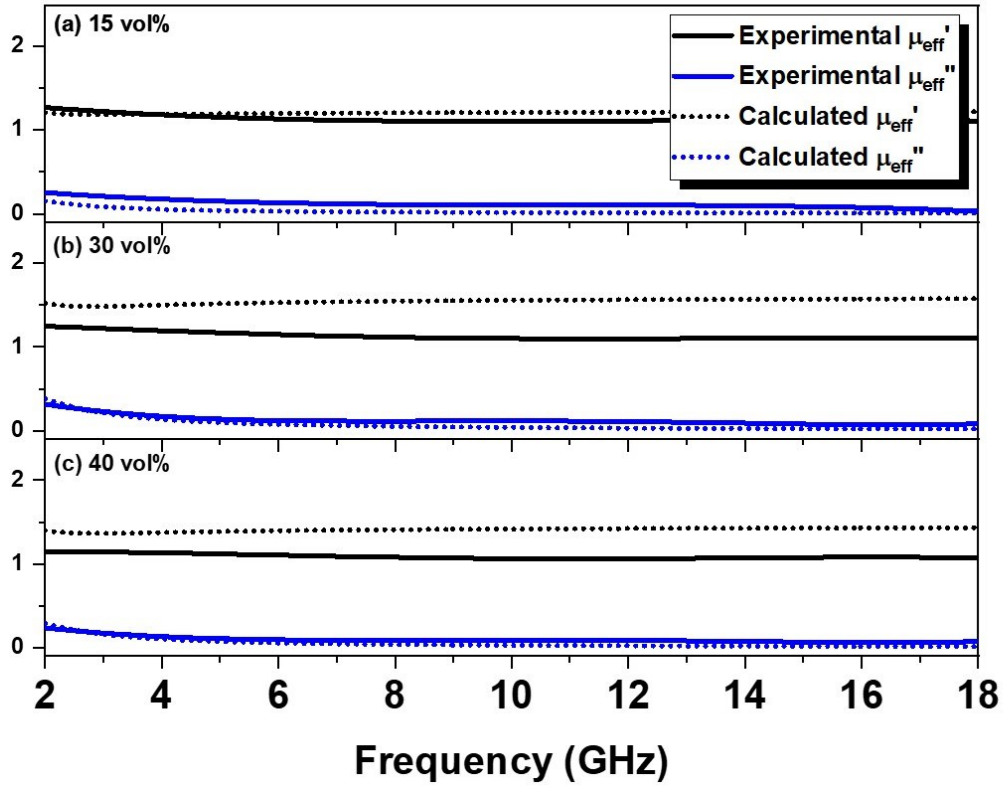


**Figure 4.22.** Calculated real part, μ′, and imaginary part, μ″, of the complex effective permeability for 10 nm $FeNi_2$ nanoparticles at volume fractions of (a) 15 vol%, (b) 30 vol%, and (c) 40 vol%.

## 4.4 CONCLUSIONS

In conclusion, new and existing methods for the synthesis of Co, Fe, Ni, CoFe, CoNi, and $FeNi_2$ nanoparticles via organic solution synthesis and thermal decomposition of the corresponding metal acetylacetonates have been implemented to produce nanoparticles of size 10 nm. The dielectric, magnetic and microwave absorption properties of the series of ferrites have been carefully investigated. Our analysis has revealed that alloys of such small sizes are weak microwave absorbers in the frequency range from 2 – 18 GHz. In general, the magnetic hysteresis of the particles studied displays a superparamagnetic nature aside from a few exceptions that may need to be re-measured. In addition, the data gives reason to believe that the microwave absorption properties of these magnetic metals and their alloys are largely governed by the dielectric behavior of the material rather than the magnetic behavior. This study should be considered with the aim of developing a library of the microwave absorption behavior of common magnetic nanomaterials in order to increase the available fundamental knowledge of microwave absorbing materials.

## 4.5 REFERENCES


1. B.S. Murty, J.W. Yeh & S. Ranganathan. *High-Entropy Alloys*. (Elsevier Inc., 2014).
2. Arthur C. Reardon. *Metallurgy for the Non-Metallurgist*. (ASM International, 2011).
3. G.G. Gnesin. Metals and Alloys of the Bronze Age: From Middle to Modern Times. *Powder Metallurgy and Metal Ceramics* **53**, (2014).
4. Miljana Radivojevic *et al.* The Provenance, use, and Circulation of Metals in the European Bronze Age: The State of Debate. *J. Arch. Res.* (2018).
5. Shaoqing Wang. Atomic Structure Modeling of Multi-Principal-Element Alloys by the Principle of Maximum Entropy. *Entropy* **15**, 5536–5548 (2013).
6. Peipei Yang, Ying Liu, Xiuchen Zhao, Jingwei Cheng & Hong Li. Electromagnetic Wave Absorption Properties of FeCoNiCrAl0.8 High Entropy Alloy Powders and its Amorphous Structure Prepared by High-Energy Ball Milling. *J. Mater. Res.* **31**, (2016).
7. Swe-Kai Chen, Y-F. Kao, T-D. Kee & Y-S. Chang. Electrochemical Passive Properties of AlxCoCrFeNi (x = 0, 0.25, 0.50, 1.00) High-Entropy Alloys in Sulfuric Acids. *Corros. Sci.* **52**, 1026 (2010).
8. Gang Zhu, Ying Liu & Jinwen Ye. Early High-Temperature Oxidation of Ti(C,N)-based Cermets with Multi-COmponent AlCoCrFeNi High-Entropy Alloy Binder. *Int. J. Refract. Met. Hard Mater.* **44**, (2014).
9. L. Jiang *et al.* Effect of Mo and Ni Elements on microstructure Evolution and Mechanical Properties of CoFenixVMoy High Entropy Alloys. *J. Alloys Compd.* **649**, 585–590 (2015).
10. M.G. Poletti & L. Battezzati. Electronic and Thermodynamic Criteria for the Occurrence of High Entropy Alloys in Metallic Systems. *Acta Mater.* **75**, 297–306 (2014).

11. Xiaoyang Ye *et al.* Synthesis and Characterization of High-Entropy Alloy AlXFeCoNiCuCr by Laser Cladding. *Adv. Mater. Sci. Eng.* **485942**, (2011).
12. Yong Zhang *et al.* Microstructures and Properties of High-Entropy Alloys. *Progress in Materials Science* **61**, 1–93 (2014).
13. Guoxiu Tong, Wenhua Wu, Ru Qiao & Jinhao Yuan. Morphology dependence of static magnetic and microwave electromagnetic characteristics of polymorphic Fe3O4 nanomaterials. *J. Mater. Res.* **26**, 1639–1645 (2011).
14. Rui Zhao *et al.* Solid-state pyrolysis of iron phthalocyanine polymer into iron nanowire inside carbon nanotube and their novel electromagnetic properties. *J. Mater. Res.* **26**, 2369–2372 (2011).
15. Biao Zhao, Wanyu Zhao, Gang Shao, Bingbing Fan & Rui Zhang. Morphology-Control Synthesis of a Core−Shell Structured NiCu Alloy with Tunable Electromagnetic-Wave Absorption Capabilities. *ACS Appl. Mater. Interfaces* **7**, 12951–12960 (2015).
16. Xiaoyan Yuan, Laifei Cheng, Luo Kong, Xiaowei Yin & Litong Zhang. Preparation of titanium carbide nanowires for application in electromagnetic wave absorption. *J. Alloys Compd.* **596**, 132–139 (2014).
17. Hui Zhang *et al.* Facile synthesis of RGO/NiO composites and their excellentelectromagnetic wave absorption properties. *Appl. Surf. Sci.* **314**, 228–232 (2014).
18. Biao Zhao *et al.* Facile preparation and enhanced microwave absorption properties of core–shell composite spheres composited of Ni cores and TiO2 shells. *Phys. Chem. Chem. Phys.* **17**, 8802–8810 (2015).
19. K. J. Vinoy & R. M. Jha. Trends in Radar Absorbing Materials. *Academy Proceedings in Engineering Sciences* **20**, 815–850 (1995).

20. K. J. Vinoy & R. M. Jha. *Radar Absorbing Materials: From Theory to Design and Characterization*. (Kluwer Academic Publishers, 1996).
21. R. F. Soohoo. *Microwave Magnetics*. (Harper and Row Publishers, 1985).
22. Yi Zhang, Boliang Zhang, Kuo Li, Guang-Lin Zhao & S.M. Guo. Electromagnetic Interference Shielding Effectiveness of High Entropy AlCoCrFeNi Alloy Powder Laden Composites. *J. Alloys Compd.* **734**, 220–228 (2018).
23. Yih-Farn Kao *et al.* Electrical, Magnetic, and Hall properties of AlXCoCrFeNi High-Entropy Alloys. *J. Alloys Compd.* **509**, 1607–1614 (2011).
24. Guiqin Wang, Lifang Wang, Yulin Gan & Wie Lu. Fabrication and microwave properties of hollow nickel spheres prepared by electroless plating and template corrosion method. *Appl. Surf. Sci.* **276**, 744–749 (2013).
25. Biao Zhao, Bingbing Fan, Gang Shao, Wanyu Zhao & Rui Zhang. Facile Synthesis of Novel Heterostructure Based on SnO2 Nanorods Grown on Submicron Ni Walnut with Tunable Electromagnetic Wave Absorption Capabilities. *ACS Appl. Mater. Interfaces* 18815–18823 (2015).
26. Guoxiu Tong *et al.* Grinding speed dependence of microstructure, conductivity, and microwave electromagnetic and absorbing characteristics of the flaked Fe particles. *J. Mater. Res.* **26**, 682–688 (2011).
27. Biao Zhao, Gang Shao, Bingbing Fan, Wanyu Zhao & Rui Zhang. Preparation and electromagnetic wave absorption properties of novel dendrite-like NiCu alloy composite. *RSC Adv.* **5**, 42587–42590 (2015).

28. Y. Wu, M. Han, T. Liu & L. Deng. Studies on the microwave permittivity and electromagnetic wave absorption properties of Fe-based nano-composite flakes in different sizes. *J. Appl. Phys.* **118**, (2015).
29. Qiushi Chen, Kaiyao Zhou, Li Jiang, Yiping Lu & Tingju Li. Effects of Fe Content on Microstructures and properties of AlCoCrFeXNi High-Entropy Alloys. *Arab J. Sci. Eng.* **40**, 3657–3663 (2015).
30. Yong Dong *et al.* Effect of Vanadium Addition on the Microstructure and Properties of AlCoCrFeNi High Entropy Alloy. *Mater. Des.* **57**, 67–72 (2014).
31. Yuping Bao, Wei An, C. Heath Turner & Kannan M. Krishnan. The Critical Role of Surfactants in the Growth of Cobalt Nanoparticles. *Langmuir* **26**, 478–483 (2010).
32. Sheng Peng, Chao Wang, Jin Xie & Shouheng Sun. Synthesis and Stabilizatoin of Monodisperse Fe Nanoparticles. *J. Am. Chem. Soc.* **128**, 10676–10677 (2006).
33. Toshitaka Ishizaki, Kenichi Yatsugi & Kunio Akedo. Effect of Particle Size on the Magnetic Properties of Ni Nanoparticles Synthesized with Trioctylphosphine as the Capping Agent. *Nanomaterials* **6**, (2016).
34. Yuanzhi Chen *et al.* Chemical Synthesis of Monodisperse Fe-Ni Nanoparticles via a Diffusion-Based Approach. *J. Nanosci. Nanotechnol.* **10**, 3053–3059 (2010).
35. R. Grössinger. A critical examination of the law of approach to saturation. *Phys. Status. Solidi. A* **66**, 665–674 (1981).
36. X. Batlle *et al.* Magnetic study of M-type doped barium ferrite nanocrystalline powders. *J. Appl. Phys.* **74**, 3333 (1993).
37. G. F. Goya, T. S. Berquó, F.C. Fonseca & M. P. Morales. Static and dynamic magnetic properties of spherical magnetite nanoparticles. *J. Appl. Phys.* **94**, 3520 (2003).

38. M. H. Cao *et al.* Single-Crystal Dendritic Micro-Pines of Magnetic α-Fe2O3 : Large-Scale Synthesis, Formation Mechanism, and Properties. *Angew. Chem.* **44**, 4197 (2005).
39. S. Ni *et al.* Hydrothermal synthesis and microwave absorption properties of Fe3O4 nanocrystals. *J. Phys. D: Appl. Phys.* **42**, (2009).
40. Michael Giroux *et al.* Size-Dependent Electromagnetic Absorption Properties of Iron Oxide (Fe3O4) Nanomaterials. *In Preparation.*
41. Michael Giroux *et al.* Radar Absorbing MFe2O4 (M = Fe, Co, Cu, Mn, Mg) Nanomaterials. *In Preparation.*
42. A. A. Khurram, S. A. Rakha, P. Zhou, M. Shafi & A. Munir. Correlation of electrical conductivity, dielectric properties, microwave absorption, and matrix properties of composites filled with graphene nanoplatelets and carbon nanotubes. *J. Appl. Phys.* **118**, 044105 (2015).
43. J. I. Gittleman, B. Abeles & S. Bozowski. Superparamagnetism and Relaxation Effects in Granular Ni-SiO2 and Ni-Al2O3 Films. *Phys. Rev. B.* **9**, 3891–3897 (1974).
44. L.Z. Wu *et al.* High Frequency Complex Permeability of Iron Particles in a Nonmagnetic Matrix. *J. Appl. Phys.* **99**, (2006).
45. Qing Li *et al.* Correlation Between Particle Size/Domain Structure and Magnetic Properties of Highly Crystalline Fe3O4 Nanoparticles. *Sci. Rep.* **7**, (2017).

# Chapter 5. An Investigation of Radar Absorbing Wood

## 5.1 INRODUCTION

Electromagnetic wave absorbers are ever present in everyday life in various military and civil applications such as stealth technology and electromagnetic interference.[1] In military/defense applications, electromagnetic wave absorbers are used to coat planes, submarines, or other vessels to improve stealth capabilities and reduce their radar cross section (RCS).[2–4] In the modern age of portable technology, electromagnetic absorbers are used in almost all forms of handheld technology including smart phones, mobile PCs, and mp3 players in order to protect humans from potential health risks posed by exposure to electromagnetic radiation.[5–7]

With the widespread use of electromagnetic wave absorbers in mind, it is an interesting question to investigate everyday materials and see if they can be made into radar absorbers. While this question is more exploratory in nature, rather than pointedly scientific, it could nonetheless hold great importance as technology advances and could address concerns we do not yet know exist. For example, creating a radar absorbing wood could allow for the construction of signal-proof buildings and/or houses without the need for a Faraday cage, which could allow for more privacy while within these buildings as cell phones could not be reached. Of military interest, this same concept could be applied to create safe rooms for defense related meetings of high importance. In most cases, using wood as a radar absorbing building material may be more cost effective and simpler than building a Faraday cage.

In Chapters 2, 3, and 4 we discussed various types of magnetic electromagnetic wave absorbers and the influences of size, doping, and alloying on electromagnetic wave absorption

behavior in an effort to further the fundamental understanding of the mechanism by which electromagnetic wave absorbers work. In Chapter 5, we aim to take these findings one step further and apply an electromagnetic wave absorber to natural basswood as a host matrix in order to determine if the same phenomenon are observed when an electromagnetic wave absorber is embedded in a host matrix. The work presented in this chapter was largely inspired by the widespread research concerning wood as a vehicle for various chemical processes conducted in Dr. Liangbing Hu's group at University of Maryland.

## 5.2 EXPERIMENTAL METHODS

*Chemicals.* All materials (metal precursors, organic solvents, ligands, crosslinking agents) were purchased from Sigma Aldrich. All chemicals were used as received.

*Synthesis Design.* All nanoparticles were synthesized under inert argon gas in a standard Schlenk line setup, unless otherwise specified. All synthesis procedures were adapted and modified from previous reports.

*Wood Design.* Natural basswood with aligned pores was provided courtesy of Dr. Liangbing Hu at University of Maryland, College Park. The basswood was supplied in dimensions of 2″ x 2″ x 7 mm (L x W x H) and was used as received.[8,9] The pores of the wood were oriented axially along the thickness of the wood (i.e. along the 7 mm edge). House vacuum was used as a suction source, coupled with standard vacuum tubing of 7 mm diameter.

### 5.2.1 Synthesis of $Fe_3O_4$ Nanoparticles

*Synthesis of 10 nm $Fe_3O_4$ Nanoparticles.*[3] 10 nm $Fe_3O_4$ nanoparticles were synthesized by the decomposition of iron (III) acetylacetonate ($Fe(acac)_3$). In a typical synthesis, iron (III) acetylacetonate (0.706 g, 2.0 mmol) was dissolved in 10 mL benzyl ether (BE) and 10 mL oleylamine, heated for 60 min at 110°C to promote decomposition of the Fe, and then refluxed for 30 min at a higher temperature (300°C). The precipitate was collected by centrifugation at 8000 rpm for 10 min, re-dispersed in ethanol, and centrifuged once again at 8000 rpm for 10 min. The final product was re-dispersed in hexanes and stabilized with 2-3 drops of oleylamine.

*Machining of the Pore-aligned Basswood.* A wooden toroid of length 7 mm, inner diameter 3 mm, and outer diameter 7 mm was cut from a piece of pore-aligned basswood using a drill press. A diamond hole saw of diameter 7 mm was used to cut the outer diameter, and a steel

drill bit of diameter 3 mm was then used to cut the center hole. The final toroid resembled an elongated donut shape and was gently sanded to remove any contamination from the cutting process.

*Impregnation of the Basswood Toroid.* The pre-cut basswood toroid was placed into an oven at 105°C for 24 hours as an initial dehydration step in order to remove all water sources from inside the pores of the wood. Immediately after the dehydration step, the toroid was weighed and the weight recorded. The toroid was then fit into vacuum tubing of 7 mm diameter and the center hole plugged with a copper rod of 3 mm diameter. This set up was chosen to maximize the suction power of the vacuum and ensure a tight seal around the wood. At this point, the vacuum was turned on and 1 mL of a 20 mg/mL hexanes solution of 10 nm $Fe_3O_4$ nanoparticles was drop cast on top of the wood using a 200 μL pipette. After 1 mL of the $Fe_3O_4$ solution was added to the wood, the vacuum was turned off, the wood removed from the vacuum tubing, flipped over, and reinserted into the tubing so the other face of the wood toroid was exposed. The 3 mm copper rod was once again fit into the center of the toroid and the vacuum turned on. The previous drop casting step was repeated on the second face of the wood toroid, resulting in a total of 2 mL of a 20 mg/mL hexanes solution of 10 nm $Fe_3O_4$ nanoparticles added. Both faces of the toroid were treated in an effort to obtain a uniform distribution of the particles in the pores. After the drop casting was complete, the vacuum was turned off, the wood removed from the vacuum tubing, and the center copper rod taken out. The wood then was placed in an oven at 70°C overnight (~12 hours) to remove any leftover hexanes. At the conclusion of the 12 hours, the wood was re-weighed and the difference was assumed to be the amount of nanoparticles remaining in the pores of the wood from the drop casting process.

### 5.2.2 Materials Characterization

Transmission electron microscopy (TEM) images were acquired on a 120 kV, FEI Tecnai 12 TWIN microscope. X-ray diffraction (XRD) patterns were collected on a PANalytical X'Pert$^3$ Powder X-Ray Diffractometer equipped with a Cu Kα radiation source (λ=0.15406). Magnetic hysteresis loops were acquired on a MicroMag 2900 Series AGM. Small angle X-ray scattering (SAXS) data was collected by a colleague of Dr. Robert Leheny, professor from the Johns Hopkins University Physics & Astronomy Department.

### 5.2.3 Electromagnetic Absorption Studies

The machined wood toroids with an outer diameter of 7 mm, inner diameter of 3 mm and thickness of 7 mm were inserted into an Keysight 85051B 7 mm airline for the microwave measurements. The complex permittivity and permeability of the composite samples were measured using a Keysight FieldFox N9918A Microwave Analyzer in the 2 – 18 GHz region and the reflection loss was calculated using the measured permittivity and permeability.

## 5.3 DISCUSSION AND RESULTS

### 5.3.1 Materials Characterization

*Synthesis of 10 nm $Fe_3O_4$ Nanoparticles.* Transmission electron microscopy (TEM) images for the synthesized 10 nm $Fe_3O_4$ nanoparticles are shown in Figure 5.1(a). The particles display a sphere-like morphology and were determined to have a mean diameter of 9.19 nm through size distribution analysis. The size distribution profile is shown in Figure 5.1(b). Figure 5.1(c) presents the typical x-ray diffraction pattern for a cubic magnetite structure as confirmed by the perfect agreement with JCPDS No. 00-09-0629. No other diffraction peaks besides those corresponding to $Fe_3O_4$ were observed, which indicates high purity of our as-synthesized products. Figure 5.1(d) displays the magnetic hysteresis loops of the 10 nm $Fe_3O_4$ nanoparticles. The saturation magnetization values ($M_s$) vary from sample to sample and were determined by assuming $M(H) = M_s + X_dH$ ($X_d$ being the high field susceptibility) at high field and extrapolating the M(H) curve to zero field (i.e. $H = 0$).[11,12] The $M_s$ was found to be 33.57 emu/g and the $H_c$ to be 5.5 Oe. Both of these values are much lower than that of bulk $Fe_3O_4$ ($M_s$ = 85 – 100 emu $g^{-1}$, $H_c$ = 115 – 150 Oe), which is expected according to established values for saturation magnetization and coercivity from a previous report.[13] As mentioned in Chapter 2, these results are likely due to special morphology-related anisotropy when considering the sub-domain size of the nanoparticles.[14]

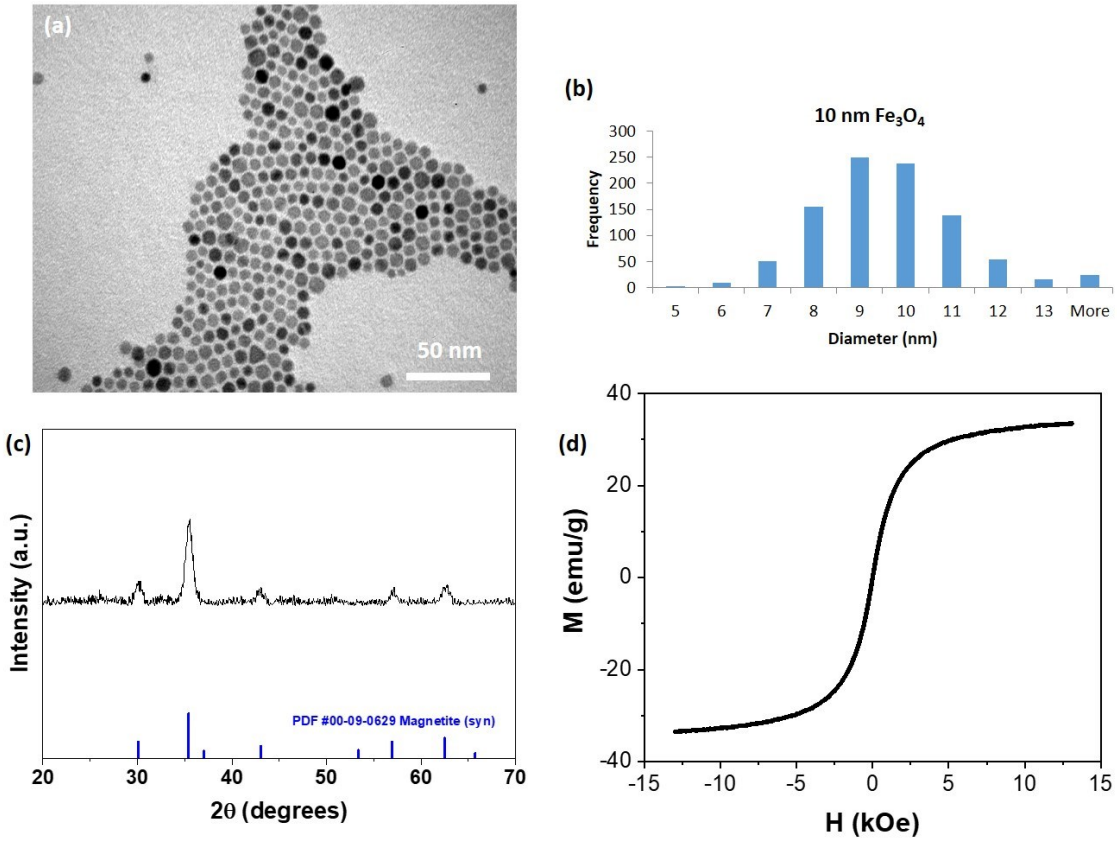


**Figure 5.1.** (a) TEM image, (b) size distribution analysis, (c) XRD pattern, and (d) hysteresis loops for the synthesized 10 nm $Fe_3O_4$ nanoparticles.

*Natural Basswood Impregnated with 10 nm Fe3O4.* Scanning electron microscopy (SEM) images for the impregnated 10 nm $Fe_3O_4$ nanoparticles are shown in Figure 5.2(a). The individual nanoparticles are unable to be seen via SEM due to their extremely small size, however the physical structure of the wood is largely visible with pore sizes ranging from a few microns to ~ 100 μm. Figure 5.2(b) presents the x-ray diffraction pattern for the $Fe_3O_4$ impregnated wood, indicating the presence of cubic magnetite nanoparticles as confirmed by the agreement with JCPDS No. 00-09-0629. The diffraction peaks in the nanoparticle impregnated wood are shifted up 1 – 2° as a result of the positioning of the wood cross section within the x-ray diffractometer. Nonetheless, no other diffraction peaks besides those corresponding to $Fe_3O_4$

were observed, which indicates high purity of our as-synthesized products. Magnetic hysteresis loops of the 10 nm $Fe_3O_4$ nanoparticle impregnated wood were not measured, but it is expected that the wood samples would display similar behavior as the pure 10 nm $Fe_3O_4$. Small angle X-ray scattering (SAXS) was conducted to gain a better understanding of the nanoscale features of, and to determine the degree of aggregation in the $Fe_3O_4$/wood composites used in the electromagnetic studies. Figure 5.3 displays SAXS diffraction patterns for both cross-sectional and surface segments of the 10 nm $Fe_3O_4$ impregnated basswood. Very little was able to be determined from the diffraction patterns and an expert at the X-ray facility described the scattering as without any real structure factor.

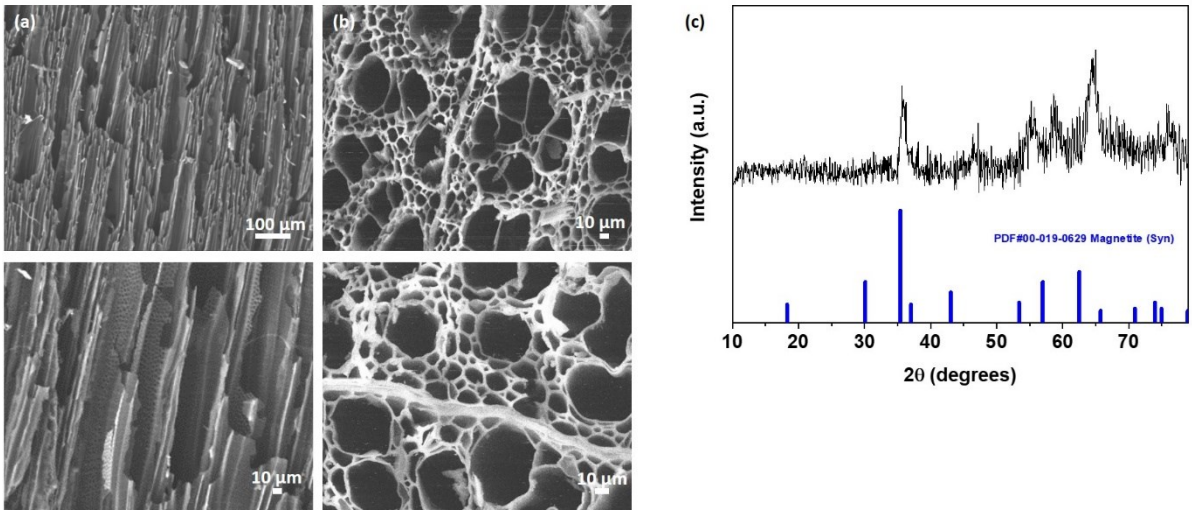


**Figure 5.2.** (a) Axial and (b) crossectional SEM images of the 10 nm $Fe_3O_4$ impregnated basswood. (c) XRD pattern of the 10 nm $Fe_3O_4$ impregnated basswood.

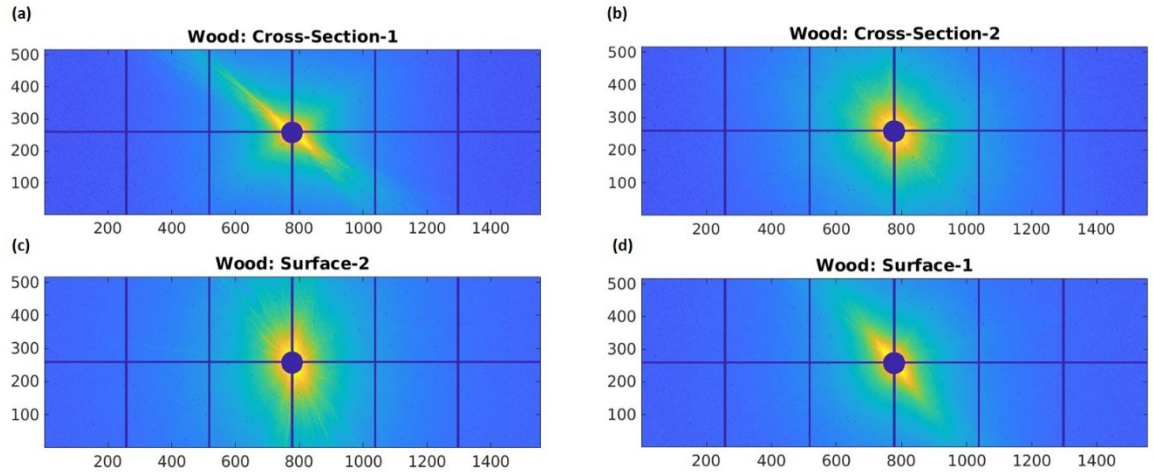


**Figure 5.3.** (a) – (d) SAXS diffraction patterns for cross-sectional and surface segments of the $Fe_3O_4$ impregnated wood.

*Nanoparticle Impregnation Protocol Development Process.* Throughout the impregnation protocol development process, a variety of impregnation methods were tested in order to ensure that the nanoparticles were actually entering and remaining in the pores of the wood rather than simply coating the surface. As described in Section 5.2 of this chapter and shown in Figure 5.4(a), the end result of this protocol development process involved the pre-impregnation machining of a wooden toroid of length 7 mm, inner diameter 3 mm, and outer diameter 7 mm, cut from a piece of pore-aligned basswood using a drill press. As previously stated, a diamond hole saw of diameter 7 mm was used to cut the outer diameter, and a steel drill bit of diameter 3 mm was then used to cut the center hole. The final toroid resembled an elongated donut shape and was then gently sanded to remove any contamination from the cutting process.

Figure 5.4(b) shows the experimental set up for the drop casting impregnation experiments. The wooden toroid was fit into a section of vacuum tubing of 7 mm in diameter and the center hole plugged with a copper rod of 3 mm diameter, in order to maximize the suction

power of the vacuum and ensure a tight seal around the wood. The $Fe_3O_4$ nanoparticle solution was then drop casted over the surface of the wood. At the conclusion of the impregnation process, the wood was removed from the vacuum tubing and visually inspected. As shown in Figure 5.4(c) both faces of the wood toroid were stained black from the 10 nm Fe3O4 impregnation process, while the sides of the toroid remained a natural wood color. This indicates that the nanoparticles were in fact penetrating into the pores of the wood rather than coating the surface.

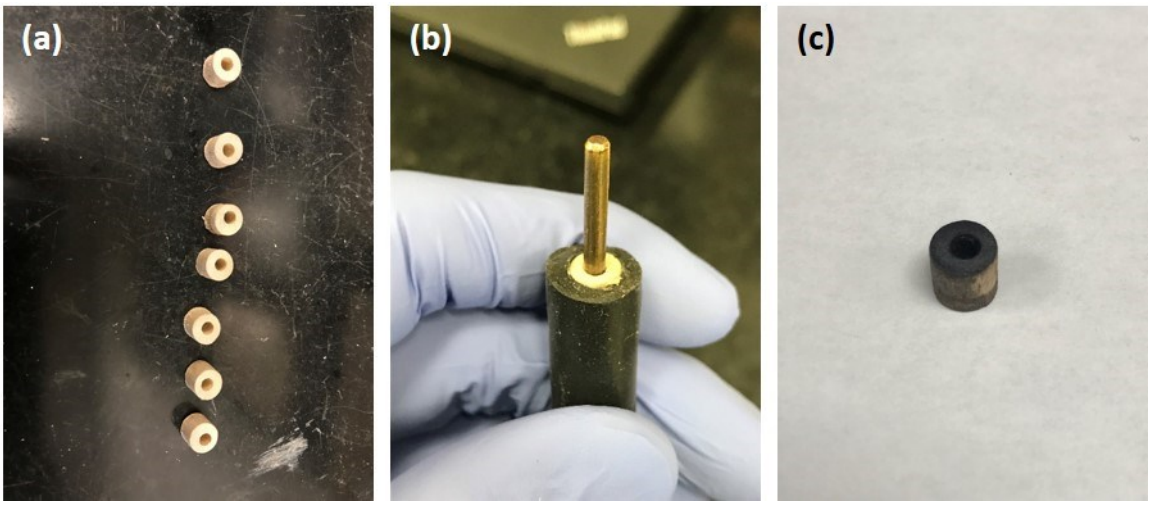


**Figure 5.4.** (a) The pre-machined, untreated wooden toroids. (b) The vacuum impregnation experimental setup. (c) 10 nm $Fe_3O_4$ impregnated basswood.

Figure 5.5 further supports this claim by demonstrating the magnetization of the impregnated wood toroid when compared to an untreated sample of the wood. As shown, in the presence of an NdFeB magnet, the impregnated wood toroid will react to the external magnetic field and can be lifted off of the benchtop surface through magnetic attraction forces, while the untreated wood remains on the benchtop.

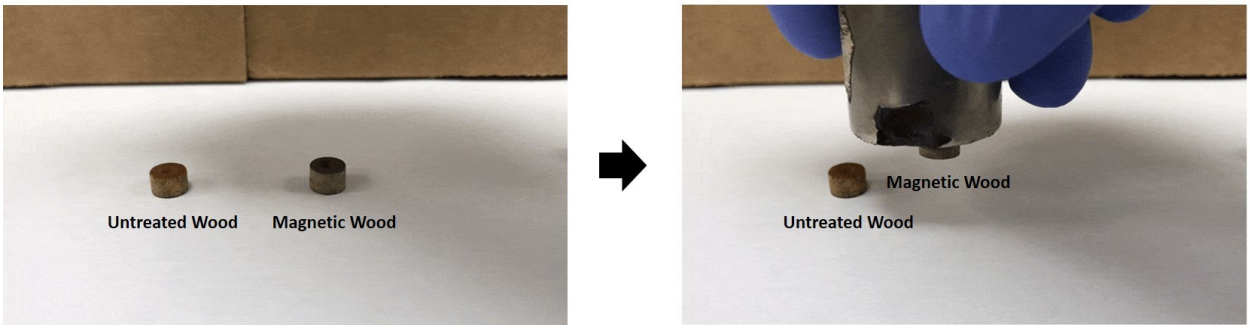


**Figure 5.5.** Screenshots of a GIF displaying the magnetization of the 10 nm Fe3O4 impregnated basswood. As shown, upon exposure to an NdFeB magnet, the treated wooden toroid responds to the magnetic attraction and is lifted off of the benchtop, while the untreated toroid remains unaffected.

### 5.3.2 Discussion of Electromagnetic Measurements

Figure 5.6 shows the data output using the 10 nm $Fe_3O_4$ nanoparticle impregnated basswood at a 2.55 vol% loading as an example. Figure 5.6(a) shows the reflection loss (RL) data for varying thicknesses (1 mm – 7 mm) of 10 nm $Fe_3O_4$ impregnated basswood 2.55 vol% nanoparticle loading. The relationship between the reflection loss of the $Fe_3O_4$ impregnated wood and frequency is calculated as follows:

$$Z_{in} = \sqrt{\frac{\mu_r}{\varepsilon_r}} \tanh j\left[\frac{2\pi f d \sqrt{\mu_r \varepsilon_r}}{c}\right] \quad (1)$$

$$R_L = 20log\left|\frac{Z_{in}-1}{Z_{in}+1}\right| \quad (2)$$

where $\varepsilon_r$ and $\mu_r$ are the relative complex permittivity and permeability of the wax composite, $c$ is the speed of light, $f$ is the frequency and $d$ is the thickness of the absorbing material. As shown in Figure 5.6(a), RL absorption peaks for 10 nm $Fe_3O_4$ impregnated basswood at a 2.55 vol% loading across all thickness on a 0.5 mm interval from 1 mm to 7 mm can be seen with a local maximum absorption of -1.23 dB at 9.07 GHz corresponding to a 7 mm thickness. It can be seen

that more intense electromagnetic wave absorption occurs at frequencies higher than our measureable range as the absorption reaches an absolute maximum of -1.78 dB at 18 GHz, once again corresponding to a 7 mm thickness. It is common for samples of increased thickness to display high intensity RL behavior at higher frequencies, however these curves are unable to be seen in the measureable frequency range of our network analyzer. Given an instrument with a more capable frequency range, these curves would be seen at frequencies of greater than 18 GHz. Figure 5.6(b) shows the real and imaginary portions of the complex permittivity and permeability across the frequency range from 2 GHz – 18 GHz for 10 nm $Fe_3O_4$ nanoparticle impregnated basswood at a 2.55 vol% loading. In general, the values of both the real ($\varepsilon'$, $\mu'$) and imaginary ($\varepsilon''$, $\mu''$) portions of the complex permittivity and permeability gradually decrease with increasing frequency. For both imaginary portions, $\varepsilon''$ and $\mu''$, a much sharper decrease can be seen early on in the frequency range, from 2 GHz < $f$ < 4 GHz. Negative values in both $\varepsilon''$ and $\mu''$ may come from errors in the instrument measurement system.[8]

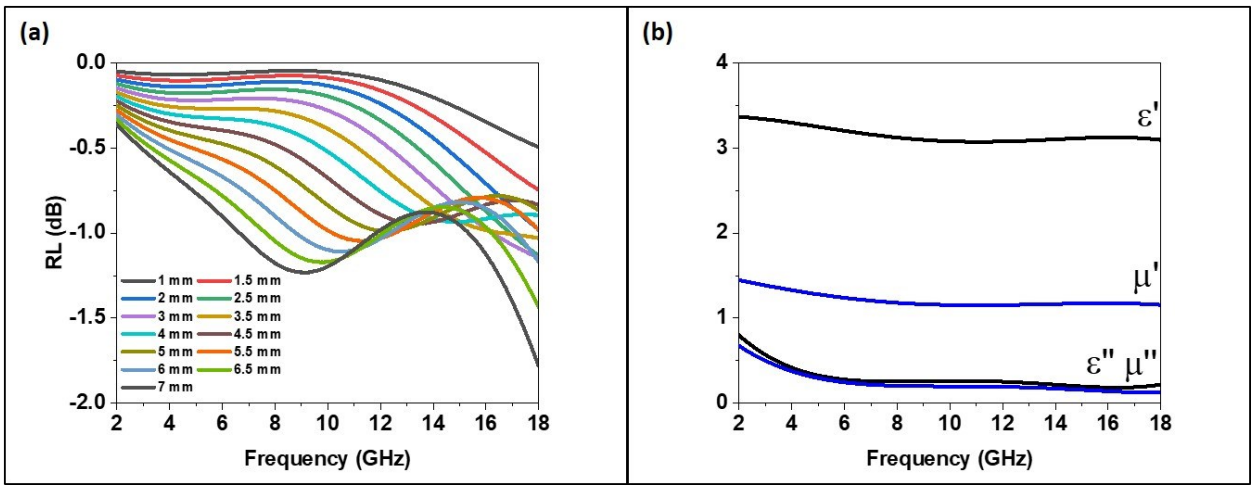


**Figure 5.6.** (a) Reflection loss for varying thicknesses (1 mm – 7 mm) of 10 nm $Fe_3O_4$ impregnated basswood at a 2.55 vol% loading. (b) Complex permittivity and permeability values for 10 nm $Fe_3O_4$ impregnated basswood at a 7 mm thickness and 2.55 vol% loading.

Figure 5.7 shows the raw reflection loss (RL) data for all loadings of 10 nm $Fe_3O_4$ (0.25, 1.3, 1.55, 2.13, and 2.55 vol%). The previous discussion concerning Figure 5.6 can be applied to any specific loading in Figures 5.7.

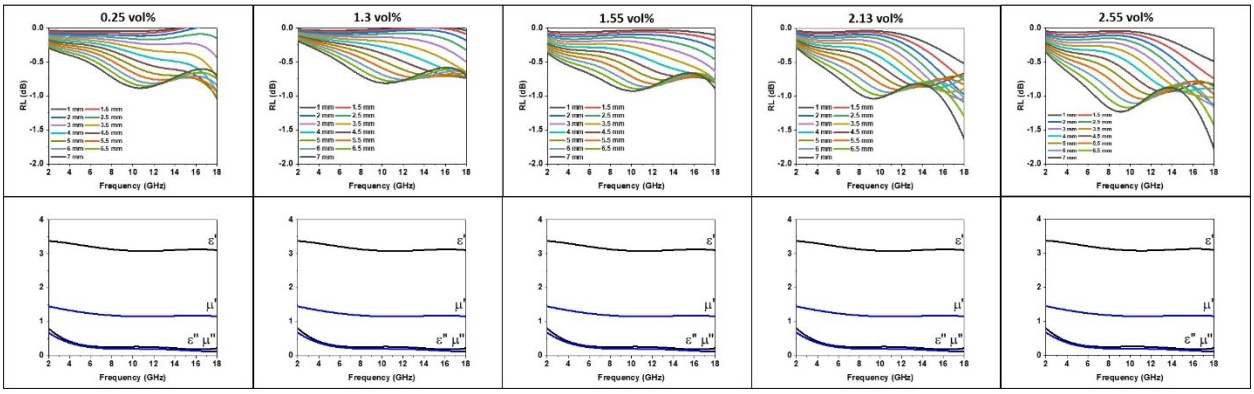


**Figure 5.7.** Raw RL data for varying loadings of 10 nm $Fe_3O_4$ impregnated basswood.

### 5.3.3 Nanoparticle Loading Dependence Effects on Electromagnetic Wave Absorption of Wood

The effects of loading dependence on the materials properties and reflection loss data of the nanoparticle impregnated wood system were measured at varying nanoparticle loadings and the data analyzed for trends. Figure 5.8(a) shows the effect of nanoparticle loading on the intensity of electromagnetic wave absorption, while Figure 5.8(b) shows the effect of nanoparticle loading on the complex permittivity, and the complex permeability of 10 nm $Fe_3O_4$ nanoparticles in a wood toroid of 7 mm thickness. In agreement with previous studies and the data presented in Chapter 2 of this dissertation, it is shown in Figure 5.8(a) that as nanoparticle loading increases, the effective absorption increases as well. The reasoning behind this phenomena is explained by the fact that as the loading of the sample increases, the overall volume of nanoparticles increases as well, thus increasing the materials ability to absorb electromagnetic radiation. Of particular interest is the observation that there is extremely little noticeable change in the complex permittivity and permeability as the nanoparticle loading increases. While the complex permittivity and permeability do increase (by several thousandths periodically throughout the frequency range from 2-18 GHz), it is not enough to be seen when plotted together and the curves look as if they overlap. As previously discussed in Chapter 2, we expect an increase in these properties as the nanoparticle loading of the sample is increased, so this somewhat negligible change in the complex permittivity and permeability is somewhat alarming at first. However, it is not a problem when taking into account that the increase in electromagnetic absorption is small as well, as the absorption capabilities are only increasing by roughly 0.5 dB from the lowest loading (0.25 vol%) to the highest loading (2.55 vol%). In essence, the results shown here are expected as a small change in complex permittivity and

permeability will produce a small change in the intensity of absorption, as governed by Equation 1.

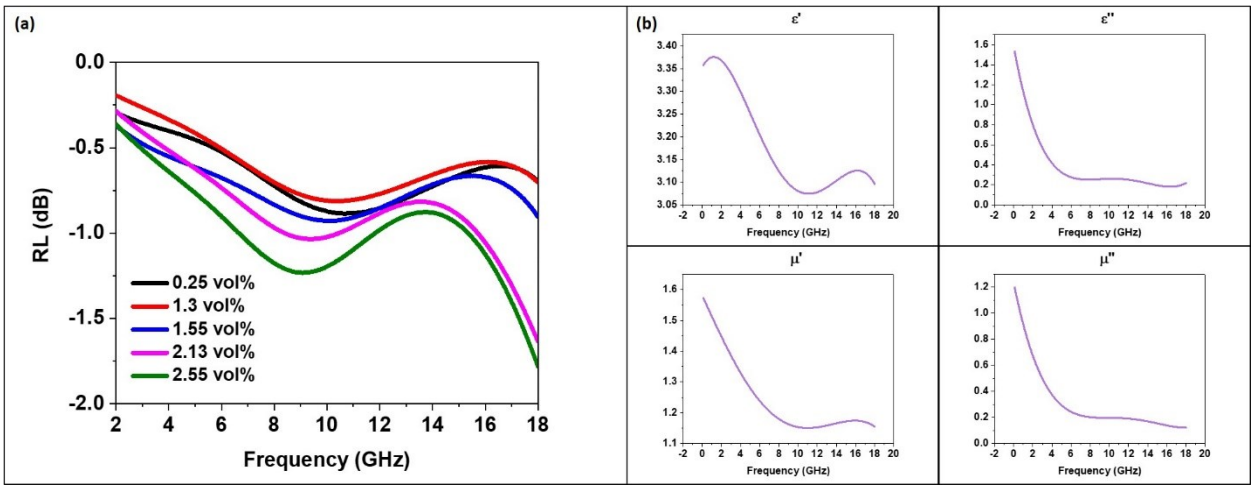


**Figure 5.8.** (a) Reflection loss for varying nanoparticle loadings of 10 nm $Fe_3O_4$ impregnated basswood at a 7 mm thickness. (b) Visualization of the effect of loading on the real and imaginary portions of the permittivity and permeability of 10 nm $Fe_3O_4$ impregnated basswood.

### 5.3.4 Effects of Pore Size on Electromagnetic Wave Absorption Properties of Wood

During our investigation of radar absorbing wood, there was reasonable concern whether or not the nanoparticle impregnated wood could be treated as a continuous medium, or it should be considered to have metamaterial-like properties in which the electromagnetic wave absorption behavior would need to be treated differently.[3,4,15] In order to answer this question, a series of experiments were done to simulate various pore sizes, see the effect on the electromagnetic wave absorption as well as the complex permittivity and permeability, and ultimately determine at which pore size the material could no longer be treated as continuous. For these experiments, the same 15 vol% 10 nm $Fe_3O_4$ nanoparticle/paraffin wax composite as discussed in Chapter 2 was pressed into a toroid of 3 mm thickness and 15 holes were drilled into it. The holes drilled in the

wax were considered to simulate the pores of wood and were drilled in various sizes ranging from 0.2 mm to 1.5 mm in diameter. The electromagnetic wave absorption and complex permittivity and permeability were measured for each hole, or 'pore' size and compared in order to see the effect of pore size. In between each experiment, the nanoparticle/wax composite was re-pressed into a pore-less, continuous 3 mm thick toroid from scratch to eliminate any influence from the previous sized pores, and the new pore size was drilled. Figure 5.9 displays the results of these experiments.

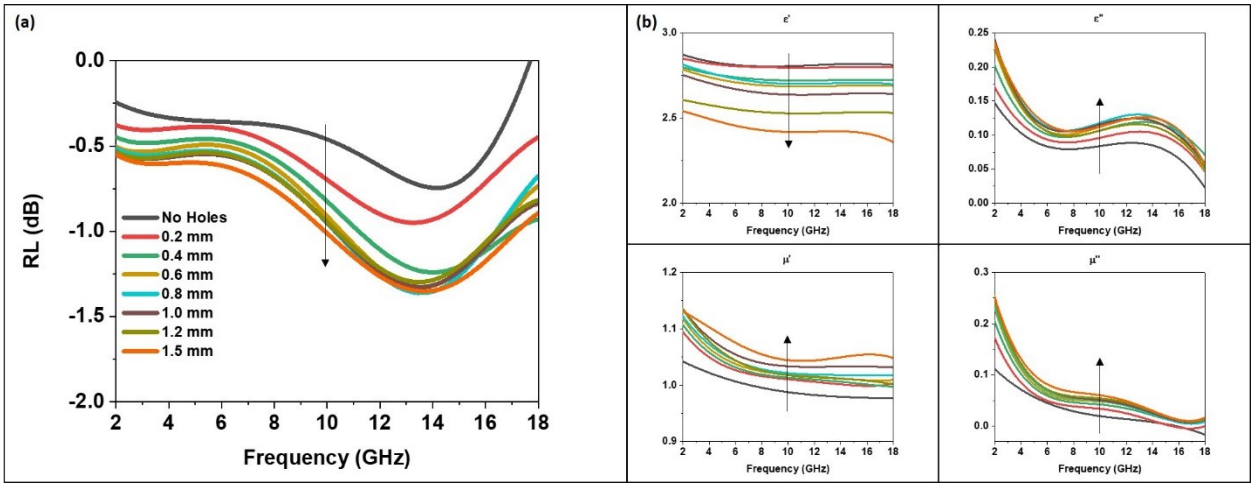


**Figure 5.9.** (a) Effect of pore size on reflection loss for a 15 vol% 10 nm $Fe_3O_4$ nanoparticle/paraffin wax composite. (b) Effect of pore size on the complex permittivity and permeability of a 15 vol% 10 nm $Fe_3O_4$ nanoparticle/paraffin wax composite. The arrows in each plot indicate the direction of influence corresponding with an increasing pore size.

As shown in Figure 5.9, the pore size has a significant, and somewhat surprising influence on the electromagnetic wave absorption properties, complex permittivity, and complex permeability of the samples. The trends are summarized in Table 5.1 below:

**Table 5.1.** Effect of Pore Size on Electromagnetic Wave Absorption, Complex Permittivity, and Complex Permeability.

| Material Property | Trend |
|---|---|
| Real Permittivity (ε′) | Decreases with increasing pore size |
| Imaginary Permittivity (ε′′) | Increases with increasing pore size |
| Real Permeability (μ′) | Increases with increasing pore size |
| Imaginary Permeability (μ′′) | Increases with increasing pore size |
| Intensity of Reflection Loss (RL) | Increases with increasing pore size |

As shown in Figure 5.9 and Table 5.1, as the pore size of the material is increased, the intensity of the reflection loss is increased as well, or in other words, the larger the pore size, the more effective a material is at absorbing electromagnetic waves. This is a surprising observation as it is expected that the electromagnetic wave absorption effectiveness would decrease from increasing pore size since there is less material to absorb the electromagnetic energy; in fact, we see the opposite. While unconfirmed at this point, it is believed that this response is due to an increased amount of internal reflections within the material itself as the pore size increases. When there are no pores in the sample, there is only one interface between air and the nanoparticle/wax composite, and this interface is perpendicular to the propagation of the incoming electromagnetic waves. In most cases such as this, when coming into contact with the air-nanoparticle interface, incoming electromagnetic waves will either be absorbed or reflected back to the receiver and away from the absorbing media.[9,10] In this situation, the absorption media only has one point of contact in which it can absorb electromagnetic energy and reduce the signal sent back to the receiver, and a large signal may be reflected. However when pores are

present, the electromagnetic waves can start to penetrate the material within the pores and become trapped inside these cavities. As a result of this, there are multiple internal reflections along the length of the material and within the pores. Upon each internal reflection, a small amount of electromagnetic energy will be absorbed, thus increasing the overall electromagnetic wave absorption of the material and decreasing the signature of the signal reflected back to the receiver. Following this logic, it is understandable that a sample with sizeable pores will be more effective in absorbing electromagnetic waves as the absorption becomes a sum of multiple internal reflections, rather than a single interaction along the boundary between the air and absorbing media. This process is illustrated in Figure 5.10 below.

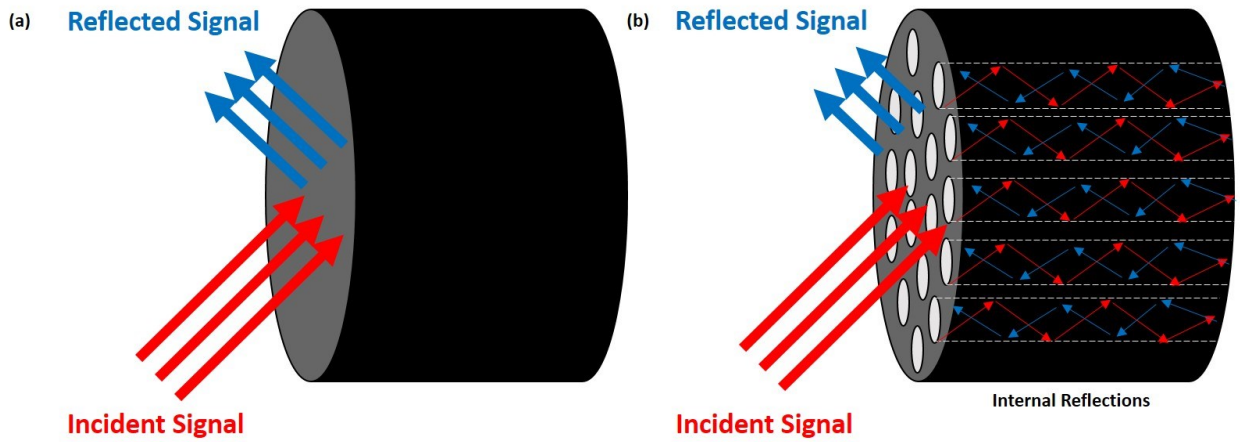


**Figure 5.10.** (a) Illustration of the reflection of incident electromagnetic waves in an absorbing media without pores. (b) Illustration of the reflection of incident electromagnetic waves in an absorbing media with pores. Multiple internal reflections occur within the pore cavity, resulting in a smaller reflected signal.

The effect of pore size on the real portions of the complex permittivity and permeability, illustrated in Figure 5.9 and discussed in Table 5.1, should be straight forward as these are both

thought of as bulk materials properties dependent upon the conductivity and the magnetization of the material, respectively. Logically, if larger holes are drilled into the toroid, less of the bulk material remains, and the conductivity and magnetization of the material decreases thus decreasing the real permittivity and permeability. This logic is demonstrated seamlessly when considering the real permittivity, however does not hold true when considering the real permeability. At this point, it is unknown why this behavior is observed; this could be an interesting question if this research was further pursued.

The effect of pore size on the imaginary portions of the complex permittivity and permeability are also illustrated in Figure 5.9 and discussed in Table 5.1. The influence of pore size on each of these parameters is for the most part expected. Both the imaginary permittivity and imaginary permeability, known as the dielectric loss and magnetic loss, respectively, increase as the pore size increases.[9,10] If it is true that the absorption capabilities of the sample are improved from increasing pore size and creating multiple internal reflections, than the observed trends in the dielectric and magnetic loss are appropriate. With increasing pore size, more surface area of the sample is exposed, allowing for more absorption of electromagnetic energy, or in other words, higher dielectric and magnetic loss. Of course, if the number of holes were increased to a maximum, there will be a critical point at which the smaller holes allow for more surface area of the sample to interact with the incoming radiation, simply because more of the smaller holes can fit within the toroidal sample. However, with our experimental parameter of 15 holes per toroid, the larger holes will have the greatest increase in exposed surface area, resulting in the most internal reflections, and thus the highest electromagnetic wave absorption. In addition, from a theoretical standpoint, increasing the dielectric and magnetic loss will

increase the electromagnetic wave absorption of a material, providing concrete backing to this observation.

As mentioned in the opening statements of this section, the purpose of this pore size study was to determine the critical pore size at which the absorbing media can no longer be considered a continuous material and would need to be reclassified as a metamaterial. Our results are somewhat inconclusive in providing an answer to this question, but do give valuable insight to the nature of our materials. While we were unable to directly answer the question of a critical pore size, we can conclude that the critical pore size must be above 1.5 mm, the maximum pore size studied due to physical limitations of the dimensions of the toroid, as there was no non-linear response observed at this pore size, as would be expected when working with a metamaterial. From this, we are able to at least partly answer our initial question and conclude that the nanoparticle impregnated basswood material can assuredly be treated as a continuous medium as the pore sizes in the basswood are 100 μm or smaller in diameter, which is significantly below any of the measured pore sizes. Further supporting this argument, in literature a material is not usually considered a metamaterial until the internal features of the material reach spacing of $\lambda/10$.[15] In our experiments, the measureable frequency range of 2 – 18 GHz corresponds to a 1.6 – 14.9 cm wavelength range of electromagnetic radiation. With a maximum pore size of 100 μm, the sub-feature spacing in the basswood is on the order of $\lambda/16000$, well below the metamaterial threshold.

A last important takeaway from this pore size study is the phenomenon that the electromagnetic wave absorption capabilities of porous media seems to increase as pore size increases (of course, until the critical pore size is reached). This discovery could have huge implications in modern radar absorbing technology, specifically of interest to defense and

military applications. As the pore size of the material increases, less mass of the material is required, thus reducing the weight of an absorber that is applied to the surface of a plane or submarine. If a porous technology was applied to the surface of military vessels, it would not only be more cost effective and require less material, but it would be more aerodynamically friendly as well.

## 5.4 CONCLUSIONS

In conclusion, we have successfully created radar absorbing wood through the impregnation of magnetic 10 nm $Fe_3O_4$ nanoparticles. The dielectric, magnetic and microwave absorption properties of the series of the nanoparticle impregnated wood have been carefully investigated, and our analysis has revealed that the same principles discussed in previous chapters hold true when a radar absorbing material is embedded into a host template such as wood. Not only is this the first instance of the synthesis of a radar absorbing wood, but it is one of the first studies concerning the creation of a radar absorbing material through the impregnation of magnetic nanoparticles. As we have shown, the basic physics and principles studied in Chapter 2 still hold when the nanoparticles are embedded into a wood matrix, and there is no reason to believe that this process couldn't be applied to a variety of hosts or templates, such as polymers or porous metal foams. In addition, we have shown that a porous material may in fact have improved electromagnetic absorption capabilities, which could lead to the development of lighter weight, more cost effective microwave absorbers for planes, submarines, or other military vessels. The study discussed in Chapter 5 should be used as building block towards exploring a new class of porous microwave absorbers and in the future, this study could help in the development of groundbreaking electromagnetic wave absorbing technology.

## 5.5 REFERENCES


1. Shibing Ni *et al.* Hydrothermal Synthesis and Microwave Absorption Properties of Fe3O4 Nanocrystals. *J. Phys. D: Appl. Phys.* (2009).
2. E. F. Knott, J. F. Shaeffer & M. T. Tuley. *Radar Cross Section*. (SciTech Pub., 2004).
3. K. J. Vinoy & R. M. Jha. *Radar Absorbing Materials: From Theory to Design and Characterization*. (Kluwer Academic Publishers, 1996).
4. K. J. Vinoy & R. M. Jha. Trends in Radar Absorbing Materials. *Academy Proceedings in Engineering Sciences* **20**, 815–850 (1995).
5. National Research Council (U.S.). Committee on Identification of Research Needs Relating to Potential Biological or Adverse Health Effects of Wireless Communications Devices. *Identification of Research Needs Relating to Potential Biological or Adverse Health Effects of Wireless Communication Devices*. (National Academic Press, 2008).
6. E. Seidenberg & H. Schimpf. Aspects of automatic target recognition with a two-frequency millimeter wave SAR. *P. Soc. Photo-Opt. Ins.* **4033**, 167–177 (2000).
7. A. Ahlbom *et al.* Possible effects of electromagnetic fields (EMF) on human health--opinion of the scientific committee on emerging and newly identified health risks (SCENIHR. *Toxicology* **246**, 248–250 (2008).
8. Fengjuan Chen *et al.* Mesoporous, Three-Dimensional Wood Membrane Decorated with Nanoparticles for Highly Efficient Water Treatment. *ACS Nano* **11**, 4275–4282 (2017).
9. Jainwei Song *et al.* Processing bulk natural wood into a high-performance structural material. *Nature* **554**, 224–229 (2018).

10. Jin Xie, Chenjie Xu, Nathan Kohler, Yanglong Hou & Shouheng Sun. Controlled PEGylation of Monodisperse Fe3O4 Nanoparticles for Reduced Non-Specific Uptake by Macrophage Cells. *Adv. Mater.* **19**, 3163–3166 (2007).
11. R. Grössinger. A critical examination of the law of approach to saturation. *Phys. Status. Solidi. A* **66**, 665–674 (1981).
12. X. Batlle *et al.* Magnetic study of M-type doped barium ferrite nanocrystalline powders. *J. Appl. Phys.* **74**, 3333 (1993).
13. G. F. Goya, T. S. Berquó, F.C. Fonseca & M. P. Morales. Static and dynamic magnetic properties of spherical magnetite nanoparticles. *J. Appl. Phys.* **94**, 3520 (2003).
14. M. H. Cao *et al.* Single-Crystal Dendritic Micro-Pines of Magnetic α-Fe2O3 : Large-Scale Synthesis, Formation Mechanism, and Properties. *Angew. Chem.* **44**, 4197 (2005).
15. Mohammed M. Bait-Suwailam. Electromagnetic Field Interaction with Metamaterials. *IntechOpen* 1–19 (2019).

# Chapter 6. Synthesis and Biofunctionalization of Magnetic $Fe_3O_4$ Nanoparticles

## 6.1 INTRODUCTION

Circulating tumor cells (CTCs) are the leading cause of metastasis, the spread of cancer away from the primary tumor to elsewhere in the body.[1–4] Enumeration of these cells could provide a wealth of information in regards to how the tumor grows and regresses, and help track the unique disease progression of a specific patient.[5] With the onset of new technologies and major scientific advancements, there has been an increased push towards "personalized medicine", where the physician tailors treatment to the specifics of an individual's disease status.[6,7] CTCs are a potential way to target chemotherapies and radiation therapy in such a way.[8] However, there have been many obstacles in finding a method with high sensitivity and high specificity to properly examine CTCs because they are so dilute in the bloodstream when compared to other blood cells (1 CTC per $10^7$ cells).[5]

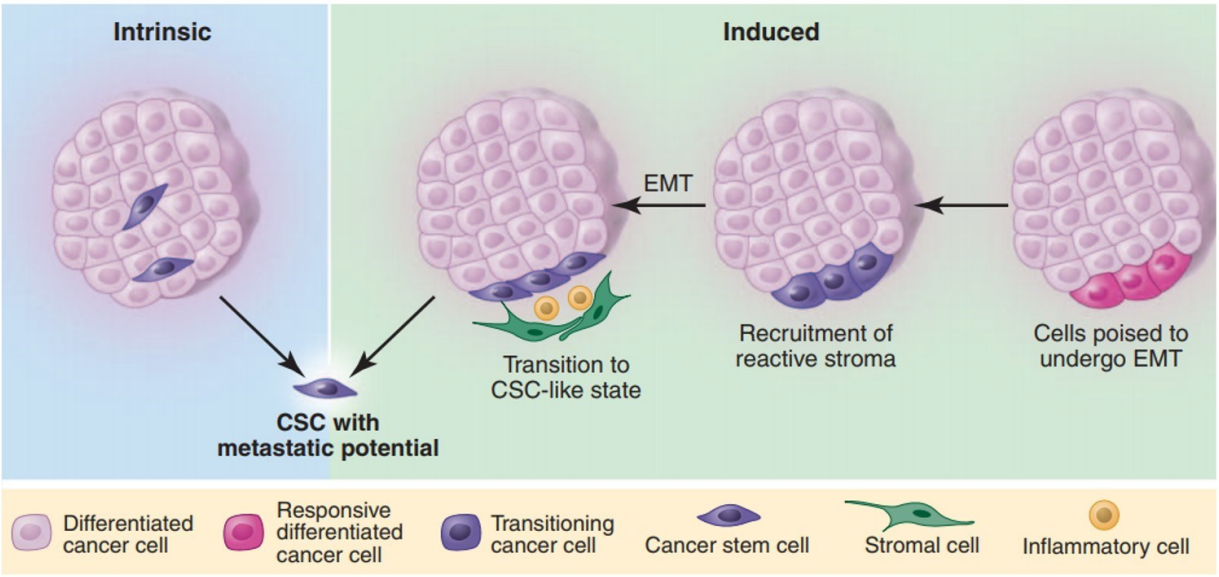


**Figure 6.1.** Circulating tumor cells in the body are the cause of metastasis, the migration of cancer cells from the primary tumor to elsewhere in the body.[5]

Magnetic separation using functionalized magnetic nanoparticles looks promising as a method of detection.[9,10] Due to the nature of these magnetic nanoparticles, aggregation caused by a magnetic moment is only induced with the close positioning of an external magnet, and upon removal of the field, the nanoparticles will no longer be aggregated, allowing them to be redispersed. This would be ideal for isolating CTCs from the bloodstream.

In addition to the need for a magnetic capture technique to collect CTCs from the bloodstream is the need for virus detection methods in food and water sources across the world.[11–13] Norovirus, a major public health issue, is the leading cause of acute gastroenteritis in the United States, and developing a sensor to detect for norovirus in industrial plants such as vegetable processing facilities would potentially prevent many future epidemics.[14] The disease is highly contagious, and contaminated produce and water are among the top contributors to

disease.[14,15] Developing a norovirus-specific sensor for industrial plants seeks to prevent norovirus outbreaks in the population.[16]

In Chapter 6, we use superparamagnetic iron oxide ($Fe_3O_4$) nanoparticles conjugated with targeted antibodies to develop synthesis protocols to make them viable for both public health and biomedical applications. Our efforts include the systematic investigation of appropriate particle size, phase transfer/ligand exchange techniques, and appropriate water soluble PEG ligands for adequate magnetic capture. Through antibody conjugation, these iron oxide particles have the potential to target certain cells in the body and treat specific diseases. Our protocols have been characterized by transmission electron microscopy (TEM) and dynamic light scattering (DLS), which are presented herein. Virus capture experiments and results are not discussed in this dissertation as the experiments were conducted by colleagues at the Johns Hopkins School of Public Health and were not our focus.

## 6.2 EXPERIMENTAL METHODS

*Chemicals.* All materials (metal precursors, organic solvents, ligands, crosslinking agents) were purchased from Sigma Aldrich. All chemicals were used as received. Antibodies were purchased through a different commercial supplier.

*Synthesis Design.* All nanoparticles were synthesized under inert argon gas in a standard Schlenk line setup, unless otherwise specified. All synthesis procedures were adapted and modified from previous reports.

### 6.2.1 Syntheses of $Fe_3O_4$ Nanoparticles

*Synthesis of 7 nm Oleylamine Stabilized $Fe_3O_4$ Nanoparticles.*[17] 7-8 nm $Fe_3O_4$ nanoparticles were synthesized by the decomposition of iron (III) acetylacetonate ($Fe(acac)_3$). In a typical synthesis, iron (III) acetylacetonate (0.706 g, 2.0 mmol) was dissolved in 10 mL benzyl ether (BE) and 10 mL oleylamine, heated for 60 min at 110°C to promote decomposition of the Fe, and then refluxed for 30 min at a higher temperature (300°C). The precipitate was collected by centrifugation at 8000 rpm for 10 min, re-dispersed in ethanol, and centrifuged once again at 8000 rpm for 10 min. The final product was re-dispersed in hexanes and stabilized with 2-3 drops of oleylamine.

*Synthesis of 20 nm Oleylamine Stabilized $Fe_3O_4$ Nanoparticles.*[18] 20 nm $Fe_3O_4$ nanoparticles were synthesized by the decomposition of iron (III) acetylacetonate ($Fe(acac)_3$) and seed-mediated growth on the previously synthesized 10 nm $Fe_3O_4$ nanoparticles. In a typical synthesis, iron (III) acetylacetonate (0.706 g, 2.0 mmol) was dissolved in 20 mL diphenyl ether (DPE) containing oleic acid (0.64 mL, 2.0 mmol), oleylamine (0.66 mL, 2.0 mmol), 1-octadecanol (2.70 g, 10.0 mmol) and 16 mg 10 nm $Fe_3O_4$ nanoparticle seeds, heated for 60 min at 110°C to promote decomposition of the Fe, and then refluxed for 30 min at a higher

temperature (300°C). The precipitate was collected by centrifugation at 6000 rpm for 10 min, re-dispersed in ethanol, and centrifuged once again at 6000 rpm for 10 min. The final product was re-dispersed in hexanes and stabilized with 2-3 drops of oleylamine.

*Synthesis of 8 nm Octanol Stabilized $Fe_3O_4$ Nanoparticles.*[19] 7-8 nm $Fe_3O_4$ nanoparticles were synthesized by the thermal decomposition of iron (III) acetylacetonate ($Fe(acac)_3$). In a typical synthesis, iron (III) acetylacetonate (0.150 g, 0.43 mmol) was dissolved in 13 mL 1-octanol and sealed in a 50 mL autoclave. The reaction-containing autoclave was put into an oven at 185°C for 15 hours to promote decomposition of the Fe and the growth of $Fe_3O_4$ nanoparticles. Once cooled to room temperature, the precipitate was collected by centrifugation in ethanol at 7000 rpm for 10 min, re-dispersed in methanol, and centrifuged once again at 10,000 rpm for 10 min. The final product was re-dispersed in hexanes.

### 6.2.2 PEG Ligand Exchange and Phase Transfer Protocols

*PEG Diacid ($M_w$ 3000) Ligand Exchange/Phase Transfer.*[17] 20 mg α,ω-Bis{2-[(3-carboxy-1-oxopropyl)amino]ethyl}polyethylene glycol (PEG diacid), 2 mg N-Hydroxysuccinimide (NHS), 3 mg N,N′-Dicyclohexylcarbodiimide (DCC), and 1.27 mg dopamine hydrochloride were dissolved in a solvent mixture of 1 mL chloroform ($CHCl_3$) and 1 mL dimethylformamide (DMF). 10 mg anhydrous sodium carbonate ($Na_2CO_3$) was added to the reaction mixture as a drying aid. The resulting solution was stirred under argon protection for 2 hours. During this time, 5 mg of 7 oleylamine stabilized $Fe_3O_4$ nanoparticles were centrifuged out of hexanes and re-dispersed in 1 mL of chloroform. At a stirring time of two hours, the $Fe_3O_4$ nanoparticles in chloroform were injected into the reaction mixture, at which point the resulting solution was let stir overnight (~12 h) to promote a ligand exchange between the oleylamine and PEG diacid. The modified particles were collected the next day by a series of steps as follows:

1. Precipitation by the addition of ~2 mL of hexanes.
2. Centrifugation for 3 min at 14,000 rpm to separate the $Fe_3O_4$ from the reaction solution.
3. Drying under vacuum for ~ 1 min to remove organics.
4. Addition of ~5 mL of deionized water (d-$H_2O$).
5. Sonication for ~15 min to ensure $Fe_3O_4$ re-dispersion in d-$H_2O$.

To complete the phase-transfer, the extra surfactants and salts were removed by dialysis for 24 hours in 1X PBS using a 12 mL Slide-A-Lyzer™ Dialysis Cassette with a 10K MWCO rating, purchased from ThermoFisher Scientific. The dialysis solution was magnetically stirred at ~800 rpm to ensure adequate removal of any extra chemicals. Careful attention was paid during the dialysis process to prevent sedimentation of the particles due to magnetic stirring, and the dialysis cassette containing the particles was removed from magnetic stirring for ~20 min every 2-3 hours and shaken to disrupt sedimentation effects. After the 24 hours of dialysis treatment, the particles were removed from the dialysis bag and used as is.

*Amino-PEG ($M_w$ 3000) Ligand Exchange/Phase Transfer.*[17] 20 mg *O*-(2-Aminoethyl)polyethylene glycol (Amino-PEG), 2 mg N-Hydroxysuccinimide (NHS), 3 mg N,N′-Dicyclohexylcarbodiimide (DCC), and 1.27 mg dopamine hydrochloride were dissolved in a solvent mixture of 1 mL chloroform ($CHCl_3$) and 1 mL dimethylformamide (DMF). 10 mg anhydrous sodium carbonate ($Na_2CO_3$) was added to the reaction mixture as a drying aid. The resulting solution was stirred under argon protection for 2 hours. During this time, 5 mg of 7 nm oleylamine stabilized $Fe_3O_4$ nanoparticles were centrifuged out of hexanes and re-dispersed in 1 mL of chloroform. At a stirring time of two hours, the $Fe_3O_4$ nanoparticles in chloroform were injected into the reaction mixture, at which point the resulting solution was let stir overnight (~12

h) to promote a ligand exchange between the oleylamine and PEG diacid. The modified particles were collected the next day by a series of steps as follows:

1. Precipitation by the addition of ~2 mL of hexanes.
2. Centrifugation for 3 min at 14,000 rpm to separate the $Fe_3O_4$ from the reaction solution.
3. Drying under vacuum for ~ 1 min to remove organics.
4. Addition of ~5 mL of deionized water (d-$H_2O$).
5. Sonication for ~15 min to ensure $Fe_3O_4$ re-dispersion in d-$H_2O$.

To complete the phase-transfer, the extra surfactants and salts were removed by dialysis for 24 hours in 1X PBS using a 12 mL Slide-A-Lyzer™ Dialysis Cassette with a 10K MWCO rating, purchased from ThermoFisher Scientific. The dialysis solution was magnetically stirred at ~800 rpm to ensure adequate removal of any extra chemicals. Careful attention was paid during the dialysis process to prevent sedimentation of the particles due to magnetic stirring, and the dialysis cassette containing the particles was removed from magnetic stirring for ~20 min every 2-3 hours and shaken to disrupt sedimentation effects. After the 24 hours of dialysis treatment, the particles were removed from the dialysis bag and used as is.

*30 Carbon Chain Length PEG Ligand Exchange/Phase Transfer.*[17] 4.9 mg *O,O′*-Bis(2-carboxyethyl)dodecaethylene glycol (30 Carbon PEG), 2 mg N-Hydroxysuccinimide (NHS), 3 mg N,N′-Dicyclohexylcarbodiimide (DCC), and 1.27 mg dopamine hydrochloride were dissolved in a solvent mixture of 1 mL chloroform ($CHCl_3$) and 1 mL dimethylformamide (DMF). 10 mg anhydrous sodium carbonate ($Na_2CO_3$) was added to the reaction mixture as a drying aid. The resulting solution was stirred under argon protection for 2 hours. During this time, 5 mg of 7 nm oleylamine stabilized $Fe_3O_4$ nanoparticles were centrifuged out of hexanes and re-dispersed in 1 mL of chloroform. At a stirring time of two hours, the $Fe_3O_4$ nanoparticles

in chloroform were injected into the reaction mixture, at which point the resulting solution was let stir overnight (~12 h) to promote a ligand exchange between the oleylamine and PEG diacid. The modified particles were collected the next day by a series of steps as follows:

6. Precipitation by the addition of ~2 mL of hexanes.
7. Centrifugation for 3 min at 14,000 rpm to separate the $Fe_3O_4$ from the reaction solution.
8. Drying under vacuum for ~ 1 min to remove organics.
9. Addition of ~5 mL of deionized water (d-$H_2O$).
10. Sonication for ~15 min to ensure $Fe_3O_4$ re-dispersion in d-$H_2O$.

To complete the phase-transfer, the extra surfactants and salts were removed by dialysis for 24 hours in 1X PBS using a 12 mL Slide-A-Lyzer™ Dialysis Cassette with a 10K MWCO rating, purchased from ThermoFisher Scientific. The dialysis solution was magnetically stirred at ~800 rpm to ensure adequate removal of any extra chemicals. Careful attention was paid during the dialysis process to prevent sedimentation of the particles due to magnetic stirring, and the dialysis cassette containing the particles was removed from magnetic stirring for ~20 min every 2-3 hours and shaken to disrupt sedimentation effects. After the 24 hours of dialysis treatment, the particles were removed from the dialysis bag and used as is.

*8 Carbon Chain Length PEG Ligand Exchange/Phase Transfer.*[17] 1.48 mg 3,6,9-Trioxaundecanedioic acid (8 Carbon PEG), 2 mg N-Hydroxysuccinimide (NHS), 3 mg N,N′-Dicyclohexylcarbodiimide (DCC), and 1.27 mg dopamine hydrochloride were dissolved in a solvent mixture of 1 mL chloroform ($CHCl_3$) and 1 mL dimethylformamide (DMF). 10 mg anhydrous sodium carbonate ($Na_2CO_3$) was added to the reaction mixture as a drying aid. The resulting solution was stirred under argon protection for 2 hours. During this time, 5 mg of 7 nm oleylamine stabilized $Fe_3O_4$ nanoparticles were centrifuged out of hexanes and re-dispersed in 1

mL of chloroform. At a stirring time of two hours, the $Fe_3O_4$ nanoparticles in chloroform were injected into the reaction mixture, at which point the resulting solution was let stir overnight (~12 h) to promote a ligand exchange between the oleylamine and PEG diacid. The modified particles were collected the next day by a series of steps as follows:

11. Precipitation by the addition of ~2 mL of hexanes.
12. Centrifugation for 3 min at 14,000 rpm to separate the $Fe_3O_4$ from the reaction solution.
13. Drying under vacuum for ~ 1 min to remove organics.
14. Addition of ~5 mL of deionized water (d-$H_2O$).
15. Sonication for ~15 min to ensure $Fe_3O_4$ re-dispersion in d-$H_2O$.

To complete the phase-transfer, the extra surfactants and salts were removed by dialysis for 24 hours in 1X PBS using a 12 mL Slide-A-Lyzer™ Dialysis Cassette with a 10K MWCO rating, purchased from ThermoFisher Scientific. The dialysis solution was magnetically stirred at ~800 rpm to ensure adequate removal of any extra chemicals. Careful attention was paid during the dialysis process to prevent sedimentation of the particles due to magnetic stirring, and the dialysis cassette containing the particles was removed from magnetic stirring for ~20 min every 2-3 hours and shaken to disrupt sedimentation effects. After the 24 hours of dialysis treatment, the particles were removed from the dialysis bag and used as is.

### 6.2.3 Antibody Conjugations

*E. Coli Antibody Conjugation.* To link E.coli antibodies to $Fe_3O_4$ nanoparticles, 5 mg of 7 nm water-stabilized $Fe_3O_4$ nanoparticles were mixed with 1-ethyl-3-(3-dimethylaminopropyl) carbodiimide (EDC) (0.20 mg, 1.0 mmol) and sulfo-N-Hydroxysuccinimide (sulfo-NHS) (0.55 mg, 0.25 mmol) for 5 minutes. The conjugates were then run through a GE Healthcare

Disposable PD 10 Desalting Column prewashed with ~20 mL 1X PBS to remove excess EDC and sulfo-NHS. 100 ug of E. Coli antibody (provided by Dr. Kellogg Schwab at the Johns Hopkins School of Public Health) was then added into the collected solution and shaken for 2 hours at 4°C. The final antibody-nanoparticle complex was collected by running through another pre-wet PD 10 desalting column. Care was taken to ensure the antibody was not exposed to a room temperature atmosphere for longer than ~20 minutes at a given time to prevent denaturing of the antibody.

*MS2 Antibody Conjugation.* To link MS2 antibodies to $Fe_3O_4$ nanoparticles, 5 mg of 7 nm water-stabilized $Fe_3O_4$ nanoparticles were mixed with 1-ethyl-3-(3-dimethylaminopropyl) carbodiimide (EDC) (0.20 mg, 1.0 mmol) and sulfo-N-Hydroxysuccinimide (sulfo-NHS) (0.55 mg, 0.25 mmol) for 5 minutes. The conjugates were then run through a GE Healthcare Disposable PD 10 Desalting Column prewashed with ~20 mL 1X PBS to remove excess EDC and sulfo-NHS. 100 ug of MS2 antibody (provided by Dr. Kellogg Schwab at the Johns Hopkins School of Public Health) was then added into the collected solution and shaken for 2 hours at 4°C. The final antibody-nanoparticle complex was collected by running through another pre-wet PD 10 desalting column. Care was taken to ensure the antibody was not exposed to a room temperature atmosphere for longer than ~20 minutes at a given time to prevent denaturing of the antibody.

*MNV Antibody Conjugation.* To link MNV antibodies to $Fe_3O_4$ nanoparticles, 5 mg of 7 nm water-stabilized $Fe_3O_4$ nanoparticles were mixed with 1-ethyl-3-(3-dimethylaminopropyl) carbodiimide (EDC) (0.20 mg, 1.0 mmol) and sulfo-N-Hydroxysuccinimide (sulfo-NHS) (0.55 mg, 0.25 mmol) for 5 minutes. The conjugates were then run through a GE Healthcare Disposable PD 10 Desalting Column prewashed with ~20 mL 1X PBS to remove excess EDC

and sulfo-NHS. 100 ug of MNV antibody (provided by Dr. Kellogg Schwab at the Johns Hopkins School of Public Health) was then added into the collected solution and shaken for 2 hours at 4°C. The final antibody-nanoparticle complex was collected by running through another pre-wet PD 10 desalting column. Care was taken to ensure the antibody was not exposed to a room temperature atmosphere for longer than ~20 minutes at a given time to prevent denaturing of the antibody.

### 6.2.4 Protein Conjugations

*Streptavidin Protein Conjugation.* To link streptavidin protein to $Fe_3O_4$ nanoparticles, 5 mg of 7 nm water-stabilized $Fe_3O_4$ nanoparticles were mixed with 1-ethyl-3-(3-dimethylaminopropyl) carbodiimide (EDC) (0.20 mg, 1.0 mmol) and sulfo-N-Hydroxysuccinimide (sulfo-NHS) (0.55 mg, 0.25 mmol) for 5 minutes. The conjugates were then run through a GE Healthcare Disposable PD 10 Desalting Column prewashed with ~20 mL 1X PBS to remove excess EDC and sulfo-NHS. 100 ug of streptavidin protein was then added into the collected solution and shaken for 2 hours at 4°C. The final protein-nanoparticle complex was collected by running through another pre-wet PD 10 desalting column. Care was taken to ensure the protein was not exposed to a room temperature atmosphere for longer than ~20 minutes at a given time to prevent denaturing of the protein.

*MBP-GFP-ActA Protein Conjugation.* To link MBP-GFP-ActA protein to $Fe_3O_4$ nanoparticles, 5 mg of 7 nm water-stabilized $Fe_3O_4$ nanoparticles were mixed with 1-ethyl-3-(3-dimethylaminopropyl) carbodiimide (EDC) (0.20 mg, 1.0 mmol) and sulfo-N-Hydroxysuccinimide (sulfo-NHS) (0.55 mg, 0.25 mmol) for 5 minutes. The conjugates were then run through a GE Healthcare Disposable PD 10 Desalting Column prewashed with ~20 mL 1X PBS to remove excess EDC and sulfo-NHS. 100 ug of MBP-GFP-ActA protein was then added

into the collected solution and shaken for 2 hours at 4°C. The final protein-nanoparticle complex was collected by running through another pre-wet PD 10 desalting column. Care was taken to ensure the protein was not exposed to a room temperature atmosphere for longer than ~20 minutes at a given time to prevent denaturing of the protein.

### 6.2.5 Materials Characterization

Transmission electron microscopy (TEM) images were acquired on a 120 kV, FEI Tecnai 12 TWIN microscope. X-ray diffraction (XRD) patterns were collected on a PANalytical X'Pert$^3$ Powder X-Ray Diffractometer equipped with a Cu Kα radiation source (λ=0.15406).

## 6.3 DISCUSSION AND RESULTS

As stated in the introduction of Chapter 6, our efforts involved in the virus capture experiments at the Johns Hopkins School of Public Health (JHSPH) were to conduct preliminary experiments to develop a nanoparticle/antibody conjugate with the ideal properties for in vivo virus capture. The protocol development steps pertaining to each step of the production process (nanoparticle synthesis, ligand exchange and phase transfer, and antibody/protein additions) are outlined in the following sections.

### 6.3.1 $Fe_3O_4$ Nanoparticle Synthesis

Transmission electron microscopy (TEM) images for both the 7 nm and 20 nm oleylamine-stabilized iron oxide nanoparticles and the 8 nm octanol-stabilized iron oxide nanoparticles are shown in Figure 6.2. All synthesized particles show a clear sphere-like morphology.

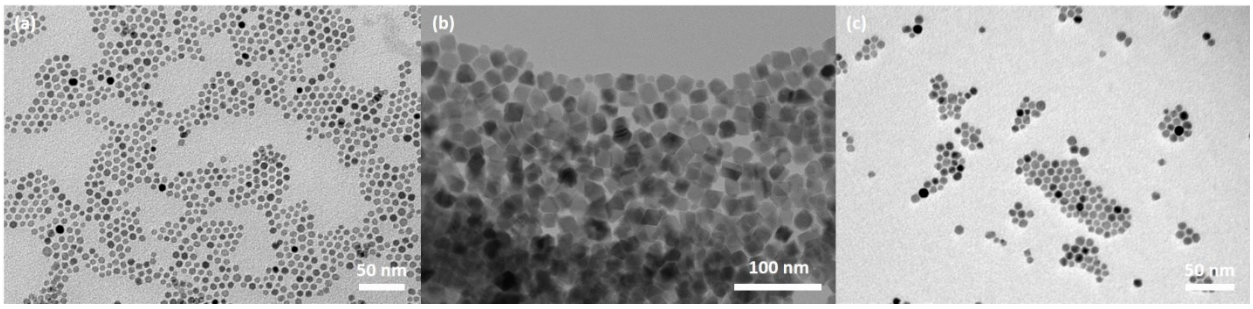


**Figure 6.2.** Transmission electron microscopy (TEM) images of (a) 7 nm oleylamine-stabilized $Fe_3O_4$, (b) 20 nm oleylamine-stabilized $Fe_3O_4$, and (c) 8 nm octanol-stabilized $Fe_3O_4$.

Through size distribution analysis, mean diameters have been determined to be 6.98 nm, 18.11 nm, and 7.80 nm for the 7 nm oleylamine-stabilized, 20 nm oleylamine-stabilized, and 8 nm octanol-stabilized particles, respectively. Size distribution profiles are shown in Figure 6.3.

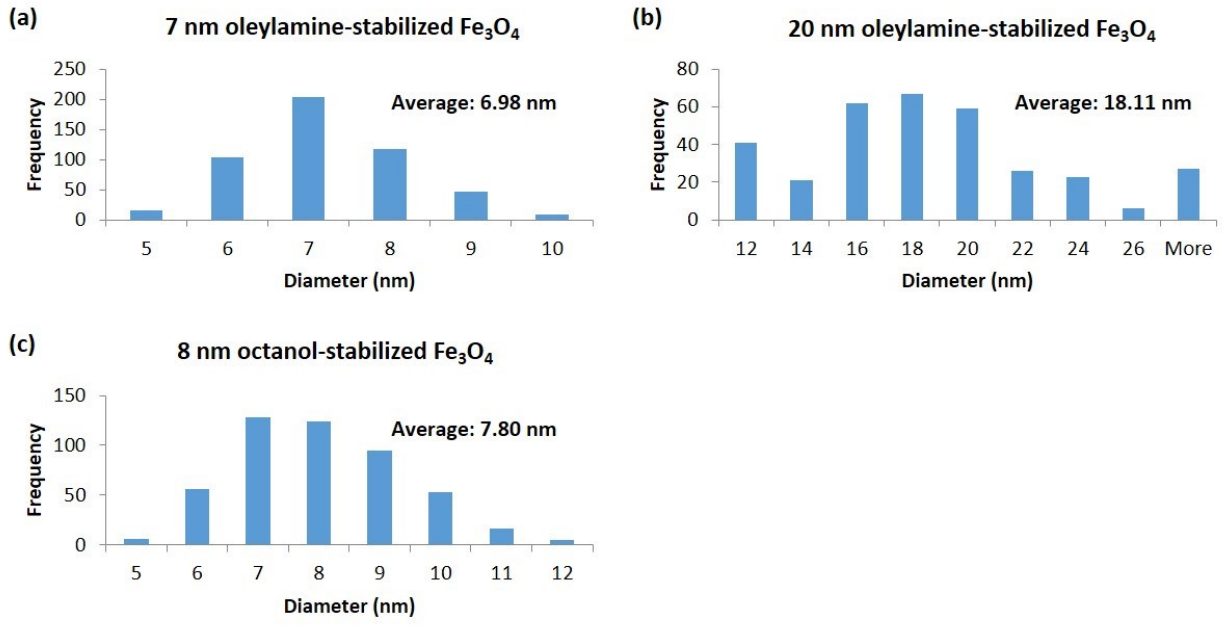


**Figure 6.3.** Size distributions of (a) 7 nm oleylamine-stabilized $Fe_3O_4$, (b) 20 nm oleylamine-stabilized $Fe_3O_4$, and (c) 8 nm octanol-stabilized $Fe_3O_4$.

Figure 6.4 presents the typical x-ray diffraction pattern for a cubic magnetite structure as confirmed by their perfect agreement with JCPDS No. 00-09-0629. No other diffraction peaks besides those corresponding to $Fe_3O_4$ were observed, indicating high purity of our as-synthesized products.

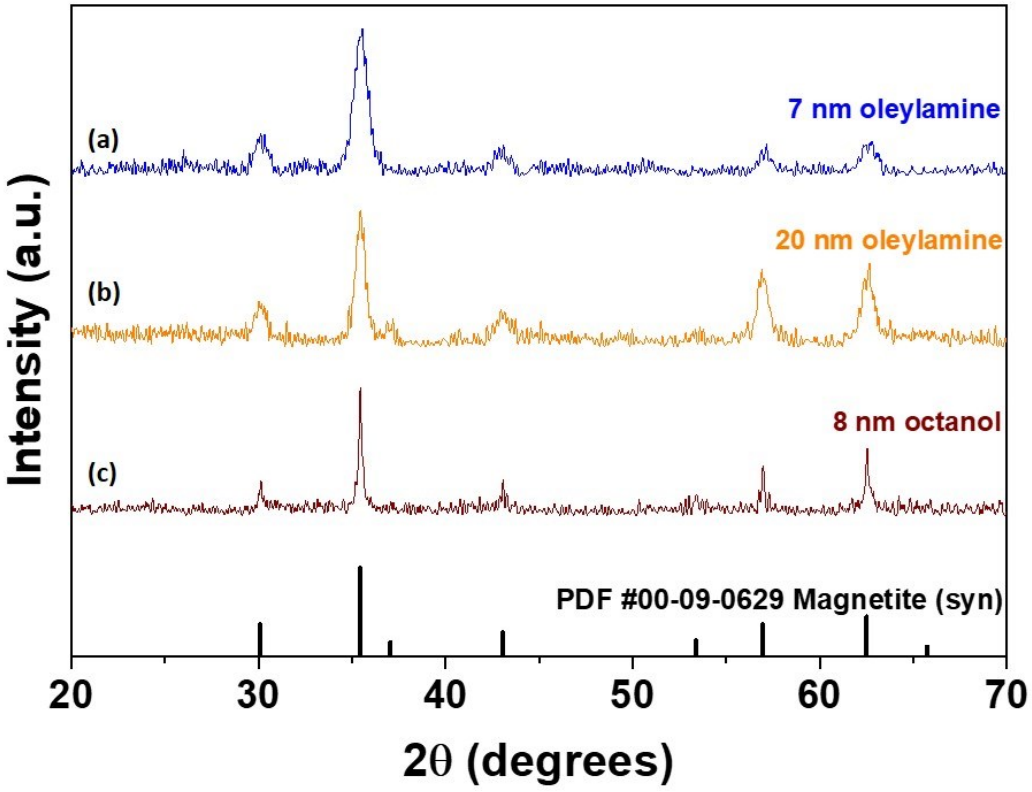


**Figure 6.4.** X-ray diffraction patterns for (a) 7 nm oleylamine-stabilized $Fe_3O_4$, (b) 20 nm oleylamine-stabilized $Fe_3O_4$, and (c) 8 nm octanol-stabilized $Fe_3O_4$.

These $Fe_3O_4$ products were synthesized for use in future ligand exchange and antibody coupling experiments with the end goal of use in virus capture experiments conducted by Dr. Kellogg Schwab at the Johns Hopkins School of Public Health. The ligand exchange and antibody coupling experiments are discussed in the coming sections. For all experiments, the 7

nm oleylamine-stabilized $Fe_3O_4$ nanoparticles were used as the standard. The 20 nm oleylamine-stabilized $Fe_3O_4$ nanoparticles were used in a small number of test experiments when trying to determine the effect of which the size of the nanoparticle has on the rate of magnetic capture. Our observation was that the 20 nm $Fe_3O_4$ nanoparticles were unstable and noticeable sedimentation occurred within a few minutes due to their larger size. No further experiments were conducted with particles of this size as the sedimentation rate is too fast for the particles to be considered for an *in vivo* virus capture experiment. The 8 nm octanol-stabilized $Fe_3O_4$ nanoparticles were used in one test to determine the effect of the binding ligand on the ligand exchange with PEG and phase transfer into water. Our observation was that there was no noticeable difference and the final concentration of water soluble particles was similar, thus, no further experiments were conducted and the 7 nm oleylamine-stabilized $Fe_3O_4$ nanoparticles were used out of convenience for ease of synthesis.

### 6.3.2 Ligand Exchanges and Phase Transfers

In the ligand exchange and phase transfer protocol development stage, the most prominent concern was the stability of the 7 nm $Fe_3O_4$ nanoparticles once transferred to water. If it can be assumed that each chain length of polyethylene glycol (PEG) will have a similar nanoparticle surface coverage, the stability of the $Fe_3O_4$ nanoparticles in aqueous solutions almost entirely depends on the length of the PEG chain in the ligand. In order to investigate this question, four different chain length PEG ligands were attached to the $Fe_3O_4$ nanoparticles and their stability analyzed. Our goal was to find a PEG chain length that would provide for enough particle stability in aqueous solution to prevent gravitational sedimentation, but would still allow for the particles to be captured by an applied external magnetic field.

Standard EDC/NHS crosslinking chemistry was used to exchange the oleylamine on the surface of the $Fe_3O_4$ nanoparticles with a water soluble PEG ligand. This process has been discussed in depth in literature and will not be a focus in this dissertation.[20] Briefly, the EDC and NHS work together to create an amide bond between the PEG and the surface of the nanoparticle to anchor the PEG and replace the oleylamine surfactant. This process could be completed using EDC alone, however the addition of NHS greatly increases the yield and efficiency of the reaction.[20] A diagram of this process is shown in Figure 6.5.

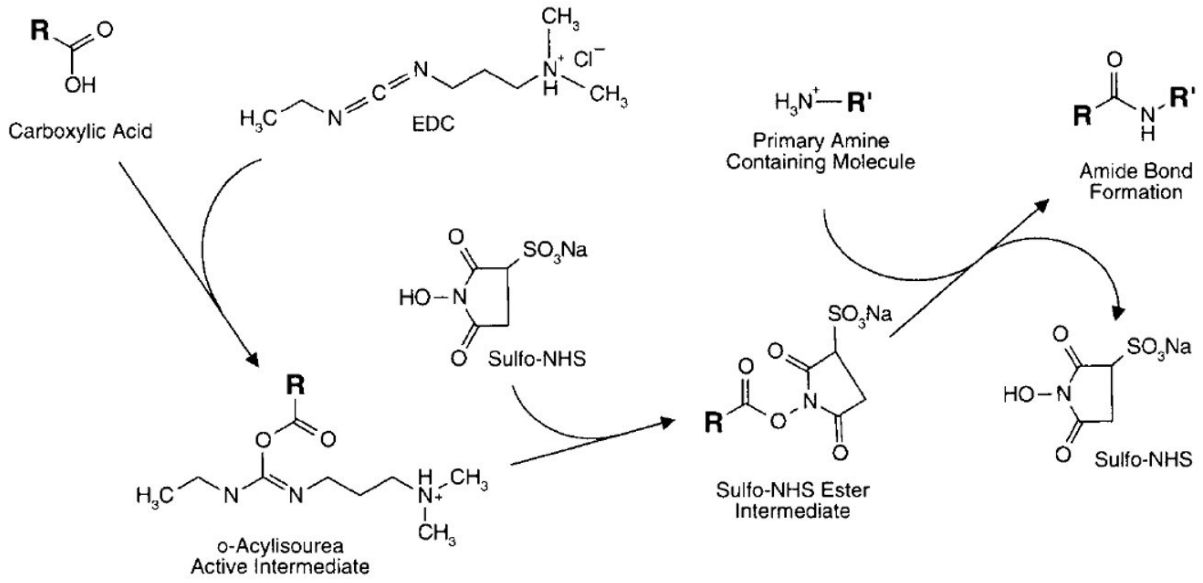


**Figure 6.5.** A schematic for the two-step amide bond formation process using EDC/NHS crosslinking chemistry.[20]

The experimental procedure for the ligand exchange and phase transfer is outlined in the Experimental Methods of this chapter and illustrated in the Figure 6.6.

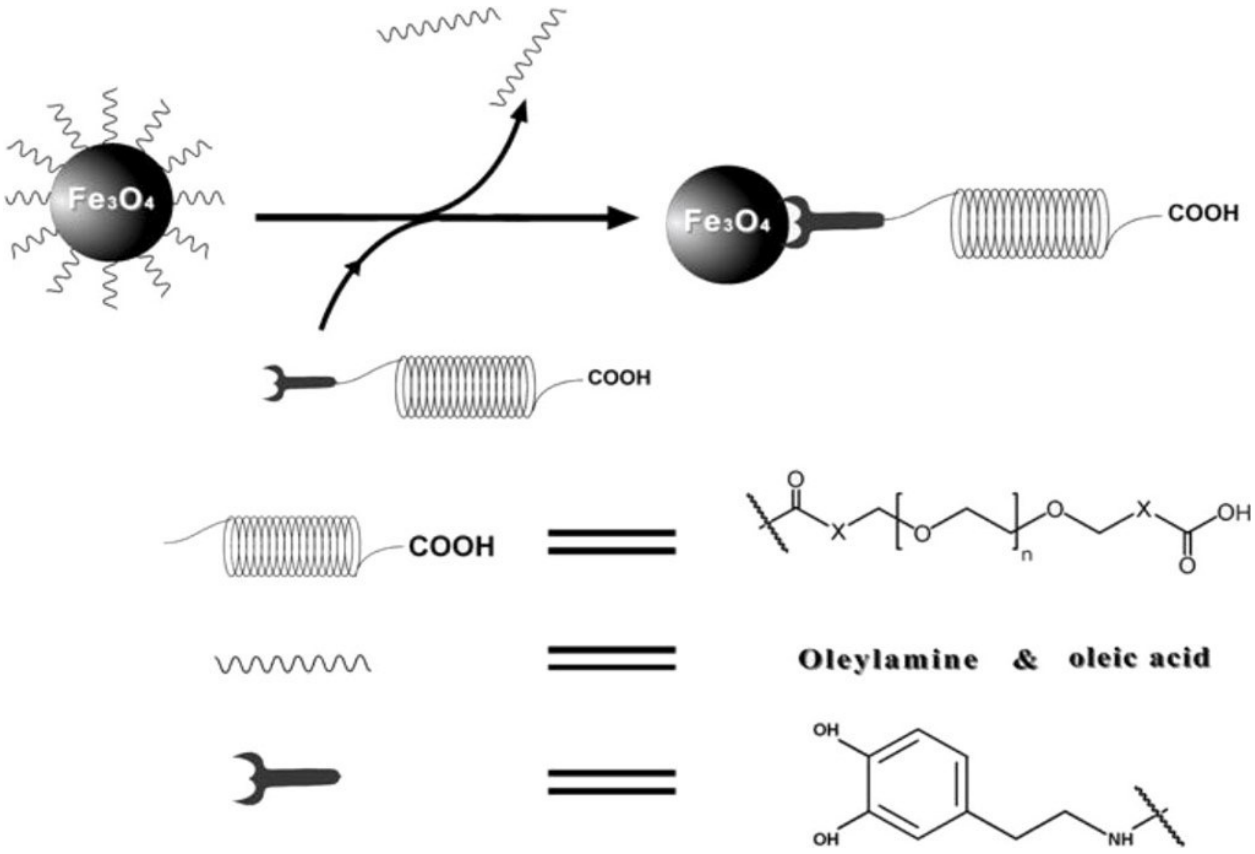


**Figure 6.6.** Surface modification of $Fe_3O_4$ nanoparticles via DPA-PEG-COOH. X=$CH_2NHCOCH_2CH_2$ for PEG3000, PEG6000, PEG20000. X is not present in PEG600 – the bonds on both sides of the X are directly linked.[17]

The four different chain length PEG ligands that were tested are as follows:

1. ~150 carbon chain length: *O*-(2-Aminoethyl)polyethylene glycol ( Amino-PEG)
2. ~100 carbon chain length: α,ω-Bis{2-[(3-carboxy-1-oxopropyl)amino]ethyl}polyethylene glycol (PEG diacid)
3. 30 carbon chain length: *O,O′*-Bis(2-carboxyethyl)dodecaethylene glycol (30 Carbon PEG)
4. 8 carbon chain length: 3,6,9-Trioxaundecanedioic acid (8 Carbon PEG)

In each case, the same ligand exchange procedure was used, as outlined in the Experimental Methods section of this chapter. Transmission electron microscopy images for 7 nm Fe3O4 nanoparticles with the corresponding PEG chain attached are shown in Figure 6.7.

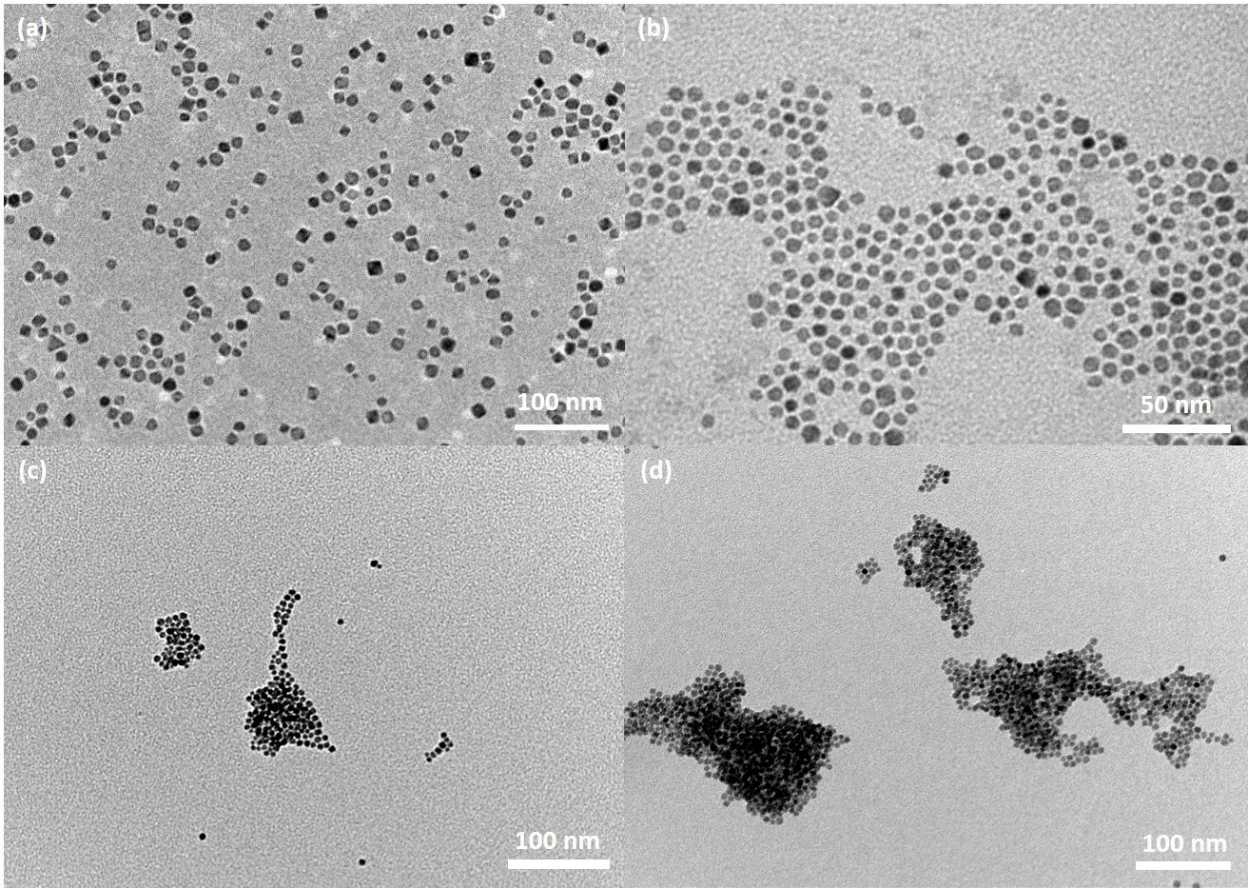


**Figure 6.7.** Transmission electron microscopy (TEM) images of water soluble 7 nm $Fe_3O_4$ with (a) *O*-(2-Aminoethyl)polyethylene glycol (~150 carbon PEG), (b) α,ω-Bis{2-[(3-carboxy-1-oxopropyl)amino]ethyl}polyethylene glycol (~100 carbon PEG), (c) *O,O′*-Bis(2-carboxyethyl)dodecaethylene glycol (30 carbon PEG), and (d) 3,6,9-Trioxaundecanedioic acid (8 carbon PEG).

As can be seen in Figure 6.7, the varying chain length PEG has a substantial effect on the results of the ligand exchange/phase transfer procedure, i.e. decreasing the chain length results in an

increase in aggregation. This is likely due surface coverage and steric effects between the particles as longer PEG chains will force more separation between the particles and help prevent aggregation. The particles are attracted to one another through their magnetic dipoles, so the longer chain lengths help to prevent the dipoles of two particles from interacting. As the PEG chain length decreases, the distance between neighboring particles decreases as well. As a result, magnetic forces will have a larger effect and promote an attraction between two particles, thus creating aggregation.

Stemming directly from the resulting aggregation is the long term stability of the $Fe_3O_4$ nanoparticles in water. Longer PEG chains create a larger hydrodynamic shell for each particle, less aggregation between particles, and thus improve stability in aqueous solution. Stability of our particles in aqueous solution was tested by placing each sample on top of an NdFeB magnet of strength ~1.2 T and measuring the length of time required for particles to sediment on the bottom of the vial. In our case, the nanoparticles with the longer amino-PEG and PEG-diacid attached could not be pulled out of solution even if left on the magnet overnight as they were too stable in aqueous solution. Keeping our goal of virus capture experiments in mind, these particles were unable to be used as they could not be magnetically captured, thus ruining the purpose of the protocol development experiments. The 8 carbon chain PEG resulted in sedimentation in a matter of minutes even without the presence of the magnet, likely from the large aggregation present in the particles. Once again, this chain length PEG was ruled out as the particles would sediment too fast and are not stable enough for *in vivo* experiments. It is easy to see how an aggregation of nanoparticles could be disruptive while circulating in the bloodstream. On the other hand, the particles with the 30 carbon chain length PEG behaved in a more favorable manner and were stable enough to remain suspended under normal gravitational forces but could

be captured in ~5 – 10 minutes upon exposure to an external magnetic field. Due to this behavior, the 30 carbon chain length PEG was chosen as the best water soluble ligand for use during the ligand exchange/phase transfer step.

### 6.3.3 Antibody Conjugations

Once an appropriate system was established, we moved on towards the goal of this project: antibody conjugation to magnetic nanoparticles. E. coli was chosen as an initial candidate for antibody conjugation due to the extensive library of information available regarding E. coli as a pathogen. However, due to unforeseen circumstances and the commercial discontinuation of the antibodies, the antibody of choice was changed to MS2, and again later changed to murine norovirus (MNV). The antibodies were attached to the nanoparticles using standard EDC/NHS chemistry as detailed previously in this chapter. Experimental protocols are outlined in the Experimental Methods section of this chapter.

Transmission electron microscopy images for 7 nm PEG functionalized Fe3O4 nanoparticles with the corresponding antibodies attached are shown in Figure 6.8.

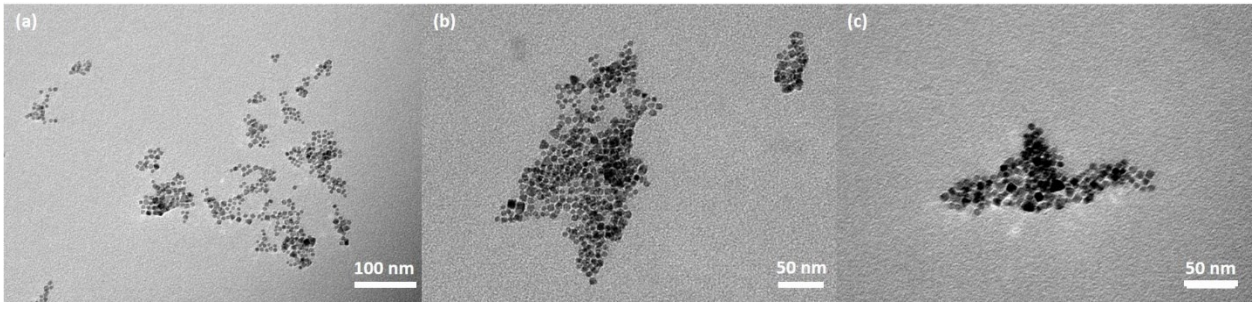


**Figure 6.8.** Transmission electron microscopy (TEM) images of (a) E.coli antibody conjugated 7 nm $Fe_3O_4$, (b) MS2 antibody conjugated 7 nm $Fe_3O_4$, and (c) MNV antibody conjugated 7 nm $Fe_3O_4$.

In each case, the antibody addition procedure resulted in a negligible change in the aggregation of the products and no loss in long term stability in aqueous solution. The presence of the antibody attached to the surface of the nanoparticles was confirmed by measuring the hydrodynamic shell of the products throughout every step of the procedure using dynamic light scattering (DLS) shown in Figure 6.9.

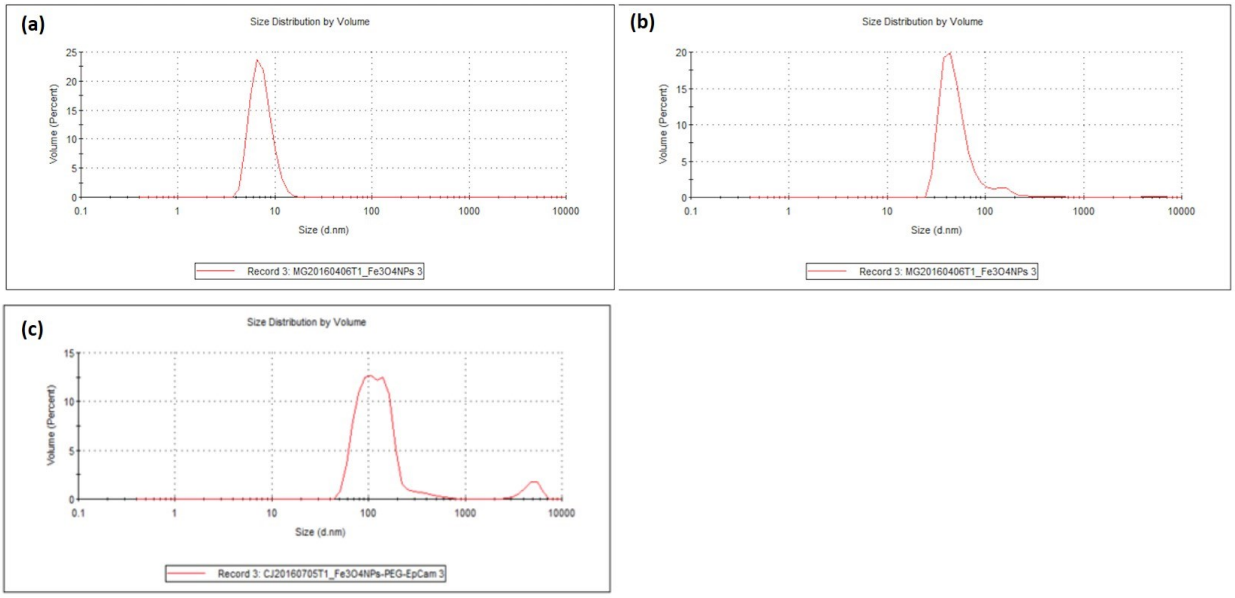


**Figure 6.9.** Dynamic light scattering (DLS) results of (a) oleylamine-stabilized 7 nm $Fe_3O_4$, (b) *O,O′*-Bis(2-carboxyethyl)dodecaethylene glycol (30 carbon PEG)-stabilized 7 nm $Fe_3O_4$, and (c) MNV antibody conjugated 7 nm $Fe_3O_4$.

DLS results in Figure 6.9(a) indicate that the original oleylamine-stabilized particles are approximately 9 nm, in agreement with the results via TEM. The 2 nm size increase is explained by the presence of oleylamine on the surface of the nanoparticles, which adds ~2 nm to the hydrodynamic shell of the nanoparticle.[21] Figure 6.9(b) indicates an increase in the hydrodynamic shell of the particles to ~50 nm from the ligand exchange and presence of *O,O′*-

Bis(2-carboxyethyl)dodecaethylene glycol, which is in agreement with reported results.[17] Figure 6.9(c) indicates a size increase in hydrodynamic shell to over 100 nm, likely indicating the presence of the attached antibody. Information on the exact hydrodynamic size of antibodies is difficult to find, however, this size increase is reasonable in comparison with other antibodies.[17]

### 6.3.4 Protein Conjugations

An attempt was made to conjugate streptavidin and *MBP-GFP-ActA* proteins to our $Fe_3O_4$ nanoparticles, however without success. The same procedure as the antibody conjugation was followed. Results are shown in the TEM images in Figure 6.10.

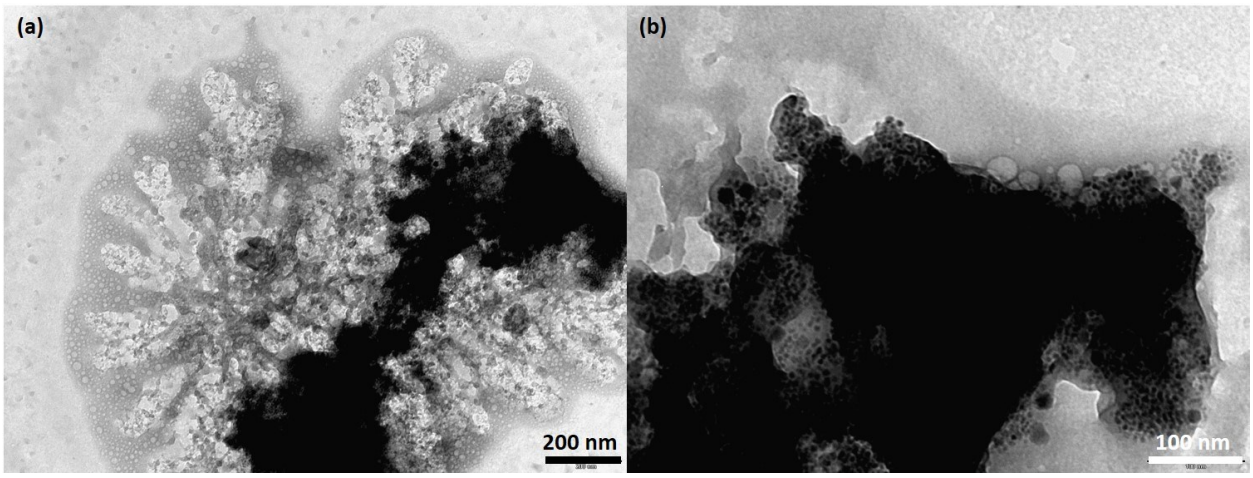


**Figure 6.10.** Transmission electron microscopy (TEM) images of (a) streptavidin and (b) *MBP-GFP-ActA* protein conjugations.

As shown in Figure 6.10, the protein conjugations resulted in an excess of organics and large amounts of aggregation. No further attempts at protein conjugation were made.

## 6.4 CONCLUSIONS

In Chapter 6, we have made great strides in developing superparamagnetic iron oxide ($Fe_3O_4$) nanoparticles conjugated with targeted antibodies as viable capture vehicles for both public health and biomedical applications. This chapter presented the entire protocol development process from start to finish: synthesis of the superparamagnetic iron oxide, ligand exchange and phase transfer of the particles to aqueous solution, and antibody conjugation. Our protocols have been characterized by transmission electron microscopy (TEM) and dynamic light scattering (DLS), confirming the presence of the antibody on the surface of the nanoparticle. We have screened particle sizes and determined that a smaller size is more advantageous to promoting long term stabilization of the particles in aqueous solution. We have also screened various PEG chain lengths and determined that an intermediate size is ideal to promote enough particle stabilization to prevent sedimentation under gravitational forces, but allow for capture in the presence of an external magnetic field. This work should be thought of as a template for which drug delivery and/or virus capture processes involving nanomaterials could be developed.

## 6.5 REFERENCES


1. Gaorav P. Gupta & Joan Massague. Cancer Metastasis: Building a Framework. *Cell* **127**, (2006).
2. Cristoph A. Klein. The Metastasis Cascade. *Science* **321**, 1785–1787 (2008).
3. Anne C. Chiang & Joan Massague. Molecular Basis of Metastasis. *N. Engl. J. Med.* **359**, 2814–2823 (2008).
4. Shyamala Maheswaran & Daniel A. Haber. Circulating Tumor Cells: A Window into Cancer Biology and Metstasis. *Curr Opin Genet Dev.* **20**, 96–99 (2010).
5. Christine L. Chaffer & Robert A. Weinberg. A Perspective on Cancer Cell Metastasis. *Science* **331**, 1559–1564 (2011).
6. Stratified, personalised or P4 medicine: a new direction for placing the patient at the centre of healthcare and health education. *Academy of Medical Sciences* (2015).
7. Thomas R> Egnew. Suffering, Meaning, and Healing: Challenges of Contemporary Medicine. *Ann Fam Med* **7**, 170–175 (2009).
8. Wieling He *et al.* Clinical Significance of Circulating Tumor Cells in Predicting Disease Progression and Chemotherapy Resistance in patients with Gestational Choriocarcinoma. *Int. J. Cancer* **144**, 1421–1431 (2019).
9. Hengyi Xu *et al.* Antibody Conjugated Magnetic iron Oxide Nanoparticles for Cancer Cell Separation in Fresh Whole Blood. *Biomaterials* **32**, 9758–9765 (2011).
10. Marisa Maltez-da Costa *et al.* Simple Monitoring of Cancer Cells Using Nanoparticles. *Nano Lett.* **12**, 4164–4171 (2012).

11. Vanessa Morton, Julie Jean, Jeffrey Farber & Kristen Mattison. Detection of Noroviruses in Ready-To-Eat Foods by using Carbohydrate-Coated Magnetic Beads. *Appl. Environ. Microbiol.* **75**, 4641–4643 (2009).
12. Saskia A. Rutjes, Froukje Lodder-Verschoor, Wim. H. M. Van Der Poel, Yvonne T. H. P. van Duijnhoven & Ana Maria de Roda Husman. Detection of Noroviruses in Foods: A Study on Virus Extraction Procedures in Foods Implicated in outbreaks of Human Gastroenteritis. *J. Food. Prot.* **69**, 1949–1956 (2006).
13. Albert Bosch *et al.* Foodbourne Viruses: Detection, Risk Assessment, and Control Options in Food Processing. *International Journal of Food Microbiology* **285**, 110–128 (2018).
14. Gary W. Brunette. *CDC Yellow Book 2018: Health Information for International Travel*. (Oxford University Press, 2018).
15. Ben Lopman. Global Burden of Norovirus and Prospects for Vaccine Development. *CDC* **1**, 1–41 (2015).
16. Duo Ma, Luhui Shen, Kaiye Wu, Chris W. Diehnelt & Alexander A. Green. Low-cost Detection of Norovirus Using Paper-based Cell-free Systems and Synbody-based Viral Enrichment. *Synthetic Biology* **3**, 1–11 (2018).
17. Jin Xie, Chenjie Xu, Nathan Kohler, Yanglong Hou & Shouheng Sun. Controlled PEGylation of Monodisperse Fe3O4 Nanoparticles for Reduced Non-Specific Uptake by Macrophage Cells. *Adv. Mater.* **19**, 3163–3166 (2007).
18. Shouheng Sun *et al.* Monodisperse MFe2O4 (M = Fe, Co Mn) Nanoparticles. *J. Am. Chem. Soc.* 273–279 (2004).
19. Nicola Pinna *et al.* Magnetite Nanocrystals: Nonaqueous Synthesis, Characterization, and Solubility. *Chem. Mater.* **17**, 3044–3049 (2005).

20. Greg T. Hermanson. *Bioconjugate Techniques*. (Elsevier Academic Press, 2009).

21. JitKang Lim, Swee Pin Yeap, Hui Xin Che & Siew Chun Low. Characterization of Magnetic Nanoparticle by Dynamic Light Scattering. *Nanoscale Research Letters* **8**, 381 (2013).

# Chapter 7. Synthesis of Magnetic and Dielectric Nanoparticle Products for Tunable Electromagnetic Wave Absorption

## 7.1 INTRODUCTION

Throughout the course of this doctoral research, many different nanoparticle products were synthesized but never fully investigated for their electromagnetic wave absorption properties. These products include various magnetic and dielectric nanoparticles, synthesized by a wide range of methods: organic solution synthesis, hydrothermal synthesis, and substrate templated synthesis. There were two main thrusts of these syntheses:

1) Investigation of magnetic and dielectric with shape anisotropy for electromagnetic wave absorption.
2) Investigation of hard magnetic materials for electromagnetic wave absorption.

The first of these thrusts, the investigation of materials displaying a shape anisotropy, is geared at developing a tunable electromagnetic wave absorbing device. Rods and wires were predominantly chosen for these studies due to the large difference in the magnetic or dielectric properties of the materials displayed when aligned to a magnetic field along the easy axis in comparison with a random orientation.[1] Stemming from the tunability in the magnetic or dielectric properties, it is thought that an aligned vs. randomly oriented materials will also display tunable electromagnetic wave absorption properties, and can thus be used as advanced materials for electromagnetic wave absorption simply by adjusting the strength of the magnetic or electric field present. It is easy to see how a material with tunable electromagnetic wave absorption properties would be of high importance for military/defense purposes, as planes and/or submarines would be able to choose appropriate frequencies to absorb by running a

current through the outside surface of the vessel. In an ideal world, a military vessel could be built out of a material with an electrical network etched into the outer surface and coated with nanomaterials with shape anisotropy of a desired composition. Then, by simply choosing a an appropriate current to run through the external electrical network, pilots would gain the capability of absorbing incoming radar waves in accordance with which radar they expect to encounter on while on field missions. In reality, this may be a difficult technology to implement, as building a plane or submarine has many other logistical challenges such as material weight, buoyancy, and stability, amongst others. Nevertheless, it is an interesting topic to explore.

The inspiration for these syntheses came from a 2014 study on the magnetic properties of cobalt nanowires from J. Ping Liu.[2] The cobalt nanowires were shown to display a high magnetization and coercivity, both of which are critical to electromagnetic wave absorption (previously discussed in Chapter 2), that is tunable by the alignment of the particles to an external magnetic field.[3,4] These results are demonstrated in Figure 7.1 (b) and (c). By aligning the nanowires, the coercivity of the material was increased from 6.5 kOe (randomly oriented) to 10.3 kOe (aligned).[2]

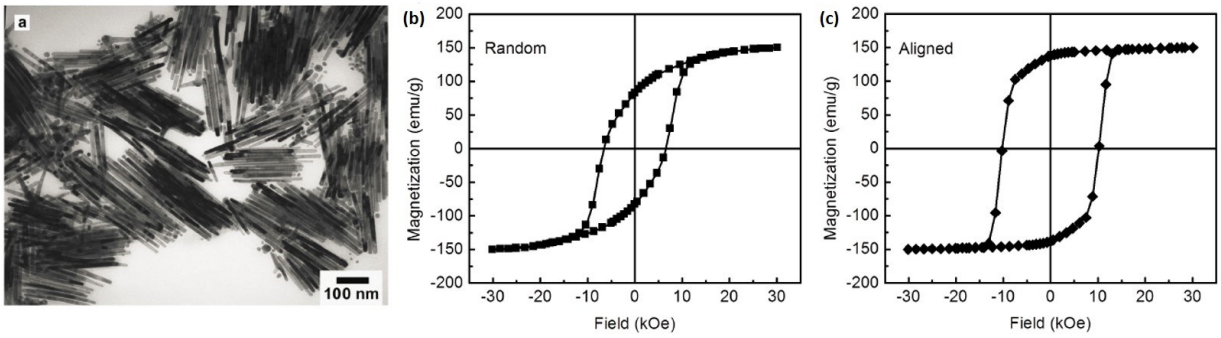


**Figure 7.1** (a) TEM image and magnetic hysteresis curves for (b) randomly oriented and (c) aligned cobalt nanowires.[2]

The tunability of the magnetic properties of these cobalt nanowires adequately demonstrated the behaviors required to begin work towards the goal of a tunable microwave absorber, thus, these nanowires were chosen as a starting point for the study. By adjusting synthetic parameters, cobalt nanowires, nanorods, and nanocubes were synthesized.

In order to approach this problem from a different angle than magnetics, it was decided to explore the tunability of the dielectric side of electromagnetic absorption. For this purpose, barium titanate ($BaTiO_3$) nanorods were chosen as a starting point due to the extremely high values of their dielectric constants which makes them a promising candidate for electromagnetic wave absorption.[5–7] Barium titanate was synthesized according to established procedures in both nanorod and nanowire morphologies.[5,6]

The second of these research thrusts involved investigating hard magnetic materials for electromagnetic wave absorption. Hard magnetic materials are known to have high magnetization and coercivity, which, as previously discussed, make them excellent candidates for electromagnetic absorption.[6,7] The inspiration for this thrust came from a study on a new FeCrSe hard magnetic alloy, by Zhidong Zhang, in which the magnetization and coercivity of the

$Fe_2CrSe_4$ alloy were able to be tuned by varying the composition of the alloy.[8] These results are shown in Figure 7.2.

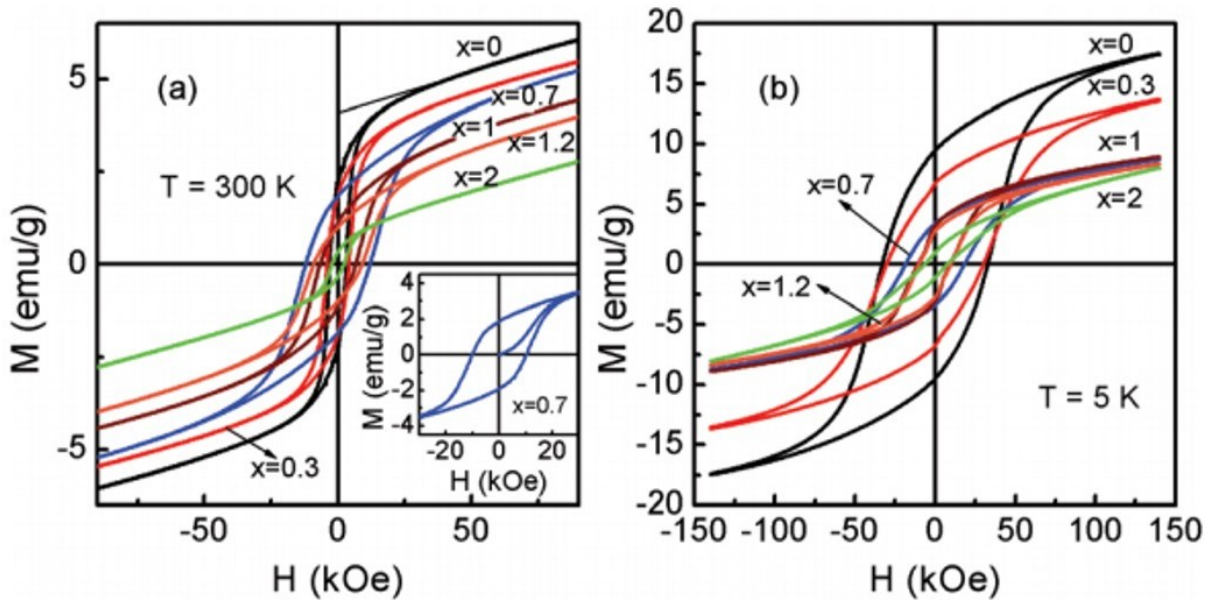


**Figure 7.2** Hysteresis loops of the as-prepared $Fe_{3-x}Cr_xSe_4$ nanostructures measured at (a) 300 K and (b) 5 K. The inset in (a) shows the magnetization curves of the $Fe_{2.3}Cr_{0.7}Se_4$.[8]

As demonstrated in the above Figure 7.2, simply by varying the composition of the FeCrSe alloy, the coercivity and magnetization can be tuned. Based on Figure 7.2(a), a composition of $Fe_{2.3}Cr_{0.7}Se_4$ results in the highest coercivity for the material, and thus was chosen as our synthetic goal for the following studies.

In Chapter 7, the synthetic protocol and characterization for the aforementioned magnetic and dielectric nanoparticles is discussed. As previously discussed, these products have yet to be investigated for their electromagnetic properties; this is largely due to logistical reasons involving experimental set up. Primarily, it is difficult to devise a system to measure the electromagnetic response of a material while aligned under an external magnetic field, or to even

make *in situ* magnetic characterizations. While these particles do hold much promise in improving the current electromagnetic wave absorbing material technology, a thorough effort will be required to adequately develop the proper characterization techniques to explain the tunability it is thought that many of these products will display. In the future stages of this project, this would be an important research thrust to keep in mind.

## 7.2 SYNTHESIS OF VARIOUS MAGNETIC NANOMATERIALS FOR ELECTROMAGNETIC WAVE ABSORPTION

### 7.2.1 Experimental Methods

*Chemicals.* All materials (metal precursors, organic solvents, ligands, substrates) were purchased from Sigma Aldrich. All chemicals were used as received.

*Synthesis Design.* All nanoparticles were synthesized under atmospheric conditions in a 50 mL Teflon lined autoclave, unless otherwise specified. All synthesis procedures were adapted and modified from previous reports.

### 7.2.2 Materials Characterization

Transmission electron microscopy (TEM) images were acquired on a 120 kV, FEI Tecnai 12 TWIN microscope. X-ray diffraction (XRD) patterns were collected on a PANalytical X'Pert$^3$ Powder X-Ray Diffractometer equipped with a Cu Kα radiation source (λ=0.15406). Scanning transmission electron microscopy (SEM) and energy-dispersive X-ray spectroscopy (EDS) characterization of nanoparticles, including spectra collected to produce the elemental maps, were conducted on a JEOL 2200FS TEM/STEM equipped with a CEOS aberration (probe) corrector and a Bruker-AXS X-Flash 5030 silicon drift X-ray detector. The microscope was operated at 200 kV, and the electron beam size was ~0.7 Å for imaging and ~2 Å for EDS analysis (probe current ~400-500 pA).

### 7.2.3 Synthesis of $Fe_3O_4$ Nanorods

*Synthesis of 100 nm $Fe_3O_4$ Nanorods.*[9] 100 nm $Fe_3O_4$ nanorods were synthesized by the decomposition of iron pentacarbonyl ($Fe(CO)_5$). In a typical synthesis, hexadecylamine (0.628 g, 2.6 mmol) was dissolved in oleic acid (6.30 mL, 19.83 mmol) and *n*-octanol (25.06 mL, 0.23

mmol), heated at 50°C, and stirred until the reaction solution became homogeneous. Once homogeneous, the reaction solution was transferred to a Teflon lined 50 mL autoclave and argon gas bubbled through for ~10 minutes. After the reaction solution had been degassed by bubbling argon, iron pentacarbonyl (5.69 mL, 43.27 mmol) was injected and the autoclave immediately sealed to prevent any inflow of atmospheric oxygen. The reaction-containing autoclave was then placed in an oven preheated to 200°C and allowed to react at this temperature for six hours, after which the autoclave was removed from the oven and allowed to cool to room temperature. The precipitate was collected by centrifugation at 8000 rpm for 10 min, re-dispersed in ethanol, and centrifuged two more times at 8000 rpm for 10 min. The final product was dried in air and re-dispersed in hexanes.

*Materials Characterization of ~100 nm $Fe_3O_4$ Nanorods.* Transmission electron microscopy (TEM) images for the as synthesized $Fe_3O_4$ nanorods are shown in Figure 7.3(a). Through size distribution analysis, the nanorods have been determined to have length of 90 – 110 nm and width of 7 – 11 nm. Figure 7.3(b) presents the typical x-ray diffraction (XRD) pattern for the $Fe_3O_4$ nanorods. All of the peaks align with the expected pattern for a cubic magnetite structure as confirmed by their perfect agreement with JCPDS No. 00-09-0629. No other diffraction peaks besides those corresponding to $Fe_3O_4$ were observed, which indicates high purity of our as-synthesized products. The synthesized nanorods would be a good candidate for a study to determine the effect of randomly oriented nanorods in comparison to aligned nanorods for electromagnetic wave absorption.

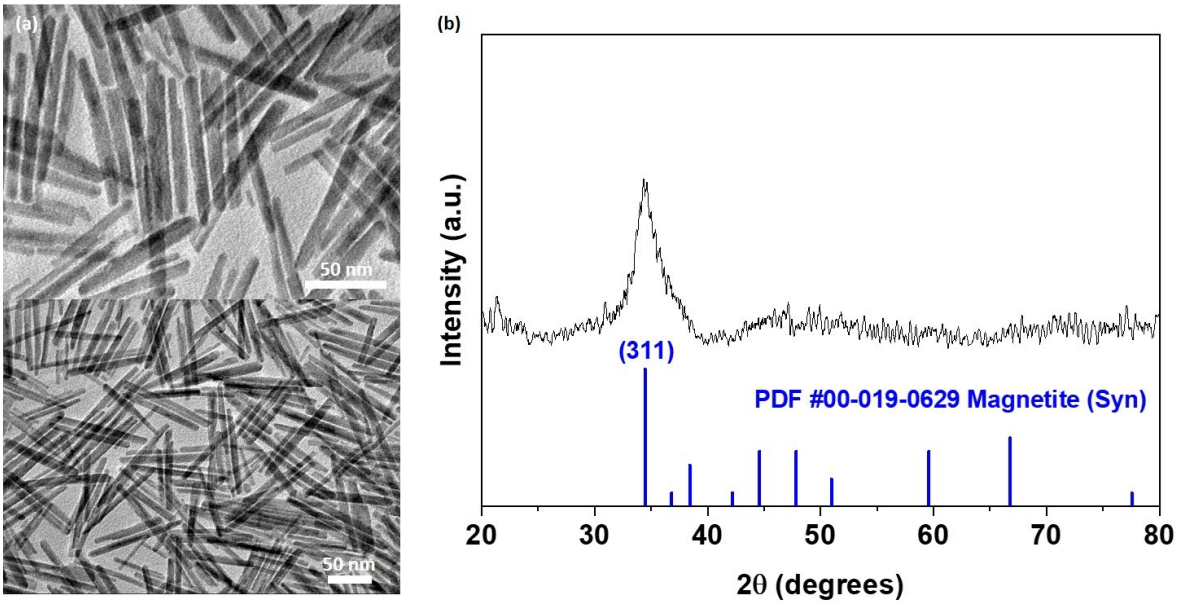


**Figure 7.3** (a) TEM images and (b) XRD pattern for $Fe_3O_4$ nanorods.

### 7.2.4 Synthesis of Co Nanowires

500 – 700 nm Co nanowires were synthesized by the decomposition of cobaltous laurate ($Co(C_{12}H_{23}O_2)_2$). This synthesis is done in a two-step process.

*(1) Synthesis of cobaltous laurate.*[2,10,11] In a typical synthesis, lauric acid ($C_{12}H_{24}O_2$) (1.763 g, 8.8 mmol) and sodium hydroxide (0.356 g, 8.4 mmol) were dissolved in 8 mL of deionized water, heated at 60°C, and stirred until the reaction solution became homogeneous (Solution 1). Simultaneously, cobalt chloride hexahydrate ($CoCl_2 \cdot 6H_2O$) (0.953 g, 4.0 mmol) was dissolved in 2 mL of deionized water (Solution 2). Once homogeneous, Solution 2 was added dropwise to Solution 1 while maintaining a reaction temperature of 60°C. The reaction was allowed to stir for 30 minutes at 60°C and then cooled to room temperature. The precipitate was collected by centrifugation in deionized water once at 10,000 rpm for 10 min, re-dispersed

in methanol, and centrifuged two more times at 10,000 rpm for 10 min. The final product was dried in air at 60°C for 12 hours.

*(2) Synthesis of 500 – 700 nm Co Nanowires.*[2] In a typical synthesis, cobalt laurate (0.206 g, 0.45 mmol), ruthenium chloride ($RuCl_3$) (0.00037 g, 0.0018 mmol), and hexadecylamine (0.058 g, 0.24 mmol) were dissolved in 6 mL of 1,2-butanediol in a 10 mL pressure vessel. The pressure vessel was sealed with a rubber stopper and purged with a 7% $H_2$, 93% $N_2$ gas mixture for five minutes at room temperature. While remaining in a purging state, the pressure vessel was placed in an oil bath and heated to 80°C for 60 minutes with magnetic stirring. After this, the pressure vessel with the rubber stopper was removed from the oil bath and immediately transferred into a glove box with Ar atmosphere to change the cap from the rubber stopper to a Teflon cap and remove the stir bar. The Teflon capped pressure vessel was then taken back out of the glove box and placed in an oven preheated to 250°C for 75 minutes, then cooled to room temperature. The precipitate was collected by centrifugation in toluene three times at 6,000 rpm for 10 min, and re-dispersed in toluene for storage.

*Materials Characterization of 500 – 700 nm Co Nanowires.* Transmission electron microscopy (TEM) images for the as synthesized Co nanowires are shown in Figure 7.4(a). Through size distribution analysis, the nanowires have been determined to have length of 500 – 700 nm and width of 20 nm. Figure 7.4(b) presents the typical x-ray diffraction (XRD) pattern for the Co nanowires. All of the peaks align with the expected pattern for cobalt as confirmed by their perfect agreement with JCPDS No. 01-089-4308. No other diffraction peaks besides those corresponding to Co were observed, which indicates high purity of our as-synthesized products. The synthesized nanowires would be a good candidate for a study to determine the effect of

randomly oriented nanowires in comparison to magnetically aligned nanowires for electromagnetic wave absorption.

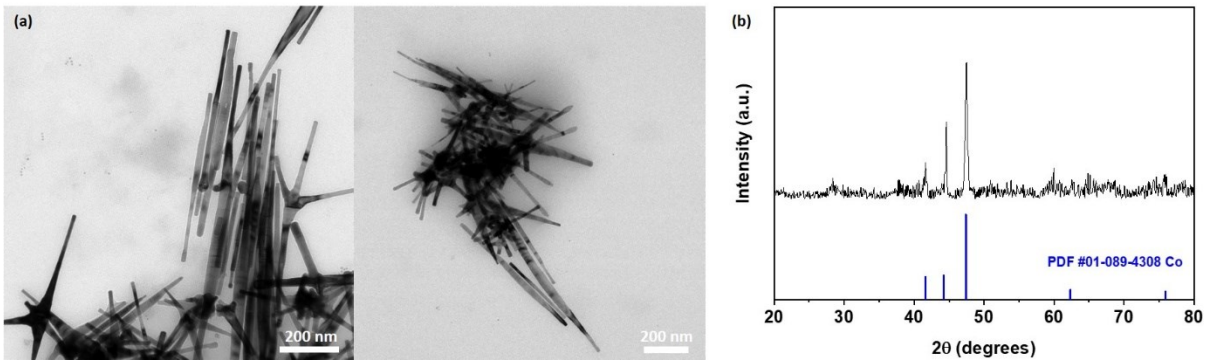


**Figure 7.4** (a) TEM images and (b) XRD pattern for Co nanowires.

### 7.2.5 Synthesis of Co Nanocubes

30 nm Co nanocubes were synthesized by the decomposition of cobaltous laurate ($Co(C_{12}H_{23}O_2)_2$). This synthesis is done in a two-step process.

*(1) Synthesis of cobaltous laurate.*[2,10,11] In a typical synthesis, lauric acid ($C_{12}H_{24}O_2$) (1.763 g, 8.8 mmol) and sodium hydroxide (0.356 g, 8.4 mmol) were dissolved in 8 mL of deionized water, heated at 60°C, and stirred until the reaction solution became homogeneous (Solution 1). Simultaneously, cobalt chloride hexahydrate ($CoCl_2 \cdot 6H_2O$) (0.953 g, 4.0 mmol) was dissolved in 2 mL of deionized water (Solution 2). Once homogeneous, Solution 2 was added dropwise to Solution 1 while maintaining a reaction temperature of 60°C. The reaction was allowed to stir for 30 minutes at 60°C and then cooled to room temperature. The precipitate was collected by centrifugation in deionized water once at 10,000 rpm for 10 min, re-dispersed

in methanol, and centrifuged two more times at 10,000 rpm for 10 min. The final product was dried in air at 60°C for 12 hours.

*(2) Synthesis of 30 nm Co Nanocubes.*[2] In a typical synthesis, cobalt laurate (0.206 g, 0.45 mmol), ruthenium chloride ($RuCl_3$) (0.00074 g, 0.0036 mmol), and hexadecylamine (0.058 g, 0.24 mmol) were dissolved in 6 mL of 1,2-octanediol in a 10 mL pressure vessel. The pressure vessel was sealed with a rubber stopper and purged with a 7% $H_2$, 93% $N_2$ gas mixture for five minutes at room temperature. While remaining in a purging state, the pressure vessel was placed in an oil bath and heated to 80°C for 60 minutes with magnetic stirring. After this, the pressure vessel with the rubber stopper was removed from the oil bath and immediately transferred into a glove box with Ar atmosphere to change the cap from the rubber stopper to a Teflon cap and remove the stir bar. The Teflon capped pressure vessel was then taken back out of the glove box and placed in an oven preheated to 250°C for 75 minutes, then cooled to room temperature. The precipitate was collected by centrifugation in toluene three times at 6,000 rpm for 10 min, and re-dispersed in toluene for storage.

*Materials Characterization of 30 nm Co Nanocubes.* The synthesis for the Co nanocubes follows the same procedure as that of the Co nanowires, however with a varied amount of ruthenium chloride. Transmission electron microscopy (TEM) images for the as synthesized Co nanocubes are shown in Figure 7.5(a). Through size distribution analysis, the nanocubes have been determined to have length of 25 – 35 nm and a wide range of widths from 10 – 30 nm. Figure 7.5(b) presents the typical x-ray diffraction (XRD) pattern for the Co nanocubes. All of the peaks align with the expected pattern for cobalt as confirmed by their perfect agreement with JCPDS No. 01-089-4308. No other diffraction peaks besides those corresponding to Co were observed, which indicates high purity of our as-synthesized products. The synthesized nanowires

would be a good candidate for a study to determine the effect of shape by comparison to the previously discussed Co nanowires, or Co nanoparticles discussed in Chapter 4, for electromagnetic wave absorption.

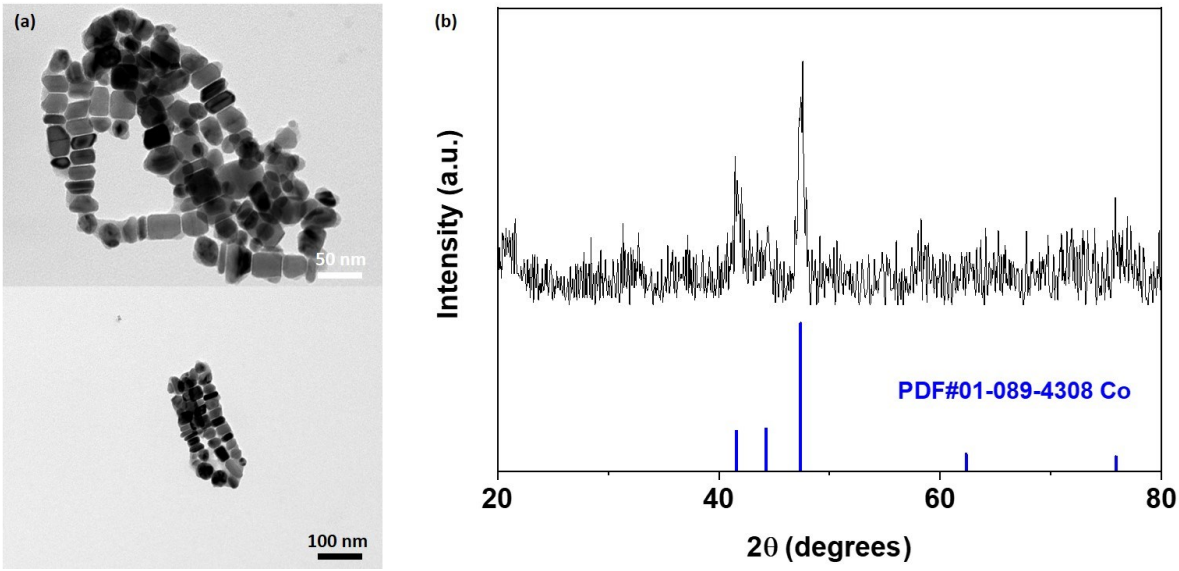


**Figure 7.5** (a) TEM images and (b) XRD pattern for Co nanocubes.

### 7.2.6 Synthesis of Co Nanorods

100 nm Co nanorods were synthesized by the decomposition of cobaltous laurate ($Co(C_{12}H_{23}O_2)_2$). This synthesis is done in a two-step process.

*(1) Synthesis of cobaltous laurate.*[2,10,11] In a typical synthesis, lauric acid ($C_{12}H_{24}O_2$) (1.763 g, 8.8 mmol) and sodium hydroxide (0.356 g, 8.4 mmol) were dissolved in 8 mL of deionized water, heated at 60°C, and stirred until the reaction solution became homogeneous (Solution 1). Simultaneously, cobalt chloride hexahydrate ($CoCl_2 \cdot 6H_2O$) (0.953 g, 4.0 mmol) was dissolved in 2 mL of deionized water (Solution 2). Once homogeneous, Solution 2 was

added dropwise to Solution 1 while maintaining a reaction temperature of 60°C. The reaction was allowed to stir for 30 minutes at 60°C and then cooled to room temperature. The precipitate was collected by centrifugation in deionized water once at 10,000 rpm for 10 min, re-dispersed in methanol, and centrifuged two more times at 10,000 rpm for 10 min. The final product was dried in air at 60°C for 12 hours.

*(2) Synthesis of 100 nm Co Nanorods.*[2] The synthesis for the Co nanorods follows the same procedure as that of the Co nanowires, however with a varied amount of ruthenium chloride. In a typical synthesis, cobalt laurate (0.206 g, 0.45 mmol), ruthenium chloride ($RuCl_3$) (0.00055 g, 0.0027 mmol), and hexadecylamine (0.058 g, 0.24 mmol) were dissolved in 6 mL of 1,2-octanediol in a 10 mL pressure vessel. The pressure vessel was sealed with a rubber stopper and purged with a 7% $H_2$, 93% $N_2$ gas mixture for five minutes at room temperature. While remaining in a purging state, the pressure vessel was placed in an oil bath and heated to 80°C for 60 minutes with magnetic stirring. After this, the pressure vessel with the rubber stopper was removed from the oil bath and immediately transferred into a glove box with Ar atmosphere to change the cap from the rubber stopper to a Teflon cap and remove the stir bar. The Teflon capped pressure vessel was then taken back out of the glove box and placed in an oven preheated to 250°C for 75 minutes, then cooled to room temperature. The precipitate was collected by centrifugation in toluene three times at 6,000 rpm for 10 min, and re-dispersed in toluene for storage.

*Materials Characterization of 100 nm Co Nanorods.* Transmission electron microscopy (TEM) images for the as synthesized Co nanorods are shown in Figure 7.6(a). Through size distribution analysis, the nanorods have been determined to have length of 100 – 130 nm and a width from 10 – 15 nm. Figure 7.6(b) presents the typical x-ray diffraction (XRD) pattern for the

Co nanorods. All of the peaks align with the expected pattern for cobalt as confirmed by their perfect agreement with JCPDS No. 01-089-4308. No other diffraction peaks besides those corresponding to Co were observed, which indicates high purity of our as-synthesized products. The synthesized nanowires would be a good candidate for a study to determine the effect of shape and compared to the previously discussed Co nanowires, Co nanocubes, or Co nanoparticles discussed in Chapter 4, for electromagnetic wave absorption.

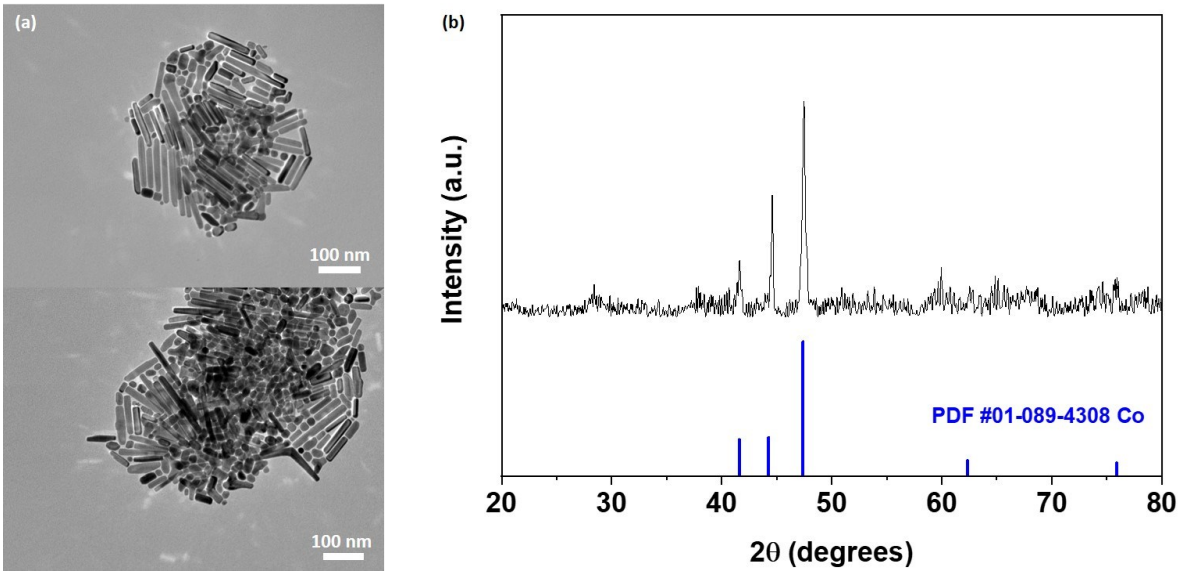


**Figure 7.6** (a) TEM images and (b) XRD pattern for Co nanorods.

### 7.2.7 Synthesis of $Fe_2CrSe_4$ Hard Magnetic Alloy

*Synthesis of 5 nm $Fe_2CrSe_4$ Nanoparticles.*[8] 10 nm $Fe_2CrSe_4$ nanoparticles were synthesized by the decomposition of iron (III) acetylacetonate ($Fe(acac)_3$) and chromium (III) acetylacetonate ($Cr(acac)_3$). In a typical synthesis, iron (III) acetylacetonate (0.371 g, 1.05 mmol) and chromium (III) acetylacetonate (0.349 g, 1.0 mmol) were dissolved in 9 mL oleylamine and

1 mL oleic acid and heated for 20 min at 180°C to promote the decomposition of the Fe and Cr. After 20 minutes, the reaction temperature was increased to 200°C and selenium powder (0.158 g, 2.0 mmol) dissolved in 3 mL of oleylamine was injected. The reaction was then refluxed for 10 min at a higher temperature (300°C) and the temperature decreased to 250°C for 60 minutes for nanoparticle growth. The precipitate was collected by centrifugation at 6000 rpm for 10 min, re-dispersed in ethanol, and centrifuged once again at 6000 rpm for 10 min. The final product was re-dispersed in hexanes and stabilized with 2-3 drops of oleylamine.

*Materials Characterization of 5 nm $Fe_2CrSe_4$ Nanoparticles.* Transmission electron microscopy (TEM) images for the as synthesized $Fe_2CrSe_4$ nanoparticles are shown in Figure 7.7(a). Through size distribution analysis, the $Fe_2CrSe_4$ nanoparticles have been determined to have an average size of 5.32 nm. Figure 7.7(b) presents the typical x-ray diffraction (XRD) pattern for the $Fe_2CrSe_4$ nanoparticles. All of the peaks align with the expected pattern for a cubic magnetite structure as confirmed by their perfect agreement with JCPDS No. 01-089-1966. No other diffraction peaks besides those corresponding to $Fe_2CrSe_4$ were observed, which indicates high purity of our as-synthesized products. The $Fe_2CrSe_4$ nanoparticles were synthesized in the composition $Fe_{2.15}Cr_{0.85}Se_4$ as determined by energy dispersive x-ray spectroscopy (EDX). The synthesized $Fe_2CrSe_4$ nanoparticles would be a good candidate for a study to explore new hard magnetic materials for electromagnetic wave absorption.

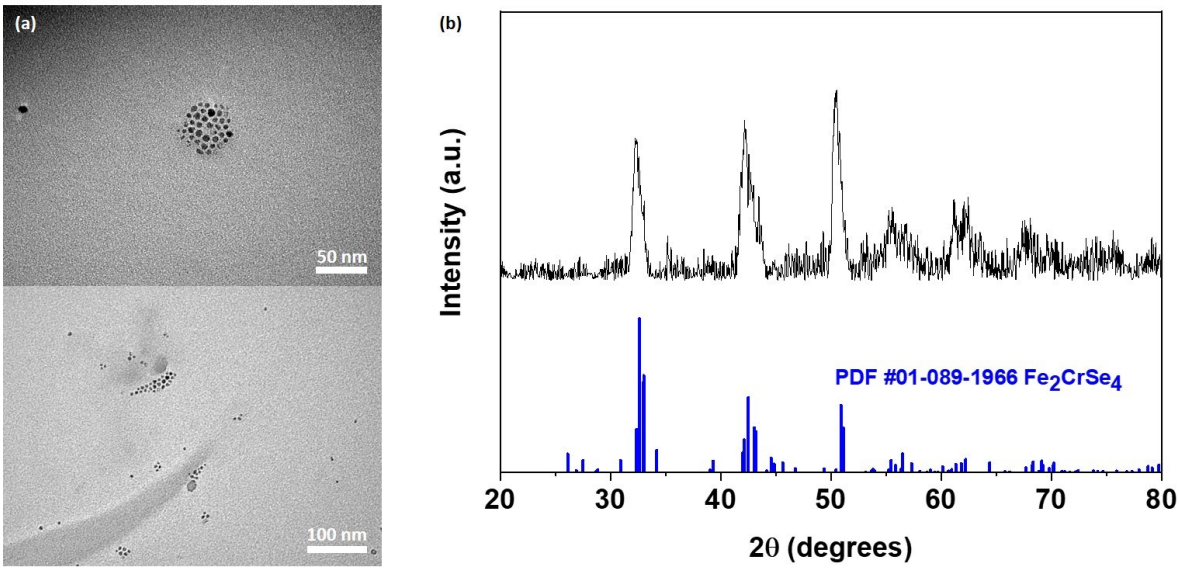


**Figure 7.7** (a) TEM images and (b) XRD pattern for $Fe_2CrSe_4$ nanoparticles.

## 7.3 SYNTHESIS OF VARIOUS DIELECTRIC MATERIALS FOR ELECTROMAGNETIC WAVE ABSORPTION

### 7.3.1 Experimental Methods

*Chemicals.* All materials (metal precursors, organic solvents, ligands, substrates) were purchased from Sigma Aldrich. All chemicals were used as received.

*Synthesis Design.* All nanoparticles were synthesized under atmospheric conditions in a 50 mL Teflon lined autoclave, unless otherwise specified. All synthesis procedures were adapted and modified from previous reports.

### 7.3.2 Materials Characterization

Transmission electron microscopy (TEM) images were acquired on a 120 kV, FEI Tecnai 12 TWIN microscope. X-ray diffraction (XRD) patterns were collected on a PANalytical X'Pert$^3$ Powder X-Ray Diffractometer equipped with a Cu Kα radiation source (λ=0.15406). Scanning transmission electron microscopy (SEM) and energy-dispersive X-ray spectroscopy (EDS) characterization of nanoparticles, including spectra collected to produce the elemental maps, were conducted on a JEOL 2200FS TEM/STEM equipped with a CEOS aberration (probe) corrector and a Bruker-AXS X-Flash 5030 silicon drift X-ray detector. The microscope was operated at 200 kV, and the electron beam size was ~0.7 Å for imaging and ~2 Å for EDS analysis (probe current ~400-500 pA).

### 7.3.3 Synthesis of Free Standing $TiO_2$ Nanorods and Conversion to $BaTiO_3$

Free standing $TiO_2$ nanorods were purchased from nanoComposix. The TiO2 nanorods were of average length 55 nm and width 15 nm, surface functionalized with stearic acid, and

suspended in 1-butanol as shown below in the material data sheet provided by nanoComposix (Figure 7.8).

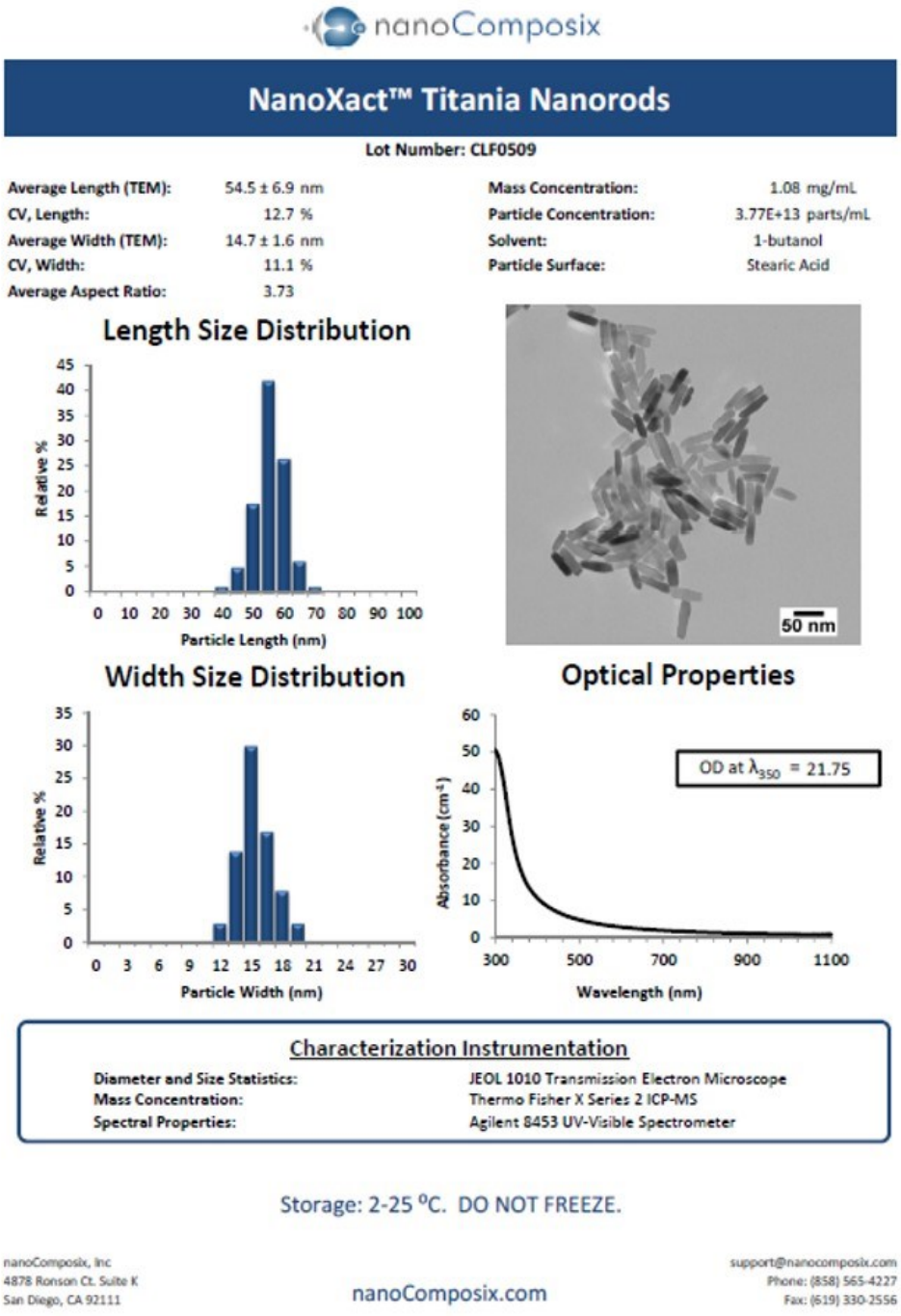


**Figure 7.8** Commercial TiO2 specs provided by nanoComposix.

*Conversion of Free Standing $TiO_2$ Nanorods to $BaTiO_3$ Nanorods.*[5,6] Commercial free standing $TiO_2$ nanorods were converted to $BaTiO_3$ by a reaction with barium hydroxide ($Ba(OH)_2$. In a typical reaction, 20 mL of 0.2 M barium hydroxide octahydrate ($Ba(OH)_2 \cdot 8H_2O$)) was mixed with 1 mg of the commercial $TiO_2$ nanorods in a Teflon lined 50 mL autoclave. The reaction-containing autoclave was then sealed and placed in an oven preheated to 210°C and allowed to react at this temperature for eight hours, after which the autoclave was removed from the oven and allowed to cool to room temperature. The precipitate was collected by washing three times, once with 0.2 M HCl, once with deionized water, and once with ethanol. The final product was dried in an oven at 600°C for 30 minutes and collected in a vial.

*Materials Characterization of Free Standing $BaTiO_3$ Nanorods.* Transmission electron microscopy (TEM) images for the as synthesized free standing $BaTiO_3$ nanorods are shown in Figure 7.9(a). Scanning electron microscopy (SEM) images for the as synthesized free standing $BaTiO_3$ nanorods are shown in Figure 7.9(b). Through size distribution analysis, the nanorods have been determined to have length of ~75 nm and width of 25 nm. The slight increase in size from the initial commercial $TiO_2$ nanorods is likely due to nanorod growth during the heating step of the conversion to $BaTiO_3$ as previously outlined. Figure 7.9(c) presents the typical x-ray diffraction (XRD) pattern for the $BaTiO_3$ nanorods. All of the peaks align with the expected pattern as confirmed by their perfect agreement reported patterns in literature.[6] No other diffraction peaks besides those corresponding to $BaTiO_3$ were observed, which indicates high purity of our as-synthesized products. Figure 7.9(d) displays the elemental composition of the $BaTiO_3$ nanorods as determined by energy dispersive x-ray spectroscopy (EDX). The $BaTiO_3$ nanorods were synthesized in the composition $Ba_{0.05}TiO_{2.98}$. Increasing the amount of $Ba(OH)_2$ in the synthetic process may help to increase the barium amount. The composition of titanium

and oxygen are as expected. Similar to the previous section on magnetic nanomaterials, the synthesized nanorods would be a good candidate for a study to determine the effect of randomly oriented nanorods in comparison to electrically aligned nanorods for electromagnetic wave absorption.

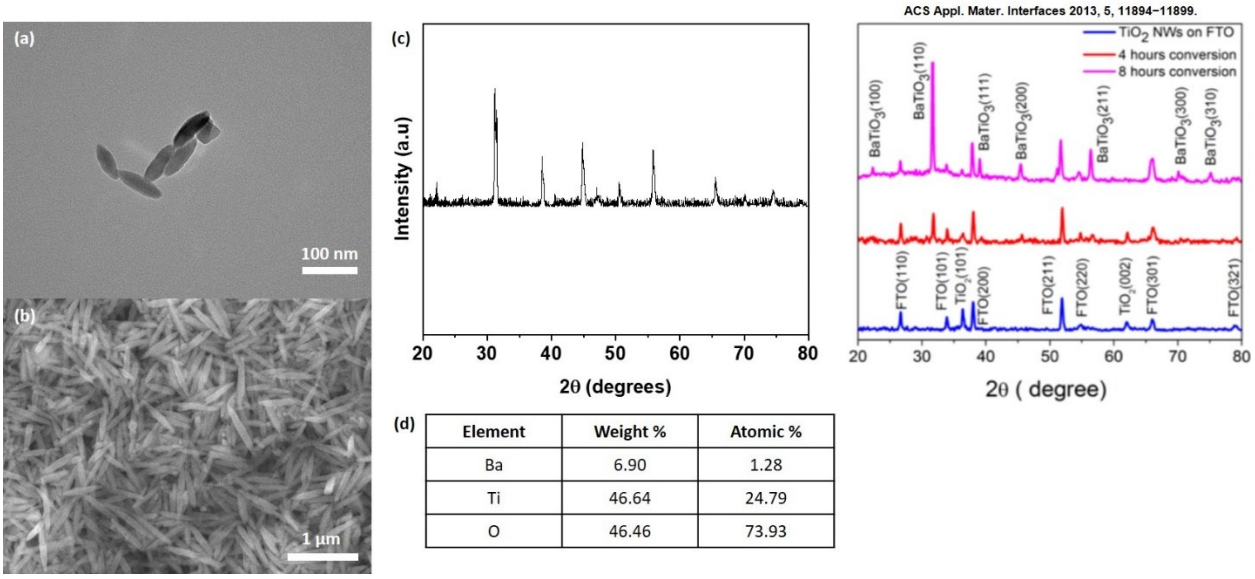


(d)

| Element | Weight % | Atomic % |
|---|---|---|
| Ba | 6.90 | 1.28 |
| Ti | 46.64 | 24.79 |
| O | 46.46 | 73.93 |

**Figure 7.9** (a) TEM image, (b) SEM image, (c) XRD pattern, and (d) EDX data for free standing $BaTiO_3$ nanorods. An inset is included to display a reported $BaTiO_3$ XRD pattern.

### 7.3.4 Synthesis of $TiO_2$ Nanorods via FTO Glass Substrate and Conversion to $BaTiO_3$

*Synthesis of $TiO_2$ Nanorods on FTO Glass Substrate.*[6] $TiO_2$ nanorods were synthesized by the decomposition of titanium isopropoxide ($C_{12}H_{28}O_4Ti$). In a typical synthesis, a 1.8 cm x 1.8 cm square of fluorine doped tin oxide (FTO) glass and titanium isopropoxide (1 mL, 3.38 mmol) were put in a Teflon lined 50 mL autoclave along with 10 mL deionized water and 10 mL hydrochloric acid. The reaction-containing autoclave was then placed in an oven preheated to 150°C and allowed to react at this temperature for five hours, after which the autoclave was

removed from the oven and allowed to cool to room temperature. Once at room temperature, the glass was removed and gently washed with ethanol and deionized water so as not to detach any $TiO_2$ nanorods.

*Conversion of $TiO_2$ Nanorods on FTO Glass Substrate to $BaTiO_3$ Nanorods.*[5,6] $TiO_2$ nanorods on the FTO glass substrate were converted to $BaTiO_3$ by a reaction with barium hydroxide ($Ba(OH)_2$. In a typical reaction, a 1.8 cm x 1.8 cm square of $TiO_2$ nanorods on FTO glass was placed in a Teflon lined 50 mL autoclave and 20 mL of 0.2 M barium hydroxide octahydrate ($Ba(OH)_2 \cdot 8H_2O$)) was added. The reaction-containing autoclave was then sealed and placed in an oven preheated to 210°C and allowed to react at this temperature for eight hours, after which the autoclave was removed from the oven and allowed to cool to room temperature. The precipitate was collected by gently washing three times, once with 0.2 M HCl, once with deionized water, and once with ethanol. The final product was dried in an oven at 600°C for 30 minutes and collected in a vial.

*Materials Characterization of $BaTiO_3$ Nanorods on FTO Glass Substrate.* Scanning electron microscopy (SEM) images for the as synthesized $TiO_2$ and $BaTiO_3$ nanorods on an FTO glass substrate are shown in Figure 7.10. Through size distribution analysis, the $TiO_2$ nanorods have been determined to have length of 500 – 800 nm and width of 100 nm. There was no size change upon conversion to $BaTiO_3$. Unfortunately, no x-ray diffraction (XRD) pattern for the $TiO_2$ or $BaTiO_3$ nanorods on FTO glass was able to be collected as the FTO glass dominated the spectrum so no $TiO_2$ or $BaTiO_3$ signal could be seen. A similar complication was encountered when determining the elemental composition of the $BaTiO_3$ nanorods by energy dispersive x-ray spectroscopy (EDX) as the signal was dominated by the tin from the substrate. Several attempts were made to remove the nanorods from the FTO glass substrate for XRD and EDX analysis

with no success. Attempted methods included sonication in a variety of organic solvents and physical scraping of the glass to try to remove the nanorods by a sheer force. Similar to the previous section on magnetic nanomaterials, the synthesized nanorods would be a good candidate for a study to determine the effect of randomly oriented nanorods in comparison to electrically aligned nanorods for electromagnetic wave absorption. However, as a disclaimer, the nanorods would need to be removed from the FTO substrate first.

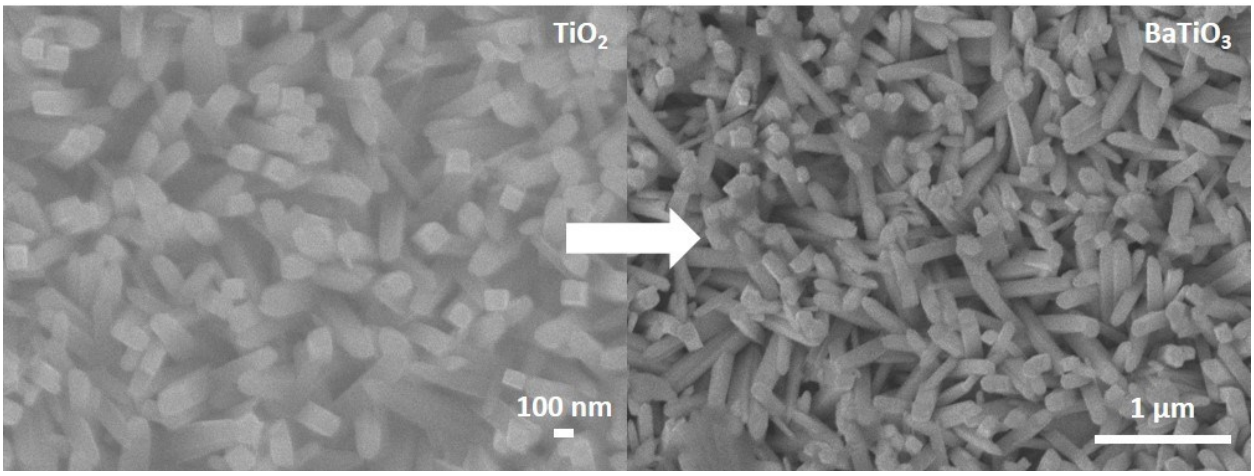


**Figure 7.10** SEM images for the conversion of $TiO_2$ on an FTO glass substrate to $BaTiO_3$.

### 7.3.5 Synthesis of $TiO_2$ Nanowires via Titanium Foil Substrate and Conversion to $BaTiO_3$

*Synthesis of $TiO_2$ Nanowires on Titanium Foil.*[5] In a typical synthesis, a 1.8 cm x 1.8 cm square of prewashed titanium foil (washed with deionized water) was placed in a Teflon lined 50 mL autoclave along with 30 mL of 1.0 M sodium hydroxide. The reaction-containing autoclave was then placed in an oven preheated to 220°C and allowed to react at this temperature for six hours, after which the autoclave was removed from the oven and allowed to cool to room

temperature. Once at room temperature, the foil was removed and immediately washed with ethanol and then soaked in 0.1 M $HNO_3$ for 1 hour. This process was repeated two more times. The foil was then removed from the nitric acid wash and dried in air at 70°C for 12 hours.

*Conversion of $TiO_2$ Nanowires on Titanium Foil to $BaTiO_3$ Nanowires.*[5,6] The $TiO_2$ nanowires on titanium foil were converted to $BaTiO_3$ by a reaction with barium hydroxide $(Ba(OH))_2$. In a typical reaction, a 1.8 cm x 1.8 cm square of $TiO_2$ nanowires on titanium foil was placed in a Teflon lined 50 mL autoclave and 20 mL of 0.2 M barium hydroxide octahydrate $(Ba(OH)_2 \cdot 8H_2O))$ was added. The reaction-containing autoclave was then sealed and placed in an oven preheated to 210°C and allowed to react at this temperature for eight hours, after which the autoclave was removed from the oven and allowed to cool to room temperature. The precipitate was collected by gently washing three times, once with 0.2 M HCl, once with deionized water, and once with ethanol. The final product was dried in an oven at 600°C for 30 minutes and collected in a vial.

*Materials Characterization of $BaTiO_3$ Nanowires on Titanium Foil.* Scanning electron microscopy (SEM) images for the as synthesized $TiO_2$ and $BaTiO_3$ nanowires on titanium foil are shown in Figure 7.11. Through size distribution analysis, the $TiO_2$ nanowires have been determined to be hundreds of microns in length, with a width close to 1 μm. Upon conversion to $BaTiO_3$, the nanowires became a more defined network as evidenced in Figure 7.11. Once again, no x-ray diffraction (XRD) pattern or energy dispersive x-ray spectroscopy (EDX) data for the $TiO_2$ or $BaTiO_3$ nanowires on titanium foil were able to be collected as the titanium foil dominated the spectrum so no $TiO_2$ or $BaTiO_3$ signal could be seen. As with the previous $TiO_2$ samples, or magnetic nanomaterials, the synthesized nanowires would be a good candidate for a study to determine the effect of randomly oriented nanowires in comparison to electrically

aligned nanowires for electromagnetic wave absorption. These nanowires could also be used to study any differences in electromagnetic behavior due to size or morphology of the dielectric materials as their size and shape greatly differ from previously synthesized $BaTiO_3$ products.

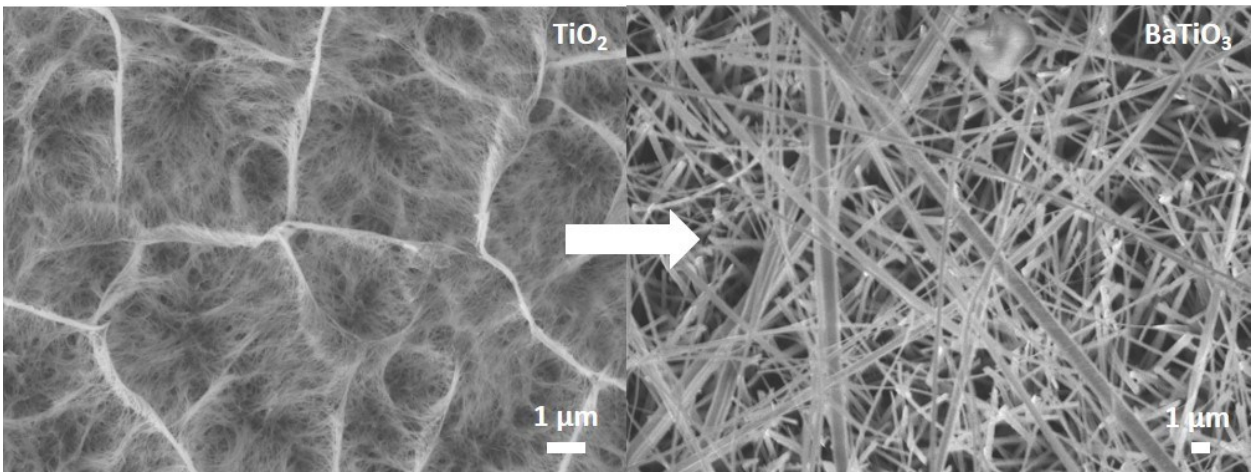


**Figure 7.11** SEM images for the conversion of $TiO_2$ on titanium foil to $BaTiO_3$.

## 7.4 CONCLUSIONS

In Chapter 7, we have synthesized a variety of new promising magnetic or dielectric nanomaterials to be studied for electromagnetic wave absorption. For the most part, these materials all display a shape anisotropy and can be aligned along an easy axis upon exposure to an external magnetic or electric field. An interesting study would involve comparing the electromagnetic response of these materials while aligned along their easy axis and while randomly oriented in order to determine the effect of shape anisotropy on electromagnetic properties and electromagnetic wave absorption. Findings from a study such as this could have large implications for future electromagnetic wave absorption technologies. We have also synthesized $Fe_{2.15}Cr_{0.85}Se_4$, a hard magnetic alloy with composition tunable coercivity and magnetization. This material has never been explored for electromagnetic wave absorption and should be characterized. The work presented in this chapter should be used as a starting point for the exploration of tunable electromagnetic wave absorbing materials.

## 7.5 RERFERENCES


1. Jizhai Cui, Scott M Keller, Cheng-Yen Liang, Gregory P Carman & Christopher S Lynch. Nanoscale Magnetic Ratchets Based on Shape Anisotropy. *Nanotechnology* **28**, (2017).
2. Kinjal Gandha, Kevin Elkins, Narayan Poudyal, Xubo Liu & J. Ping Liu. High Energy Product Developed from Cobalt Nanowires. *Scientific Reports* **4**, (2014).
3. K. J. Vinoy & R. M. Jha. *Radar Absorbing Materials: From Theory to Design and Characterization*. (Kluwer Academic Publishers, 1996).
4. K. J. Vinoy & R. M. Jha. Trends in Radar Absorbing Materials. *Academy Proceedings in Engineering Sciences* **20**, 815–850 (1995).
5. Aneesh Koka & Henry A. Sodano. A Low-Frequency Energy Harvester from Ultralong, Vertically Aligned BaTiO3 Nanowire Arrays. *Adv. Energy Mater.* **4**, 1301660 (2014).
6. Zhi Zhou, Haixong Tang & Henry A. Sodano. Vertically Aligned Arrays of BaTiO3 Nanowires. *ACS Appl. Mater. Interfaces* **5**, 11894–11899 (2013).
7. Yongmin Ko, Hyunhee Baek, Younghoon Kim, Miseon Yoon & Jinhan Cho. Hydrophobic Nanoparticle-Based Nanocomposite Films Using In Situ Ligand Exchange Layer-by-Layer Assembly and Their Nonvolatile Memory Applications. *ACS Nano* **7**, 143–153 (2013).
8. Shao-jie Da Li, Wei Liu & Zhidong Zhang. High Curie Temperature and Coercivity Performance of Fe3-xCrxSe4 Nanostructures. *Nanoscale* **7**, 5395–5402 (2015).
9. Haiyan Sun *et al.* Solvothermal Synthesis of Tunable Electroactive Magnetite Nanorods by Controlling the Side Reaction. *J. Phys. Chem. C* **116**, 5276–5281 (2012).
10. Yaghoub Soumare *et al.* Kinetically Controlled Synthesis of Hexagonally Close-Packed Cobalt Nanorods with high Magnetic Coercivity. *Adv. Funct. Mater.* **19**, 1971–1977 (2009).

11. Sanjay Kulkarni, Mahesh Alurkar & Anil Kumar. Polymer Support with Schiff Base Functional Group with Cobaltous Palmitate as Oxidation Catalyst for Cyclohexane. *Appl. Catal. A* **142**, 243–254 (1996).

# Chapter 8. Conclusions and Future Directions

## 8.1 CONCLUSIONS AND FUTURE DIRECTIONS

Utilization of the unique properties of nanoscale materials to help better understand and improve the current state of radar absorbing materials (RAMs) has motivated the work presented throughout this dissertation. In the rapidly advancing technological world which exists today, it is more important than ever that new radar absorbing technologies are developed to meet the demands of consumers.[1–4] In the public health sector, new RAMs are needed to protect humans from electromagnetic radiation emitted from cell phones, lap tops, and other portable media devices.[5–7] In the military and defense sector, new RAMs are needed to combat the inevitable improvements in radar detection systems and help our military achieve stealth.[8–10] Through our investigation of RAMs we put extra emphasis on their real world applicability and attempted to be as realistic as possible in designing our experiments. While much of the research in this field in academia is directed towards developing new RAM technologies regardless of end stage applicability, our approach was to step back and lay the ground work for developing RAMs from first principles by investigating the fundamentals by which these materials work.[10] With this approach, it may actually be possible to build the 'perfect absorber' from first principles as each stage of the absorber development process will be studied in immense detail.

Our first study presents a detailed investigation of the effect of nanoparticle size on electromagnetic wave absorption properties.[11] In this particular case, we compared the electromagnetic wave absorption capabilities of five different sizes of $Fe_3O_4$ nanoparticles: 5 nm, 10 nm, 20 nm, 100 nm, and a micron size. Using fundamental organic solution synthesis theory and techniques, we were able to develop protocols for the synthesis of monodisperse $Fe_3O_4$ in the

nanoscale sizes (5 nm, 10 nm, 20 nm, and 100 nm), while the micron size was purchased from a commercial supplier.[12–14] We then characterized the structural, compositional, and magnetic properties of the particles and measured their electromagnetic wave absorption properties. It was seen that as nanoparticle size increases, the intensity of electromagnetic wave absorption increases while the frequency of absorption decreases (i.e. larger particles are more effective than smaller particles and are effective at lower frequencies). Upon further investigation it was seen that this behavior is largely due to the saturation magnetization, $M_s$, of the materials. The larger particles had a larger $M_s$, and thus a higher magnetic loss, or $\mu''$, and were more effective at absorbing the electromagnetic radiation.[15,16] We then investigated the effect of mixing sizes of $Fe_3O_4$ together and determined that the response is governed by standard exchange coupling mechanisms. As a basis for this system has already been laid, future studies using this system could involve the construction of a multilayer absorber with discretely arranged spacing between the layers. It would be an interesting study to determine if layered sizes have the same effect as mixed sizes, and at what spacing the layers become apparent in the electromagnetic absorption response.

Following the blueprint in the first study, the second study presents a detailed investigation of the effect of doping on electromagnetic wave absorption properties.[17] In this study, we compared the electromagnetic wave absorption capabilities of five different 5 nm ferrites of composition **M**$Fe_2O_4$: $Fe_3O_4$, $CoFe_2O_4$, $MnFe_2O_4$, $CuFe_2O_4$, and $MgFe_2O_4$. Once again, using fundamental organic solution synthesis theory and techniques, we were able to develop protocols for the synthesis of monodisperse ferrite nanoparticles of size ~5 nm and of **M**:Fe composition 1:2.[14] We then characterized the structural, compositional, and magnetic properties of the particles and measured their electromagnetic wave absorption properties. In terms of

electromagnetic wave absorption intensity, the following trend was observed: $CoFe_2O_4 \approx MnFe_2O_4 \approx Fe_3O_4 < MgFe_2O_4 < CuFe_2O_4$. In terms of electromagnetic wave absorption frequency, the following trend was observed: $CuFe_2O_4 < CoFe_2O_4 < MnFe_2O_4 \approx MgFe_2O_4 \approx Fe_3O_4$. Interestingly enough, upon further investigation it was seen that this behavior is largely due to the dielectric properties of the materials rather than the magnetic properties. As our study focused on the magnetic properties of the materials, a future study with this system should delve into the dielectric properties of the materials in order to determine how they play a role in governing the electromagnetic absorption responses, and why the dielectric properties have a greater influence than do the magnetic properties.

The third study follows the same blueprint as the first and second, and presents a detailed investigation of the effect of alloying on electromagnetic wave absorption properties. In this effort, we compared the electromagnetic wave absorption capabilities of three different 5 nm magnetic materials and their bimetallic alloys: Fe, Co, Ni, FeCo, CoNi, and $FeNi_2$. Once again, using fundamental organic solution synthesis theory and techniques, we were able to develop protocols for the synthesis of monodisperse nanoparticles of size ~5 nm.[18–21] We then characterized the structural, compositional, and magnetic properties of the particles and measured their electromagnetic wave absorption properties. In terms of electromagnetic wave absorption intensity, the following trend was observed: CoNi ≈ CoFe ≈ FeNi2 ≈ Ni < Co < Fe. In terms of electromagnetic wave absorption frequency, the following trend was observed: Fe < Co < Ni < $FeNi_2$ ≈ CoNi < CoFe. It was expected that the alloyed particles would display a hybrid response of their two ground state metal components, however upon further investigation it was seen that all of the alloyed nanoparticles display less effective electromagnetic wave absorption capabilities than their ground state counterparts and are in fact worse absorbers. A future study

with this system should further explore the effects of alloying with other systems and systems of higher order, such as a ternary or quaternary alloy, to gain a more firm understanding of the role that alloying plays in governing the electromagnetic absorption responses. A promising study would be to investigate the electromagnetic wave absorption properties of high entropy alloys, an area of research gaining much attention in recent years.

In Chapter 5, we leave the realm of fundamental investigation of electromagnetic wave absorption and enter into a more application-like study. In this chapter, we aimed to take our findings in Chapters 2 – 4 one step further and apply a radar absorbing material to natural basswood to determine if the same principles discovered at the fundamental level still hold when the absorbing media is embedded into a porous host matrix. In this study, we once again utilized our organic solution synthesis expertise to synthesize 10 nm $Fe_3O_4$ nanoparticles.[13] Through trial and error we were able to develop an efficient and adequate impregnation process through which the $Fe_3O_4$ was inserted into the pores of the basswood. We then characterized the structural, compositional, and magnetic properties of the wood/particle composite and measured the electromagnetic wave absorption properties. The data shows that the basic physics and principles studied in Chapters 2 – 4 still hold when the nanoparticles are embedded into a wood matrix, and there is no reason to believe that this process couldn't be applied to a variety of hosts or templates, such as polymers or porous metal foams. In addition, we have shown that a porous material may in fact have improved electromagnetic absorption capabilities, which could lead to the development of lighter weight, more cost effective microwave absorbers for planes, submarines, or other military vessels. A future effort in this direction should involve expanding this process into a variety of host media, such as metal foams or other porous metals, which will be more applicable to functional building materials for planes or submarines.

Our next exploration continues the theme of magnetic nanoparticles but shifts focus to their biofunctionalization and applications in the biomedical and public health sectors. Specifically, we look into the use of magnetic nanoparticles as vehicles for use in drug delivery in the treatment of circulating tumors cells (CTCs) as well as for use in wastewater treatment and virus capture techniques.[22–25] Similar to Chapter 5, we utilized our organic solution synthesis expertise to synthesize 10 nm $Fe_3O_4$ nanoparticles. Through a systematic investigation we were able to develop efficient and adequate techniques for the preparation of these nanoparticles as biofunctional materials. Our efforts presented the entire protocol development process from start to finish: synthesis of the superparamagnetic iron oxide, ligand exchange and phase transfer of the particles to aqueous solution, and antibody conjugation.[13,14,26] Included in our investigation was the screening of appropriate particle size and appropriate length of water soluble PEG ligands for adequate magnetic capture either *in vivo* or *in vitro*. In both cases, our findings suggest that there is an optimum size of nanoparticle, and optimum length of PEG chain for magnetic capture. The optimum size is an intermediate size of ~10 nm, as smaller particles are too stable in aqueous environment and cannot be captured, while larger particles succumb to gravitational sedimentation forces too quickly to be considered for an *in* vivo experiment. Similarly, the optimum chain length PEG was determined to be intermediate size as it is long enough to promote particle stabilization to prevent sedimentation under gravitational forces, but still allow for capture in the presence of an external magnetic field. Future work should build on this study and treat this study as a template for which drug delivery and/or virus capture processes involving nanomaterials could be developed.

Finally, our last endeavor circles back to the application of magnetic nanoparticles for electromagnetic wave absorption and explores the synthesis of various magnetic materials with a

shape anisotropy that could be used for electromagnetic wave absorption.[27] For this study, rods and wires were predominantly chosen due to the large difference in the magnetic properties the materials display when aligned to a magnetic field along the easy axis in comparison with a random orientation.[9,10] Stemming from the tunability in the magnetic or dielectric properties, it is thought that an aligned vs. randomly oriented materials will also display tunable electromagnetic wave absorption properties, and can thus be used as advanced materials for electromagnetic wave absorption simply by adjusting the strength of the magnetic or electric field present. Materials synthesized in this work include $Fe_3O_4$ nanorods, Co nanowires, Co nanocubes, and Co nanorods.[28,29] Future studies in this direction should involve comparing the electromagnetic response of these materials while aligned along their easy axis and while randomly oriented in order to determine the effect of shape anisotropy on electromagnetic properties and electromagnetic wave absorption.

## 8.2 REFERENCES


1. M. Salerno *et al.* Fluorescence imaging of surface plasmon fields. *Appl. Phys. Lett.* **10**, 404–406 (2002).
2. M. Todorovic, S. Schultz, J. Wong & A Scherer. Writing and reading of single magnetic domain per bit perpendicular patterned media. *Appl. Phys. Lett.* **74**, 2516–2518 (1999).
3. M. Rutnakornpituk *et al.* Formation of cobalt nanoparticle dispersions in the presence of polysiloxane block copolymers. *Polymer* **43**, 2337–2348 (2002).
4. R. S. Molday & D. Mackenzie. Immunospecific ferromagnetic iron-dextran reagents for the labeling and magnetic separation of cells. *J Immunol Methods* **52**, 353–367 (1982).
5. National Research Council (U.S.). Committee on Identification of Research Needs Relating to Potential Biological or Adverse Health Effects of Wireless Communications Devices. *Identification of Research Needs Relating to Potential Biological or Adverse Health Effects of Wireless Communication Devices*. (National Academic Press, 2008).
6. E. Seidenberg & H. Schimpf. Aspects of automatic target recognition with a two-frequency millimeter wave SAR. *P. Soc. Photo-Opt. Ins.* **4033**, 167–177 (2000).
7. A. Ahlbom *et al.* Possible effects of electromagnetic fields (EMF) on human health--opinion of the scientific committee on emerging and newly identified health risks (SCENIHR. *Toxicology* **246**, 248–250 (2008).
8. E. F. Knott, J. F. Shaeffer & M. T. Tuley. *Radar Cross Section*. (SciTech Pub., 2004).
9. K. J. Vinoy & R. M. Jha. *Radar Absorbing Materials: From Theory to Design and Characterization*. (Kluwer Academic Publishers, 1996).
10. K. J. Vinoy & R. M. Jha. Trends in Radar Absorbing Materials. *Academy Proceedings in Engineering Sciences* **20**, 815–850 (1995).

11. Michael Giroux *et al.* Size-Dependent Electromagnetic Absorption Properties of Iron Oxide (Fe3O4) Nanomaterials. *In Preparation.*
12. S. Ni *et al.* Hydrothermal synthesis and microwave absorption properties of Fe3O4 nanocrystals. *J. Phys. D: Appl. Phys.* **42**, (2009).
13. Jin Xie, Chenjie Xu, Nathan Kohler, Yanglong Hou & Shouheng Sun. Controlled PEGylation of Monodisperse Fe3O4 Nanoparticles for Reduced Non-Specific Uptake by Macrophage Cells. *Adv. Mater.* **19**, 3163–3166 (2007).
14. Shouheng Sun *et al.* Monodisperse MFe2O4 (M = Fe, Co Mn) Nanoparticles. *J. Am. Chem. Soc.* 273–279 (2004).
15. R. F. Soohoo. *Microwave Magnetics*. (Harper and Row Publishers, 1985).
16. L. Z. Wu, J. Ding, H. B. Jiang, L. F. Chen & C. K. Ong. Particle size influence to the microwave properties of iron based magnetic particulate composites. *JMMM* **285**, 233–239 (2005).
17. Michael Giroux *et al.* Radar Absorbing MFe2O4 (M = Fe, Co, Cu, Mn, Mg) Nanomaterials. *In Preparation.*
18. Yuping Bao, Wei An, C. Heath Turner & Kannan M. Krishnan. The Critical Role of Surfactants in the Growth of Cobalt Nanoparticles. *Langmuir* **26**, 478–483 (2010).
19. Sheng Peng, Chao Wang, Jin Xie & Shouheng Sun. Synthesis and Stabilizatoin of Monodisperse Fe Nanoparticles. *J. Am. Chem. Soc.* **128**, 10676–10677 (2006).
20. Toshitaka Ishizaki, Kenichi Yatsugi & Kunio Akedo. Effect of Particle Size on the Magnetic Properties of Ni Nanoparticles Synthesized with Trioctylphosphine as the Capping Agent. *Nanomaterials* **6**, (2016).

21. Yuanzhi Chen *et al.* Chemical Synthesis of Monodisperse Fe-Ni Nanoparticles via a Diffusrion-Based Approach. *J. Nanosci. Nanotechnol.* **10**, 3053–3059 (2010).
22. Gaorav P. Gupta & Joan Massague. Cancer Metastasis: Building a Framework. *Cell* **127**, (2006).
23. Cristoph A. Klein. The Metastasis Cascade. *Science* **321**, 1785–1787 (2008).
24. Anne C. Chiang & Joan Massague. Molecular Basis of Metastasis. *N. Engl. J. Med.* **359**, 2814–2823 (2008).
25. Shyamala Maheswaran & Daniel A. Haber. Circulating Tumor Cells: A Window into Cancer Biology and Metstasis. *Curr Opin Genet Dev.* **20**, 96–99 (2010).
26. Nicola Pinna *et al.* Magnetite Nanocrystals: Nonaqueous Synthesis, Characterization, and Solubility. *Chem. Mater.* **17**, 3044–3049 (2005).
27. Jizhai Cui, Scott M Keller, Cheng-Yen Liang, Gregory P Carman & Christopher S Lynch. Nanoscale Magnetic Ratchets Based on Shape Anisotropy. *Nanotechnology* **28**, (2017).
28. Kinjal Gandha, Kevin Elkins, Narayan Poudyal, Xubo Liu & J. Ping Liu. High Energy Product Developed from Cobalt Nanowires. *Scientific Reports* **4**, (2014).
29. Haiyan Sun *et al.* Solvothermal Synthesis of Tunable Electroactive Magnetite Nanorods by Controlling the Side Reaction. *J. Phys. Chem. C* **116**, 5276–5281 (2012).

## Curriculum Vita

Michael Giroux was born in Olney, Maryland and raised in Damascus, Maryland. He attended Washington College beginning in the fall of 2010 and graduated in the spring of 2014 with a major in chemistry and a minor in mathematics. At Washington College, he conducted research in both organic chemistry, while helping to synthesize $C_{72}$, "the missing fullerene", and in materials science, while studying the control of hydrophobicity in common zeolites. His work resulted in a publication on the control of hydrophobicity in Zeolites X and A, and an undergraduate thesis on the entirety of his work. Following completion of his undergraduate degree, Michael began his Ph.D. in Chemical and Biomolecular Engineering at The Johns Hopkins University in Baltimore, Maryland in the fall of 2014, studying the applications of magnetic nanomaterials as electromagnetic wave absorbers.

**Publications:**

1. "Size-Dependent Electromagnetic Wave Absorption Properties of Iron Oxide ($Fe_3O_4$) Nanomaterials." Giroux, M.; Xue, H.; Goyal, M.M.; Zhang, S.; Mohapatra, J.; Wang, C. *In preparation.*

2. "Radar Absorbing $MFe_2O_4$ (M = Fe. Co, Cu, Mn, Mg) Nanomaterials." Giroux, M.; Cocolas, A.; Hoffmann, E.; Ahn, H.J.; Xue, H.; Goyal, M.M.; Zhang, S.; Mohapatra, J.; Wang, C. *In preparation.*

3. "Alloying Effects on Radar Absorbing Nanomaterials." Giroux, M.; Hoffmann, E.; Ahn, H.J.; Xue, H.; Goyal, M.M.; Zhang, S.; Mohapatra, J.; Wang, C. *In preparation.*

4. “Electromagnetic Wave Absorbing Wood Created Through the Impregnation of Magnetic Nanomaterials.” Giroux, M.; Gan, W.; Zhang, S.; Goyal, M.M.; Hu, L.; Wang, C. *In preparation.*

5. “Tunable Intrinsic Strain in Two-dimensional Transition Metal Electrocatalysts.” Wang, L.; Zeng, Z.; Gao, W.; Maxson, T.; Raciti, D.; Giroux, M.; Pan, X.; Wang, C.; Greeley, J. *Science.* **2019**, 363, 870 – 874.

6. “Migration of Cobalt Species within Mixed Platinum-Cobalt Oxide Bifunctional Electrocatalysts in Alkaline Electrolytes.” Wang L.; Zeng, Z.; Ma, C.; Xu, F.; Giroux, M.; Chi, M.; Greeley, J.; Wang, C. *Journal of the Electrochemical Society.* **2019**, 166 (7), F3093 – F3097.

7. “Core-Shell Nanostructured Cobalt-Platinum Electrocatalysts with Enhanced Durability.” Wang, L.; Gao, W.; Liu, Z.; Zeng, Z.; Liu, Y.; Giroux, M.; Chi, M.; Wang, G.; Greeley, J.; Pan, X.; Wang, C. *ACS Catalysis.* **2018**, 8, 35 – 42.

8. “Plating Precious Metals on Nonprecious Metal Nanoparticles for Sustainable Electrocatalysts.” Wang, L.; Zeng, Z.; Ma, C.; Liu, Y.; Giroux, M.; Chi, M.; Jin, J.; Greeley, J.; Wang, C. *Nano Letters.* **2017**, 17, 3391 – 3395.

9. “Platinum-nickel Hydroxide Nanocomposites for Electrocatalytic Reduction of Water.” Wang, L.; Zhu, Y.; Zeng, Z.; Lin, C.; Giroux, M.; Jiang, L.; Han, Y.; Greeley, J.; Wang, C.; Jin, J. *Nano Energy.* **2017**, 31, 456 – 461.

10. “Conductive Wood Nanostructure for High Performance Electromagnetic Interference Shielding.” Gan, W.; Chen, C.; Giroux, M.; Zhong, G.; Wang, Y.; Ping, W.; Song, J.; Xu, S.; He, S.; Jiao, M.; Wang, C.; Hu, L. *Submitted.*

11. “Unprecedented Electromagnetic Interference Shielding from Three-dimensional Bicontinuous Nanoporous Graphene.” Kashani, H.; Giroux, M.; Johnson, I.; Han, J.; Wang, C.; Chen, M. *Submitted.*

12. “Synthesis of Metal Oxide Nanoparticles by Rapid, High-Temperature 3D Microwave Heating.” Zhong, G.; Xu, S.; Chen, C.; Kline, D.; Giroux, M.; Pei, Y.; Jiao, M.; Liu, D.; Mi, R.; Xie, H.; Yang, B.; Wang, C.; Zachariah, M.; Hu, L. *Submitted.*

13. “An Undergraduate Research Experience: Synthesis, Modification, and Comparison of Hydrophobicity of Zeolites A and X.” Giroux, M.; Sahadeo, E.; Libera, R.; Maurizi, A.; Giles, I.; Marteel-Parrish, A. *Polyhedron.* **2016**, 114, 42 – 52.